DEVELOPMENT OF AN EPITHERMAL/FAST NEUTRON SCATTERING TECHNIQUE FOR VOID FRACTION MEASUREMENT IN TWO-PHASE SYSTEMS WITH PORTABLE NEUTRON SOURCES

by

PETER S.L. YUEN, B.Sc.(Hons), M.Sc., M.Eng.

A Thesis
Submitted to the School of Graduate Studies
in Partial Fulfillment of the Requirement
for the Degree
Doctor of Philosophy
McMaster University

1985

ISBN 0-315-30582-7

VOID MEASUREMENT WITH PORTABLE NEUTRON SOURCES

DOCTOR OF PHILOSOPHY (1985) McMASTER UNIVERSITY
(Engineering Physics and Nuclear Engineering) Hamilton, Ontario

TITLE: Development of an Epithermal/Fast Neutron Scattering Technique for Void Fraction Measurement in Two-Phase Systems with Portable Neutron Sources

AUTHOR: Peter S.L. Yuen, B.Sc.(Hons) (University of Manitoba)
M.Sc. (University of Manitoba)
M.Eng. (McMaster University)

SUPERVISOR: Professor S. Banerjee
Professor D.A. Meneley

NUMBER OF PAGES: xix, 260

Abstract

A technique to measure void fraction in a two-phase flow system using the multiple scattering of neutrons from portable neutron sources was investigated. There exists evidence from a previous investigation with a neutron beam extracted from a nuclear research reactor, that the basic technique is attractive. The counting rate of multiply-scattered, thermalized neutrons was found to be nearly linear with void fraction and independent of flow regime. However, early investigation with a portable neutron source revealed that these advantages were not realized in all situations.

In the present work, the objective, then was to determine the conditions under which the advantages of linearity and flow pattern independence could be achieved with portable neutron sources. Experiments were carried out to study the effect of various parameters on the neutron counting rate. It was found that parameters like symmetry of neutron sources, test-section to detector distances, and detection energy bin did not affect the technique significantly. More significant parameters were flow patterns, test-section inside diameter, test-section wall thickness, presence of neutron reflector material around the test section, and incident neutron spectrum. From the trends observed in the parametric study, it was found that near linearity with void fraction and flow pattern independence could be achieved by tailoring the energy spectrum of the incident neutron beam, e.g. by moderating neutrons emitted by a given source. The amount of

moderation required decreased with test-section inside diameter, test section wall thickness, and the addition of neutron reflector material surrounding the test-section. This finding was verified with experiments conducted for four different test sections.

The reasons for these experimental observations were clarified by studying the effect of monoenergetic incident neutron groups with Monte Carlo simulation, the result of which was further interpreted with thermalization probability considerations. The Monte Carlo study revealed that each monoenergetic neutron group results in a different response in terms of thermalized neutron counting rate, which, in general, is neither linear with void fraction nor flow regime independent. However, linearity and flow regime independence could be achieved by superimposing the effect of different energy groups, i.e. by tailoring the neutron spectrum. In practice, this is achieved by appropriately moderating the neutron beam from a given source.

Based on the understanding achieved, a conceptual design of a portable void fraction meter, and a design procedure are suggested.

Acknowledgements

It is with pleasure and gratitude that I acknowledge the useful discussions and help of Dr. E. Hussein in Monte Carlo calculations throughout the course of the present work. I would like to thank Mrs. B. Martin for her encouragement and care for me and my family during those seemingly lonely and helpless hours. Gratefully acknowledged are the useful discussions with Professors A.A. Harms and T.J. Kennett of McMaster University. I would like to thank Dr. W.T. Hancox and Mr. K.H. Ardron of Atomic Energy of Canada Limited for their encouragement to finish this thesis. I am grateful to my wife, Agnes, for her patience, tolerance, encouragement, and understanding. Thanks are due to Mr. M. Lau for the use of his computer and his help in typing this thesis. Finally, for the financial support, patience, care, kindness, understanding, encouragement, guidance, and enlightenment, of my advisors, Professors S. Banerjee and D.A. Meneley, my greatest gratitude.

TABLE OF CONTENTS

LIST OF FIGURES

LIST OF TABLES

To my wife, Agnes, and my kids

CHAPTER ONE

THE PROBLEM

1.1 IMPORTANCE OF TWO-PHASE FLOW IN NUCLEAR ENGINEERING AND OTHER ENERGY RELATED INDUSTRIES

Gas-liquid two-phase flow is found in many industries. Obvious examples are industrial heat exchangers where boiling and condensing flows are involved. Other two-phase flow systems are found in the process, chemical, petroleum and related industries. In these industries, the major application is the transport of gas-liquid mixtures in pipelines and also in boilers, condensers, distillation columns, and absorption towers. Two-phase flow is also important in the conventional power industry such as steam plants with turbine, boiler, and condenser systems. Air conditioning and refrigeration, cryogenics, and sewage treatment are other common industrial systems involving two-phase flow.

Although two-phase flow has received attention from a variety of industries, it received the most impetus from the nuclear power industry over the past three decades. Two-phase flow dominates the coolant circuit of boiling water reactors (BWR) where coolant is allowed to boil in the reactor core, and steam is produced to drive a turbine. In a pressurized water reactor (PWR) or pressurized heavy water reactor such as the CANDU type, the primary heat transport system is kept under high pressure to prevent boiling. However, boiling two-phase flow may occur during a postulated Loss of Coolant Accident (LOCA) where

the reactor coolant goes through depressurization due to a break in the coolant circuit. Boiling two-phase flow is, however, the normal mode of operation of pressurized reactor steam generators (secondary side) where the pressure is kept lower so that the water boils after heat exchange with the primary heat transport system. It is thus clear that, in nuclear reactors, two-phase flow study is important not only in steady state design (normal operation) but also for predictions of system behaviour in transients, and particularly, in postulated accidents.

Because of the great importance of two-phase flow in the nuclear as well as non-nuclear industry, it is appropriate here to discuss briefly the behaviour of two-phase flow.

1.2 BEHAVIOUR OF TWO-PHASE FLOW

An essential feature of two-phase flow is the presence of moving interfaces that make theoretical predictions of flow parameters immensely more difficult than in single-phase flow (for reviews of single-phase flow, see for example, Bird et al <1>). To further complicate the problem, these interfaces are distributed in many different patterns depending on many flow parameters such as gas and liquid superficial velocities and heat transfer. These patterns are known as flow regimes. In horizontal systems, commonly encountered flow regimes are bubbly, slug, stratified, wavy stratified, annular, and dispersed flow. In vertical systems, the main flow regimes are bubbly, slug, churn, annular, and dispersed flow. In rewetting situations found in quenching a very hot pipe, the liquid may flow in the

core region, resulting in inverted annular flow. Excellent discussions and predictions of these common flow regimes are found in Collier <2>, Wallis <3>, and Ginoux <4>.

Successful predictions of two-phase flow behaviour depend on the use of appropriate models. The main structure of any two-phase flow model is provided by averaged equations for the conservation of mass, momentum, and energy. These equations by themselves are not "closed", but require empirical information, sometimes called "constitutive" relationships, that are dependent on flow regimes. This situation arises because, in analogy to turbulent single-phase flow, it is often necessary and sufficient to predict two-phase flow parameters that are "averaged" in some sense. Thus, averaging procedures are followed to derive averaged conservation equations from the local instantaneous equations. Excellent reviews and discussions of these procedures are found in Agee et al <5>, Boure <6>, Hughes et al <7>, and Yadigaroglu and Lahey <8>. The resulting conservation equations are much simpler than the original formulation. Without much loss of generality, these equations, in one-dimensional form, and along the direction of flow in a duct (z-axis), are

Mass

$$\frac{\partial}{\partial t}\overline{\alpha_k \langle \rho_k \rangle} + \frac{\partial}{\partial z}\overline{\alpha_k \langle \rho_k u_k \rangle} = -\overline{\langle \dot{m}_k \rangle_i} \qquad (1.1)$$

Momentum

$$\frac{\partial}{\partial t}\overline{\alpha_k \langle \rho_k u_k \rangle} + \frac{\partial}{\partial z}\overline{\alpha_k \langle \rho_k u_k^2 \rangle} + \overline{\alpha_k \frac{\partial}{\partial z}\langle p_k \rangle} - \frac{\partial}{\partial z}\overline{\alpha_k \langle \tau_{zz,k} \rangle} - \overline{\Delta p_{ki} \frac{\partial}{\partial z}\alpha_k}$$

$$= \overline{\alpha_k \langle \rho_k F_{z,k} \rangle} - \overline{\langle \dot{m}_k u_k \rangle_i} - \overline{\langle \Delta p'_{ki} \rangle_i} + \overline{\langle (\vec{n}_k \cdot \vec{\tau}_z) \rangle_i} + \overline{\langle (\vec{n}_w \cdot \vec{\tau}_z) \rangle_w} \qquad (1.2)$$

Energy

$$\frac{\partial}{\partial t}\alpha_k\langle\rho_k(h_k+\frac{u_k^2}{2})\rangle + \frac{\partial}{\partial z}\alpha_k\langle\rho_k u_k(h_k+\frac{u_k^2}{2})\rangle$$

$$-\alpha_k\frac{\partial}{\partial t}\langle p_k\rangle + \Delta p_{ki}\frac{\partial}{\partial t}\alpha_k + \frac{\partial}{\partial z}\alpha_k\langle q_{z,k}\rangle - \frac{\partial}{\partial z}\alpha_k\langle\vec{n}_z\cdot(\vec{\tau}_k\cdot\vec{v}_k)\rangle$$

$$= -\langle[\dot{m}_k(h_k+\frac{u_k^2}{2}) + \vec{n}_k\cdot\vec{v}_i\Delta p'_{ki} + \vec{n}_k\cdot\vec{q}_k - \vec{n}_k\cdot\vec{v}_k\cdot\vec{\tau}_k]\rangle_i$$

$$- \langle(\vec{n}_k\cdot\vec{q}_k)\rangle_w + \alpha_k\langle(\rho_k\vec{v}_k\cdot\vec{F}_k + Q_k)\rangle \qquad (1.3)$$

In the above equations, the subscript k refers to the phase k, i refers to total volume average of a quantity summed over the interfacial area, and w refers to the variable's value at the wall. Bracketed quantities are volume averages, while quantities with over-bars are ensemble averages. Reviews of these averaging operators from a mathematical viewpoint have been given by Delhaye and Achard <9>, Ishii <10>, and Nigmatulin <11>. The quantity α_k is the volume fraction occupied by phase k over the total flow volume. Other flow parameters such as density, velocity along the z-direction, pressure, energy, and enthalpy are denoted by ρ, u, p, E, and h respectively. The quantity $\dot{m}_k$ is the interphase mass transfer, $\vec{F}$ is the external force, $\vec{\vec{\tau}}$ is the stress tensor, $\vec{n}_k$ is a unit vector normal to the interface, $\vec{q}$ is the heat flux, and Q is the external heat source. The quantity

Δp_{ki} is the difference between the average interfacial and average phase pressure and $\Delta p'_{ki}$ is the difference between the local and average interfacial pressure.

The above equations can be further supplemented with interfacial jump conditions (Banerjee and Chan <12>) that pose certain restrictions on the right hand side of the equations, the equations of state for each phase, and the relationship $\Sigma \alpha_k = 1.0$. This approach of writing separate sets of equations for each phase and coupling them with interfacial jump conditions is generally called "multifluid" modelling. This approach is relatively new and is still in the developmental stage. However, it has been shown (Banerjee and Hancox<13>) that for many physically important situations, the most powerful and physically appealing approach is to consider the interaction between the phases explicitly and therefore the "multifluid" approach is necessary.

Generally, in "multifluid" modelling, although the averaged conservation equations are simpler than the original instantaneous and local equations, information is lost in the averaging process and, to complete any model, the missing information must be supplied by auxilliary relationships.

While Eqs. (1.1), (1.2), (1.3) together with the associated constitutive equations appear to result in a very complicated model, considerable simplification can be obtained in some situations where the level of sophistication embodied in the multifluid model is not needed. The approach is then to combine the separate phase conservation equations into mixture equations.

Without elaborating on the details of simplification of multifluid conservation equations into mixture equations, it is sufficient to comment that, with jump condition applied to interfaces and summing the phasic conservation equations over the two-phases, the following "mixture" conservation equations are obtained:

Mass

$$\frac{\partial \rho}{\partial t} + \frac{\partial G}{\partial z} = 0 \tag{1.4}$$

where mixture density $\rho = \Sigma\, \alpha_k \rho_k$

mixture mass velocity $G = \Sigma\, \alpha_k \rho_k u_k$

Momentum

$$\frac{\partial G}{\partial t} + \frac{\partial}{\partial z}(G^2 v') + \frac{\partial p}{\partial z}$$

$$= \sum \frac{1}{V} \int_{a_{kw}} \vec{n}_z \cdot (\vec{n}_w \cdot \vec{\tau}_k) ds$$

$$= \tau_w \tag{1.5}$$

where $v' = \Sigma\, x_k^2 / \alpha_k \rho_k$

and x_k = flow quality of phase k

$= (\alpha_k \rho_k u_k)/(\Sigma\, \alpha_k \rho_k u_k)$

τ_w = wall shear stress

Energy

$$\frac{\partial}{\partial t}\rho\left(e + \frac{G^2 v'}{2\rho}\right) + \frac{\partial}{\partial z}\left[G\left\{h + \frac{(Gv'')^2}{2}\right\}\right]$$

$$= -\sum \frac{1}{V} \int_{a_{kw}} (\vec{n}_{kw} \cdot \vec{q}_k)\, ds$$

$$= q_w \qquad (1.6)$$

where

q_w = total wall heat flux

$v''^2 = \Sigma (x_k^3 / (\alpha_k \rho_k)^2)$

h = flow enthalpy = $\Sigma x_k h_k$

e = internal energy = $\Sigma \hat{x}_k e_k$

$\hat{x}_k = (\alpha_k \rho_k)/(\Sigma \alpha_k \rho_k)$

In general, in the above mixture equations, the phases are not at thermal or mechanical equilibrium, so empirical correlations still have to be used to close Eqs. (1.4), (1.5), and (1.6), in addition to the usual ones for wall shear stress and heat flux. The equations of state for each phase $h_k = h_k(p_k, \rho_k)$ are also assumed to be known.

The mixture equations can be further simplified depending on the application. If the phases are assumed to be in equilibrium with each other, then a particularly simple and quite useful set of mixture equations is obtained. It is called the homogeneous equilibrium (equal velocity-equal temperature) model and essentially ignores all interfacial transfer processes. This model is a well established one and is widely used in practice to calculate quantities like pressure drop and wall-fluid heat transfer. This is a sort of pseudo-single phase formulation. In

particular, for steady state one-dimensional homogeneous equilibrium flow in a duct, the conservation equations become

Mass

$$G = \rho_m u = \text{constant} \tag{1.7}$$

Momentum

$$G\frac{du}{dz} = -G\frac{dp}{dz} - \frac{P}{A}\tau_w - \rho_m g \cos\theta \tag{1.8}$$

Energy

$$\frac{1}{A}\frac{dq}{dz} - \frac{1}{A}\frac{dw}{dz} = G\frac{d}{dz}\left(h + \frac{u^2}{2} + gz\right) \tag{1.9}$$

In the above equations A and P represent the duct area and perimeter, τ_w is the average wall shear stress, dq/dz is the heat transfer per unit length of duct, z is the vertical co-ordinate, and θ is the inclination of the duct to the vertical. The mixture density $\rho_m = \rho_g \alpha + \rho_f(1-\alpha)$ with ρ_g and ρ_f referring to density of the gas and liquid phase respectively.

Thus, dependent on the required level of sophistication, two-phase flow behaviours can be described by different forms of conservation equations for mass, momentum, and energy, viz, multifluid, mixture, or homogeneous mixture equations. In any case, the description must be completed by auxilliary or constitutive relationships.

1.3 NECESSITY FOR DEVELOPMENT OF TECHNIQUES FOR VOID FRACTION MEASUREMENT

Re-examining the different forms of conservation equations in the multifluid model (Eq.(1.1-1.3)), the mixture

equation model (Eq.(1.4-1.6)), or the homogeneous mixture model (Eq.(1.7-1.9)), it is noticed that the parameter void fraction α appears either explicitly or implicitly in all these equations. This is not surprising as a two-phase flow implies that α lies between 0 and 1. The void fraction α is thus an important two-phase flow parameter profoundly affecting the behaviour of two-phase flow. For example, α determines the average density ρ, pressure drop, and heat transfer.

Because of the importance of α in two-phase flow, the need to develop a technique to measure this parameter may be considered in terms of modelling (research) and measurement instrumentation (operational flow).

Necessity in Modelling

As mentioned before, the description of two-phase flow must be completed with constitutive relationships supplementing the conservation equations. These constitutive relationships are not universal but differ in different situations. At present, much work is still being conducted in the development of constitutive relationships, particularly those needed to complete the multifluid model. Very often, an accurate measurement of void fraction is necessary in the verification of a proposed constitutive equation. For example, in Eq.(1.2), $\overline{\alpha_k \langle u_k^2 \rangle}$ must be related to $\overline{\alpha_k}\,\overline{\langle u_k \rangle^2}$ by a distribution coefficient C_k by

$$C_k = \overline{\alpha_k \langle u_k^2 \rangle} \,/\, \overline{\alpha_k}\,\overline{\langle u_k \rangle^2} \qquad (1.10)$$

If the form of the distribution coefficients are known, the

l.h.s. of the conservation equations can be written in terms of $\overline{\rho_k}$, $\overline{\alpha_k}$, $\overline{\langle u_k \rangle}$ and $\overline{\langle h_k \rangle}$. At the present stage of knowledge, very little data on distribution coefficients are available. Any proposed form of the distribution coefficients needs verification and an accurate measurement of the local and cross-section averaged void fraction is needed.

Necessity in Measurement Instrumentation

For two-phase flow in operating systems, it is often necessary to measure a given parameter. In order to do so, it may be necessary to measure secondary parameters, such as void fraction. For example, in heavy oil/tarsand industries, high pressure wet steam is used to crack, soften, and pressurize an underground crude formation before oil extraction. It is often necessary to measure the quality x of the wet steam in an a steam injection line. Steam quality x is related to void fraction α by

$$x = 1 \Big/ \left(1 + \frac{\rho_f}{\rho_g} \frac{u_f}{u_g} \frac{(1 - \alpha)}{\alpha} \right) \qquad (1.11)$$

where ρ_f, ρ_g = density of water and steam

u_f, u_g = velocity of water and steam

Thus, in order to measure steam quality x, one must measure α along with ρ_f / ρ_g and u_f / u_g.

From the above discussion, it is clear that techniques to measure void fraction are desirable.

There is a wide range of techniques to measure void fraction to-date. An extensive survey of existing techniques will be given in Chapter 2. As will be clear then, these various techniques have both advantages and disadvantages, and the value of each technique depends on the particular application. In the development of the present technique, neutrons of both high and low energy are used as a probe. Neutrons are chosen because of their ability to penetrate metal pipe walls and their sensitivity to hydrogeneous material. In Chapter 2, this will be discussed in more detail.

CHAPTER TWO

LITERATURE SURVEY AND STATEMENT OF PROBLEM

2.1 INTRODUCTION

In this chapter, a literature survey on various existing techniques to measure void fraction is presented. Some of these techniques are well established and some are still at a developmental stage.

A survey of the literature reveals a variety of void fraction measurement techniques. Excellent review papers on this subject can be found in Banerjee and Lahey <14>, Hewitt and Lovegrove <15>, and Lahey <16>. The literature survey presented in this chapter is by no means exhaustive. However, it should cover the essential areas and most of the latest developments. Towards the end of this chapter, the motivation for the development of the neutron scattering technique is discussed. Work related to the present investigation is briefly reviewed. The objectives and scope of the present work are also defined.

2.2 LITERATURE SURVEY

In a review of void fraction measurement techniques, techniques discussed are often classified either on the basis of techniques used, e.g. local or global, intrusive or non-intrusive, direct or indirect, etc. In the present discussions, the techniques are broadly classified according to the physical principle on which a technique operates. Thus, the techniques

discussed are classified as (1) mechanical, (2) thermal, (3) sonic, (4) electromagnetic radiation, (5) electrical, and (6) nuclear. In discussing each technique, the physical principle is briefly discussed, and a discussion of its advantages and disadvantages as well as its range of application is given.

2.2.1 Mechanical Methods

This class of methods includes quick-closing valves, static head methods, and natural frequency method.

2.2.1.1 Quick-closing valves

This is the most extensively used direct method for measuring void fraction. It measures void fraction directly by simultaneously closing quick-closing valves placed at the inlet and outlet ends of the test section. After measuring the amount of liquid trapped between the two valves, the liquid fraction is determined, and the complement yields the void fraction.

Quick-closing valves have been used to obtain volume averaged void fraction for about three decades. Examples are works of Johnson and Abou-Sabe <17>, Hewitt et al <18>, and more recently, Banerjee et al <19>. Most of the work was done in low pressure systems. Successful designs of quick-closing valves for high pressure systems (10.5 MPa) have been found in Agostine et al <20>.

For this technique to be accurate, the valves should be designed in such a way that the flow is not disturbed when the valves are open and they should close very quickly (10-20 ms) and simultaneously. At the same time, a pressure relief mechanism

must be actuated to remove the pressure so that the valves are not damaged. If one valve closes faster than the other, a systematic error is introduced to the liquid trapped and if the volume between the valves is small, the error can be significant.

By the nature of this technique, the measured void fraction is the volume averaged void fraction between the two valves. The volume averaged void fraction will fluctuate if the identical experiment is repeated. An ensemble average for the volume averaged void fraction must therefore be obtained by repeating the experiments.

From the above discussions, it is clear that, although this technique can be used for both transient and steady state measurements, it is better used for steady state experiments. Another aspect of this technique is that this method interrupts operation of the system and is, therefore, primarily used for research purposes and for calibration of other void measurement devices.

2.2.1.2 Static head method

In certain situations, the pressure drop is dominated by the gravitational component term. Such a situation may be found in depressurization of large vessels. In this case, the pressure drop between two locations separated vertically is approximately proportional to the mixture density ρ ($\rho = \rho_g \alpha + \rho_f (1-\alpha)$) between them. This method has been used by Banerjee and Jolly <21> in a vessel blowdown experiment where the mixture density or void fraction measured by this method was compared with that measured by quick-closing valves. The obvious disadvantage of

this technique is its limited application.

2.2.1.3 Natural frequency method

The device used in this method consists of a "U"-shaped tube through which a gas-liquid mixture flows. The set-up is forced into vibration by magnetic forces. The geometry of the "U" shaped tube can be regarded as that of the opposite legs of a tuning fork excited by the magnetic forces. The natural frequency of the "tuning fork" is given by

$$\tau^2 = 4\pi^2 m / k_0 \qquad (2.1)$$

where τ = period of oscillation

k_0 = constant

m = total mass of pipe and fluid

The total mass m can be split up into two terms leading to two calibration constants as

$$\tau^2 = k_1 + k_2 \rho \qquad (2.2)$$

where ρ = mixture density of the fluid. The two constants k_1 and k_2 can be determined by measuring τ when the pipe is full and empty of the liquid. Smith <22> indicates that the instrument is quite accurate for densities between 250 and 500 kg/m^3.

2.2.2 Thermal Methods

In this class of techniques, the local void fraction is measured indirectly by sensing the temperature of the fluid. It includes hot wire and film anemometers and micro-thermocouples.

2.2.2.1 Hot wire and film anemometry

The basic principle of the device is based on Joule heating and convective cooling of a heating element inserted into the flow as a probe. The probe is usually used in "constant temperature" mode. In this case, the probe temperature is maintained constant in a fluctuating velocity field. In order to do this, the current through the resistive heating element must vary to compensate for the convective heat losses. The current can be shown to vary with the heat transfer coefficient of the fluid. Since the heat transfer coefficient is very different for liquid and vapour, it is easy to differentiate between the phases around the probe. When the probe is surrounded by liquid, the heat transfer rate is high, and the current flow increases. Likewise, the current flow decreases when the probe is surrounded by vapour. This device can thus be used to measure local void fractions. A histogram showing the probability of signal level shows two peaks, one for the liquid and the other for the gas. The time averaged local void fraction can be obtained by directly integrating the areas of the histogram.

Hot wire and film anemometry had been used by Hsu et al <23>, Goldsmidt <24>, Delhaye <25>, Shiralkar <26>, and Kobori <27>. One of the major problems is probe deterioration in conducting media like water. To extend life, conical quartz-coated hot film probes have proved reasonably successful in low

temperature applications. The other disadvantage is that it is intrusive and therefore interferes with the flow.

2.2.2.2 Micro-thermocouples

Micro-thermocouples may be used for measuring local void in situations where a difference of temperature exises between the liquid and vapour phases. Such situation may arise, for example, when cold liquid is injected into a hot vapour-filled system, e.g. reflooding experiments, or during conduction controlled bubble growth in a superheated liquid. With appropriate signal processing, it is possible to separate the temperature of the liquid phase from that of the vapour. Histograms of the temperature recorded gives the frequency of temperature of each phase as well as the local void. However, like the hot-wire and film anemometers, this method is intrusive and interferes with the flow. The most successful reported use of micro-thermocouples has been by Delhaye and Semeria <28>.

2.2.3 Electromagnetic radiation method

In this class, the probe used is electromagnetic radiation with wavelengths ranging from that of microwaves, infrared, ultraviolet, to that of visible light (optical). In the optical technique, included are optical local probes, light attenuation, and scattering techniques.

2.2.3.1 Microwave absorption

A method to determine fluid density in liquid hydrogen/ hydrogen vapour flows by determining the resonance frequency of a microwave cavity formed by part of the system has been described

by Wenger and Smetana <29>. The technique has also been applied by Stuchly et al <30> to measurements in organic liquid-vapour systems. Microwave techniques have recently been proposed for the measurement of liquid levels in a nuclear reactor <31>. The system is intrusive in that a wave guide must be inserted in the reactor. The difference in frequence between the reflected and emitted signal can be used to infer the location of the steam-water interface.

2.2.3.2 Infrared and ultraviolet attenuation

Infrared attenuation

The operational principle of this technique is the differential absorption of infrared radiation of a given wavelength by water, steam, and a noncondensible gas such as air. Usually, if there are n components in the flow system, n number of different wavelengths are used. The first wavelength is chosen such that it is significantly absorbed by none of the components and is used as a reference beam. The remaining n-1 wavelengths are chosen so that each is significantly absorbed by one component. By measuring the attenuation of the infrared the void fraction can be inferred. Barschdorff et al <32>, in an experiment to measure concentration of air in a flow consisting of water, steam, and air, used three different infrared wavelengths. Snyder and Baker <33> used infrared radiation of 0.9 and 3.0 μm to study high quality steam.

The disadvantage of this technique is that its application is limited to high void regions.

Ultraviolet attenuation

This method is quite similar to the method of infrared attenuation. Ramaswamy et al <34> has shown that, when 1-Butene gas is added in trace quantity to noncondensible gas such as air, ultraviolet light of wavelength 1850^{o}A is significantly attenuated by the noncondensible gas but not by steam or water. The void fraction in an air-water system can then be measured. However, this technique is limited to application in high qualities where the water droplets are small enough so that the scattering of light is negligible.

2.2.3.3 Optical methods

Optical techniques include (i) optical probes and (ii) light attenuation techniques.

Optical probes

Optical probes are used for the measurement of local void fraction. The basic principle of operation is based on Snell's Law, ie. a light ray, travelling from a denser medium with refractive index n_1 to a less dense medium with refractive index n_2 ($n_1 > n_2$) will be internally reflected at the interface of the two media if the angle of incidence ϕ_i is greater than a critical incident angle ϕ_c. Note that

$$\phi_c = \sin^{-1} (n_2 / n_1) \qquad (2.3)$$

If one has a glass probe cut at 45^{o} and the tip of the probe is

inserted into the fluid, a light ray co-axial with the axis of the probe, can be totally reflected twice and returned in the original direction if the tip is surrounded by air, and will be lost in liquid water by refraction. Then, the presence of void or liquid will give rise to "on" and "off" light signals.

Several investigators have developed fibre optics devices to carry light rays for the measurements of void fraction in low temperature air-water flow <35, 36, 37>. The miniaturized optical probe recently developed by Jones and Zimmer <38> appears attractive for measuring both local void fraction and interface velocity. For high temperature probes, a high temperature optical fibre (e.g. sapphire) and an appropriate tip (e.g. diamond or sapphire) must be used. Examples of optical probes for high temperature are found in Vince et al <39, 40>.

Light attenuation technique

A light beam is attenuated when passing through a bubbly or droplet flow. The amount of attenuation is directly proportional to the effective interfacial area. For bubbly flow, assuming the validity of Beer's Law where $I/I_0 = \exp(-\mu x)$, the problem reduces to determining the void dependence of the macroscopic cross-section μ. Lockett et al <41> have shown that the appropriate expression for μ in low void regions($\alpha < 0.38$) is given by

$$\mu = 6 \alpha K / 9.21 D_b \qquad (2.4)$$

where $K = 1.08$

D_b = bubble diameter in metres

By measuring I/I_0 and μ, and if the bubble size D_b is known, then α can be deduced. The disadvantage of this technique is that it is only applicable in low quality (bubbly) and high quality (droplet) flows. Its application to high temperature steam-water flow is also difficult.

Another example of the technique using light attenuation is found in the optical digital interferometer developed by Lahey et al <42>. A square flow channel is subdivided into meshes defined by two arrays of LED's placed on adjacent sides of the flow channel. Each light detector placed on the opposite side of an LED senses the light beam only if there is no liquid-gas interfaces in the beam path. Void fraction can thus be measured by the number of nodes occupied by liquid-gas interfaces. This method is applicable only in either low or high void regions.

2.2.4 Sonic Methods

2.2.4.1 Pulse echo

In this technique, an ultrasonic transmitter/receiver is attached to the outside of a test section. When an emitted ultrasonic wave reaches a vapour/liquid interface, the signal is returned to the transducer due to a large acoustic impedance mismatch. The time difference between the emitted wave and the returning signal yields the location of the gas-liquid interface. Experiments indicate that the technique can detect single bubble or droplet location and size, and is therefore likely to be useful in high quality droplet, or low quality bubbly flow <14>. This technique has also been used to measure film thickness by

Chang et al <43>.

2.2.4.2 Pulse transmission

This technique has been used by Chang et al <44> to measure void fraction in bubbly flow at void fraction less than 0.2. In this technique, it is assumed that an ultrasonic beam cannot penetrate any part of a bubble that lies in its path. The amount of attenuation of the beam by multi-bubbles is proportional to the projected blocked area of the beam.

2.2.4.3 Sound speed measurement

The speed of sound in a two-phase mixture is strongly dependent on void fraction (mixture density) and flow regime. In a homogeneous flow, the sound speed is much lower than that of liquid or vapour alone. It can be shown that, for low-quality bubbly flow, by measuring the sonic velocity in a homogeneous two-phase mixture the void fraction. α can be measured <16>.

2.2.5 Electrical Techniques (Impedance Probes)

The electrical impedance (resistance and capacitance) of a two-phase mixture depends on the void fraction as well as phase distribution. Void fraction can thus be measured. Electrical impedance techniques can be broadly classified into those suitable for cross-sectional averaged void fraction (global Z-probes) and those for local void fraction measurement (local Z-probes)

2.2.5.1 Global Z-probes

The basic assumption in the global Z-probes is that the impedance Z of a two-phase mixture is adequately modelled by a resistance R, in parallel with a capacitance C. For a frequency f, the impedance Z is given by

$$Z(f) = 1 / \sqrt{(1/\bar{R})^2 + (2\pi f \bar{C})^2} \qquad (2.5)$$

where $\bar{R}$ = void fraction dependent resistance

$\bar{C}$ = void fraction dependent capacitance

Dependent on the frequency of excitation, the impedance is dominated by the resistance (low frequency) or the capacitance (high frequency). In principle, by measuring either the resistance or capacitance, one can measure void fraction. However, both these two quantities are dependent also on phase distribution, and the instrument must be calibrated and used with some knowledge of the flow regime. Moreover, the capacitance is also much dependent on temperature.

Impedance probes have been developed or used by Hoogendorn <45>, Cimorelli and Evangelisti <46>, van Vonderan and van Vlaardingen <47>, Carrard and Ledwidge <48>, Subbotin et al <49>, and Rosehart et al <50>. More recently Merilo et al <51> developed a global void gauge employing three pairs of diametrically oppositely placed electrodes excited by a three phase rotating field. Low frequency excitation is used to

compensate for changes in liquid resistivity. A co-axial capacitance probe has been used to measure the void fraction in two phase helium and nitrogen flow in test sections of 6.35 and 2.75 mm ID by Khalil and McIntosh <52>.

2.2.5.2 Local Z-probes

Local Z-probes generally consist of small co-axial probes which are inserted into the flow field to measure local void fraction. The common disadvantage is that the flow may be disturbed owing to the intrusive nature of the probe. Three modes of excitations are commonly used: DC, AC, and RF excitation.

In DC excitation, the impedance is dominated by the resistivity of the mixture (see Eq.(2.5)) and one has higher current flow when the tip is in liquid than in vapour. This technique has been used in steam/water experiments by Kobori <53, 54>. In this mode, the advantage is that the circuits used are simple and inexpensive. The disadvantages, however, lie in the sensitivity of the liquid resistivity to temperature. Moreover, a polarization problem may occur where electrochemical attack and deposits may age and damage the probes.

In AC (low frequency) excitation, a co-axial probe is driven at a fixed frequency. A threshold is set such that, when the probe is surrounded by liquid, there will be an output signal and none in vapour. The averaged local void fraction can be obtained by time averaging. Low frequency AC excitation has the advantage of relatively low cost and can eliminate probe damage and polarization problems. Disadvantages include some

sensitivity to liquid resistivity and the requirement of AC circuitry. An example of AC excited local Z-probe device is found in Arave et al <55>.

In RF (high frequency) excitation, only the dielectric constant of the two-phase fluid is sensed (see Eq.(2.5)). A threshold is needed to discriminate between "on" and "off" signals for the probe being surrounded by vapour and liquid respectively as another case of the AC excitation. The main disadvantage lies in the requirement of sophisticated and expensive RF circuitry. The advantages, however, lie in the immunity to polarization problems and 60 cycles interference. Examples of RF excitated local void probes are found in Vince et al <56> and Abuaf et al <57>.

2.2.6 Nuclear Methods

This is probably the most widely used class of void fraction measurement techniques. In these techniques, the interaction of various nuclear radiations with liquid phase is utilized in measuring void fraction. The commonly used types of nuclear radiation include β-rays, X-rays, γ-rays, and neutrons. In using these types of radiation, two common approaches are adopted. Radiation from a source, after interacting with a two-phase mixture, is either measured in the attenuation or scattering mode. Apart from using radiation from a source, radiation can be produced in situ by neutron activation or a radioactive source can be introduced into the flow. Also, the measurement of nuclear magnetic resonance (NMR) has been

attempted.

The main advantage of this class of techniques is its non-intrusive nature and its mobility. The disadvantages are the possible requirement of shielding against the radiation and expensive equipment. Let us now discuss the various methods.

2.2.6.1 Nuclear magnetic resonance (NMR)

Recently, the measurement of nuclear magnetic resonance was applied to the measurement of void fraction by Lynch and Segel <58> and most recently by Saxe <59>. In this technique, a small amount of paramagnetic salt is introduced into the flow and is then subjected to a magnetic field. The spin angular momentum of a nucleus, by virtue of its nuclear magnetic moment, will be aligned in a specific orientation. The amount of radio-frequency energy necessary for re-orientation is then related to the amount of liquid. By this, void fraction is measured.

2.2.6.2 Beta-ray attenuation

Because of the relatively short interaction range of ß-rays, this technique is only applicable in high quality (high void) flow, see English et al <60>, Styrikovich and Nevstruva<61>, Perkins et al <62>, and Zirnig <63>.

The principle of operation is that a beta particle beam, after passing through a two-phase mixture, is partially attenuated. The unattenuated part of the beam is related to the incident beam by

$$I = I_0 \exp(-\rho f_0 x) \qquad (2.6)$$

In the above equation, x is the beam path length through the two-phase medium, ρ the mixture density, and f_0 the mass attenuation coefficient of the two-phase mixture for beta-particle attenuation.

This technique is expected to be applicable in high quality flow. However, it cannot be used in flow channels with thick metal walls as the beta rays are easily absorbed by metal.

2.2.6.3 X-ray attenuation

X-ray attenuation devices operates on similar principles as the ß-ray technique. The device can be operated at very high intensity and low photon energies. The attenuation coefficient of water increases sharply at low energies. Thus, the sensitivity to void in the beam path can be very high. Another advantage is that it can be operated at high intensity. The disadvantage is that X-rays are always easily absorbed by metal and therefore cannot be used in high pressure systems. Since X-ray are exponentially attenuated, void fraction determination is quite flow regime dependent. Moreover, one common problem with X-ray devices are inherent fluctuations and drift. A reference beam for normalization is thus often necessary. Dual beam systems have been developed by Schrock <64> and Smith <65>. More

recently, the dual beam system of Vince and Lahey <66> has been used to measure chordal averaged void fraction and to identify flow regimes objectively.

Multi-beam X-ray systems have been developed to measure local void fraction and for flow regime "visualization". A high intensity 31-beam system has been developed by Jeandey <67> and a design optimization of the system was reported by Fournier and Jeandey <68>.

Recently, computerized tomographic (CT) scanners have been developed to reconstruct patterns inside a flow channel. In these CT scanners, high intensity single or multibeams traverse the flow cross-section from different projections to yield sufficient information on the distribution of local voids. Examples of these X-ray CT scanners are found in Schlosser et al <69, 70>, Iizuka et al <71>, and Ikeda et al <72>. Multibeam, high speed scanners which can reconstruct void distribution every 5 ms has been developed by Narabayashi et al <73>.

2.2.6.4 Gamma ray techniques

Gamma rays generally have higher energy than X-rays. Dominant interactions between gamma rays and any material are (i) photoelectric effect for low energy, (ii) Compton scattering for intermediate energy, and (iii) pair production for high energy. Gamma rays of very high energy can also activate some material by (γ,n) reactions. Gamma rays that have high enough energy to penetrate a metal wall are not very sensitive to the fluid content. Thus, care must be taken in the choice of gamma energy for a particular application. Gamma ray techniques can be

broadly classified into attenuation and scattering. Lately, activation techniques have also been developed.

Gamma attenuation

The basic principle, similar to the attenuation of other radiation, is that the intensity of a gamma ray beam is attenuated by the liquid phase according to

$$I(\ell)d\ell = I_i d\ell \exp(-\mu D(\ell)(1 - \alpha_c)) \qquad (2.7)$$

where μ = linear attenuation coefficient

ℓ = position across the beam profile

D = physical chordal length of flow channel at ℓ

α_c = chordal averaged void fraction

I_i, I = intensity of incident and exident gamma beam

The transmitted (unattenuated) beam strength is given by the integral of Eq. (2.7). Since α_c is dependent on phase distribution, the transmitted beam strength depends on α as well as liquid phase distribution, except in the case of high energy gamma rays, small flow channel size, where Eq. (2.7) is close to being linear upon Taylor's Expansion of the exponential term. The other disadvantage is that gamma rays are normally highly attenuated by tube walls but to a lesser degree by the fluids. This constitutes a problem in high pressure systems with low fluid to solid volume ratios.

In spite of the disadvantages mentioned, this technique has been employed in numerous investigations. Studies using it

in two-phase flow in tubes includes those by Bailey et al in 1955 <74> to LeVert et al <75> in 1973. Measurements in annuli are reported by Evangelisti et al <76> and Zakharova et al <77>. Measurement in tube bundles are reported by Gustaffsson et al <78>. More recent work on single beam gamma densitometer are found in Chan and Banerjee <79> and Fortescue <80>.

The principle for the single beam densitometer has been extended to multiple beam arrays. Such devices are required for larger pipes in order to take the phase distribution effect into account. Three-beam gamma densitometers have been independently developed by Lassahn <81> and Heidrick et al <82>. Algorithms have been developed with which the signals from the beams can be processed to determine void fraction and flow regime. A 5-beam gamma densitometers has been developed by John et al <83> and used in conjunction with a drag disc turbine transducer to measure mass flow rate <84>. "Multi-beam" systems effected by a single beam but with multi-dectors or by scanning have also been developed. Hau and Banerjee <85> used a scanning narrow single beam densitometer in conjunction with a pitot tube for mass flow rate in an air-water system. A rotating fan-beam has been used for reconstruction of phase distribution by Kulacki et al <86>. A single beam, multi-detector system is being developed by Chan <87> for measurement of chordal void fraction and flow regime identification in a 50.8 mm diameter pipe.

Gamma scattering

The principle of operation is based on the well-known Compton Scattering and the Klein-Nishina Equation for the

differential Compton Scattering cross-section. The energy of a Compton scattered gamma photon depends on the energy of the incident gamma photon and the angle of scattering. Using a collimated narrow beam of monoenergetic gamma rays and a well collimated gamma ray detector, the counting rate of Compton scattered gamma photons (by energy discrimination) depends on the local density or void fraction at the point where the directions of collimations intersect. By counting the Compton scattered gamma photons, local void fraction in complex flow channel geometries can be measured. However, this technique is probably not suitable for transient experiments as the counting rate tends to be small.

The gamma scattering technique has been applied to measurements of local void fractions in the center subchannel of a 4 x 4 array of electrically heated rods with 4 heated walls by Zielke et al <88>. The development of a gamma scattering densitometer has been applied to measurement of local void fraction in eccentric and concentric annular test sections by Ohkawa and Lahey <90>.

The gamma scattering technique has been extended to tomographic reconstruction of phase distribution by Kondic and Lassahn <91>. In this technique, a collimated gamma beam traverses a test section and an energy-sensitive gamma detector is collimated within a wide angle to view the entire traversed chord. The energy spectrum of the detected gamma rays is a convolution of the Compton scattered gamma photons throughout the chord. Relationships were developed for the reconstruction of the local void fractions (phase distribution) by deconvolution

procedures.

Gamma activation (Pulsed Photon Activation)

This technique uses the activation of ^{16}O by Bremstralung gamma rays. Because of its similarity to the Pulsed Neutron Activation technique to be discussed later and for historical reasons, the discussion of this technique is postponed till later section (see section 2.2.6.5).

2.2.6.5 Neutron techniques

Because neutrons are electrically neutral, they penetrate metal pipe walls better than gamma rays and X-rays. Consequently, high pressure systems can be considered. Unlike gamma and X-rays, neutron beams are often more sensitive to the fluid than to metal walls. This is especially true if neutron transparent metals like zirconium or aluminum are used with thermal neutrons, and stainless or carbon steel with fast neutrons.

Neutrons have been used to measure void fraction in the past. However, it appears that it has attracted more attention recently than before. Techniques using neutrons can be broadly classified as activation, attenuation, and scattering.

Activation

Pulsed neutron activation (PNA)

This technique has been vigorously pursued by Kehler <92, 93> and Perez-Griffo et al <94, 95>. This technique is meant for the measurement of mass flow rate. However, it can also measure

air-water or steam-water mixture density. In this technique, the ^{16}O in water or steam is activated by a pulse of fast neutrons ($E_n \sim 14$ MeV). Because of the small activation cross-section ($\sigma = 100$ mb), the spatial distribution of the activation product ^{16}N would be quite uniform at the plane of activation. Consequently, the amount of ^{16}N produced would be directly proportional to the oxygen density or mixture density. The required high energy neutrons were obtained from a pulsed neutron generator in Kehler but from the LINAC at RPI in Perez-Griffo.

The ^{16}N decays with a half-life of 7.2 s, emitting 6.2 MeV gamma rays. If the gamma rays emitted are detected downstream of the point of activation, then the cross-sectional average density at the time of the pulse and at the location of the activation plane can be calculated. The total activity A detected is given by

$$A = \frac{z_0}{\beta \, \Delta z} \int_0^\infty \frac{1}{t} C(t) \, e^{\lambda t} \, dt \qquad (2.8a)$$

where z_0 is the distance between the neutron source and the detector, Δz is the size of the detector window, β is a constant factor dependent on geometry, t is the elapsed time from the time of the neutron pulse, C is the number of counts in time dt, and λ is the decay constant.

If A_0 is the activity for a pipe fully filled with water, then the mean density for an activity A is

$$\rho = A \, \rho_f / A_0 \qquad (2.8b)$$

where ρ is the mixture density and ρ_f is the liquid density.

Pulsed photon activation (PPA)

This technique has been developed by Lin et al <96>. It is quite similar to the PNA technique. In addition to the $^{16}O(n,p)^{16}N$ reaction used in the PNA technique, there is a $^{16}O(\gamma,n)^{15}O$ reaction which produces a 122 s half-life positron emitter (^{15}O). The ^{15}O is identified by the 511 keV annihilation gamma peak. The high energy gamma ray (15.7 MeV threshold) needed for the PPA technique is produced by the electron beam in the LINAC at RPI hitting a Bremstralung target. The Bremstralung gamma ray activates the ^{16}O and the analysis is then identical to the PNA technique. The difference, however, is the the counting rate of the 511 keV gamma peak is much higher; probably due to the higher efficiency of the NaI detector at a lower gamma energy. Historically, this technique was discovered when an intense "mysterious" 511 keV gamma peak was observed in the PNA developmental work carried out at RPI.

Neutron attenuation

Neutron attenuation has been largely limited to thermal neutrons. Thermal neutron beams from research nuclear reactors have been used to determine void fraction by Moss et al <97>, Harms et al <98>, and Younis <99>. The basic principle of this technique is the exponential attenuation of the thermal neutron

beam. Neutron transmission measurements were carried out in bubbly, churn, and slug flow by Hancox et al <100>. They used a gating technique to obtain discrete transmission measurements over time intervals much smaller than the dominant void fluctuation period. This technique utilizing thermal neutrons is limited to relatively small test sections since the mean free path of a thermal neutron in water is about 3 mm. Younis et al <101> have also demonstrated the time-fluctuation of a transmitted thermal neutron beam through a flow channel can be used to identify flow regimes. A transportable thermal neutron gauge has been developed and used to measure high void fractions in water-steam mixtures by Frazzoli et al <102>.

The attenuation of fast neutrons has also been used. A method has been developed by Tominaga et al <103> where transmitted fast neutrons from ^{252}Cf neutron sources are measured by organic scintillators having pulse shape discrimination properties for the discrimination of gamma rays.

Single scattering of fast neutrons

When a neutron collides with a water element, the energy of the recoil neutron depends on the angle of recoil. Hussein <104> has shown that, when a beam of monenergetic fast neutrons is incident on a test section containing hydrogenous material, and several neutron detectors are placed at different angles with respect to the incident neutron beam to detect scattered neutrons, the counting rate of scattered neutrons of different recoil energies can be used to unfold the phase distribution, ie, local void fraction. The requirement of this technique is that

only neutrons suffering a single collision be counted. It has been shown <104> that this requirement can be met when the mean free path of the incident neutrons is longer than the diameter of the test section. This technique has the advantage of measuring local void fraction in transient situations.

Multiple neutron scattering

Multiple scattering leading to thermalization of fast neutrons by hydrogenous material has been used to measure void fraction. This class of techniques is based on the phenomenon that the neutrons, on passing through materials of high scattering cross-section (or moderating ratio), are slowed down to thermal energies. The fractional loss in energy when a neutron collides with an atom is greatest for the hydrogen atom. Therefore, by passing a beam of fast neutrons through a series of materials of varying hydrogen density, a relationship should be observed between hydrogen content and measured thermal neutron intensity. However, the complexity of neutron moderation theory does not lend itself as readily to a simple mathematical treatment as does thermal neutron transmission. Thus, in this technique, the usual experimental approach is to prepare a standard calibration curve from samples of known hydrogeneous material content and to relate the measured thermal neutron intensity of an unknown sample to this curve. This technique has been applied in moisture determination with californium-252 sources <105> and in steam volume fraction determination in pipe with 14 MeV neutrons <106>.

The combination of moderation and attenuation of fast

neutrons by hydrogenous materials containing strong absorbers of thermal neutrons has been used. In a strong thermal neutron absorber, the thermal flux is directly related to the moderation of the fast neutron flux in the immediate vicinity. Sha and Bonilla <107> performed an out-of-pile experiment employing this technique to determine void fractions. Fast neutrons from a Sb-Be neutron source were used and boron was dissolved in a 76-203 mm diameter pipe to increase the attenuation coefficient of the water in the pipe. Optimum application of this technique requires test sections larger than 25 mm.

The scattering of epithermal/fast neutrons has been used to measure void fractions for two-phase flow in pipes. Preliminary work was reported by Rousseau <108> and Banerjee <109>. These investigations indicated that the technique was promising. Further work was carried out in this direction by Banerjee et al <110>, Yuen <111>, and Banerjee et al <112>. Interrogating the hydrogenous content in test sections with an epithermal/fast neutron beam from a research reactor, it was shown that the neutron scattering method of measuring void is fairly flow regime independent. Moreover, the scattered thermalized neutron flux varies linearly with void fraction. This result was found to hold in rod bundle as well as tubular test sections. However, the feasibility of extending this technique to a portable system with a neutron source rather than the reactor beam port and to larger pipe sizes and different pipe wall thicknesses is not tested. This forms the bulk of the present investigation.

Ducros <113>, in parallel to the work by Banerjee and Yuen, has also studied the feasibility of measuring void fraction by the technique of multiple scattering of epithermal/fast neutrons. With Monte Carlo studies, Ducros has shown that, for a test section of a given inside diameter, there exists a monoenergetic group of incident neutrons such that the counting rate of thermalized neutron flux decreases monotonically with void fraction α and is independent of flow patterns. This required the incident energy of (monoenergetic) neutrons to increase with the inside-diameter of the test section.

2.3 OBJECTIVES OF PRESENT WORK

The above survey reveals a rich collection of techniques to measure local or volume averaged void fractions. In principle, a technique originally designed to measure local void fraction can be used to yield information on averaged void fraction by placing a number of local probes at different locations in an experimental volume and taking the average. However, all of them have some disadvantages in terms of interference of operation, interference with the flow, difficulties in calibration, suitability in high pressure, limited void range of application, or high cost in required equipment.

While quick-closing valves are widely used for measuring volume averaged void fraction, they are not desirable for routine use since the process must be interrupted repeatedly. Probes measuring local void fraction like hot wire anemometers, micro-thermocouples, optical probes, and local Z-probes are widely

used. However, they all disturb the flow. Non-intrusive techniques are found in light attenuation, ultrasonic, and global impedance probes. However, light attenuation cannot be used in high pressure systems. Ultrasonic technique can be used only in either low (bubbly flow) or high void (droplet flow) regions. Global impedance probes have difficulties in calibration since the impedance of the mixture fluid depends strongly on temperature. For nuclear techniques, beta and X-rays, while being non-intrusive, cannot be used in high pressure systems because of absorption in the system walls. Gamma ray techniques suffer from the same disadvantage though to a lesser degree. All these techniques are also affected by flow regime and the results depend on the manner in which the two-phase fluids are distributed in the measurement volume. This leaves neutron-based techniques as attractive candidates.

Epithermal/fast neutrons are not strongly attenuated by metal pipe walls. At the same time, neutrons are very sensitive to hydrogenous material like water, steam, or oil because a neutron can, in principle, lose a large part of its energy in a single collision. This makes it an attractive candidate for application in high pressure systems. Needless to say, this technique is also non-intrusive.

2.3.1 Review of Previous Work

In previous works, Yuen <110, 111, 112> has demonstrated that, using a collimated epithermal/fast neutron beam from a research nuclear reactor on a test section containing air-water

mixtures, the scattered (thermalized) neutron flux varies in a fairly linear manner with void fraction and the response is also fairly flow independent. This is briefly reviewed in the following paragraph.

The typical experimental set-up used to test the neutron scattering technique is shown in Figure 2.1. A neutron beam from the McMaster Research Reactor, stripped of subcadmium neutrons ($E_n < 0.5$ eV), was made incident on a test section. The test section consisted of an aluminum tube sealed at one end. The tube was 152 mm long with wall thickness of 1.6 mm. The inside diameter of a typical test section was 51 mm. Aluminum inserts of different shapes and volumes were placed inside the test section to simulate air (aluminum being quite transparent to neutrons). The rest of the space inside the test section was filled with water, forming a simulated air-water test section of different void fractions and flow regimes. Three different flow regimes were simulated, namely, annular, inverted annular, and stratified flow regimes. A ^{3}He neutron detector (mainly sensitive to thermal neutrons) was placed at 90° to the neutron beam axis to count scattered neutrons slowed down after suffering multiple collisions.

In the typical experimental set-up, neutrons counted by the detector must have suffered multiple collisions before escaping from the test section because it is highly unlikely that an incident neutron is thermalized in a single collision. An incident neutron, after suffering multiple collisions, probably has lost memory of its initial direction and the location of the first collision. In other words, there is no preference for

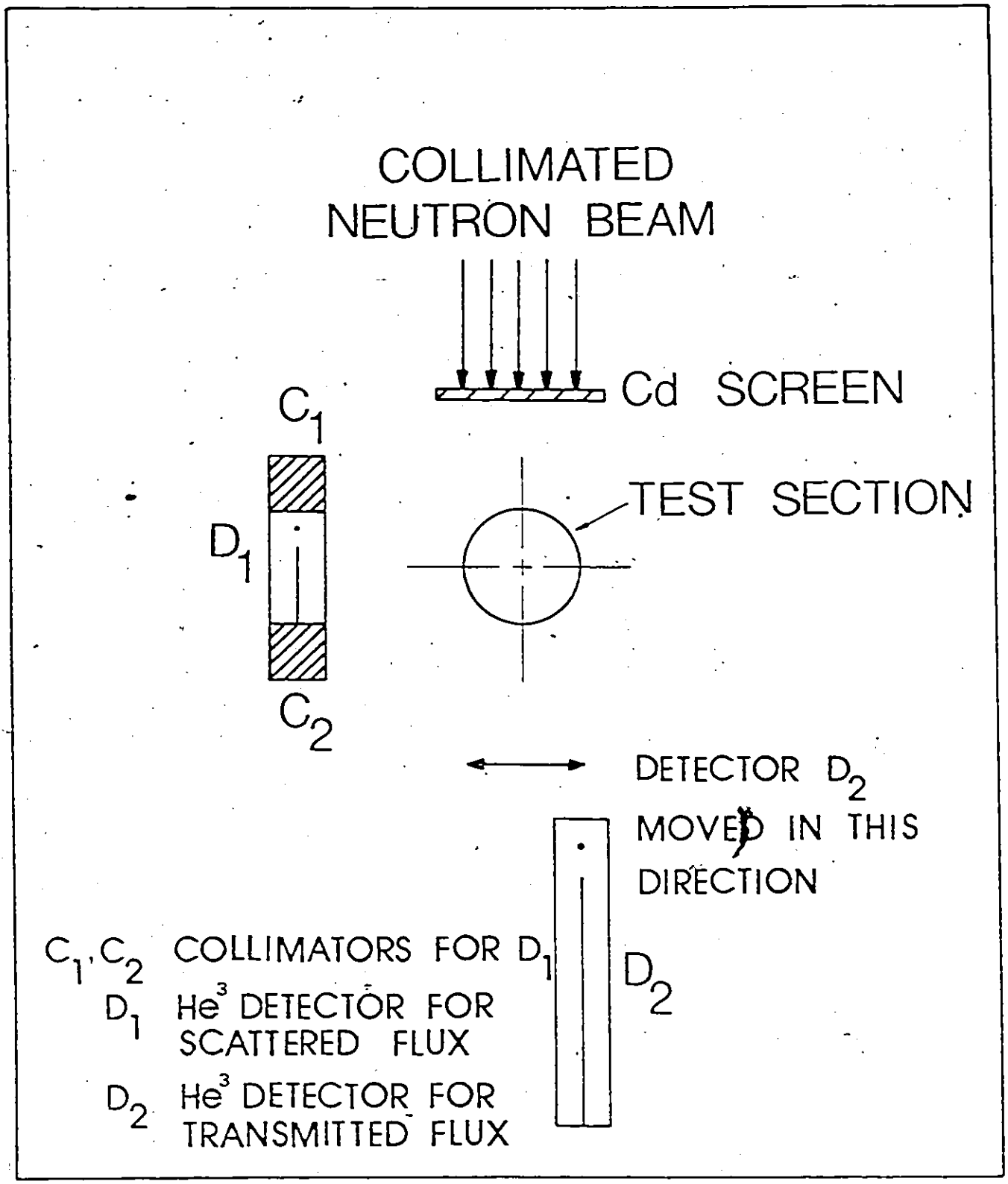

Figure 2.1 Experimental set-up in previous work <111> to test the neutron scattering technique for void fraction measurement

thermalization sites inside the test section, and every water element acts as a source of thermalized neutrons with uniform density. Thus, it was postulated that the counting rate of the scattered (thermalized) neutrons were:

(a) linear with void fraction,

(b) fairly independent of flow regime.

The above hypothesis implies that α would be related to the scattered neutron counting rate $N(\alpha)$ by

$$\alpha = \frac{N(0) - N(\alpha)}{N(0) - N(1)} \qquad (2.9)$$

where $N(0)$ and $N(1)$ are scattered neutron counting rate for full and empty test section respectively. The hypothesis was tested by correlating α obtained by Eq.(2.9) against a known α for a given test section.

A typical result obtained for the 51 mm test section is shown in Figure 2.2. From this figure, it was observed that the hypothesis held very well for test sections with radially symmetric water phase distribution, ie. annular and inverted annular flow regimes. The maximum deviation from linearity was equivalent to $\Delta\alpha=0.06$ for the inverted annular flow regime. For radially asymmetric flow regime, ie, the stratified flow regime, the deviation from linearity was quite severe. The most severe deviation occurred at the two extreme configurations where the water phase is close to or away from the detector. The deviation was equivalent to $\Delta\alpha=0.09$. However, it was observed that the value of α determined by Eq.(2.9) was quite equi-distant from the

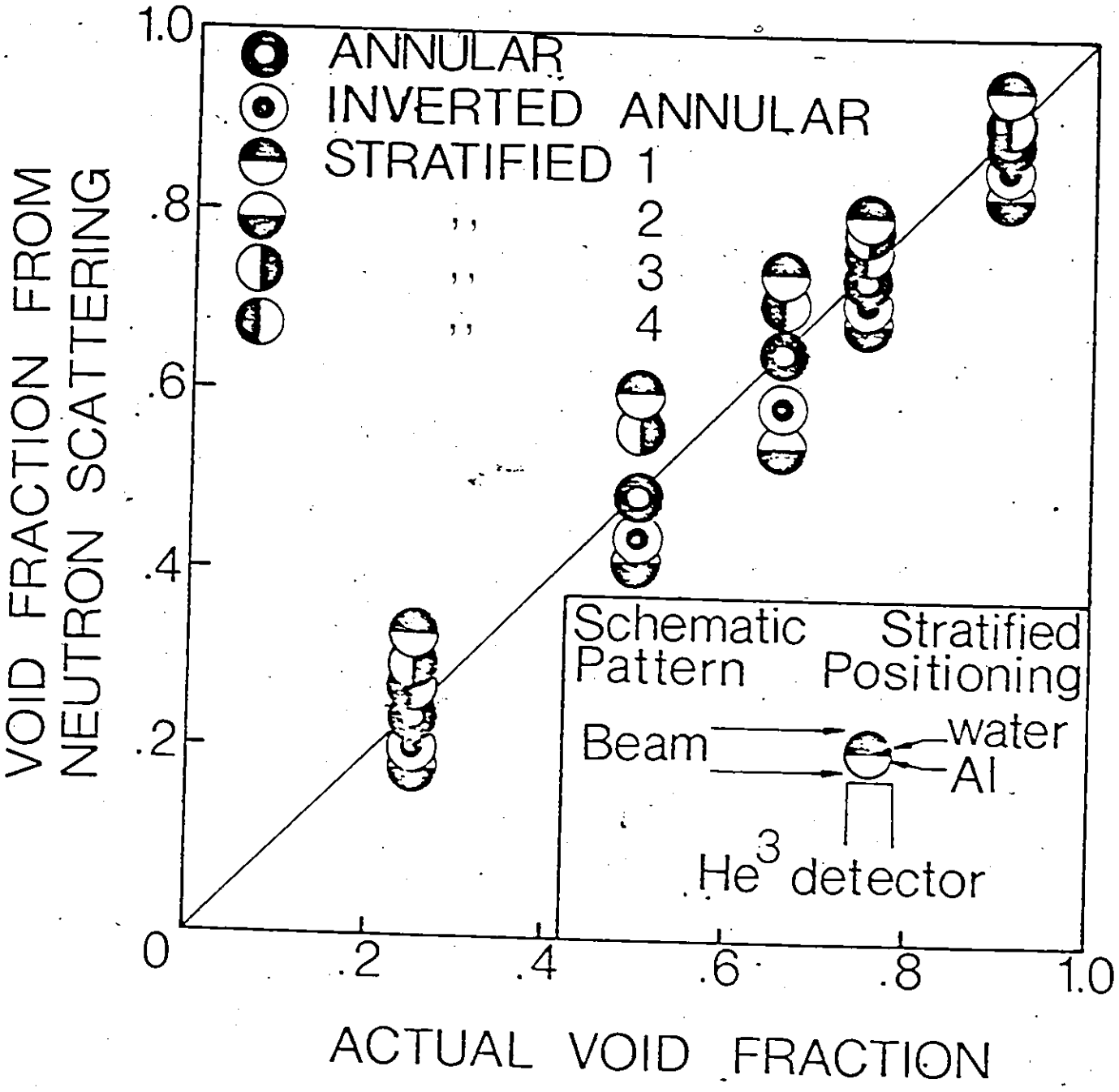

Figure 2.2 Typical result obtained in previous work <111> for a test section of 50.8 mm diameter

perfect correlation (the "45° line). This implied that if an additional detector were placed diametrically opposite to the first detector, and the average of the void fraction experimentally determined were taken, this average value would be quite linear with the actual α.

It was then concluded that the neutron scattering technique is fairly independent of flow regimes and the detector response is quite linear with void fraction. It was recognised that this technique has the following advantages:

(i) the detector response is fairly linear with α so that only two points for calibration are needed,

(ii) fairly flow regime independent,

(iii) the linearity implies that the time averaged $\bar{N}(\bar{\alpha})$ in steady state measurement is also linear with $\bar{\alpha}$, regardless of flow pattern,

(iv) applicable throughout a wide range of void fraction,

(v) highly sensitive to change of void fraction α,

(vi) applicable in high pressure systems where thick metal pipe walls are present.

The above advantages are desirable. Linear detector response implies that only two calibration points (α = 1 and 0) are needed. This makes it easy to calibrate the instrument "in-situ" for various combinations of pipe size, incident neutron intensity, detector efficiency, and test-section to detector distance, etc. If the detector response is not linear, intermediate values of α are needed in the calibration, and very often, this may not be possible. Linear detector response with α

also implies that it is flow regime independent. The second advantage (ii) implies that knowledge of flow regime is not necessary in the measurement of void fraction. This is particularly desirable as the identification of flow regime is often difficult. The third advantages (iii) is also attractive. Very often, an instrument is calibrated with stagnant test sections, and the calibration curve so obtained is used for measuring time averaged void fraction $\bar{\alpha}$ in steady state measurements. If the calibration curve is non-linear, the time averaged detector response $\bar{N}(\bar{\alpha})$ does not necessarily follow the same calibration curve (see Appendix F), resulting in systematic errors. However, a linear calibration curve implies that $\bar{N}(\bar{\alpha})$ is also linear with $\bar{\alpha}$ (see Appendix F). The attractiveness of other advantages ((iv) to (vi)) is self-evident.

2.3.2 Discrepancy Observed in Portable System (Expt #0)

From discussions in the last subsection, the neutron scattering technique seems to be very attractive. However, one must note that the development was conducted with a neutron beam from a nuclear reactor. The application of this technique thus is limited. Before the present work started, attempts were made to eliminate this disadvantage by testing the technique with portable neutron sources.

The first step taken was to repeat the test-experiment discussed in section 2.3.1 with a portable ^{241}Am/Li neutron source. The experimental set-up was similar except the incident source neutrons were provided by an isotropic ^{241}Am/Li source which was placed on one side of the test section as shown in

Figure 2.3. Thin walled aluminum tubes co-axial with the test section were inserted into the test section. Selected spaces inside the test section were filled with water to form stagnant air-water test sections of different void fractions and different flow patterns (annular and inverted annular). The procedure used to analyse experimental results was as follows.

Define a dimensionless neutron counting rate ν by

$$\nu = \frac{N(\alpha) - N(1)}{N(0) - N(1)} \qquad (2.10)$$

If the linearity hypothesis holds, then Eq.(2.10) implies

$$\nu = 1 - \alpha \qquad (2.11)$$

The linearity hypothesis was thus tested by plotting ν against (known) α. The result is shown in Figure 2.4. In this figure, the statistical error in ν at 68% confidence level was calculated (see Appendix A) but not explicitly shown as the error bars so obtained were comparable in size to the data points.

From Figure 2.4, it is evident that ν is both non-linear with α and flow pattern dependent, apparently invalidating the linearity hypothesis. This discrepancy aroused renewed interest in the technique and demanded further study before a portable system could be designed.

2.3.3 Objectives of the Present Work

We have seen that the neutron scattering technique

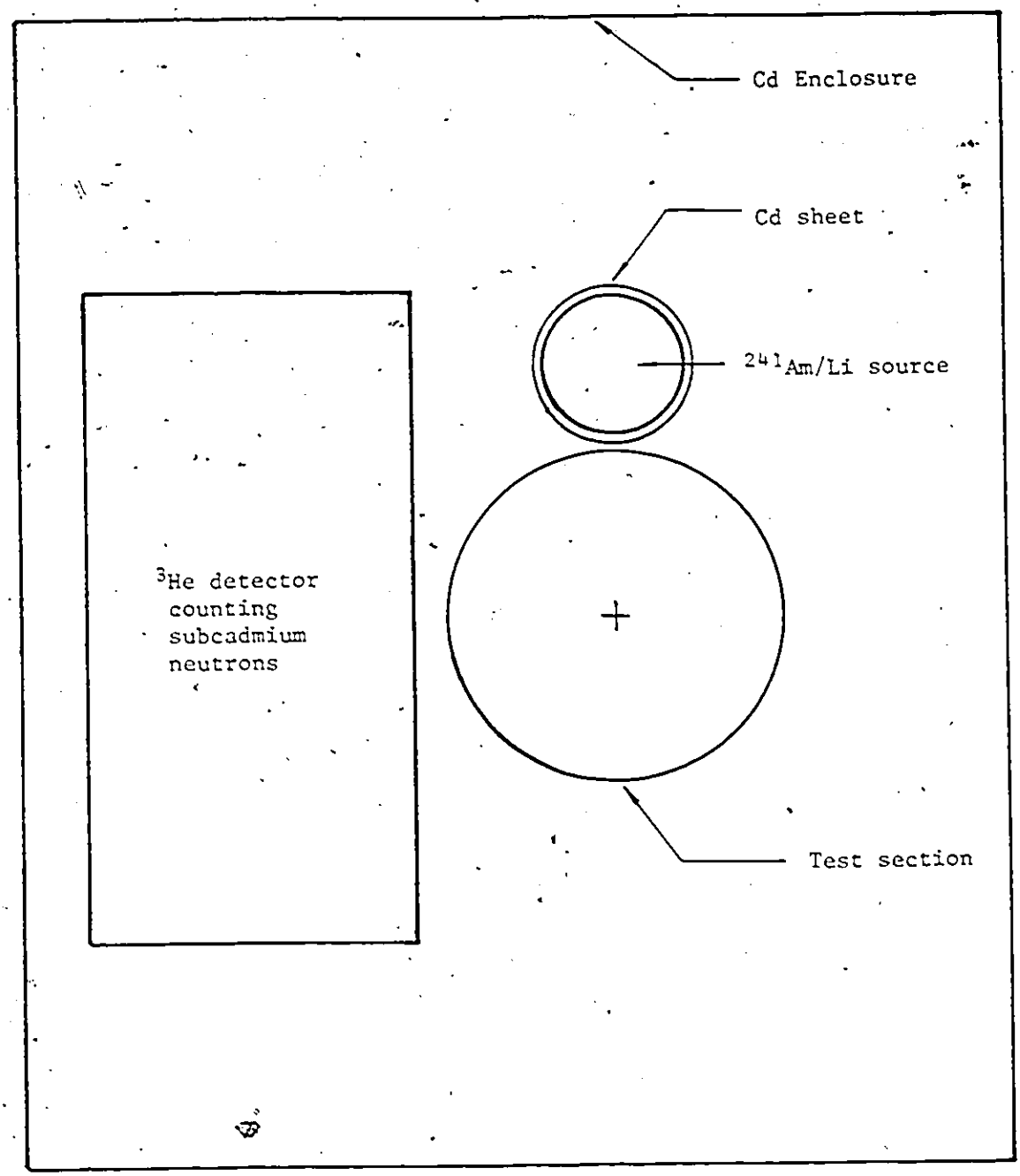

Figure 2.3 Experimental set-up in Expt #0 to test the neutron scattering technique using a portable ^{241}Am/Li neutron source

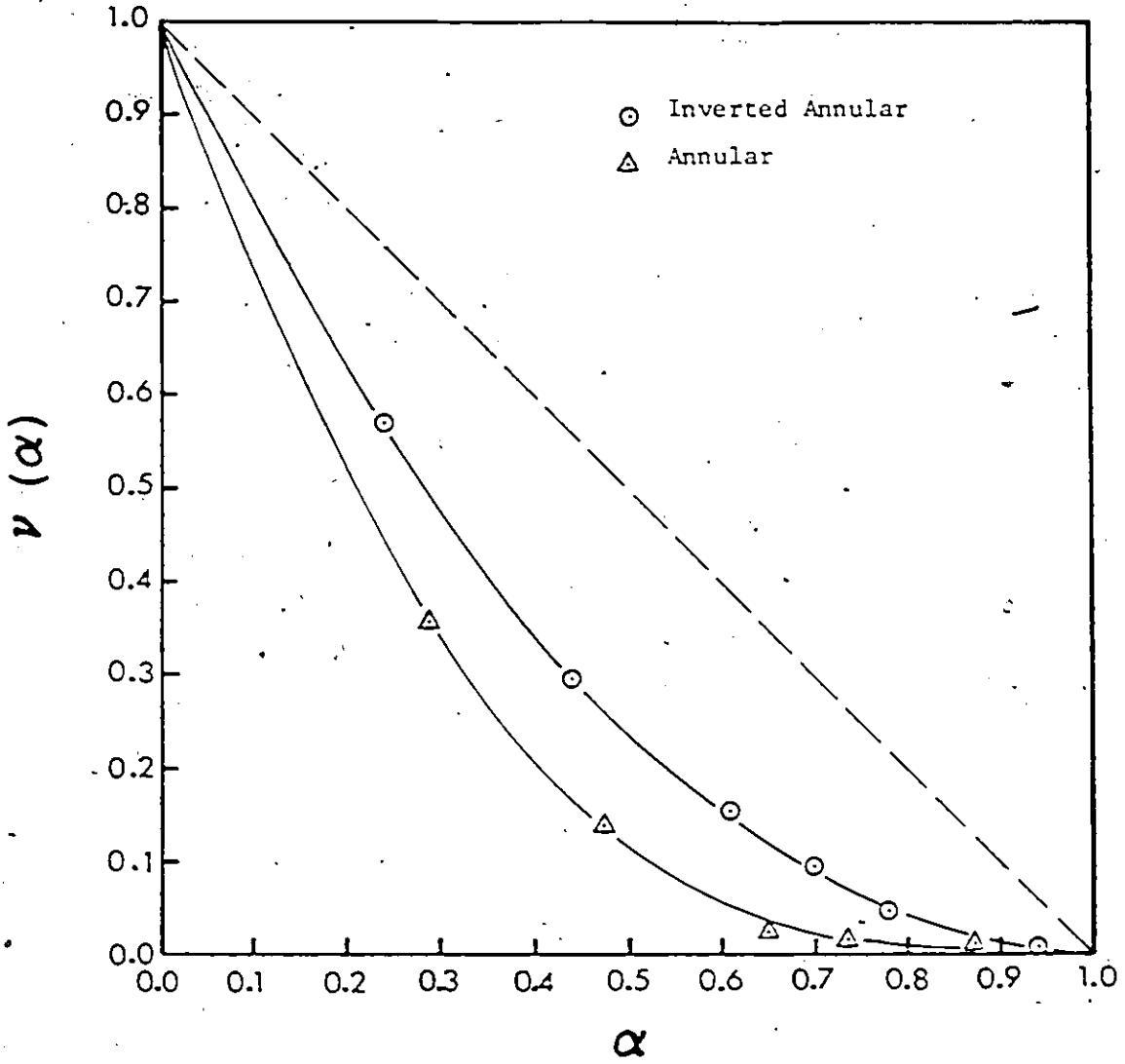

Figure 2.4 Result of Expt #0 showing non-linearity and flow pattern dependence in neutron detector response to void fraction α

developed in the previous work proved to have attractive advantages but suffers from the lack of portability. When attempts were made to add portability to the technique by implementing it with portable neutron sources, the main advantages of the technique in linearity and flow regime independence were lost. This dilemma triggered further investigation. Thus, the objectives of the present work became the following:

Objectives

1. To identify and evaluate the effect of various parameters on the technique regarding linearity and flow regime independence of the neutron counting rate with regard to α.
2. From findings obtained in the fulfillment of objective (1), derive conditions under which linearity and flow regime independence can be realized in a portable measurement system.
3. To gain an understanding of the important factors governing instrument response.
4. To arrive at a design procedure for a portable void fraction meter based on the results of these investigations.
5. To arrive at a conceptual design for a portable void fraction meter

2.3.4 Scope of Work

To fulfil these objectives, several sets of experiments were conducted. In each experiment, the effect of a particular parameter on linearity and flow regime independence was studied.

Parameters that have the more significant effects on instrument response were identified. Trends involving these more important parameters were tied together into a hypothesis which is qualitative in nature, suggesting conditions under which linearity and flow regime independence could be achieved with portable neutron sources. Experiments were then conducted to verify this hypothesis.

After the verification of the hypothesis by experiments, attempts were made to understand its basis. This required additional information on neutron behaviour in the experimental set-up. This information could not be provided with experiments alone. Monte Carlo simulations were then used to perform "numerical experiments" to fill in the missing information.

The Monte Carlo results, although useful in supplementing experiments, were essentially numerical experiments. Attempts were then made to explain the Monte Carlo results with simple theories —— simple of necessity because many neutron scattering processes are not easily treated. The purpose was to gain a deeper understanding of the technique and provide a good theoretical support for the hypothesis formed from the experimental results.

Based on all this, a design procedure for a portable system to implement the technique was derived.

From the above discussions, it is noticed that experiments and Monte Carlo simulations formed the backbone of the investigation. Hence, Chapter 3 will be devoted to background discussion on the experimental and computational (Monte Carlo) aspects. The results will be given in Chapters 4 and 5.

CHAPTER THREE

DESCRIPTION OF EXPERIMENTAL AND COMPUTATIONAL WORK

3.1 INTRODUCTION

As mentioned previously, experiments and Monte Carlo computations were two important aspects of the present investigation. In this chapter, these aspects will be described. For the experimental part, brief descriptions are presented for the equipment used, equipment set-up, the equipment assembly, and experimental procedure. For the computational part, arguments are presented suggesting Monte Carlo computations are the most suitable semi-theoretical tool to study neutron behaviour in the present problem. The basic philosophy of Monte Carlo computations and the MORSE computer code used to implement the method are described. The necessary modifications made on the MORSE code are discussed. Finally, preparation of the code (input information) for solving this problem is described.

3.2 EXPERIMENTAL ASPECTS

3.2.1 Experimental Equipment

The major experimental equipment used in the basic set-up is shown schematically in Figure 3.1. The set-up consists of a neutron source, a test section, a neutron detector, and a set of pulse counting electronics. The neutron source emits neutrons which are scattered by the water elements inside the test section. The scattered neutrons are detected by the neutron

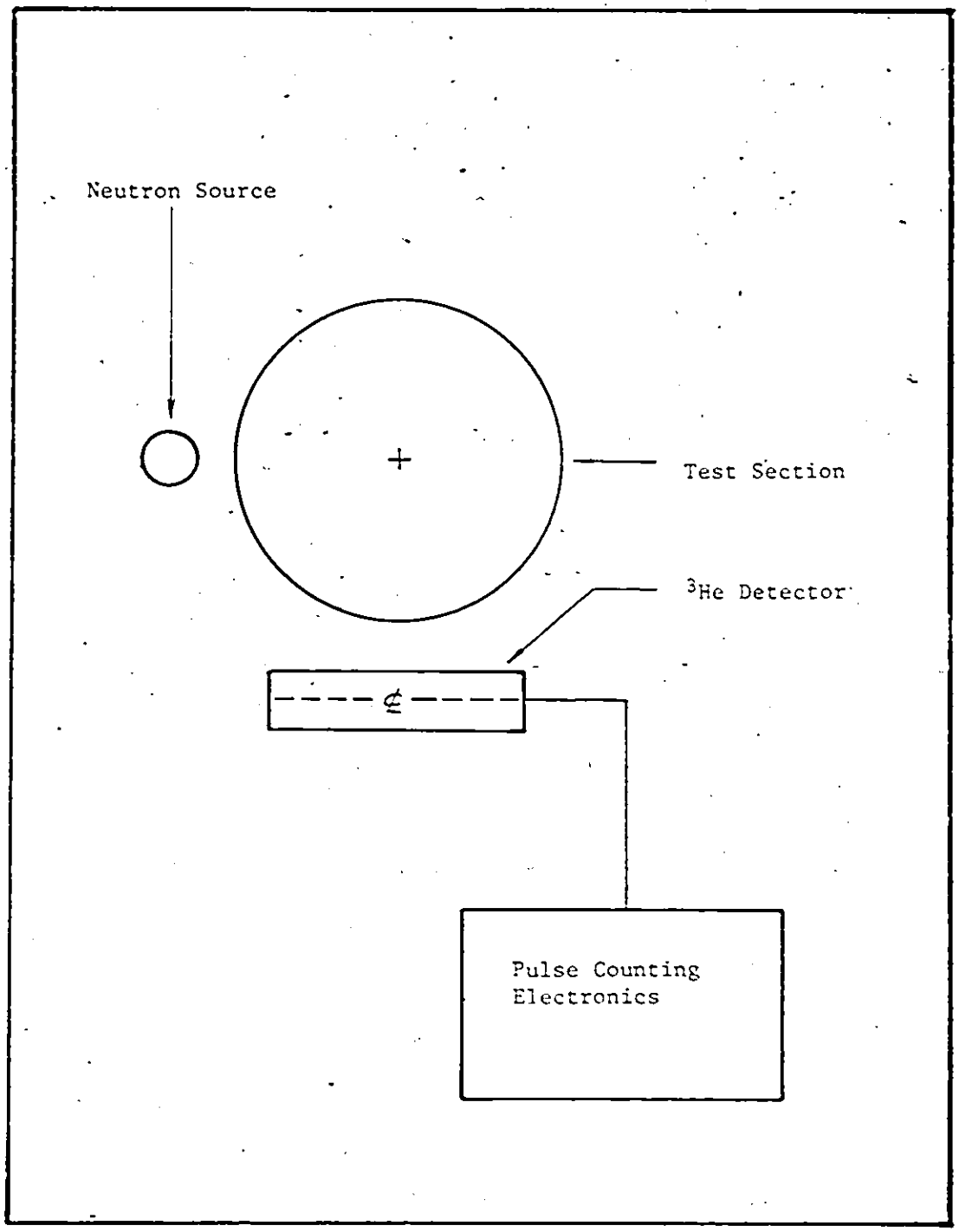

Figure 3.1 Schematic of major components in experimental equipment used in the present work

detector, giving rise to electric pulses, each of which corresponds to a single neutron. The electronic pulses from the neutron detector are processed and counted by the set of pulse counting electronics. Each of these four major components is described in more detail in the following.

3.2.1.1 Neutron sources

Neutrons are produced <114> in spontaneous fission, (α,n) reactions, photoneutron reactions, accelerated charged particle reactions and in a nuclear reactor. In the present work, neutrons were produced through either spontaneous fission or the (α,n) reaction. They were ^{241}Am/Li, ^{252}Cf, and ^{241}Am/Be neutron sources. Each of these sources is now described.

^{241}Am/Li source

An ^{241}Am/Li neutron source produces neutrons by the (α,n) reaction, i.e,

$$^{4}_{2}\alpha + ^{7}_{3}Li \longrightarrow ^{10}_{5}B + ^{1}_{0}n + Q \qquad (3.1)$$

The Q value is -2.79 MeV. This thresold energy is provided by the ^{241}Am alpha particle which has an energy of 5.48 MeV. Due to the low cross-section of the ^{7}Li(α,n)^{10}B reaction, the neutron yield per 10^6 alphas is only 1.1 <114>. Hence, a large quantity of ^{241}Am is needed. The neutron source used was a 3.7×10^{10} Bq source yielding a neutron output rate of 4×10^4 n/s. Physically, the neutron source was a cylindrical capsule, 22.4 mm in diameter and 31 mm in height (see Figure 3.2a). The neutron energy

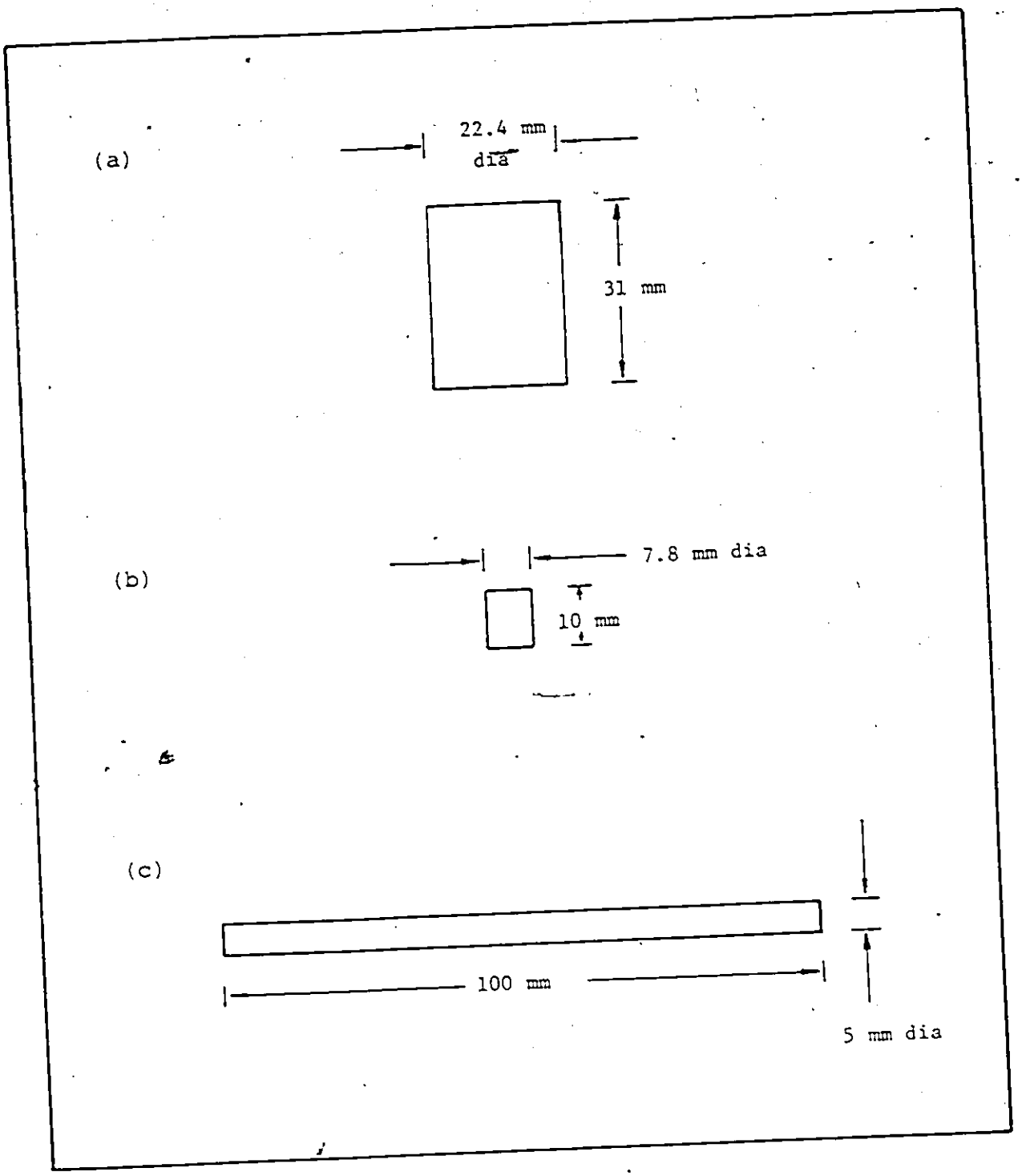

Figure 3.2 Physical dimensions of portable neutron sources:

(a) $^{241}Am/Li$
(b) ^{252}Cf
(c) $^{241}Am/Be$

spectrum of the ^{241}Am/Li neutron source is shown in Figure 3.3 <115>. The neutron energy peaks at around 100 keV and decreases to around 1.4 MeV. The average neutron energy is 0.4 MeV. This neutron source is the "softest" among the three sources used.

^{252}Cf neutron source

A ^{252}Cf source is a common spontaneous fission neutron source <114>. Its half-life is 2.65 years. Apart from spontaneous fission, this source also decays by alpha decay. The neutron yield is 0.116 n/Bq where the activity is that of the combined alpha and spontaneous fission. On a unit mass basis, each micro-gram of the source produces 2.3×10^6 n/s. Compared with other isotopic active material, ^{252}Cf sources involve very small amounts of active material, and can therefore be made in very small sizes. This can be seen in the physical dimensions of the ^{252}Cf sources used (see Figure 3.2b). Two such sources were used. Each was in the form of a cylindrical capsule of 7.8 mm diameter and 10 mm in height. The source content is 0.1 µg corresponding to 2.0 MBq emitting 2.3×10^5 n/s.

The energy spectrum of a ^{252}Cf source is shown in Figure 3.3 <116>. The spectrum peaks at about 1 MeV, although a significant yield of neutron extends to as high as 8 or 10 MeV. The average energy is 2.8 MeV.

^{241}Am/Be neutron source

Neutrons are produced by the (α,n) reaction. The alpha emitter is ^{241}Am. The target material is beryllium. The neutron production reaction is

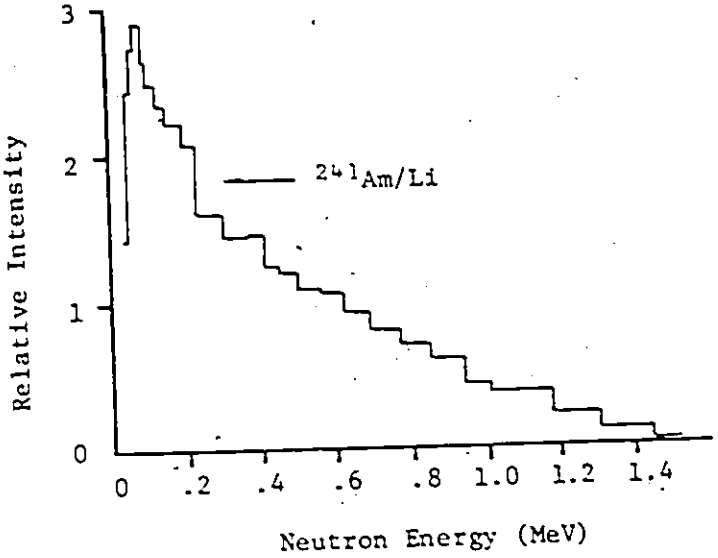

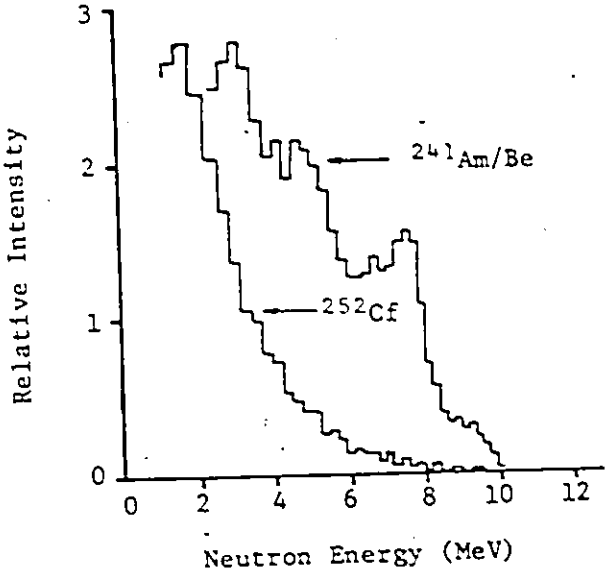

Figure 3.3 Neutron energy spectra of neutron sources used <115, 116>

$$ {}^{4}_{2}\alpha + {}^{9}_{4}Be \longrightarrow {}^{12}_{6}C + {}^{1}_{0}n + Q \qquad (3.2) $$

The Q value of this reaction is +5.71 MeV.

Two ^{241}Am/Be sources were used. Each was a 3.7×10^{9} Bq line source, emitting 2.2×10^{5} n/s. Each source was in the form of a cylindrical stainless steel capsule 100 mm long and 5 mm in diameter (see Figure 3.2c).

The neutron spectrum of the ^{241}Am/Be source is shown in Figure 3.3 <116>. The energy of the neutrons varies from about 2 MeV to a maximum of about 10 MeV. The average energy is 5.1 MeV. This is the "hardest" of the three sources used in the present work.

The relevant data for the three neutron sources used in the present work are given in Table 3.1.

3.2.1.2 Test sections

In the experiments, four test sections were used. Each test section consisted of a metal tube sealed at one end. The height of each tube was 152 mm. A sample is shown in Figure 3.4. The open end of the tube could be covered with a thin aluminum lid (3.2 mm thick) tightened onto the tube with screws to anchor floating parts in the test section (see next paragraph). Two test sections, I and III, were made from aluminum tubes. They are referred to as thin aluminum walled test sections. The other two

TABLE 3.1

NEUTRON SOURCES

Neutron Source	# Sources Used	Activity (Bq)	Neutron emission rate (s^{-1})	Average energy (MeV)
$^{241}Am/Li$	1	$3.7x10^{10}$	$4.0x10^{4}$	0.4
^{252}Cf	2	$2.0x10^{6}$	$2.3x10^{5}$	2.8
$^{241}Am/Be$	2	$3.7x10^{9}$	$2.2x10^{5}$	5.1

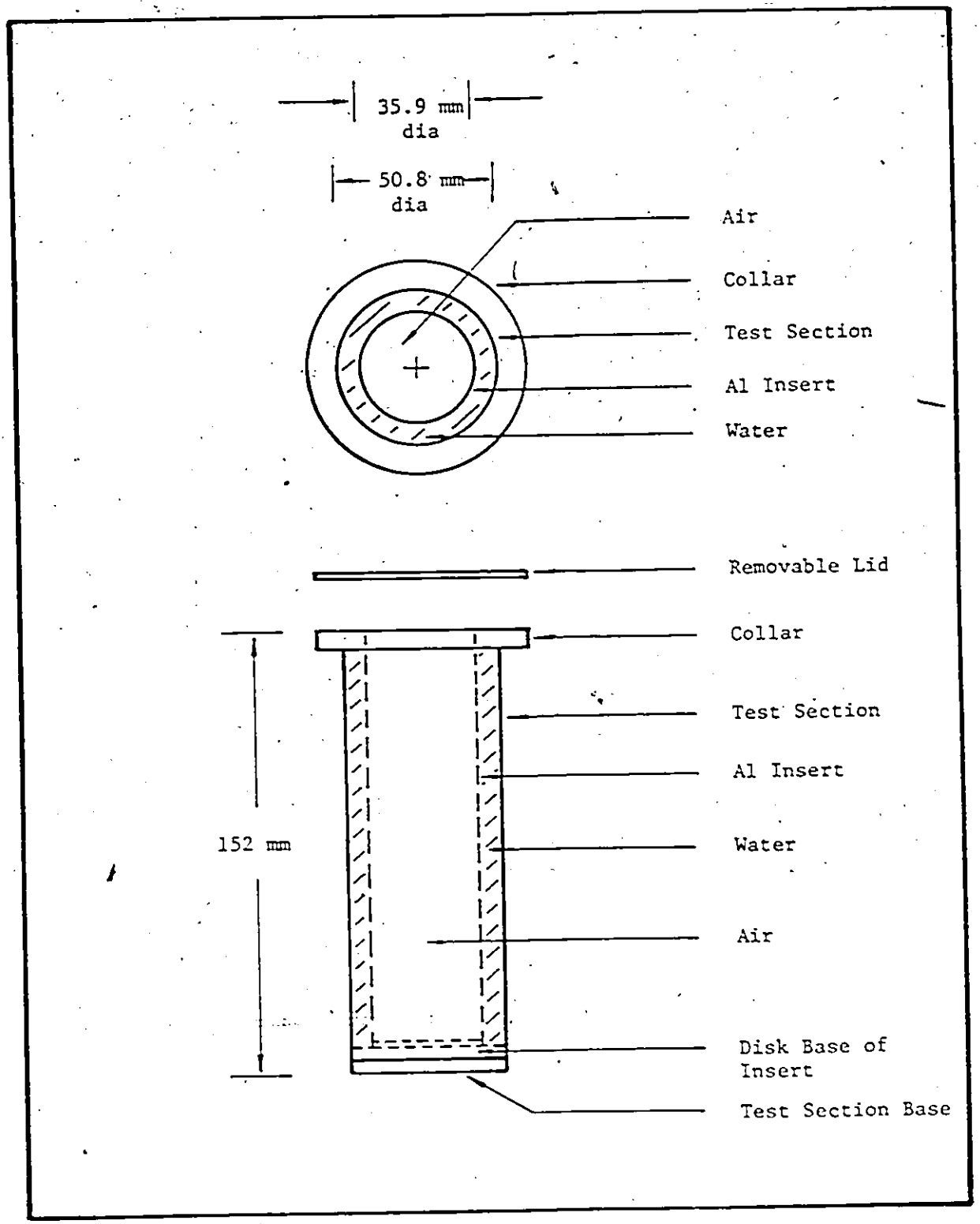

Figure 3.4 Test section containing an aluminum insert for air-water partition, simulating a test section (ID = 50.8 mm) with annular flow pattern of $\alpha = 0.5$

test sections, II and IV, were made from carbon steel tubes, and are referred to as thick carbon steel walled test sections. The dimensions of these four test sections are given in Table 3.2. These four test sections simulated tubular flow channels of two inside diameters, 50.8 and 127 mm. Since aluminum is quite transparent to neutrons, the aluminum walls in test sections I and III could be considered practically non-existent. These two test sections were used to study neutron behaviour in the water elements inside the test sections in order to develop a theoretical understanding of the phenomena. Test sections II and IV simulated thick walled pipes used in high pressure systems found in most industrial applications. These two test sections were used to study the neutron scattering technique in practical situations.

Typical two-phase mixtures were simulated in the following way. Thin walled aluminum inserts were made. A sample is shown in Figure 3.4. It is sealed at the bottom with a thin aluminum disk, 1.6 mm thick, and with a diameter equal to the ID of the test section. When it was inserted into a test section, the space either inside or outside this insert could be filled with water to form a simulated two-phase flow pattern. After the water was filled, the test section was covered with the lid to prevent the insert from floating. For example, the sample shown in Figure 3.4 represents a 50.8 mm test section containing a stagnant air-water mixture of 0.5 void fraction in annular flow.

Many aluminum inserts were made to yield air-water mixtures for both the 50.8 and 127 mm test sections for various

TABLE 3.2

DIMENSIONS OF TEST SECTIONS

TEST SECTION	WALL MATERIAL	HEIGHT (mm)	ID (mm)	OD (mm)
I	aluminum	152	50.8	57.2
II	carbon steel	152	50.8	69.8
III	aluminum	152	127.0	133.4
IV	carbon steel	152	127.0	152.4

void fractions. However, these inserts were made to simulate three flow patterns, namely, annular, inverted annular, and stratified flow. The three flow regimes are representative of flow situations found in various industries, including the nuclear industry. Annular and stratified flows are commonly found in horizontal systems, e.g. pipelines. Inverted annular flow occurs in quenching situations. It is sufficient to investigate the neutron behaviour in these three representative cases.

3.2.1.3 ^{3}He neutron detector

The detection of neutrons requires some type of interactions between neutrons and the detector. There are several mechanisms by which the interaction with matter takes place and each of these is the basis of a potential method of detection. The most useful ones are as follows <117>:

(i) neutron induced transmutations in which the product particles make detection possible. Examples are (n,α), (n,p), (n,γ), and (n, fission) reactions.

(ii) neutron-induced transmutations which result in radioactive nuclei giving information on the neutron flux that induced the radioactivity.

(iii) elastic scattering of neutrons in which the recoil particle is charged and is capable of being detected.

In the present work, ^{3}He neutron detectors were used. They operate by method (i), the reaction being <117>:

$$^{3}He + n \longrightarrow {}^{3}H + p + 765\ keV \qquad (3.3)$$

where 765 keV is the Q value of the reaction.

This reaction has good properties for neutron detection. The cross-section, starting with 5400 barns for thermal neutrons and dropping to about 1 barn for neutrons of 2 MeV energy <118>, varies smoothly over the entire energy range of interest and has no resonance. It is a detector most efficient for the detection of thermal neutrons. Also, there are no excited daughter products.

From a simplified view point, a ^3He neutron detector consists of ^3He gas contained under pressure with a mixture of Kr and CO_2 in a cylindrical metal tube. A thin wire suspended at the centre of the tube is positively biased at about 1 to 2 kV while the metal case is grounded. These serve as an anode and a cathode. The triton and proton, being charged particles, will dissipate all their shared energy in the reaction to produce ion-pairs. The number of ion-pairs is proportional to the total energy of the triton-proton system, which is in turn linearly related to the kinetic energy of the incident neutron. These ion-pairs are collected at appropriate electrodes, giving rise to a pulse whose size varies linearly with the kinetic energy of the incident neutron. The signal is then processed by a set of pulse counting electronics.

Two ^3He detectors, purchased from HARSHAW, were used. Each was cylindrical in shape, 140 mm long and 50.8 mm in diameter. The length of the active volume was 101.6 mm. The pressure of the ^3He gas was 0.2 MPa (2 atmospheres).

3.2.1.4 Pulse counting electronics

The pulse counting electronics system used in the present work consisted of a charge-sensitive preamplifier, a linear amplifier, a timing single channel analyser (SCA), a delay amplifier, a linear gate, a multi-channel analyser (MCA), and a timer/counter. Most of this electronics equipment are available commercially as "plug-in" standard Nuclear-Instrument-Modules (NIM). Details of the circuitry of these NIM modules can be found in the literature <119> and will not be repeated here. However, the function, particularly the characteristic input-output, of the electronics used will be briefly discussed as the following.

Charge-sensitive preamplifier

As mentioned before, upon the detection of a neutron, a quantity of charge is collected at the anode of the detector. The charge-sensitive preamplifier integrates this charge with a feedback capacitor. Thus, the detection of a neutron results in a fast rise and slow decay voltage pulse at the preamplifier output (see Figure 3.5). The maximum voltage output V_0 and decay time τ are respectively given by

$$V_0 = Q_D/C_f \tag{3.4}$$

$$\tau = R_f C_f \tag{3.5}$$

where Q_D = charge released by the detector

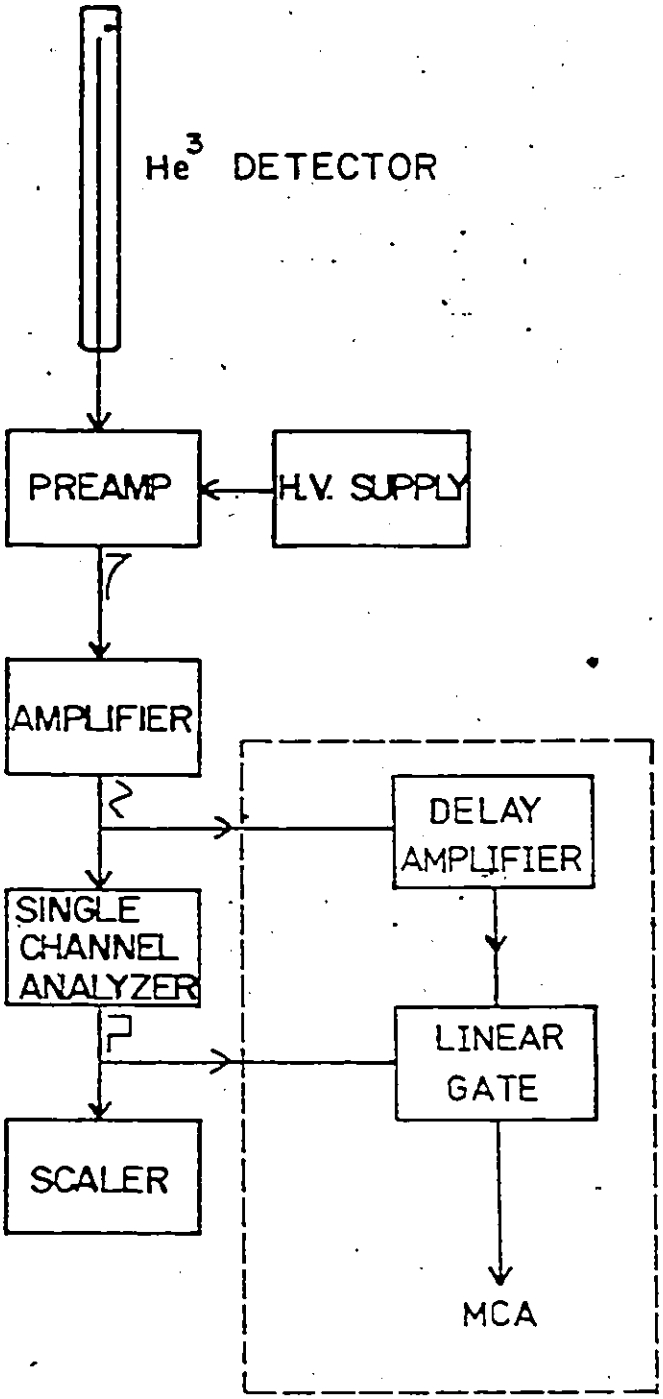

Figure 3.5 Schematic of Pulse counting electronics system

C_f = feedback capacitance

R_f = feedback resistance

The charge-sensitive preamplifiers used in the present work are HARSHAW NB-28 general purpose preamplifiers.

Linear amplifier

A linear amplifier takes a preamplifier output at its input. Through CR-RC pulse shaping, the linear amplifier output is Gaussian shaped (unipolar) and the height of the centroid is proportional to that of the preamplifier output signal V_0. Alternatively, through double differentiation, with CR-RC-CR pulse shaping, the linear amplifier output extends both above and below the baseline (bipolar) with the centroids being proportional to the preamp output (see Figure 3.5).

The linear amplifiers used in the present work are HARSHAW NA-23 amplifiers.

Delay amplifier

A delay amplifier inputs an analogue signal and reproduces it at its output (unit gain) at a later preset time interval (micro-second range). It is useful in setting SCA windows. An ORTEC 427 delay amplifier was used in the present work.

Single channel analyser (SCA)

This instrument has both a lower-level and upper-level discriminator that can be set to define a range of acceptance of linear amplifier outputs. The region between the lower-level and

upper-level discriminator settings is called the SCA window. A linear amplifier output whose amplitude falls within the window results in a logic pulse at the output of the SCA. This logic output can be counted by a scaler or used to trigger other NIM modules such as a linear gate. Single channel analysers used in the present work are HARSHAW NC-12.

Linear gate

A linear gate has two inputs, one for linear input and one for gate input. The linear input normally accepts analogue (linear amplifier output) signals. The gate input takes logic pulses from an SCA. When the linear gate encounters a gating input from the SCA, the "gate" inside is opened for a fixed time interval (<20 μs). If an analogue pulse enters the linear gate during this time interval this analogue pulse will be let through the gate and appears at the gated output. Pulses that arrive at times when the gate is closed will be grounded. This instrument is useful in coincidence counting and setting windows for the SCA. The linear gate used in the present work is an ORTEC 426.

Multichannel analyser (MCA)

A multi-channel-analyser (MCA) essentially consists of an analogue to digital converter (ADC) and a memory bank (channels). When an analogue pulse (linear amplifier output) of a particular height V enters the ADC, it is analysed according to its height by the ADC. One count is then added to a channel in the memory which is linear with respect to the pulse height and stores the number of counts corresponding to heights $V \pm \Delta V$. In the present work a TRACOR NORTHERN TN-1705 MCA is used.

Timer/counter (scaler)

A timer/counter (scaler) accumulates the number of logic pulses from the SCA over a preset time span.

Having described the essential features of the basic set of equipment, the experimental set-up is now described in the following section.

3.2.2 Experimental Set-up

The description of the experimental set-up includes the setting of the neutron counting electronics system (detector and pulse counting electronics) and the general assembly of apparatus and equipment for experiments.

3.2.2.1 Setting of neutron counting electronics system

Neutron counting was extensively carried out in experiments performed with the ^{3}He detector and the pulse counting electronics arranged in a set-up schematically shown in Figure 3.5. A typical pulse height spectrum for a ^{3}He detector is shown in Figure 3.6. This is a spectrum that would appear on the screen of the MCA if the linear amplifier outputs were fed directly to the MCA.

Referring to Figure 3.6, region A in the spectrum is due to gamma rays from the neutron source and electronics noise. Region B is due to the so called "wall effect" <117>. A count in this region is due to an emitted proton (from the detection of neutron) hitting the detector capsule wall before fully dissipating its kinetic energy. Region C is the thermal/epithermal neutron peak. Region D is due to neutrons of

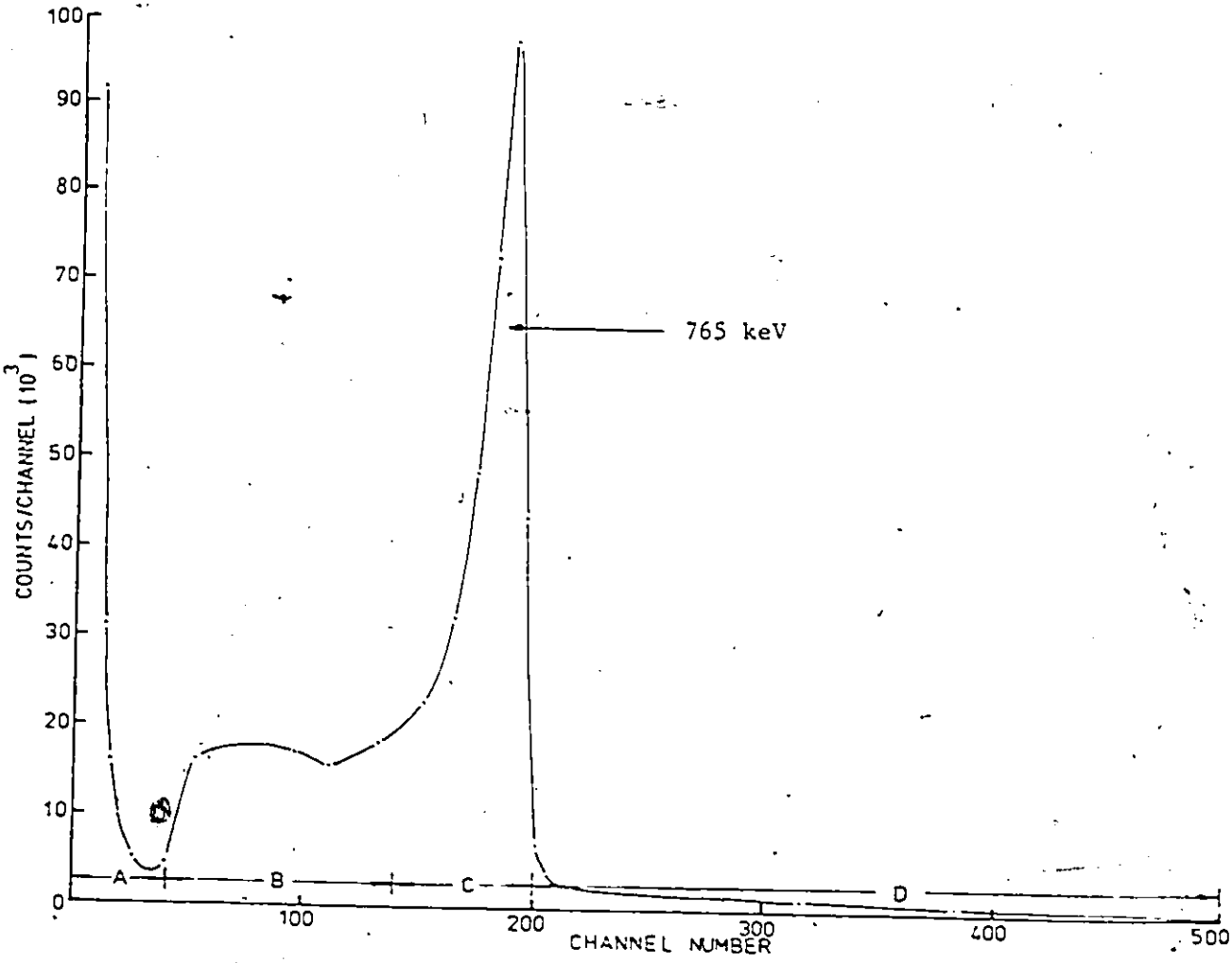

Figure 3.6 Typical pulse height spectrum of a ^3He detector responding to thermal neutrons

higher energy. Region B to D are all due to neutron events but not region A. Thus, it is important to exclude pulses in region A from being counted. This was accomplished by setting the SCA window properly (gating).

The setting of the SCA window was carried with the delay amplifier, the linear gate, and MCA, as shown in Figure 3.5.

An analogue pulse from the linear amplifier is split into two identical components through a "tee" at the linear amplifier output. One component is fed through the delay amplifier and the other through the SCA with the window fully open. The delay amplifier output signal is externally triggered by the SCA output on an oscilloscope. Delay in the delay amplifier was adjusted so that the delay amplifier and SCA output signals would emerge at the same time. After this crucial step of synchronizing the delay amplifier and the SCA outputs, the SCA logic output signal is split into two, one being fed to a scaler and the other into the gate input of the linear gate, while the delay amplifier output signal is fed into the input of the Linear Gate. Since both the inputs are synchronized, the delay amplifier output pulse is "let through" the opened gate triggered by the SCA logic trigger pulse and emerges at the linear gate output. The linear gate output is analysed by the MCA, and only the part of the pulse height spectrum that falls within the SCA window might be analyzed and appear in the spectrum. The other region of the pulse height spectrum will be "wiped out". With the window in the SCA fully opened, a self-gating neutron energy spectrum is obtained, identical to that shown in Figure 3.6. The lower

discriminator level of the SCA is then raised until pulses in region A disappeared. After this is completed the SCA discriminates against the pulses in region A. The electronics in the dotted box (see Figure 3.5) were then removed. The timer/counter (scaler) then counted only neutron events, and the system is ready for neutron counting.

It is an essential feature in this neutron scattering technique to count neutrons that are thermalized. Although the neutron counting electronics system was set to count neutron events, further steps were taken to ensure the counting of only thermal neutrons. This was accomplished with the procedure of "differential counting". To implement this procedure, the ^3He detector was provided with a cylindrical sleeve (cap) made of cadmium sheet 0.8 mm thick. Cd has a very high absorption cross-section of 7200 barns for 0.18 eV neutron <120>, and is very efficient in removing neutrons of energy lower than ~0.5 eV (cadmium cut-off). For each stagnant test-section of a given α, the ^3He detector was first shielded with the cadmium sleeve, and the average counting rate of scattered, epicadmium neutrons (E_n > 0.5 eV) was measured. The cadmium sleeve was then removed, and the average counting rate of both subcadmium (E_n < 0.5 eV) and epicadmium, scattered neutrons was also measured. Thus, the difference yielded the number of subcadmium neutrons. This "differential counting" procedure was considered adequate for the purpose of counting only thermalized neutrons.

3.2.2.2 Assembly of apparatus and equipment

Since portable neutron sources were used, the experiments

were conducted inside a thermalhydraulics laboratory in the Nuclear Research Building, McMaster University. The neutron source strengths were generally weak and posed minimal health hazard. Thus, no extensive shielding for health reasons was necessary. The general experimental set-up is depicted in Figure 3.7. The essential apparatus was placed on a table 0.6 m high and supported by Dexion legs. The table top was made of aluminum plate 12.7 mm thick and 0.7 m x 0.7 m in area. The aluminum plate was lined completely with a cadmium sheet 0.5 mm thick. A Cd enclosure with a removable top and wall thickness 0.5 mm, confined a space inside which the neutron source, test section and the ^{3}He detector were placed. The purpose for this cage was to shield the ^{3}He detector from thermalized neutrons reflected back from the surrounding.

In an experiment, one of the four test sections was placed upright on the table top. The ^{3}He detector was suspended horizontally on one side of the test section with a retort stand. The axis of the cylindrical detector was always at mid-height of the test section. The mid-points of the active volume of the detector and the test section formed an axis C_2-C_3 (see Figure 3.7). The length of the C_2-C_3 axis (detector to test section distance) varied, dependent on the object of each experiment. One of the three neutron sources was suspended at mid-height of the test section on one side such that the axis C_1-C_2 formed by the centres of the neutron source and the test section was perpendicular to the axis C_2-C_3. The neutron source used was always wrapped in cadmium sheet to remove subcadmium neutrons from the source. Again, the length of the C_1-C_2 axis varied,

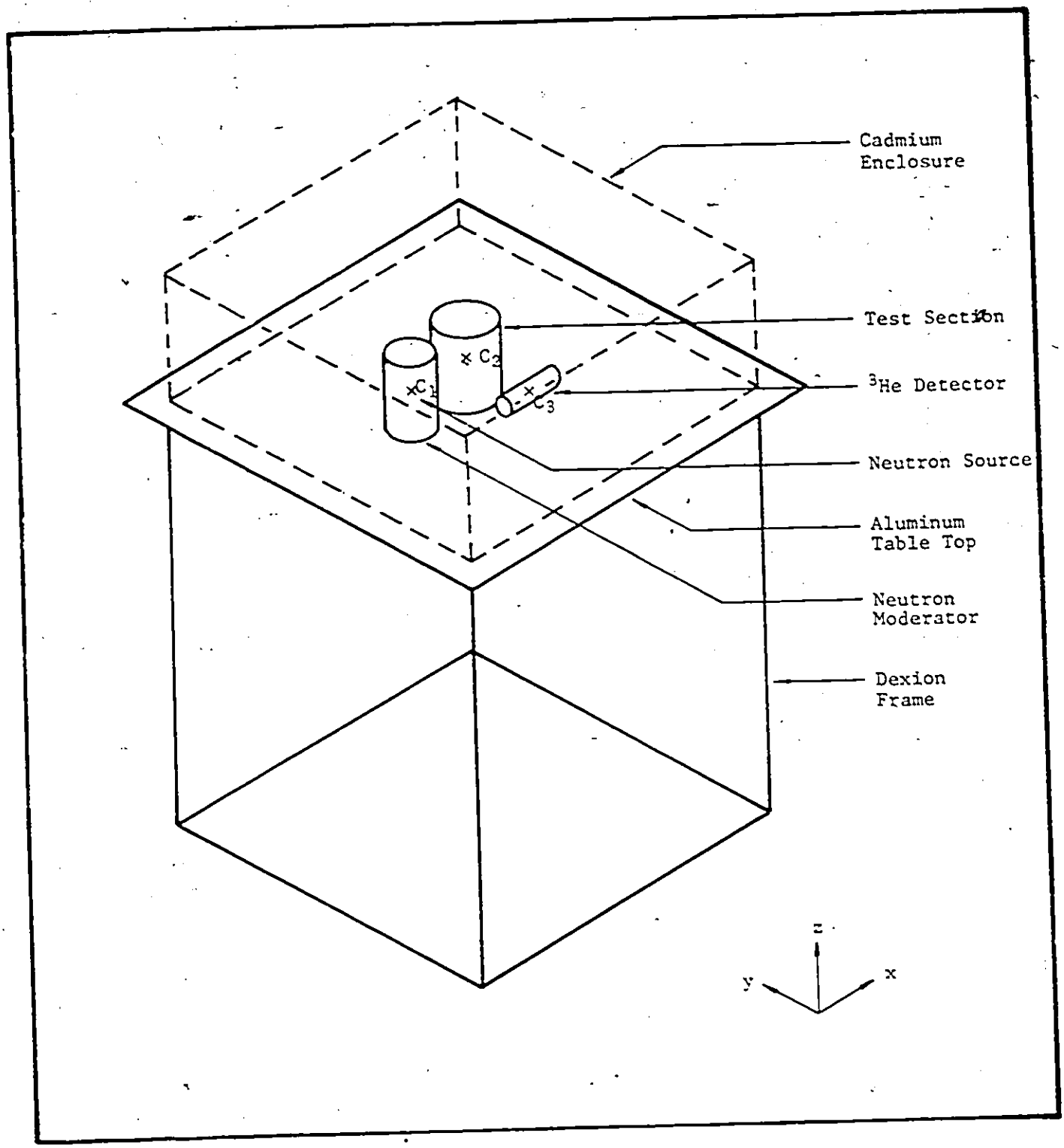

Figure 3.7 Typical assembly of experimental equipment and apparatus used in the present investigation

dependent on the object of an experiment.

The arrangement given above was a basic general set-up. Other modifications were possible. In some experiments, it was necessary to alter the energy spectrum of the incident neutrons to the test section. In that case, a neutron source was suspended in an empty thin walled aluminum tube (neutron source tube) which was in turn immersed in a can of water (neutron moderator-can). The diameter of a neutron moderator-can varied to yield incident neutrons of different energy spectra. The moderator-can was completely covered with cadmium sheet in most experiments to remove subcadmium neutrons emerging from the moderator-can so that incident source neutrons to the test section had energies above that of the cadmium cut-off (E_n>0.5 eV). The outside diameters of the neutron source tubes for the ^{241}Am/Li, ^{252}Cf, and ^{241}Am/Be sources were 28 mm, 12.7 mm, and 12.7 mm, respectively.

In some experiments, the effect of the presence of hydrogeneous material (neutron reflector) around the test section was studied. In that case, the cadmium enclosure was lined on the outside with layers of paraffin wax. Each layer was made by thin wax tiles 51 mm wide, 102 mm long, and 6.4 mm thick. These paraffin wax layers acted as reflectors for neutrons.

The general experimental set-up described above was simple but versatile. It was suitable for studying the effects of various parameters in order to gain better understanding of the neutron scattering technique. More details on these parameters, particularly the experimental results will be given

in Chapter 4. Experimental procedures will be described in the next section.

3.2.3 Experimental Procedure

In the present work, the object of each experiment was to study the effect of a parameter on the neutron scattering technique regarding linearity and flow pattern independence. A particular experimental set-up might vary, dependent on the parameter being studied, the experimental procedure was the same for all experiments, and is described as the following.

The experimental equipment was set up for a particular experiment, i.e, a test section was chosen, a particular detector to test-section distance was fixed, a neutron source with or without moderator was placed beside the test section, and the cadmium enclosure was lined with or without wax layers. An aluminum insert was inserted into the test section, and the test section was filled partially with water to yield a test section containing stagnant air-water mixture of a given void fraction and flow pattern. The ^{3}He detector was covered with the cadmium sleeve. Neutrons were counted with the shielded detector together with the pulse counting electronics over a sampling time period (usually 1000s). Counting was repeated several times to obtain an ensemble average of epicadmium neutrons. The cadmium sleeve was then removed, and an ensemble average for the sum of subcadmium and epicadmium neutrons was similarly obtained. The difference in the two quantities yielded the counting rate of subcadmium neutrons.

The aluminum insert was replaced with another one and the

procedure of differential neutron counting was repeated. An experiment was completed when the counting rates of subcadmium neutrons scattered by test sections of a number of void fractions and at least two flow patterns (annular and inverted annular) were obtained.

The subcadmium neutron counting rates were converted to the dimensionless neutron counting rate ν (see Eq.(2.10) in section 2.3.2) and were plotted against the known void fractions and flow patterns. By comparison with results of other experiments, the effect of each parameter regarding linearity and flow pattern independence was inferred.

The description of the experimental aspects in the present investigation is now completed. The experimental results and inferencies drawn will be given in Chapter 4. The next section is devoted to discussions on the computational aspects.

3.3 COMPUTATIONAL ASPECTS

During the investigation, it was necessary to calculate the scattered neutron fluxes at a detector in a typical experimental set-up. In other words, the equation governing neutron behaviour in a system typical of the experiments was to be solved. Thus, the fundamental equation for neutron transport and common solution methods are first discussed in the following subsection.

3.3.1 Boltzmann Transport Equation and Solution Methods

3.3.1.1 Boltzmann Transport Equation

The void fraction and simulated two-phase flow did not vary in the experiments described here. Thus, the neutron equation to be solved was the steady state Boltzmann Transport Equation <121>. It is stated here without proof:

$$\vec{\Omega}\cdot\nabla\phi(\vec{r},E,\vec{\Omega}) + \Sigma_t(\vec{r},E)\phi(\vec{r},E,\vec{\Omega})$$
$$= \int_0^\infty dE' \int_{4\pi} d\vec{\Omega}' \Sigma_s(\vec{r},E'\to E,\vec{\Omega}'\to\vec{\Omega})\phi(\vec{r},E',\vec{\Omega}') + S(\vec{r},E,\vec{\Omega}) \qquad (3.6)$$

In Eq. (3.6), $\vec{r}$ = position variable

E = kinetic energy of neutron

$\vec{\Omega}$ = unit vector along the neutron's direction of motion

$(\vec{r},E,\vec{\Omega})$ = denotes the general six-dimensional phase space

$\Sigma_t(\vec{r},E)$ = total neutron cross-section

$\Sigma_s(\vec{r},E'\to E,\vec{\Omega}'\to\vec{\Omega})$ = double differential neutron scattering cross-section <121>

$\phi(\vec{r},E,\vec{\Omega})$ = directional flux density of neutrons <121>

The various terms in this equation are interpreted as the following.

The term $\vec{\Omega}\cdot\nabla\phi$, is the net convective loss (leakage) of neutrons per unit phase space volume. The term $\Sigma_t(\vec{r},E)\phi(\vec{r},E,\vec{\Omega})$ is the removal rate per unit spatial volume of neutrons with energy about E, moving in a direction about $\vec{\Omega}$. The term $S(\vec{r},E,\vec{\Omega})$ is the source neutrons emitted per phase space volume at the spatial point $\vec{r}$ with energy about E and direction about $\vec{\Omega}$. The term $dE'd\vec{\Omega}'\Sigma_s(\vec{r},E'\to E,\vec{\Omega}'\to\vec{\Omega})\phi(\vec{r},E,\vec{\Omega}')$ is called the scattering-in

term. It is the gain of neutrons per unit phase space volume about $(\vec{r},E,\vec{\Omega})$ contributed from neutrons of all energy E' and directions $\vec{\Omega}'$. The Boltzmann Transport Equation is therefore basically an equation for neutron balance (conservation).

3.3.1.2 Solution methods for the Boltzmann Transport Equation

There are several common methods to tackle the Boltzmann Transport Equation. These include (i) the Spherical-Harmonics method, (ii) Diffusion Theory, (iii) Discrete Ordinates techniques, and (iv) Monte Carlo method. Excellent discussions on these solution techniques are found in the literature <121,122> and will not be repeated here, except that brief comments on the first three techniques are given as the following.

(i) Spherical-Harmonics method

In this method, the directional flux density $\phi(\vec{r},E,\vec{\Omega})$ is expressed as a linear combination of the complete set of Spherical Harmonics $Y_n^m(\vec{\Omega})$ as

$$\phi(\vec{r},E,\vec{\Omega}) = \sum_{n=0}^{\infty} \sum_{m=-n}^{n} \phi_n^m(\vec{r},E) Y_n^m(\vec{\Omega}) \qquad (3.7)$$

with $Y_n^m = Y_n^m(\mu,\varphi)$

$$= \left\{ \frac{(2n+1)(n-m)!}{(n+m)!} \right\}^{\frac{1}{2}} P_n^m(\mu) \exp(im\varphi) \qquad (3.8)$$

In Eq.(3.7), $\phi_n^m(\vec{r},E)$ is the "coefficient" of the corresponding Spherical Harmonic Function and is to be solved. The double differential neutron scattering cross section $\Sigma_s(\vec{r},E'\to E,\vec{\Omega}'\to\vec{\Omega})$ is similarly expanded in terms of Spherical Harmonics, and the Boltzmann Transport Equation is reduced to an infinite set of coupled differential-integral equations.

As an example, in a one dimensional, cylindrically symmetrical, and sourceless situation, each equation in the infinite set assumes the form <121>.

$$n\frac{\partial}{\partial z}\phi_{n-1}(z,E) + (n+1)\frac{\partial}{\partial z}\phi_{n+1}(z,E) + (2n+1)\Sigma_t(z,E)\phi_n(z,E)$$

$$= (2n+1)\int_0^\infty dE'\Sigma_{sn}(z,E'\to E)\phi_n(z,E') \qquad (3.9)$$

The complexity of solution can often be somewhat simplified by considering only the first few orders of n. The "P_N approximation" results when $\frac{\partial}{\partial z}\phi_{N+1}$ is neglected. In principle, with suitable boundary conditions imposed, the first N equations can be solved for ϕ_0, ϕ_1, ..., ϕ_N, although it is still a formidable job.

Unfortunately, the extension of such schemes to two or three dimensions, for which all $\phi_n^m(\vec{r},E)$ have to be determined,

results in such cumbersome equations that, except for the P_1 approximation, alternative methods for attacking such problems are preferred. In the present work, the geometry of the experimental set-up (neutron source, test section, and detector) was not one dimensional. Also, the P_1 approximation, as it will become clearer in the next section, was not adequate. For these reasons, the Spherical Harmonics method was not adopted.

(ii) Diffusion Theory (P_1 Approximation)

If the directional neutron flux density $\phi(\vec{r},E,\vec{\Omega})$ can be approximated by the P_1 approximation in the Spherical Harmonics expansion, i.e. near isotropic scattering, it can be shown that the Boltzmann Transport Equation can be reduced to the familiar Diffusion Equation used often in nuclear reactor analyses <121,122>.

The Diffusion Equation for a non-fissionable medium is stated as:

$$-\nabla\cdot D(\vec{r},E)\nabla\phi(\vec{r},E) + \Sigma_t(\vec{r},E)\phi(\vec{r},E)$$

$$= \int_0^\infty \Sigma_s(\vec{r},E'\rightarrow E)\phi(\vec{r},E')dE' \qquad (3.10)$$

In Eq.(3.10), $D(\vec{r},E)$ is called the diffusion coefficient.

Certain limitations are inherent to diffusion theory: (1) the scattering process is assumed to be isotropic in the laboratory frame of reference, (2) the directional neutron flux density is nearly isotropic, (3) the diffusing medium must be a weak absorber, (4) the results are not valid for regions within

two to three mean free paths of boundaries, strong sources, and strong sinks.

In our situation, scattering by hydrogen is not isotropic in the laboratory frame of reference <120>, violating limitation (1). The dimension of the test section is comparable with the mean free path of a high energy neutron, e.g. mean free path for a 2 MeV neutron is close to 50 mm in water. Any part inside the test section is within two or three mean free paths to the boundary formed by the source neutron field and the test section wall, violating limitation (4). Due to the violation of limitations, the diffusion equation was not adopted.

(iii) Discrete-Ordinates method

In the Discrete Ordinate Method, attempts are made to find $\phi(\vec{r},E,\vec{\Omega})$ for a discrete number D of directions $\vec{\Omega}_d(d=1,2,\ldots,D)$. It can be shown <122> that the Boltzmann Transport Equation can be replaced by a set of D equations

$$\vec{\Omega}_{xd}\frac{\partial}{\partial x}\phi(\vec{r},E,\vec{\Omega}_d)+\vec{\Omega}_{yd}\frac{\partial}{\partial y}\phi(\vec{r},E,\vec{\Omega}_d)+\vec{\Omega}_{zd}\frac{\partial}{\partial z}\phi(\vec{r},E,\vec{\Omega}_d)+\Sigma_t(\vec{r},E)\phi(\vec{r},E,\vec{\Omega}_d)$$

$$=\int_0^\infty dE'\left[\sum_{n=0}^{\infty}\sum_{m=-n}^{n}\Sigma_{sn}(\vec{r},E'\to E)\right]\left[\sum_{d=1}^{D}w_{d'}Y_n^m(\vec{\Omega}_{d'})\phi(\vec{r},E',\vec{\Omega}_{d'})\right]Y_n^m(\vec{\Omega}_d) \qquad (3.11)$$

These discrete-ordinate equations couple the directional flux in a given w_d, to all other chosen directions. The mathematical form of the equation is suited to solution by iterative procedures.

From the computational point of view, because of iterative procedures, fluxes at regions of less interest have to be calculated simultaneously in order to solve for fluxes at more important regions. In our case, since we are most interested in estimating the neutron flux at a particular spatial point (detector), this method was not preferred.

In the present work, the Monte Carlo method was adopted. This method is discussed in more detail as in the next section.

3.3.2 Monte Carlo Method and the MORSE Code

3.3.2.1 Monte Carlo method

The Boltzmann Transport Equation can be reduced to three equivalent forms, the Integral Flux Density Equation, the Integral Event Density Equation, and the Integral Emergent Particle Density Equation <123>. These three equations serve as a basis for the Monte Carlo method as an alternative technique to solve for $\phi(\vec{r},E,\vec{\Omega})$. The procedures of the Monte Carlo method can be found in the literature <121,122,124> and therefore will only be discussed briefly here.

In the life of a neutron, an "event" is something that happens to a neutron. For example, the neutron appears at a certain location with a certain energy and direction of travel, interacts at a particular location and loses a certain amount of

energy. A "case history" is, then, a sequence of events beginning and ending according to some preselected criteria. A case history is then followed, often with the help of a high speed computer, by determining the outcomes of particular events according to the probability of occurence of individual events. For example, in our case, a neutron from a neutron source is "born" with certain energy and flight direction. By means of random number generation <122>, the neutron energy and flight direction are assigned according to known probability distribution of source neutron energies and flight directions. Once the outcome of this event is determined (neutron energy and flight direction picked) the neutron is assumed to fly in a straight line until it interacts with the medium at a particular location. The location of interaction is determined according to the probability distribution function for interaction location. At the location of interaction, the kind of interaction, i.e. scattering, absorption, etc, is again determined according to the probability of each kind of interaction given by the corresponding cross-sections. If the interaction is determined to be scattering, the energy and flight direction of the neutron after scattering is then picked according to the probability distribution functions of energy and flight direction. This composite process is repeated until the neutron is either absorbed or when it reaches a location far away from the detector. The case history is then ended. In principle, after following a very large number of case histories, the quantity of interest, e.g. the number of thermal neutrons arriving at a

detector site per source neutron (average of contributions) can be determined. This approach is called the analogue Monte Carlo method where the random walk of the neutron is followed "honestly" according to known probability distribution function of events.

The analogue Monte Carlo approach is attractive because of its simplicity. However, it suffers from one disadvantage because of its inherent statistical nature. The quantity of interest is obtained by averaging the outcomes of a large number of histories. The accuracy of the average (square root of variance) is governed by the Central Limit Theorem <121,122>. In essence, this Theorem says that the square root of the variance σ, varies inversely as the square root of the number of histories m. Very often, because of the small probability of a source particle (neutron) yielding the quantity of interest, a very large number of histories is required for acceptable accuracy. In that case, an exceedingly large amount of computer time would be required, making the technique impractical. For example, in the present investigation, we are interested in the number of thermal neutrons arriving at the detector for each source neutron. The probability that a high energy source neutron, after the random walk in the test section, will be thermalized and reach the detector is expected to be small. A very large number of histories would be required to yield the quantity of interest with acceptable accuracies. To circumvent this difficulty, the non-analogue Monte Carlo approach is often adopted, as discussed in the following.

The essential idea of the non-analogue Monte Carlo

approach is to distort the basic probabilities that determine the outcome of each event in such a way that the occurrence of a "favourable" event is enhanced in order to reduce the variance. However, great care must be taken to adjust the "weight" of a particle (neutron) so that the statistical properties of the case histories are not distorted. For example, a source neutron with initial weight 1 interacts with a medium at a collision site. Suppose the probability of collision and absorption are 0.9 and 0.1 respectively. The particle is "forced" to scatter, i.e. increasing artificially the probability of scattering from 0.9 to 1.0. As a result, the random walk is forced to continue. However, in order to keep the case histories unbiased, the weight of the particle after the collision must be reduced from 1.0 to 0.9. This procedure saves computer time that could otherwise be wasted in tracking histories that are prematurely ended by absorption of the particle. Other techniques involving particle weight adjustment are called Splitting and Russian Roulette <121,122,124>.

To reduce the variance in a quantity of interest, a non-analogue scoring technique can also used. After the direction and energy of a particle emerging from a collision is determined in the the random walk process, the probability that this particle could arrive at the detector at the next flight along with the energy is calculated. Calculated also is the energy of the neutron if it could reach the detector. The weight of the particle is multiplied with this probability and is accumulated to contribute to the quantity of interest. This non-analogue

scoring technique is called the next-event estimator and is justified by the Integral Flux Density Equation.

From the above discussions, it can be seen that the Monte Carlo Method is a more suitable method for handling the type of problem in the present work. The complex 3-dimensional geometry of the set-up (neutron source, test section, and detector) can be handled with ease by virtue of the random walk process. It also calculates the quantity of interest at a localized point (detector) efficiently. In the present work, the Monte Carlo procedures were implemented with the MORSE computer code. This code is described in the following subsection.

3.3.2.2 The MORSE computer code

The Multigroup Oak Ridge Stochastic Experiment (MORSE) code is a Monte Carlo neutron and gamma ray transport code. A copy was obtained from the Radiation Shielding Information Centre, ORNL, and was used in the present work for the implementation of the Monte Carlo procedures. This code can solve mulitigroup transport problems by using neutron, gamma ray, or coupled neutron-gamma cross-section libraries. Also, it solves problems by implementing the non-analogue Monte Carlo procedures. The detail of this code can be found in the documentation manual <123>. Only brief descriptions are given here.

The MORSE code contains subroutines grouped in modular forms. Figure 3.8 is a flow chart showing the logic and relationship between main code modules in the MORSE code. The SOURCE module generates a source particle. After a particle is

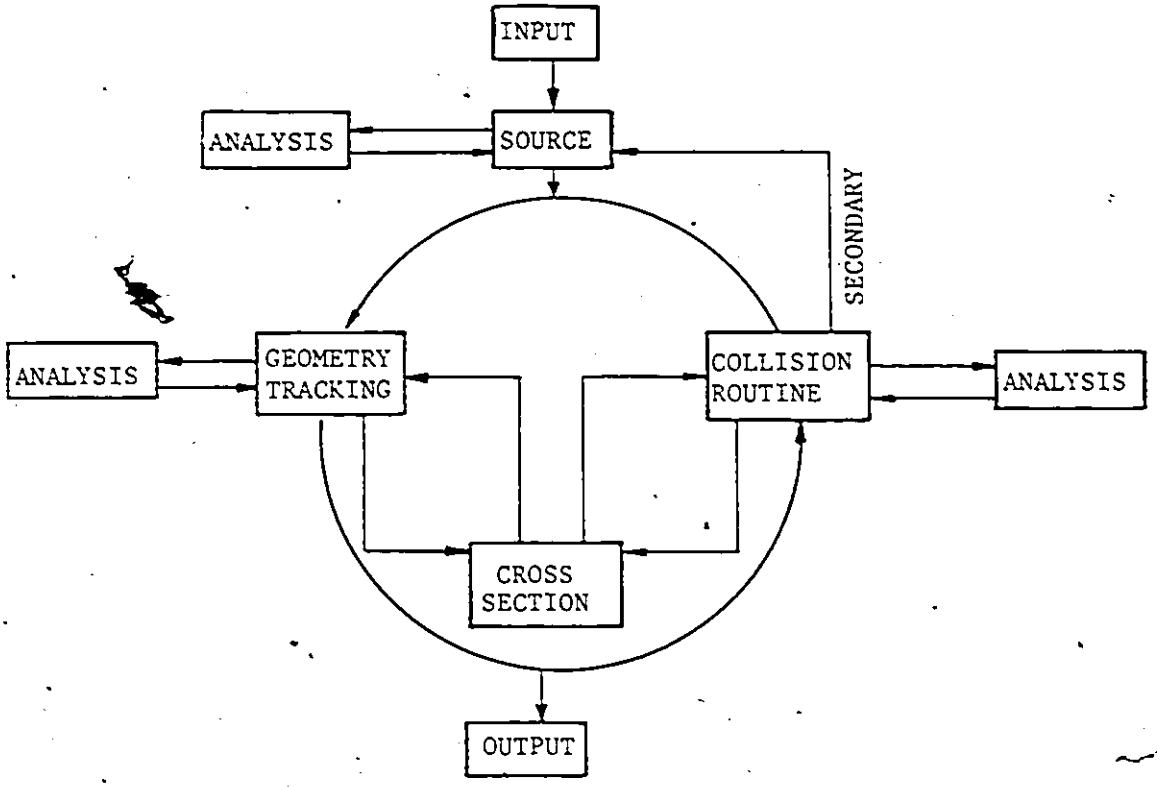

Figure 3.8 Flow diagram of main modules in MORSE

generated, the TRACKING module generate the histories and perform major bookkeeping. The GEOMETRY module is required for tracking from collision to collision. The geometry is described as unions and intersects (OR and AND Boolean algebra operations) of primary geometrical bodies (spheres, cubes, paralleloped, etc) to compose complicated geometries. The COLLISION module determines energy loss, change of direction and secondary generation of gamma rays at a collision site. The CROSS-SECTIONS module is needed to provide information both in the collision and the tracking processes. The ANALYSIS module is used to estimate the contribution of a random walk to the parameters of interest. "Analysis" of events may be obtained during the tracking process (track length/unit volume or boundary crossing estimates) and at the collision sites (collision density or next event estimators). The "analysis" may also make use of the CROSS-SECTION module as required by the used estimators. The INPUT module reads input cards. A copy of the Input instructions is shown in Appendix B. The OUTPUT module prints the input cards and the result of analyses. Having described the MORSE code, the next subsection describes how the MORSE code was implemented to solve problems.

3.3.3 Implementation of the MORSE Code

To implement the MORSE code, some modifications were necessary. The modifications are described in this subsection. After modification, correct input cards had to be prepared before running the code for problem solving. Essential characteristics of MORSE inputs for solving our types of problems are described. Finally, the specific set-up of the code for

solving three typical types of problems in this work is described.

3.3.3.1 Modification

Although the MORSE code is quite a flexible code, it was necessary to modify some parts of it to handle the problems in this work. The major changes were in the source particle geometry and the neutron albedo subroutines. They are discussed here.

Source particle geometry modification

The MORSE code inherently assumes the geometry of a point source the spatial co-ordinates of which are to be defined in Card C in the INPUT set (see Appendix B). In some of the problems, a beam was to be used and modification was made. A beam geometry was simulated by generating a point source neutron the x-coordinate of which was randomly picked within a beam width defined in the x-direction. This was achieved first by adding a READ statement in the INPUT subroutine to accept the half-width of the beam. The subroutine MSOUR was then modified so that the input variable XSTART (x-coordinate) was overridden. Instead, a CALL statement R=SFLRAF(0) from the Random Number Package <123> was added to generate a number between -1 and 1. The half-width of the beam was then multiplied by this random number and assigned to XSTART. The code would thus generate a different x-coordinate for a source particle to start a new case history.

Albedo subroutine modification

The MORSE code was provided with a "dummy" subroutine ALBDO for modification to handle albedo problems. As mentioned

in Section 3.2.2.2, in some experiments, the test section was surrounded by a cadmium enclosure which in turn was lined with wax layers acting as neutron reflectors. To simulate similar experiments a region was assigned as an albedo region. When a neutron hit this region, instead of tracking the neutron through, computer time was greatly saved by calculating the average probability of the neutron being reflected and the average energy of the reflected neutron through the use of albedo coefficients. The neutron, with its weight reduced according to the probability thus calculated would continue on with the random walk. The dummy subroutine ALBDO was replaced by a set of statements to do this. This modified subroutine ALBDO was developed by Hussein <125>. A listing of it is shown in Appendix C. In addition, the modified subroutine ALBDO checked the energy of the reflected neutron. If it fell below the cadmium cut-off energy (0.5 eV), the history would be terminated. This conformed with the presence of the cadmium enclosure.

3.3.3.2 Characteristics of typical MORSE input in the investigation

The essential characteristics of typical MORSE inputs for solving problems in the present work are described here. However, it is not meant to cover every input variable in the code. For detailed input instructions, Appendix B should be referred to.

Number of histories

In Card B, the product of the two variables NSTRT and NITS determines the total number of histories to be followed in a

run. The number of histories determines the accuracy in a quantity of interest. Usually, one to three thousand histories were followed in a run to yield a fractional standard deviation of 5% in the neutron fluence (time integrated flux) at the detector site.

Source neutron information

In some runs, a point, isotropic source was used. In this case, the original version of MORSE, which assumes point source geometry was used. The co-ordinates of the point source were defined in Card D (see Appendix B). The angular distribution of neutron from the source was assigned (0 for UNIP, VINP, and WINP in Card D). In some runs, a beam geometry was used. In this case, the modified version was used. The beam was chosen to be in the y-direction. The half width of the beam was entered along with the x, y, and z co-ordinates in Card D. The x-coordinate would vary to simulate a beam geometry. The direction cosines of source neutrons were assigned in Card D (0,1,0) for a beam in the y-direction. In either case, the energy spectrum of the source neutrons was defined. In some runs, monoenergetic source neutrons were used. The source neutron energy was defined in terms of the energy group number IG entered in the variable ISOUR in Card C. In some runs, multi-group energy source neutrons were used. The spectrum was then entered in Cards E1 and E2.

Energy group definition

Thirty three energy groups were defined for source

neutron energy, neutron cross-sections, and analyses. The group structure is shown in Table 3.3. Notice that Group 33 corresponds to subcadmium neutron energy and would be used interchangeably throughout this dissertation. These groups were used in all runs and were entered in Card F.

Neutron cross-section

A set of 33 group, P_8, neutron cross-section had been prepared by Hussein <125> and was available for the present work.

This set of cross-sections was entered through Cards XA to XG to create "probability tables" by the MORSE code. A "probability table" so created for an element or compound consisted of total cross-section, scattering cross-section, and the group to group down-scatter probabilities. These probabilities were used by the code to determine the outcome of an event in the random walk process, collision location, energy, and direction of a scattered neutron. Probability tables were created for ^{1}H, ^{2}H, air, ^{27}Al, ^{56}Fe, ^{3}He, and ^{112}Cd. These tables were created once and for all, and stored on tape for recall in subsequent runs.

System geometry

Through the combinatorial geometry module <123> in the code, complicated general three dimensional material configurations were described by considering unions, difference, and intersects of simple bodies such as spheres, boxes, cylinders, etc. In effect, the problem space was divided into unique zones. Zones were grouped into regions which had the same material. For example, the geometry of a solid aluminum rod with

TABLE 3.3

NEUTRON ENERGY GROUP STRUCTURE IN MORSE

ENERGY GROUP (IG)	LOWER EDGE (eV)	UPPER EDGE (eV)
1	1.22E 07	1.49E 07
2	1.00E 07	1.22E 07
3	8.18E 06	1.00E 07
4	6.70E 06	8.18E 06
5	5.49E 06	6.70E 06
6	4.49E 06	5.49E 06
7	3.33E 06	4.49E 06
8	2.47E 06	3.33E 06
9	1.83E 06	2.47E 06
10	1.49E 06	1.83E 06
11	1.10E 06	1.49E 06
12	8.21E 05	1.10E 06
13	6.08E 05	8.21E 05
14	3.02E 05	6.08E 05
15	1.11E 05	3.02E 05
16	6.74E 04	1.11E 05
17	3.18E 04	6.74E 04
18	2.48E 04	3.18E 04
19	1.93E 04	2.48E 04
20	1.17E 04	1.93E 04
21	7.10E 03	1.17E 04
22	4.31E 03	7.10E 03
23	2.03E 03	4.31E 03
24	9.61E 02	2.03E 03
25	4.54E 02	9.61E 02
26	2.14E 02	4.54E 02
27	1.01E 02	2.14E 02
28	2.90E 01	1.01E 02
29	8.32E 00	2.90E 01
30	3.06E 00	8.32E 00
31	1.13E 00	3.06E 00
32	4.14E-01	1.13E 00
33	0.00	4.14E-01

two holes drilled through it could be set up in the following way.

Referring to Figure 3.9, the co-ordinates for three cylindrical bodies could be defined in Cards CGB as bodies 1, 2, and 3, so that bodies 1 and 2 were inside body 3. Zones 1 and 2 could then be defined in Cards CGC as identical to bodies 1 and 2 respectively. Zone 3 could be defined as the space inside body 3 but outside bodies 1 and 2. Then zones 1 and 2 could be grouped into regions 1 through Cards CGD. Zone 3 could be identified as region 2. Regions 1 and 2 could then be identified as air and aluminum in Cards CGE. After these steps, the desired geometry of the aluminum rod with two holes could be set up.

In the code, there are also provisions for defining three special regions, the white, black, and albedo regions. A white region is a vacuum and is completely transparent to neutrons. A black region is a neutron sink, and when a neutron enters this region, the random walk is terminated and another case history starts. When a neutron enters an albedo region, tracking momentarily stops, and the subroutine ALBDO is called to perform albedo calculations. These special provisions were used in some of the runs.

Albedo regions

The wax layers in some experiments were simulated by albedo regions. The albedo coefficients necessary for the albedo calculations were taken from those listed by Radkowsky <126>. These coefficients were orginally derived by solving the transport equation and had been tested against experiments, and

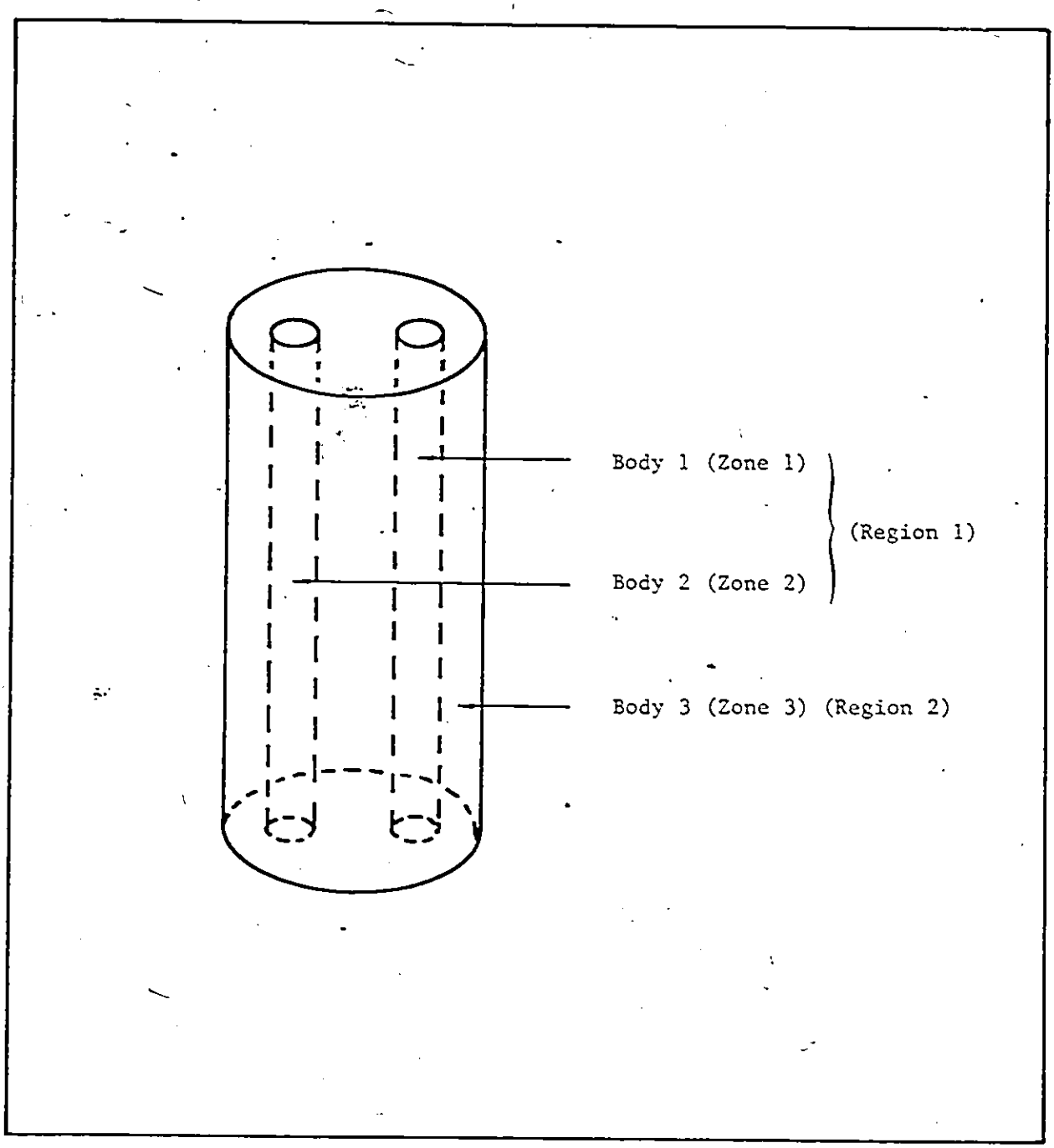

Figure 3.9 Geometry definition in MORSE: example of an aluminum rod with two holes

were considered adequate for analyses in the present work.

Scoring

To calculate the neutron fluences at the detector (quantity of interest), a point detector was used as a next-event estimator. The point detector was placed at the centre of the space occupied by a ^{3}He detector in the geometry set-up. The co-ordinates and response function of the point detector were entered in Cards CC and FF in the SAMBO Analysis Input deck. The point detector could then estimate the neutron fluence for all the 33 groups and give the uncertainty in the estimate in terms of fractional standard deviations.

The above discussions completes the general procedures of input cards preparation. In the next section, the input set-up for three specific types of problems will be discussed more specifically.

3.3.3.3 Specific Input Set-Up for Problem Solving

Three types of problems were solved with the MORSE code. They were (i) simulation of experiments for comparison, (ii) study of the effect of monoenergetic source neutrons, and (iii) calculation of moderated neutron source energy spectra. The INPUT set-up for each type of problem is discussed as follows.

Simulation of experiments and results

The MORSE code was first used to simulate Expt #0(see Section 2.3.2). Recall that, in Expt #0, the neutron scattering technique was tested with a portable ^{241}Am/Li neutron source, and results indicated that the neutron detector response was not

linear with α nor flow regime independent, contrary to the results obtained in work done with a reactor neutron beam. This controversy triggered the present work. The purposes of simulating this experiment with the MORSE code were (i) to test the mastery of the usage of this code, and (ii) to countercheck the validity of the results of Expt #0.

The system geometry set-up in the code input was simple. Referring to Figure 3.10, the geometry of the 51 mm test section I_1 containing an air-water mixture of a given void fraction and water phase distribution (annular or inverted annular) was set up. A point, isotropic, neutron source was defined at the same position relative to the test section as in the actual experiment. The energy spectrum of the $^{241}Am/Li$ source (see section 3.2.1.1) was entered to define the energy distribution of the point source. A point detector was defined at the centre of the ^{3}He detector in the actual experiment. The assembly of apparatus and equipment was placed inside a box which defined the problem space. The space outside this box was assigned to be a black region (neutron sink). The code was then run to estimate the subcadmium neutron fluence at the point detector for the given test section by following about 3000 histories. The simulation was repeated for all the values of void fractions and water phase distributions covered in the actual experiment by changing the geometry of the air-water mixture inside the test section.

After all the necessary runs were made, the detected subcadmium neutron fluences, being proportional to the actual

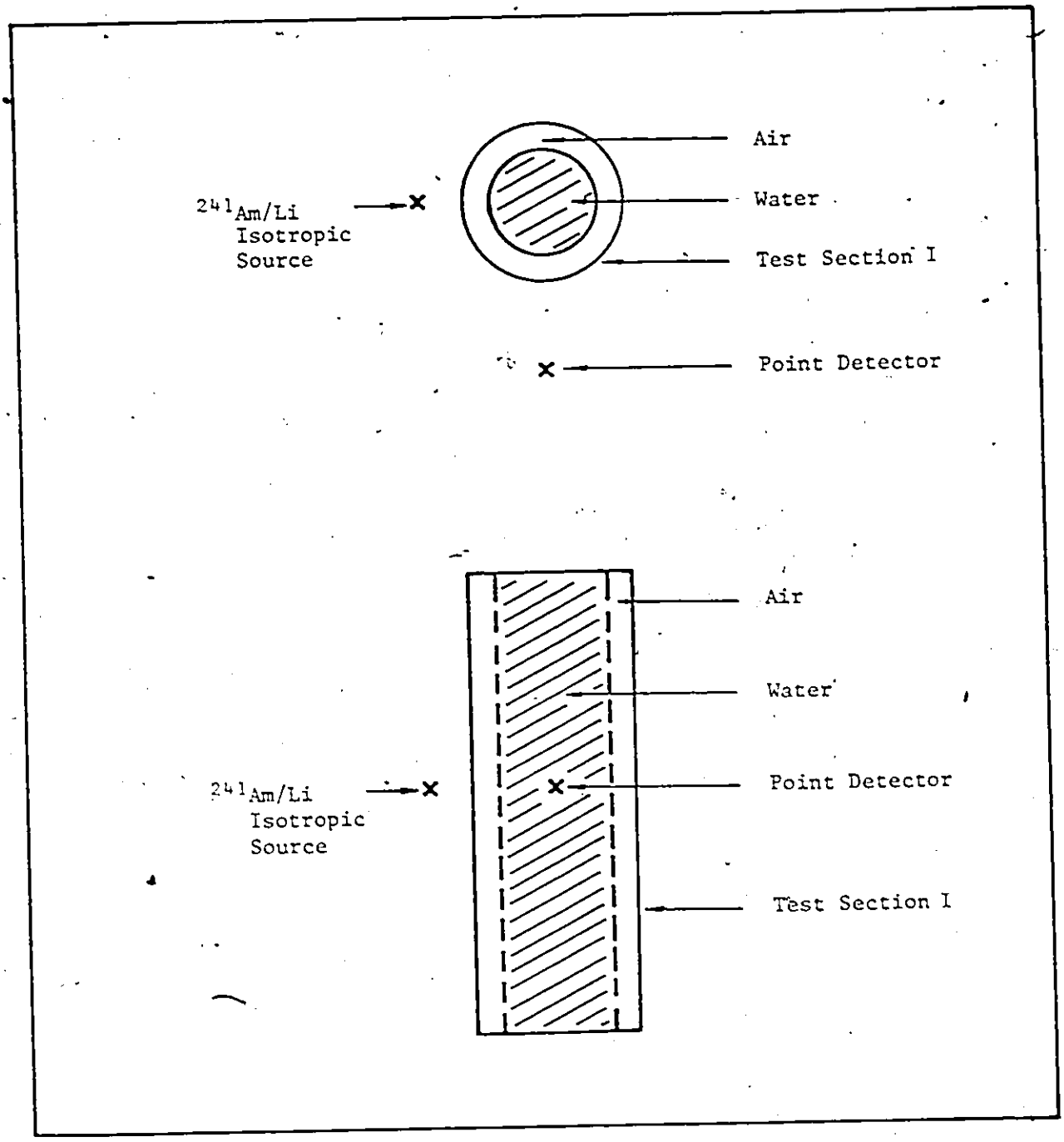

Figure 3.10 Geometry set-up for Monte-Carlo simulation of Expt #0

neutron counting rate, were converted to the dimensionless neutron counting rate ν. The result is shown in Figure 3.11 along with that obtained for the actual experiment. From this figure, it is evident that the experiment and simulation agreed very well.

From this simulation experience, the mastery of the usage of the MORSE is considered proven. More importantly, it is confirmed the results for Expt #0 were valid.

Monoenergetic source neutron effect

It was found, at one point, during the investigation, that it was important to study the effect of source neutron energy regarding linearity and flow regime independence of detector response. MORSE was called upon to perform "numerical experiments" for the study.

The system geometry set-up for such an experiment is shown in Figure 3.12. The test-section geometry was first set up. A beam geometry was defined for source neutrons incident at mid height of the test section. However, single group energy was assigned to the source neutrons. For annular water distribution, the beam width was the same as the inside diameter of the test section for all void fractions, and the initial "weight" of a source neutron was assigned to be 1. For inverted annular water distribution, the beam width was adjusted to equal the diameter of the water core, and the initial weight was adjusted inversely with the water core diameter. This importance sampling technique was adopted to save computing time which would otherwise be wasted in tracking some of those neutrons streamming through the

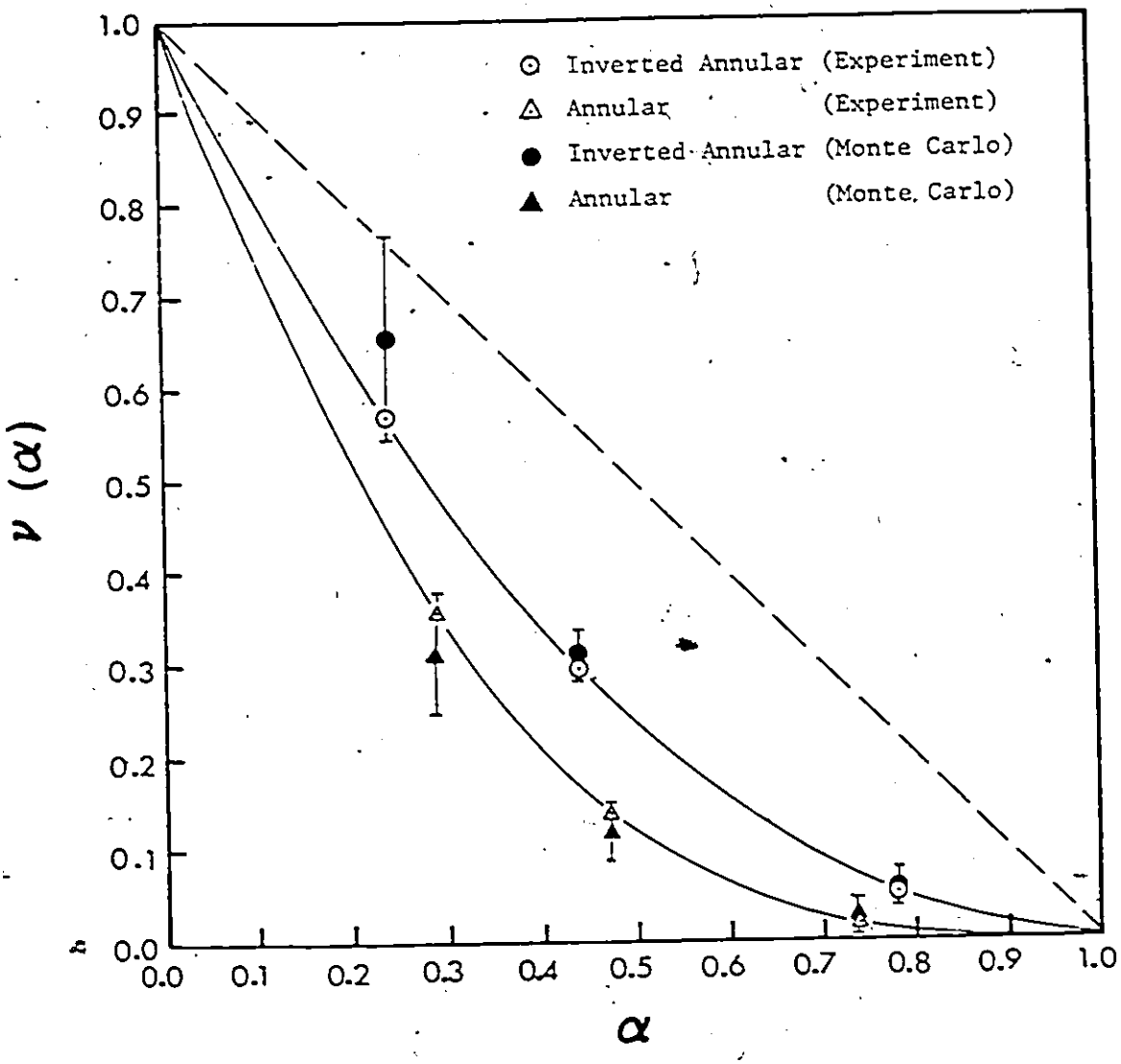

Figure 3.11 Comparison of Monte Carlo simulation and experimental result for Expt #0

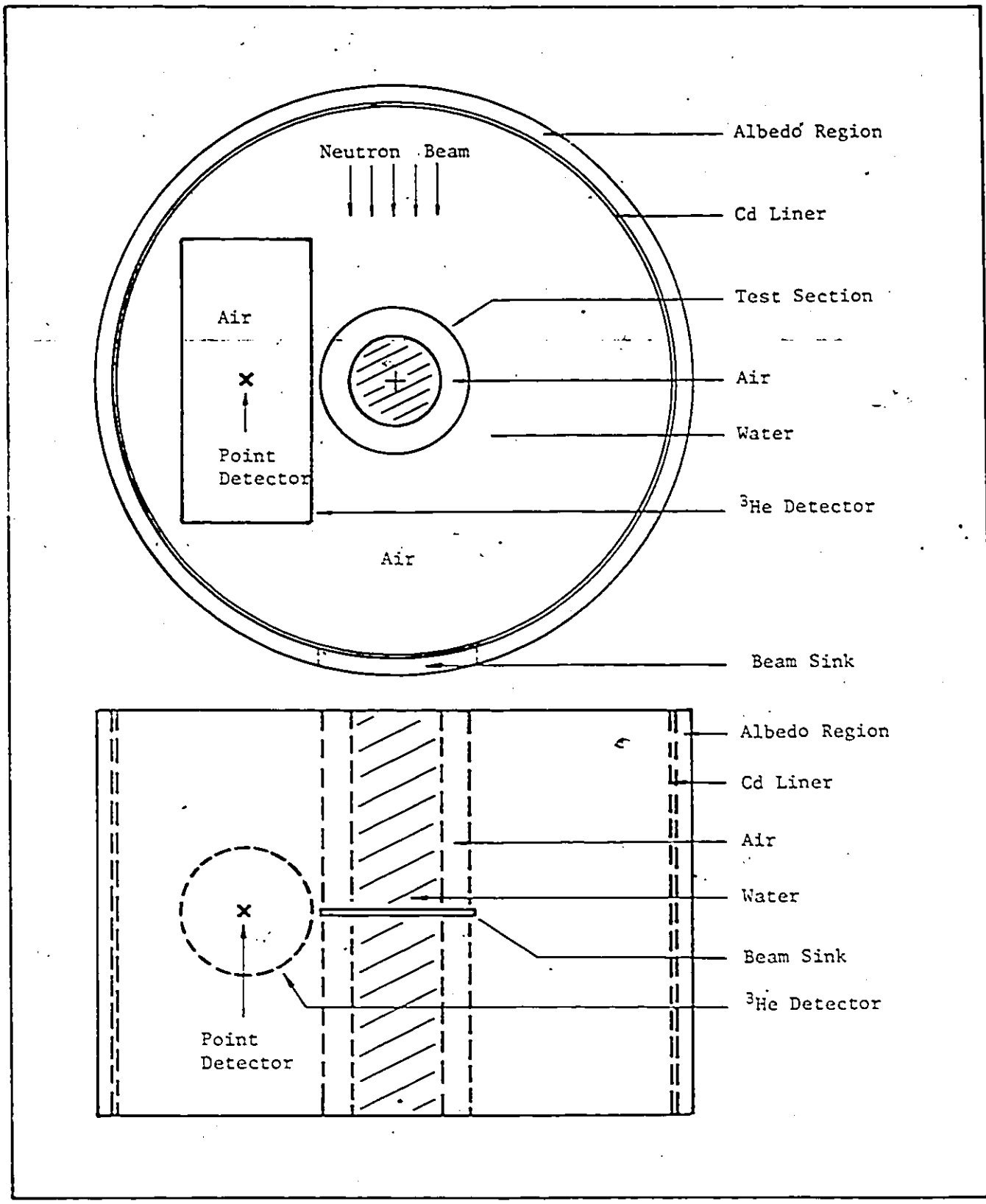

Figure 3.12 Typical geometry set-up in Monte Carlo "numerical experiments" to study the effect of monoenergetic source neutrons using a neutron beam geometry

test section. A point detector was placed at mid-height beside the test section and at right angle to the beam direction to estimate subcadmium neutron fluence. The assembly of neutron source, test section, and detector was enclosed in a cylindrical space confined by albedo surfaces. The cylindrical confinement space was set up instead of a box because, occasionally, in the case of a box, a neutron was found "trapped" at the intersection of two flat surfaces and the code went into an infinite loop trying to determine the direction of the next flight. The top and bottom of the cylindrical confinement space were open for neutrons to escape. A slot with an infinitesimal height, and a width equal to that of the beam, was set up in the albedo region diametrically opposite to the beam. The slot served as a window for uncollided source neutron to escape in order to determine the fraction of uncollided source neutrons.

With the set-up mentioned above, for a given single group source energy, the subcadmium neutron fluences were estimated at the point detector for a set of void fractions and the two water distributions. This process was repeated for several source energy groups ranging from high to low in order to complete the study for one test section size (51 mm thin walled test section I). Similar runs were carried out for the 127 mm thin walled test section III. The results of these runs were crucial in the interpretation of actual experimental results. They will be presented at appropriate places in later chapters.

Calculation of moderated source neutron spectra

As will be clearer in the next two chapters, it was

necessary to calculate the energy spectrum of neutrons emerging from a cylindrical water moderator which embedded a neutron source.

Referring to Figure 3.13, a hollow source tube was placed inside a cylindrical can filled with water. A point source was suspended at the centre of the source tube. The respective energy spectrum of the neutron source was assigned to the point source. The dimensions of the geometry set-up were identical to those in experiments where a neutron source was moderated to provide incident neutrons for a test section. A point detector was placed at mid-height beside the moderator-can to measure neutron fluences in all 33 energy groups. Because of the cylindrical symmetry of the moderator-can, the fraction of neutrons in each energy group, a_i, emerging from the side of the the moderator-can would be proportional to the product of the measured neutron fluence and the group energy width ΔE_i. Thus the energy spectrum, $a_i = \phi_i \Delta E_i / \sum_i \phi_i \Delta E_i$.

Two of such calculations were made, one for the ^{241}Am/Li and the other for the ^{241}Am/Be source. The result will be presented in later chapters with discussions.

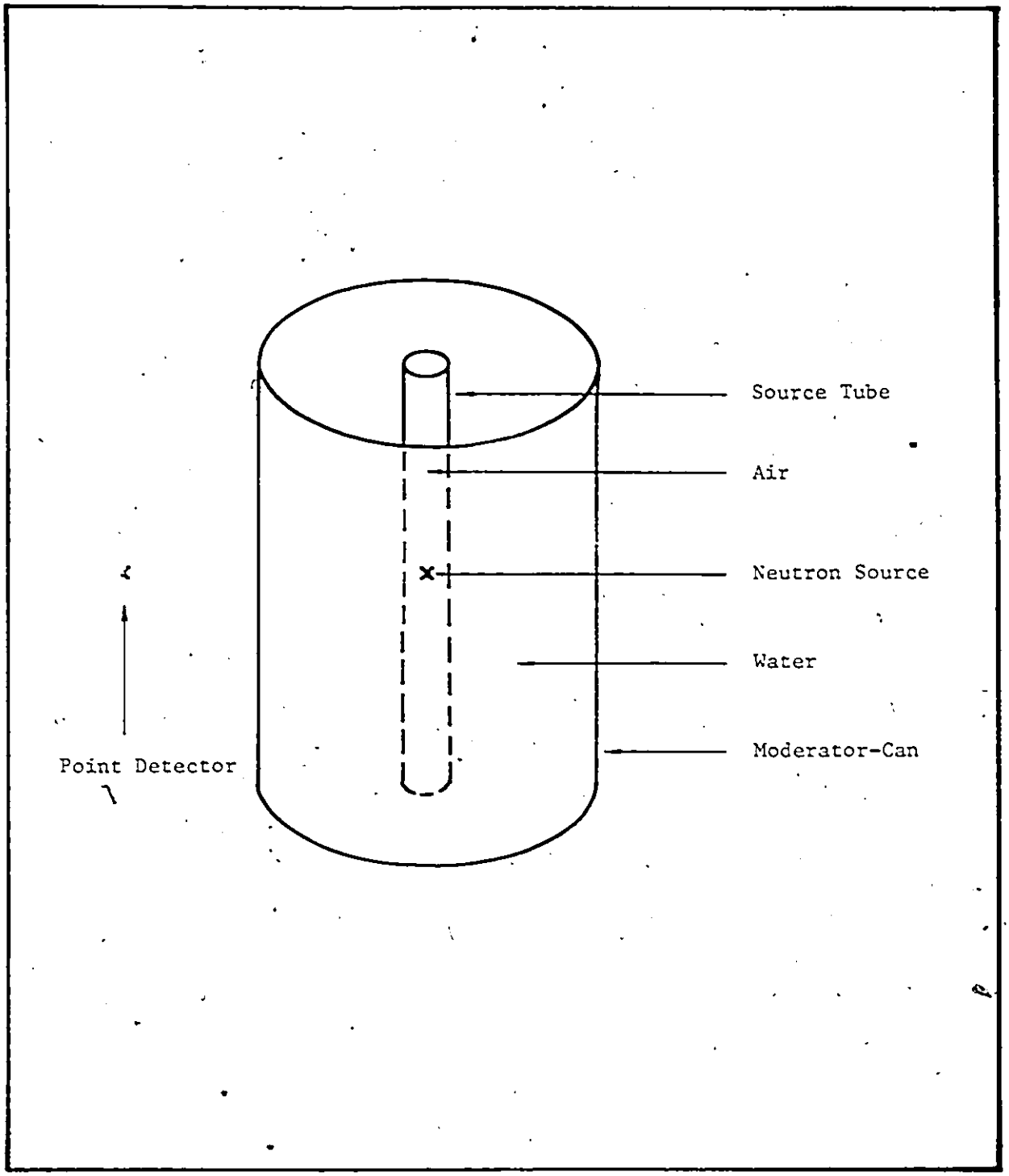

Figure 3.13 Geometry set-up in Monte Carlo calculations of the energy spectrum of neutrons emerging from a moderator (neutrons subsequently used as incident neutrons to test section)

CHAPTER FOUR

EXPERIMENTAL RESULTS

4.1 INTRODUCTION

Let us recall that the main objective of the present investigation is to find the conditions under which the neutron scattering technique, implemented with a portable neutron source possessing a continuous energy spectrum, is linear with void fraction and flow regime independent. A parametric study was first carried out experimentally to identify parameters which affect the technique significantly regarding linearity and flow regime dependence. In this chapter, experimental results for the parametric study are presented. From the experimental observations, a hypothesis, qualitative in nature, is formed regarding conditions to be fulfilled. Results of experiments to verify the hypothesis are also given. At the end of this chapter, based on the hypothesis formed, an appropriate set-up for a portable void fraction meter is introduced.

4.2 PARAMETRIC STUDY WITH TEST SECTION CONTAINING WATER WITH RADIAL SYMMETRY

In experiments conducted for the parametric study, experimental set-ups as discussed in section 3.2.2.2 were used. In particular, stagnant air-water test sections of annular and inverted annular flow patterns were used in each experiment. The water phase distribution in either case had radial symmetry with respect to the central axis of a test section. Representative

experimental results are presented in the following subsections to illustrate the effect of each parameter. Information on the set-up for each experiment is given in Table 4.1 for quick reference.

4.2.1 Experimental Results

4.2.1.1 Effect of Flow Pattern (Expt #1, 2, and 3)

The result of Expt #0 (see section 2.3.2) and the Monte Carlo simulation of it (see section 3.3.3.3) showed that the dimensionless neutron counting rate ν defined by Eq.(2.10) was non-linear with α and flow pattern dependent in the 51 mm test section I. Three more experiments, Expts #1, 2, and 3 were conducted to examine the effect of this parameter (flow pattern) in the larger carbon steel test section IV (ID = 127 mm, OD =152 mm). The test-section to dectector distance was 114 mm.

Expt #1 was conducted with two ^{241}Am/Be neutron sources attached horizontally on the outside wall of the test section diametrically opposite to each other and wrapped inside cadmium sheet. The result is shown in Figure 4.1. Both non-linearity and flow pattern dependence are observed for $\alpha > 0.3$.

Expt #2 was conducted with two ^{252}Cf sources attached to the test section outside wall as in Expt #1. The result is shown in Figure 4.2. The behaviour of ν is very similar to that in Expt #1. However, ν is slightly higher.

Expt #3 was conducted with a single ^{241}Am/Li neutron source attached to the outside wall of the test section. The result is shown in Figure 4.3. Again, loss of linearity and flow regime dependence are observed. However, ν is observed to be

TABLE 4.1

PARAMETERS IN EXPERIMENTS

Expt #	Test-section	Neutron source	Neutron source symmetry	D_{td} (mm)	D_{st} (mm)	d_m (mm)	Neutron reflector presence
0	I	S1	1-A	114	46	0	No
1	IV	S3	2-S	114	79	0	No
2	IV	S2	2-S	114	80	0	No
3	IV	S1	1-A	114	88	0	No
4	IV	S3	2-S	381	79	0	No
5	IV	S2	1-A	114	80	0	No
6	III	S1	1-A	114	78	0	No
7	III	S2	2-S	114	71	0	No
8	I	S1	1-A	114	46	0	Yes
9	I	S1	1-A	114	75	83	No
10	I	S1	1-A	114	89	110	No
11	I	S1	1-A	114	94	120	No
12	I	S1	1-A	114	89	110	No
13	I	S1	1-A	114	89	110	yes
14	I	S1	1-A	114	89	110	No
15	II	S1	1-A	114	92	105	Yes
16	III	S3	1-A	114	113	83	Yes
17	IV	S3	1-A	114	116	70	Yes
18	IV	S3	1-A	114	116	70	Yes
19	IV	S3	1-A	114	116	70	Yes

D_{td} - test-section to detector distance

D_{st} - source to test-section distance

d_m - moderator diameter

S1 - $^{241}Am/Li$

S2 - ^{252}Cf

S3 - $^{241}Am/Be$

1-A - Single neutron source
2-S - Two neutron sources placed diametrically opposite to to each other

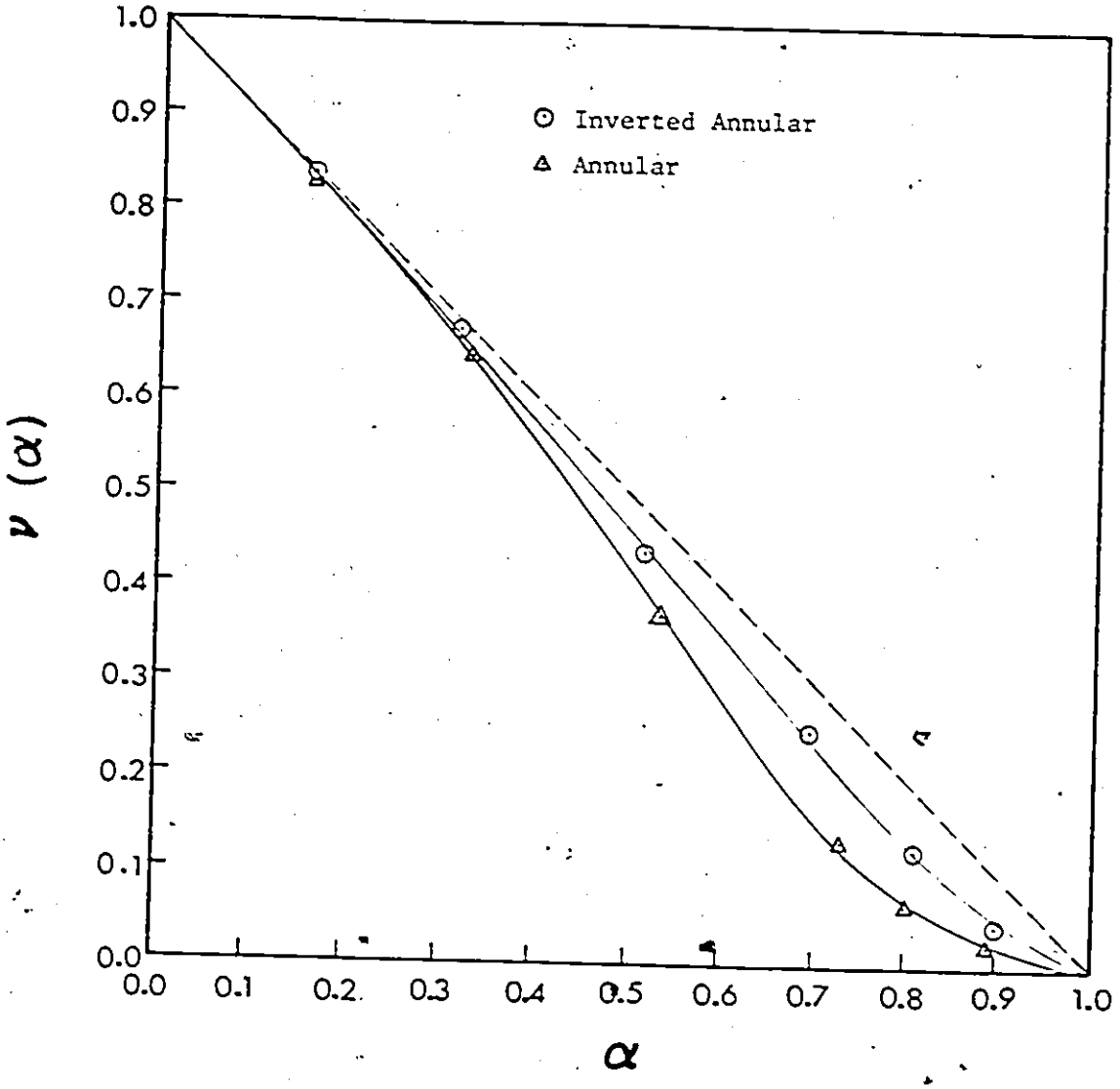

Figure 4.1 Result of Expt #1 using ^{241}Am/Be sources on test section IV (ID = 127 mm, OD = 152 mm), showing the dependence of ν on flow pattern and non-linearity with α

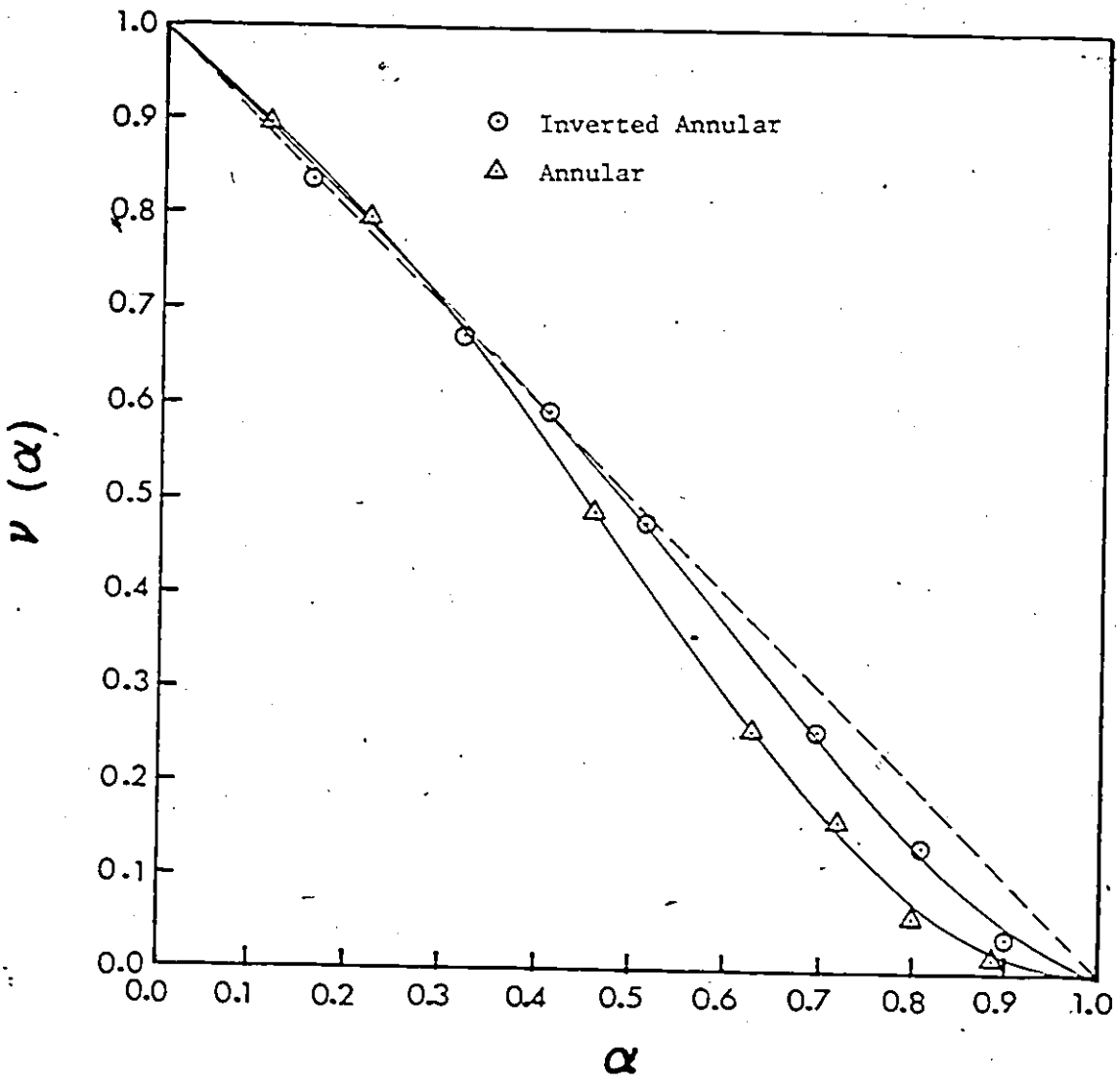

Figure 4.2 Result of Expt #2 using ^{252}Cf sources on test section IV (ID = 127 mm, OD = 152 mm), showing the dependence of ν on flow pattern and non-linearity with α

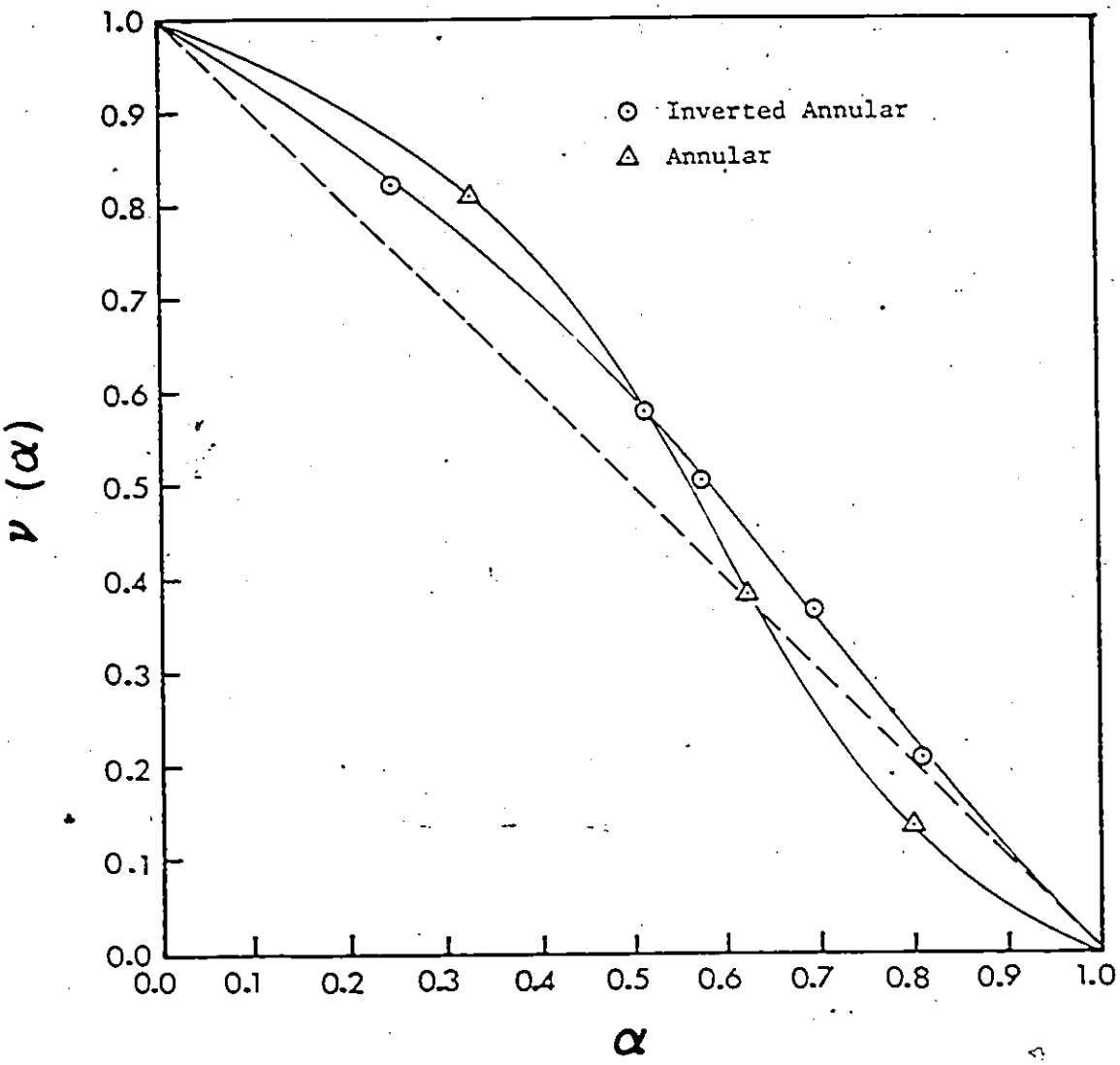

Figure 4.3 Result of Expt #3 using an $^{252}Am/Li$ source on test section IV (ID = 127 mm, OD = 152 mm), showing the dependence of ν on flow pattern and non-linearity with α

still higher than in expt #1 and 2. Roughly speaking, the linearity prediction (Eq.(2.11)) would have underestimated α (ν "bulging" above the linear line) for both flow regime except for annular flow (with $\alpha > 0.63$).

From the experimental results of these three experiments, it appears that, despite different neutron sources, ν is non-linear and flow pattern dependent, a phenomenon already observed in a test section of smaller inside diameter. It is therefore concluded that ν, in general, is not linear with α, at least not with portable neutron sources.

From the results of Expt #1 to 3, there is one interesting observation made. The average energy of the neutron source energy spectra decreases in the order of $^{241}Am/Be$ (5.1 MeV), ^{252}Cf (2.8 MeV), and $^{241}Am/Li$ (0.4 MeV). Reviewing the results of Expt #1-3, one can see that there is a consistent trend developed. The ν, which can only assume values between 0 and 1, seem to increase for both flow patterns as the spectrum weighted average energy of neutron source spectrum decreases throughout the entire range of α. This trend proved to be important as the work developed.

4.2.1.2 Effect of test-section to detector distance (Expt #4)

It was thought that the flow pattern dependence could be caused, at least to some extent, by the difference in distance between the test section and the neutron detector. If the detector were moved further away from the test section, the totality of water elements in the test section would act more like a point source of subcadmium neutrons to the detector, and

the flow pattern dependence of detector response would diminish if this geometric effect were the major cause for flow regime dependence. Expt #4 was conducted to investigate the effect of test-section to detector distance.

The set-up of Expt #4 was identical to that of Expt #1 (see section 4.2.1.1) except, in this case, the test-section to detector distance was 381 mm compared with 114 mm in Expt #1. For comparison with Expt #1, the results of these two experiments are shown together in Figure 4.4. The behaviour of ν in both experiments is hardly different.

It is concluded that the test-section to detector distance does not significantly affect the behaviour of ν, at least not for radially symmetric flow patterns. It therefore, cannot account for the loss of linearity nor the flow pattern dependence.

4.2.1.3 Effect of symmetry of neutron sources (Expt #5)

For all experiments conducted with the ^{241}Am/Be and ^{252}Cf, two sources were placed diametrically opposite to each other. It was thought that the symmetry of neutron sources might affect the behaviour of ν, i.e., ν might be different if two neutron sources were placed at the same side of the test-section instead of diametrically opposite to each other.

When a neutron enters the test section, the probability dP that it will suffer a collision at dx about a distance x, is

$$dP = \Sigma_s \exp(-\Sigma_s x)\, dx \qquad (4.1)$$

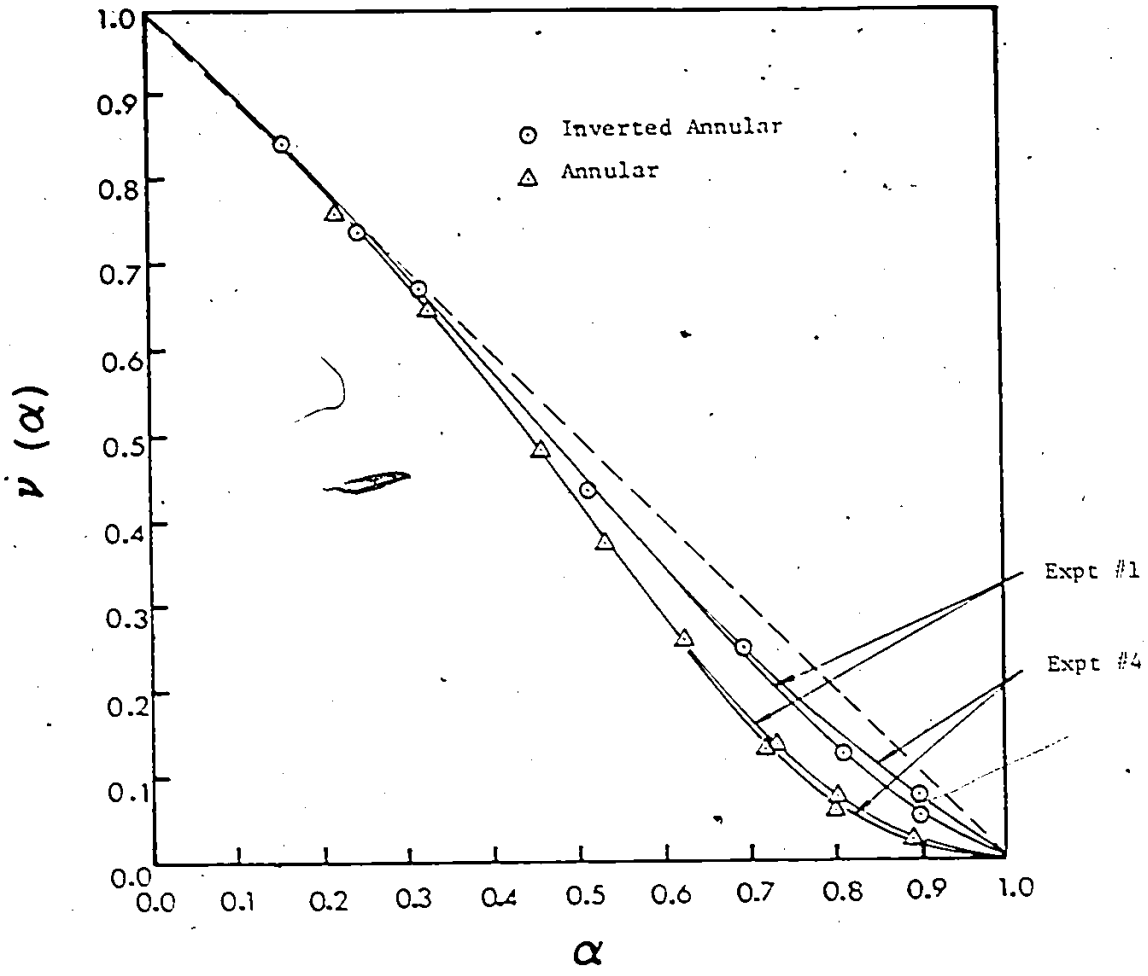

Figure 4.4 Comparison between Expts #4 and 1 showing that the effect of test-section to detector distance is negligible, given that the test-section to detector distances were 381 mm and 114 mm respectively

where Σ_s is the macroscopic cross-section of scattering. If two neutron sources are placed at the same side of the test section instead of being diametrically opposite to each other, the distribution of the first-collision sites for the incident neutrons would be less uniform in the former case. Expt #5 was conducted to investigate this effect.

In Expt #5, the experimental set-up was identical to that of Expt #2, except a single ^{252}Cf source was placed on one side of the test section instead of two placed diametrically opposite to each other as in Expt #2. The results of Expt #5 and 2 are compared as shown in Figure 4.5. From this figure, it is evident that the behaviour of ν is almost identical in the two experiments. It is fair to say that, for radially symmetric flow regimes, the behaviour of ν is not affected by the symmetry of neutron sources. This finding is not surprising. Because of the radial symmetry of the flow pattern, detected neutrons which originated from the neutron source on the right are merely "mirror reflections" of those from the source on the left. However, one must be cautious when the flow pattern does not have radial symmetry, i.e. stratified flow. The discussion of the effect of symmetry of neutron sources on radially non-symmetric flow patterns, however, is postponed to later sections. The finding in this experiment, however, removes the doubt related to the validity of experimental results using a single neutron source. For example, only one $^{241}Am/Li$ source was available and many experiments were conducted with this neutron source.

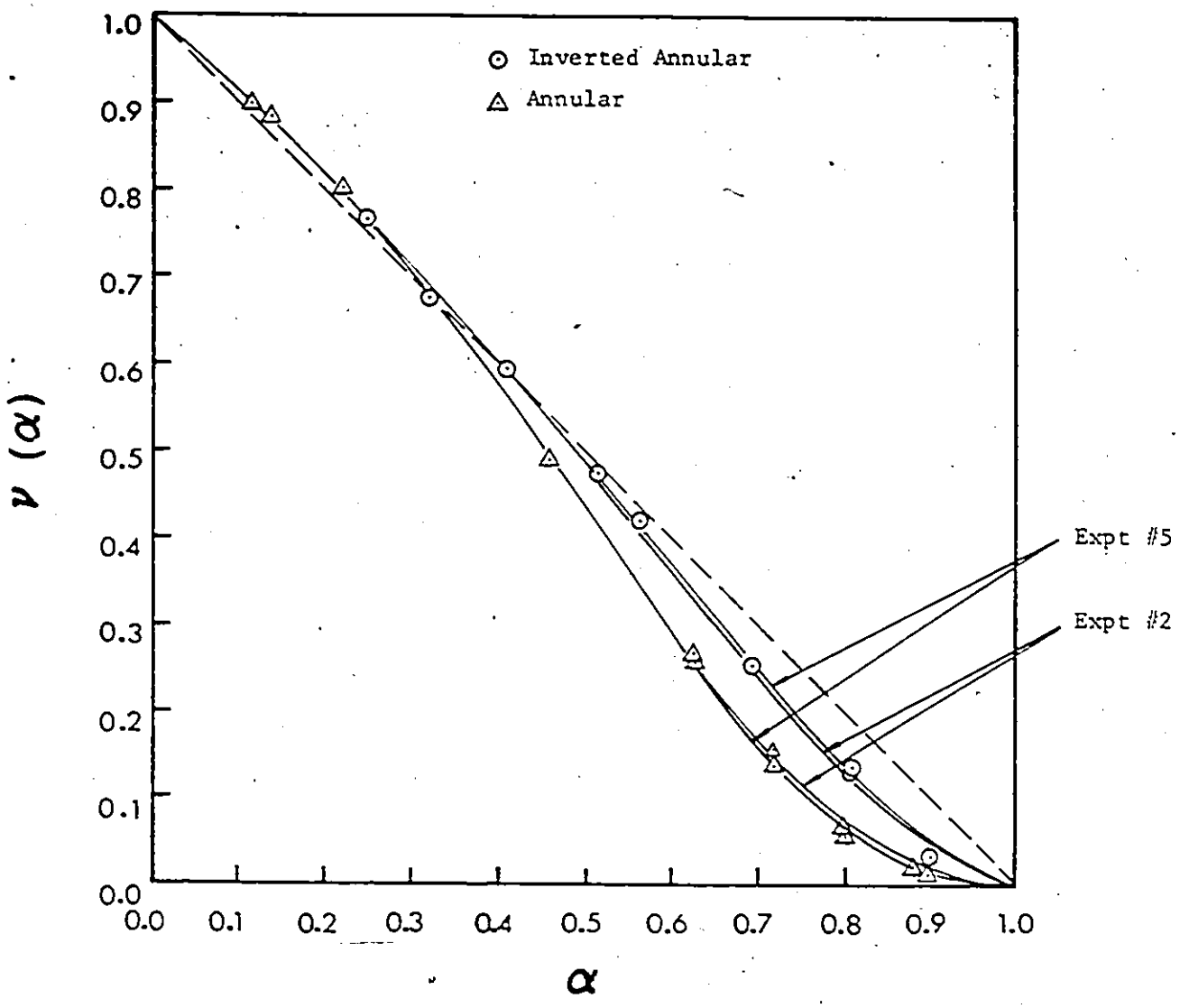

Figure 4.5 Comparison between Expt #5 and 2 showing that neutron source symmetry does not significantly affect $\nu(\alpha)$

4.2.1.4 Effect of neutron detection energy bin

The ^{3}He detector is most sensitive to subcadmium neutrons. However, being an 1/v efficiency dependent detector, it is also quite sensitive to epicadmium neutrons. It is interesting to investigate the effect of counting epicadmium and subcadmium neutrons together (enlarging the neutron detection energy bin).

The data obtained in the process of "differential counting" in Expt #2 was used for the investigation. The neutron counts obtained without shielding the detector with the cadmium sleeve were the sum of subcadmium and epicadmium neutrons. The dimensionless neutron counting rate ν was determined in the same manner as for subcadmium neutrons. This ν is shown in Figure 4.6 together with the ν for subcadmium neutrons. From this figure, it seems that ν is increased only slightly when the epicadmium neutrons are included. Since the inclusion of epicadmium neutrons does not restore the linearity, further efforts are concentrated at understanding the behaviour of subcadmium ν.

4.2.1.5 Effect of test-section size (Expt #6)

Expt #6 was conducted to investigate the effect of the inside diameter of the test section. In this experiment, the thin aluminum walled test section III (ID = 127 mm) and the $^{241}Am/Li$ source were used. The results of this experiment are compared with those in Expt #0 which was conducted with the same neutron source but with test section I (ID=51 mm). The comparison is shown in Figure 4.7. From this Figure, it is

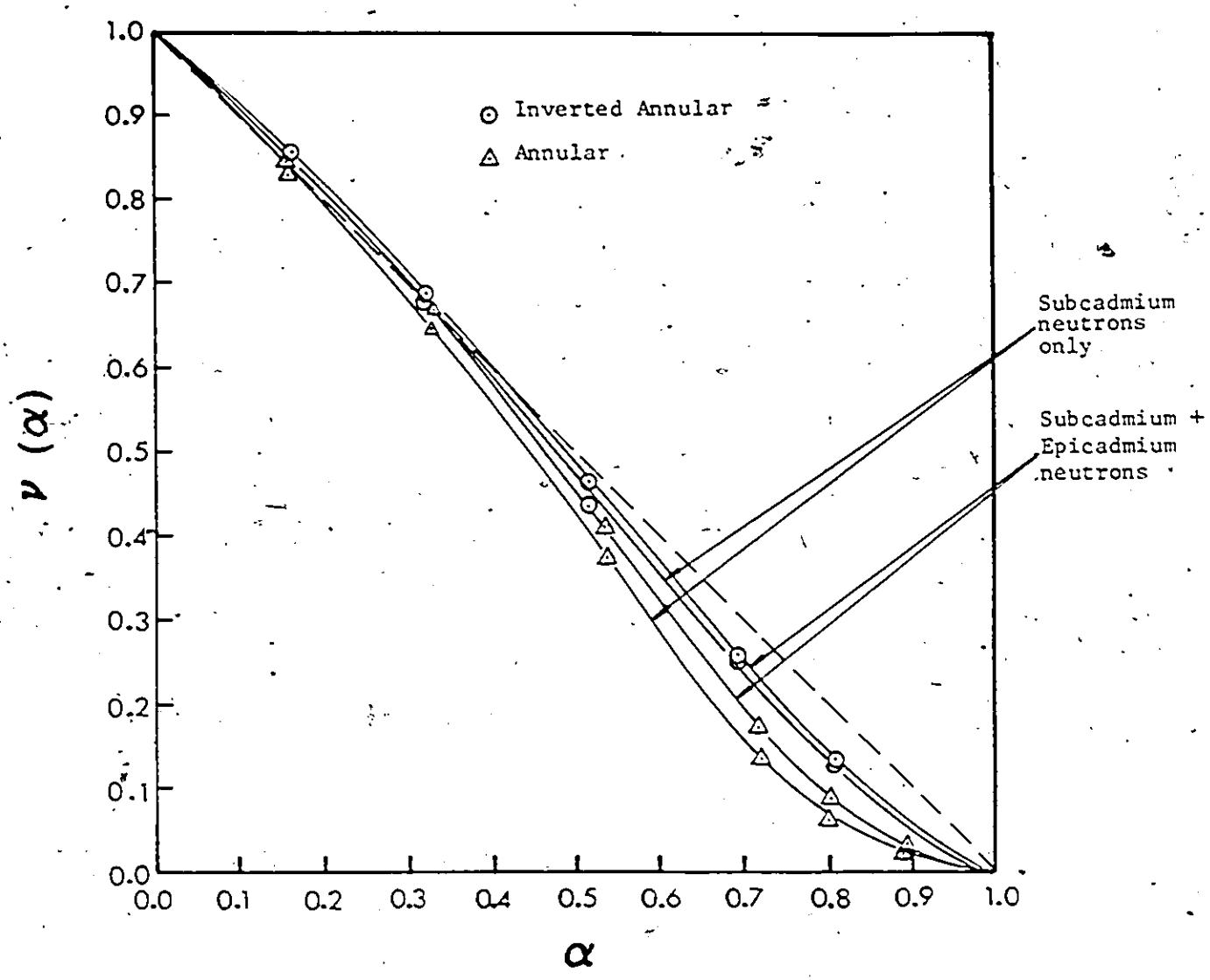

Firgure 4.6 The small effect obtained by enlarging the neutron detection energy bin from subcadmium to subcadmium plus epicadmium neutrons is shown

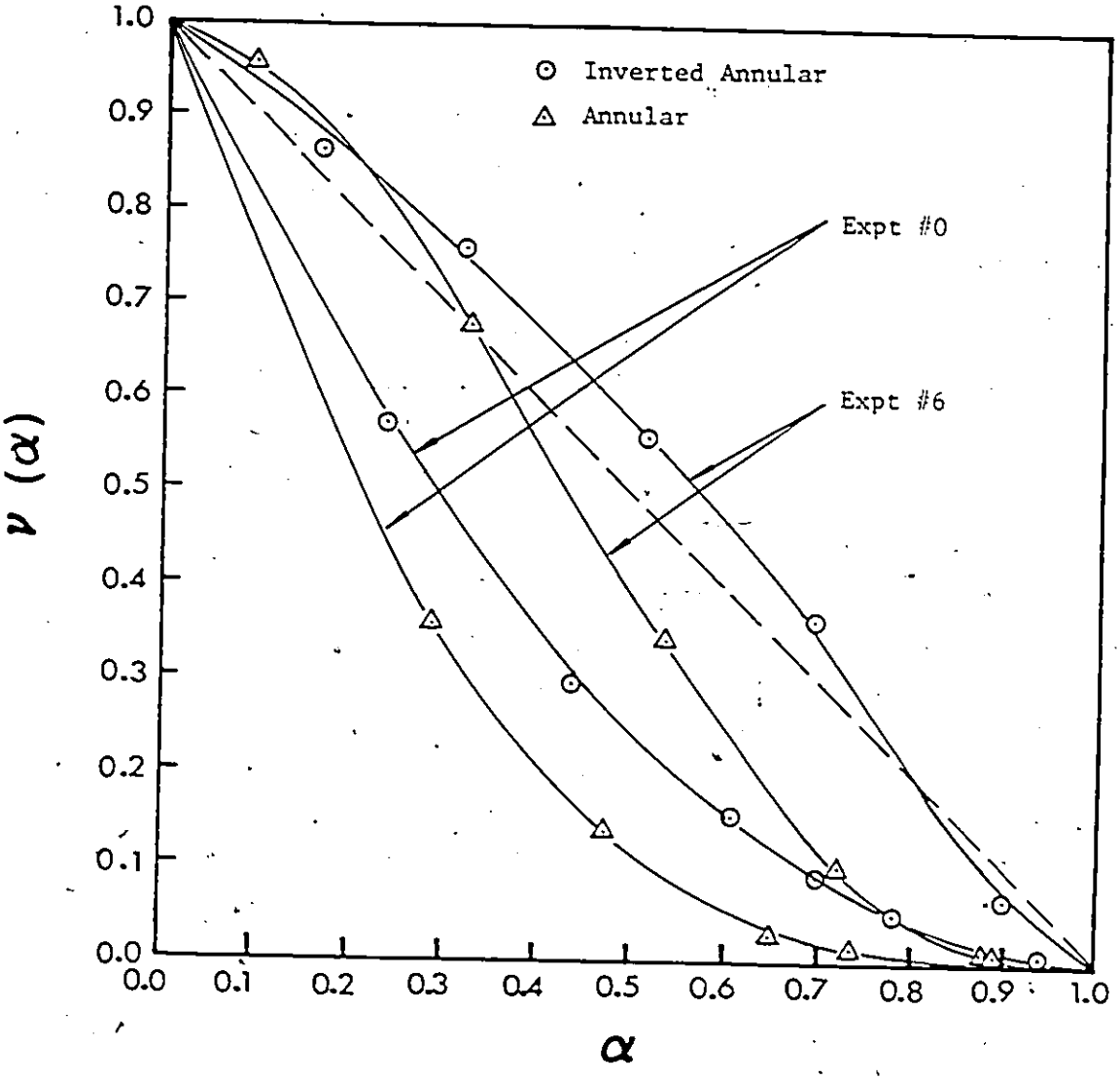

Figure 4.7 Comparison between Expts #6 and 0 showing a general increase in the dimensionless counting rate $\nu(\alpha)$ with test section inside-diameter for a fixed α, given that the same $^{241}Am/Li$ neutron source was used but the ID of test section in Expt #0 increased from 51 mm to 127 mm in Expt #6

evident that ν increases as the diameter of a test section for the same neutron source. This applies to both annular and inverted annular flow patterns. If the linearity hypothesis was assumed, it would have severely overestimated α (ν "sagging" below the linear line) for both flow patterns for the 51 mm test section I throughout the entire range of α. However, the same hypothesis would have underestimated α for the inverted annular flow up to $\alpha=0.8$ for the 127 mm test section. It also underestimated α for the annular flow up to $\alpha=0.32$. There is a marked "improvement" for the larger test section as the maximum deviation from linearity $\Delta\alpha$ for the 51 mm test section is 0.39 and that for the 127 mm test section is 0.16, both for the annular flow.

It is concluded that the test section ID affects the behaviour of ν significantly for a given neutron source, and generally the effect is an increase in ν for increased test section ID at the same void fraction.

4.2.1.6 Effect of test section wall (Expt #7)

In industrial applications, pipes with thick metal walls are often encountered. It is interesting to investigate the effect of the thickness of metal pipe wall on the behaviour of ν.

Expt #7 was conducted to investigate the effect of pipe wall thickness. In this experiment, the 127 mm thin walled aluminum test section III was used. Two ^{252}Cf neutron sources were placed on the test section wall diametrically opposite to each other. This set-up was similar to that in Expt #2 where the test section used was the 127 mm thick carbon steel walled test

section IV, and comparison is made between these two experiments.

The comparison between Expt #7 and 2 is shown in Figure 4.8. In both cases, ν is below the linear line except for $\alpha <$ 0.3 for the thick carbon steel walled test section. However, it is evident that ν increased for both flow patterns as the test section wall thickness increased. Moreover, the increase in ν is more significant in the annular flow pattern than the inverted annular one. Since the thin aluminum test section wall is quite transparent to neutrons, we can imagine that the thin walled test section has 0 thickness. It can be concluded then, for the same neutron source, carbon steel pipe wall thickness would increase ν and the increase in ν is more pronounced in annular flow than in inverted annular flow.

4.2.1.7 Effect of neutron reflector (albedo) (Expt #8)

In the design of a portable void fraction meter, biological shielding is often introduced. Shielding material for neutrons inevitably consists of hydrogenous material. These hydrogenous materials, placed around a test section, act as a reflector for neutrons and will likely affect the neutron counting rate and thus ν.

To investigate the effect of neutron reflector, Expt #8 was conducted with a set-up identical to that of Expt. #0. In both experiments, the source used was the ^{241}Am/Li source, and the test section used was the 51 mm thin aluminum walled test section I. However, the Cd enclosure was lined with a layer of paraffin wax on the inner wall. That is, the test section was surrounded by neutron reflector material. In this experiment,

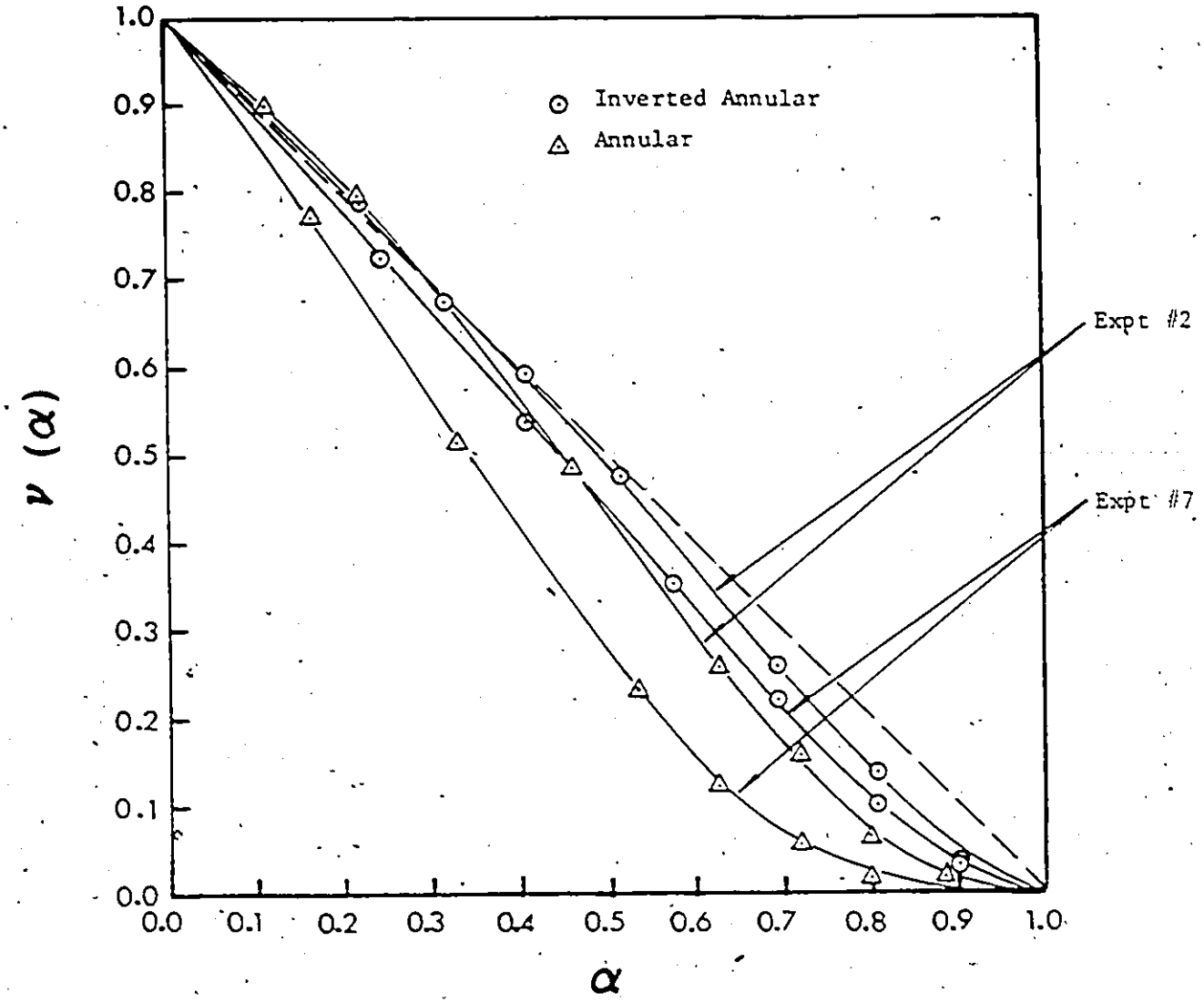

Figure 4.8 Comparison between Expt #7 and 2 showing a general increase of $\nu(\alpha)$ with test-section wall thickness, given that the ID's of test-sections in both experiments were 127 mm but the carbon steel test section wall thickness in Expt #2 and 7 were 12.5 and 0 mm respectively

only the inverted annular flow was considered.

Comparisons are shown in Figure 4.9. From this Figure, it is evident that the presence of the wax reflector increases ν resulting in a less severe overestimate of α.

The hydrogenous reflector is not providing just an additional amount of hydrogenous material. In that case, ν would not have increased, because a constant neutron counting rate would have been added and would have cancelled each other by the definition of ν. It fundamentally affects neutron behaviour and thus ν.

4.2.1.8 Effect of input neutron energy spectrum (Expt #9,10,11,12)

It has been mentioned in section 4.2.1.1 that there was a trend observed from Expt #1-3. The trend is that, for a test section of a given ID, ν at a given α increases as the average energy input (incident) neutrons decreases.

Consider also the experimental results of Expt #6 and 7. They are shown together in Figure 4.10. Recall these two experiments were conducted with the 127 mm thin aluminum walled test section III. The difference is that the ^{241}Am/Li and ^{252}Cf sources were used in Expt #6 and 7 respectively. The average energy of neutrons from the ^{252}Cf (2.8 MeV) is much higher than that for the ^{241}Am/Li (0.4 MeV). From Figure 4.10, it seems that incident neutrons with lower average energy would result in an increase in ν for both flow regimes. This is consistent with the trend observed in Expt #1-3. It is thus concluded that for a given test section, the input (incident) neutron energy spectrum

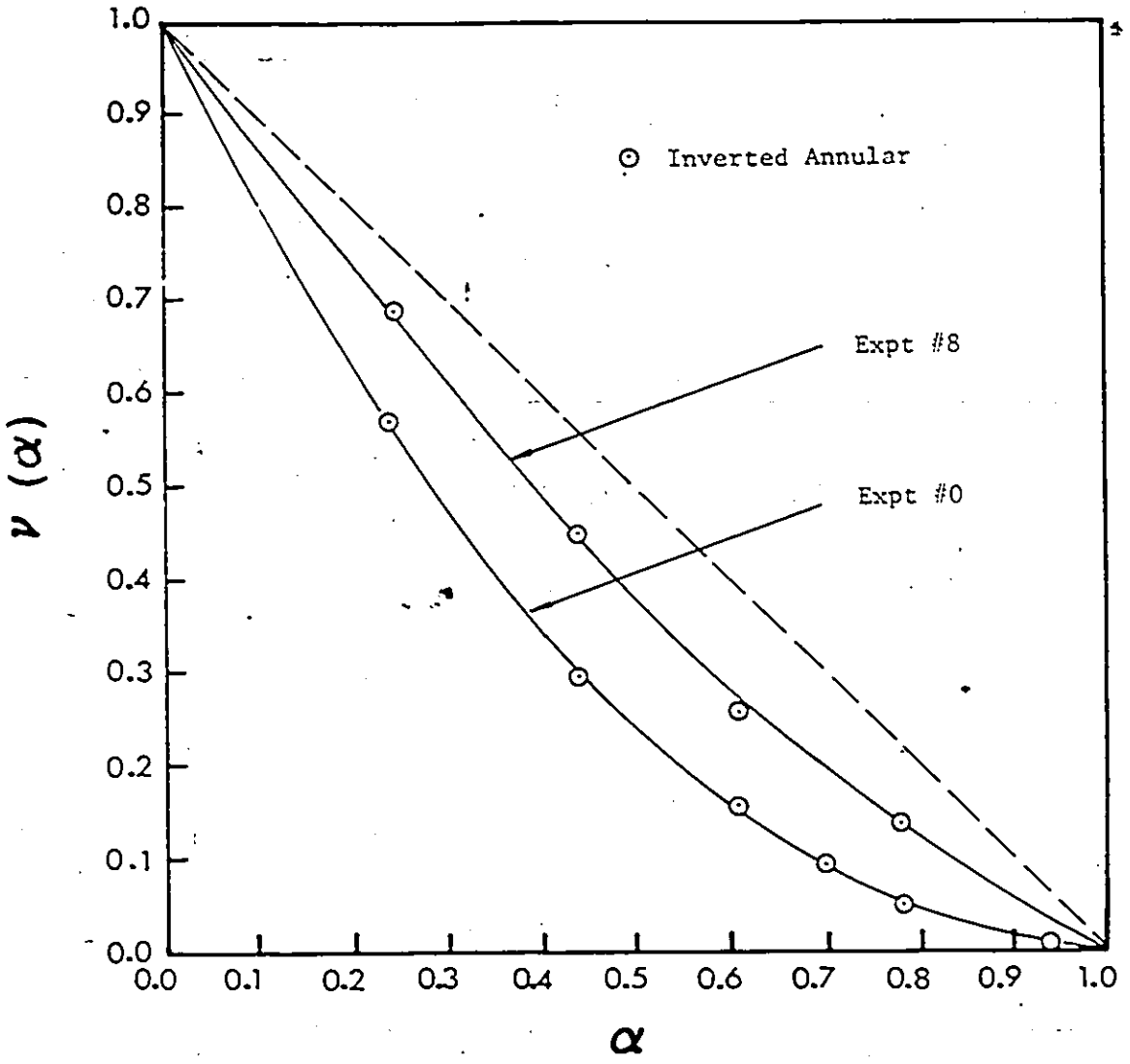

Figure 4.9 Comparison between Expt #8 and 0 showing a general increase of $\nu(\alpha)$ with the addition of neutron reflector material around the same test section and with the neutron source (^{241}Am/Li) being used

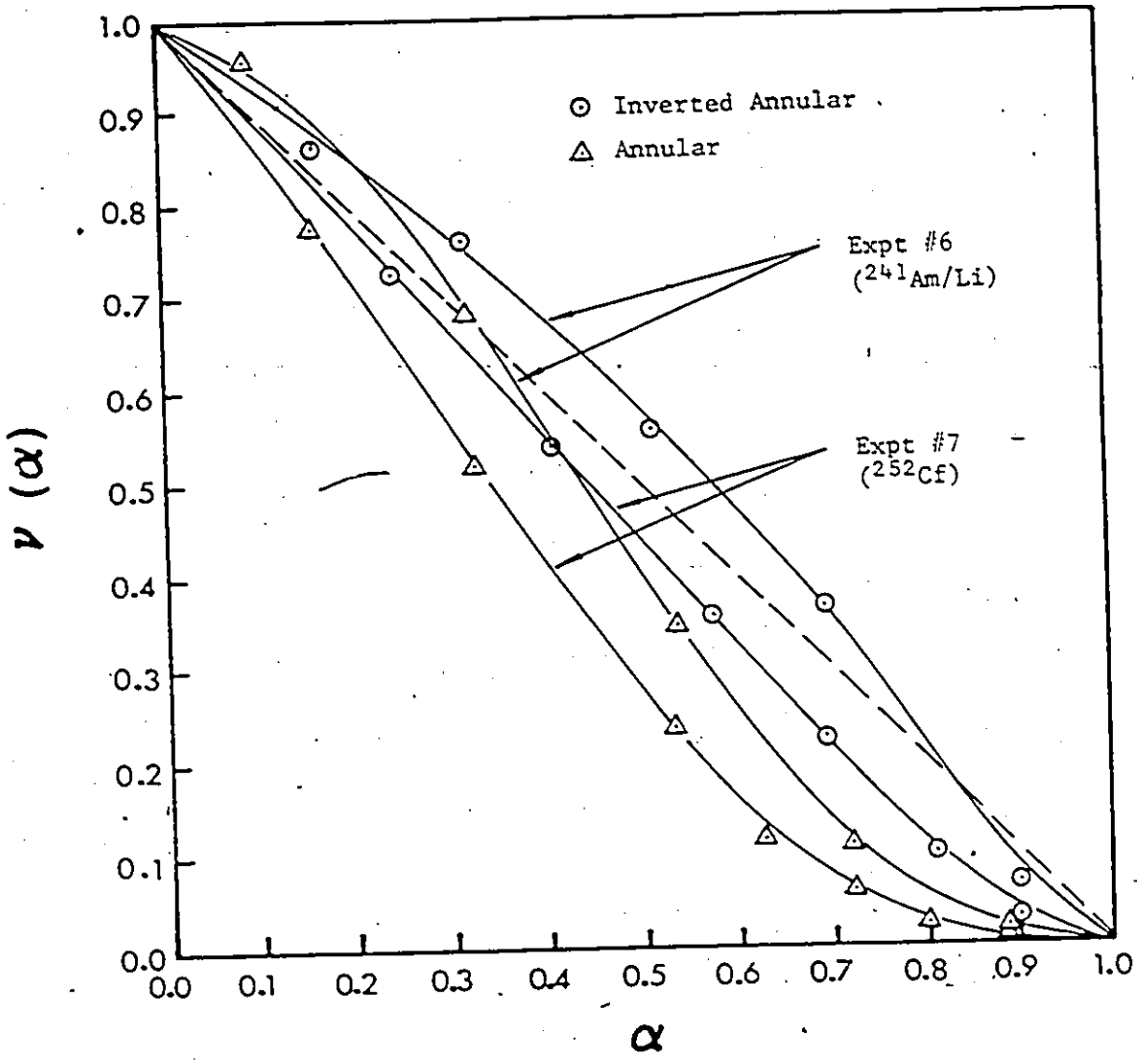

Figure 4.10 Comparison between Expt #6 and 7 showing a general increase of $\nu(\alpha)$ as the average energy of incident neutrons decreases, given that the average neutron energy of ^{241}Am/Li and ^{252}Cf are 0.4 and 2.8 MeV respectively

is a parameter that affects the technique significantly.

The observed trend that ν changed significantly and systematically with the input neutron energy spectrum suggested that there is at least one spectrum such that ν can be close to being linear and thus near flow pattern independent. For example, consider the result of Expt #0 which triggered the present work. Since $\nu(0)$ and $\nu(1)$ assume the value of 1 and 0 by definition and the consistently observed trend that ν increases when the average energy of input neutrons decreases, one would expect ν to increase and approach the $(1-\alpha)$ line if "softer" input neutrons than the ^{241}Am/Li source are used. A series of experiments (Expt #9-11) was conducted to verify this.

As in Expt #0, the 51 mm thin aluminum walled test section I was used for these experiments. The ^{241}Am/Li neutron source was, however, moderated with moderator-cans (see section 3.2.2.2) of different diameters which are shown in Table 4.2. The moderators were not wrapped with cadmium sheet. The input neutrons to the test section therefore contained some subcadmium components which could be viewed as very low energy neutrons. The experiments were conducted for inverted annular flow test sections only.

The results of these three experiments are shown in Figure 4.11 together with that of Expt #0. From this figure, it is evident that, as the moderator diameter increases, the average energy of the input neutrons decreases and ν increases as expected. At moderator diameter D=110 m, ν is everywhere close to $(1-\alpha)$. The maximum deviation is less than 0.03. When D was further increased to 120 mm, ν further increased because of

TABLE 4.2

DIMENSIONS OF MODERATORS

Expt #	Height (mm)	Diameter (mm)
9	152	83
10	152	110
11	152	120

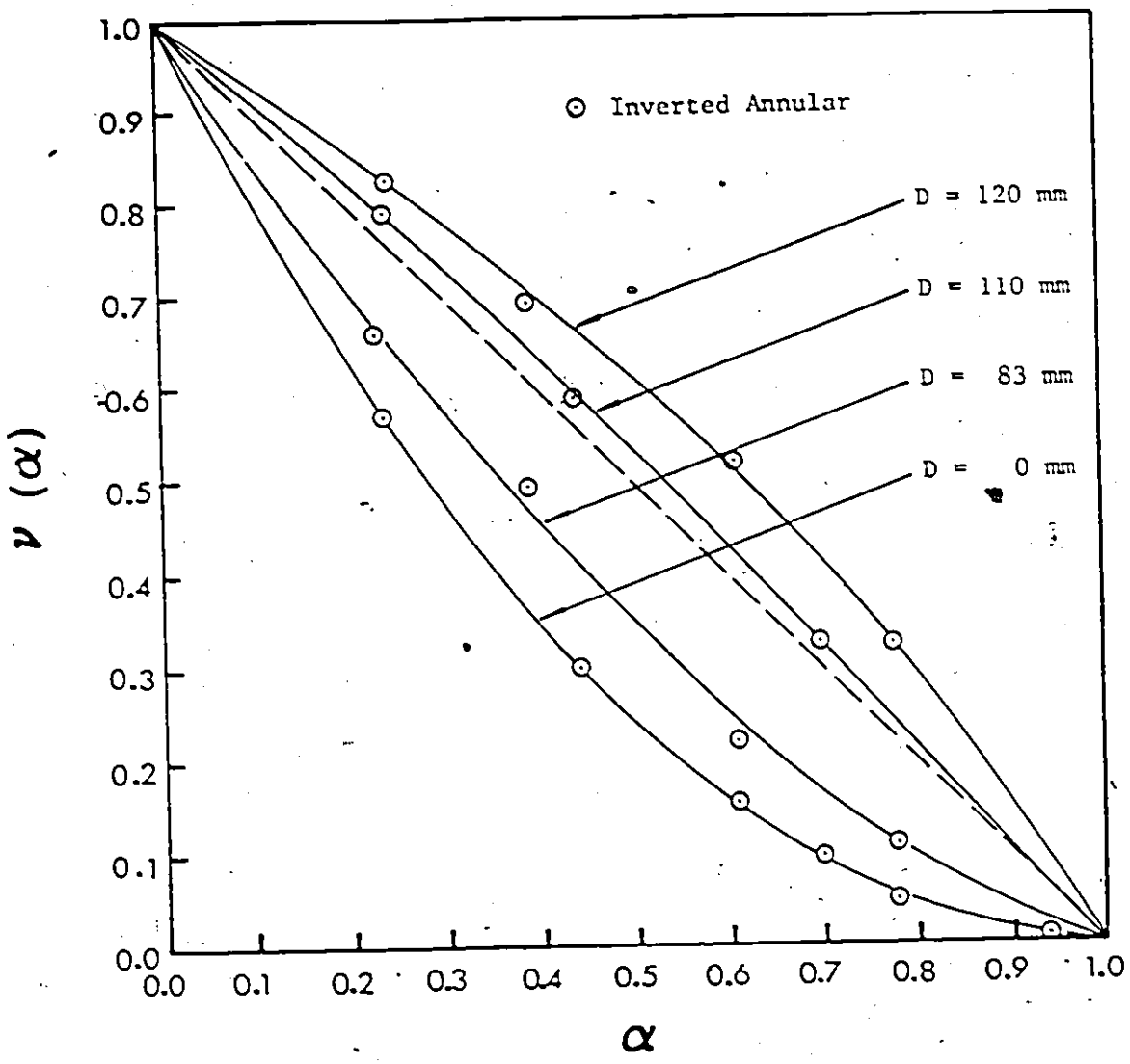

Figure 4.11 Results of Expt #0, 9, 10, and 11 showing the progressive increase of $\nu(\alpha)$ as the source neutron moderation increases (average energy of incident neutrons decreasing)

"overmoderation". The results of this set of experiments indicate that the input (incident) neutron spectrum is a very important parameter affecting the neutron scattering technique. There is at least one optimum incident neutron spectrum that gives rise to a near linear response, which is desirable.

In Expt #10, linearity was observed. Flow pattern independence was tested by conducting Expt #12. This experiment was a repeat of Expt #10 except for annular flow pattern test sections. The result is shown in Figure 4.12. From this figure, it seems that, with the appropriate moderator diameter (appropriate input neutron energy spectrum), near linearity and flow pattern independence can be achieved at the same time. The input neutron energy spectrum was then recognised as a key parameter that affect the technique most significantly.

This completed the parametric study.

4.2.2 Summary of Parametric Study

The effects of a number of parameters have been studied. These parameters include:

(a) flow pattern

(b) test-section to detector distance

(c) symmetry of neutron sources

(d) neutron detection energy bin

(e) test section inside diameter

(f) test section wall thickness

(g) addition of neutron reflector materials

(h) input neutron energy spectrum

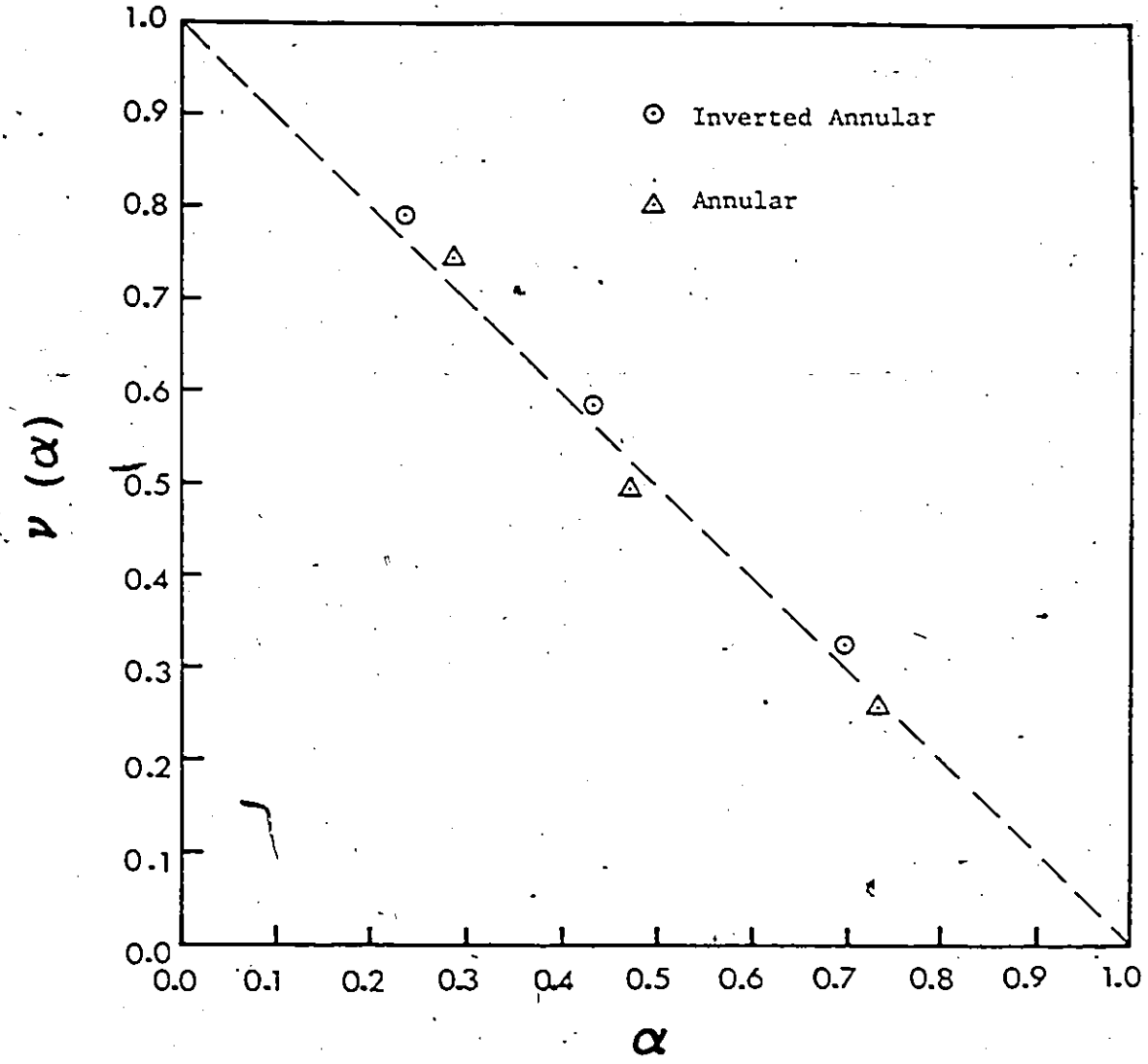

Figure 4.12 Result of Expt #12 showing the achievement of linearity and flow pattern independence for test section I with an appropriate incident neutron energy spectrum which resulted from the moderation of the ^{241}Am/Li source with a moderator diameter of 110 mm and consisted partly of subcadmium neutrons

The finding can be summarized as the following:

(1) The counting rate of subcadmium neutrons is flow pattern dependent and non-linear with α in general.

(2) The parameters (b), (c), and (d) do not affect the technique significantly.

(3) Parameters (e), (f), (g), and (h) are more significant parameters with regard to linearity and flow pattern independence.

(4) For a given input neutron energy spectrum, the effect of parameters (e), (f), and (g) is that the dimensionless counting rate ν increases with test section inside diameter, test section wall thickness, and the addition of neutron reflector.

(5) Out of the set of more important parameters, parameter (h), the input neutron energy spectrum seems to be the most important one. For a given test section, the dimensionless subcadmium neutron counting rate ν increases when the ratio of low to high energy input neutrons increases. There seems to be an optimum spectrum such that the resulting ν can be fairly linear and flow pattern independent. This spectrum can be achieved by moderating a given neutron source with a moderator of appropriate dimensions (or moderating power).

4.3 FORMULATION OF HYPOTHESIS AND VERIFICATION EXPERIMENTS

4.3.1 The Hypothesis

We have qualitatively discussed the crucial information obtained from the parametric study. The key factor is the input neutron energy spectrum. For a test section of a given diameter,

a particular spectrum (or spectra) is required to give linearity and flow pattern independence. Another question needs to be answered. It relates to how the required input neutron energy spectrum depends on test section inside diameter, test section wall thickness, and the addition of neutron reflector material around the test section.

This can be answered qualitatively. We have learned that, for a given input neutron energy spectrum, ν increases with test section diameter, test section wall thickness, and the addition of neutron reflector material. We also learned that ν increases when the low energy component in the input neutron energy spectrum increases. Thus, it is inferred that, as the test-section inside-diameter increases, the ratio of high to low energy neutrons in the input spectrum must increase, i.e., the spectrum weighted average energy must increase. In practice, this determines the choice of a portable neutron source. For example, we have seen that, for the 51 mm test section I, an unmoderated ^{241}Am/Li source yields ν values that fall below the $(1-\alpha)$ line. When the source was moderated appropriately, ν increased to become near-linear with α. However, when the same unmoderated source was used on the 127 mm test section III (Expt #7), ν bulges above the $(1-\alpha)$ line. Moderation of the source will only push ν further up. In other words, the ^{241}Am/Li source does not possess enough high energy neutrons for the 127 mm test section. It implies that a harder neutron source is needed.

Since ν increases with test section wall thickness and the addition of neutron reflector, the required spectrum must

also shift to the high energy side.

The hypothesis can therefore be stated formally as the following:

If the neutron scattering technique is implemented with a neutron source, the scattered (thermalized) neutron counting rate is likely to be non-linear with void fraction and flow pattern dependent. Suppose, for a given combination of test-section inside diameter, wall thickness, and surrounding neutron reflector material, a chosen neutron source results in overestimates of void fraction throughout the entire range (α=0 to 1). Linearity and flow pattern can be achieved by moderating this neutron source with a specific moderator diameter generating an incident neutron energy spectrum appropriate for the given test-section combination. The required moderator diameter decreases and thus the spectrum weighted average energy of the resulting appropriate incident neutron spectrum increases with the test-section inside diameter, wall thickness, and the presence of surrounding neutron reflector material.

4.3.2 Verification Experiments

Attempts were made to experimentally verify the hypothesis. The object of these experiments was to show that for a given combination of test-section inside-diameter, wall thickness, neutron reflector, and an appropriately chosen neutron source, linearity can be achieved by appropriately moderating the neutron source (generating an appropriate incident neutron spectrum). The results are shown as the following.

4.3.2.1 Test section I with neutron reflector (Expt #13)

Expt #13 was conducted with the 51 mm thin aluminum wall test section I using the ^{241}Am/Li source moderated by a moderator-can of 110 mm diameter. The cadmium enclosure was lined with a single layer of paraffin wax on the outside. The moderator-can was wrapped with cadmium sheet to remove subcadmium neutrons. The result is shown in Figure 4.13.

From Figure 4.13, it is evident that, for this specific combination of test-section ID, wall thickness, and the neutron reflector, an appropriate input neutron spectrum was achieved by moderating the ^{241}Am/Li source. Near-linearity and flow pattern independence is observed.

4.3.2.2 Test section I without neutron reflector (Expt #14)

Expt #14 was conducted by repeating the previous Expt #13 with the paraffin wax layers removed. The result is shown in Figure 4.14. From this figure, it is evident that ν falls below the $(1-\alpha)$ line, indicating that the neutron spectrum is not an appropriate one. However, notice the moderator diameter of 110 mm and the set-up is the same as in Expt #10 and 12 except that the subcadmium input neutrons were not removed in Expt #10 and 12. It has already been shown that the 110 mm diameter moderator was the correct one for the 51 mm test section I without neutron reflector. The input neutron spectrum of the present experiment #14 is short of the subcadmium component resulting in a higher spectrum weighted average energy. As expected, the spectrum is no longer suitable. However, this input neutron spectrum is suitable for the 51 mm test section I

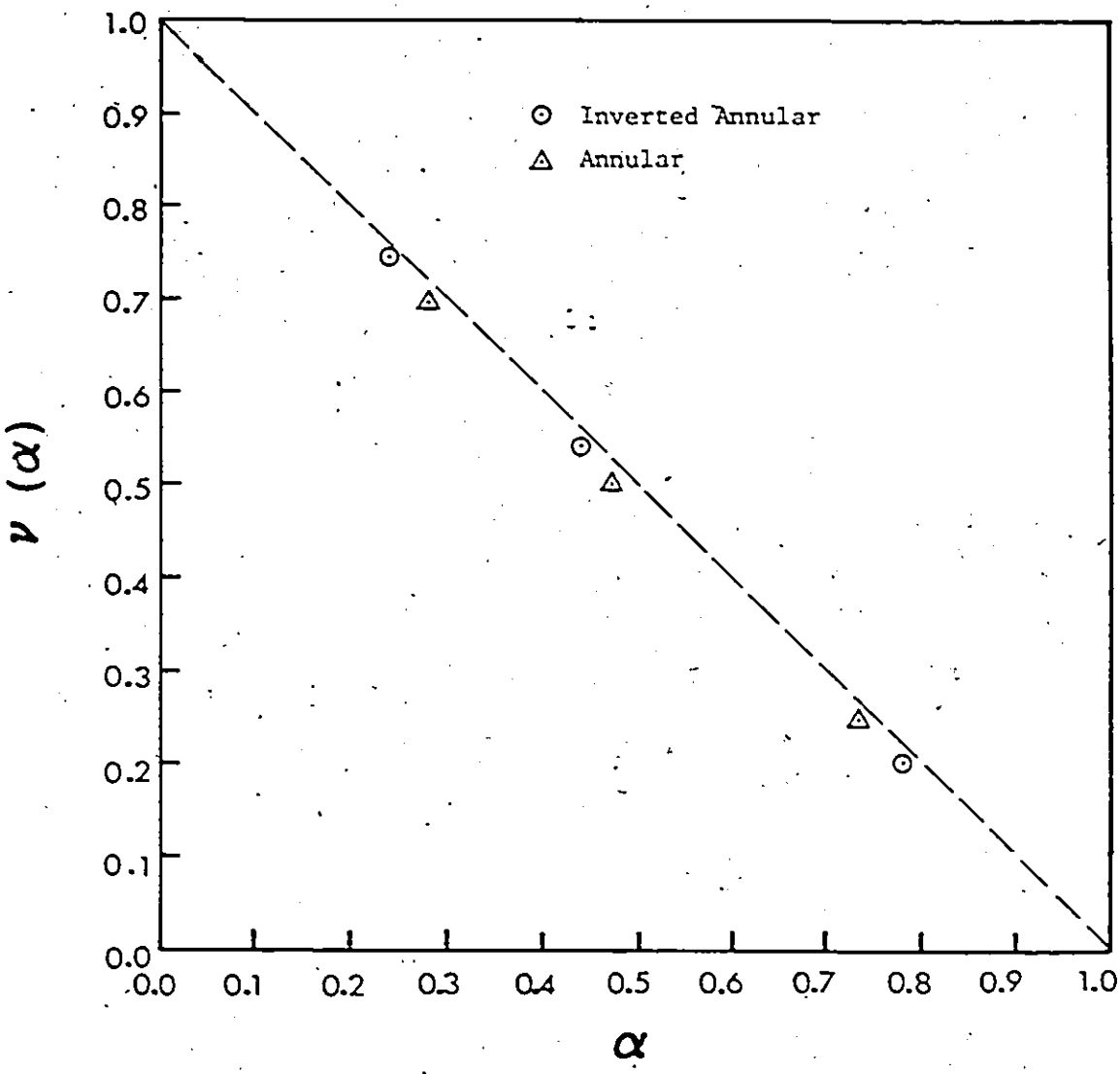

Figure 4.13 Result of Expt #13 showing the achievement of linearity and flow pattern independence with an incident neutron spectrum consisting of only epicadmium neutrons but with neutron reflectors around the test section I

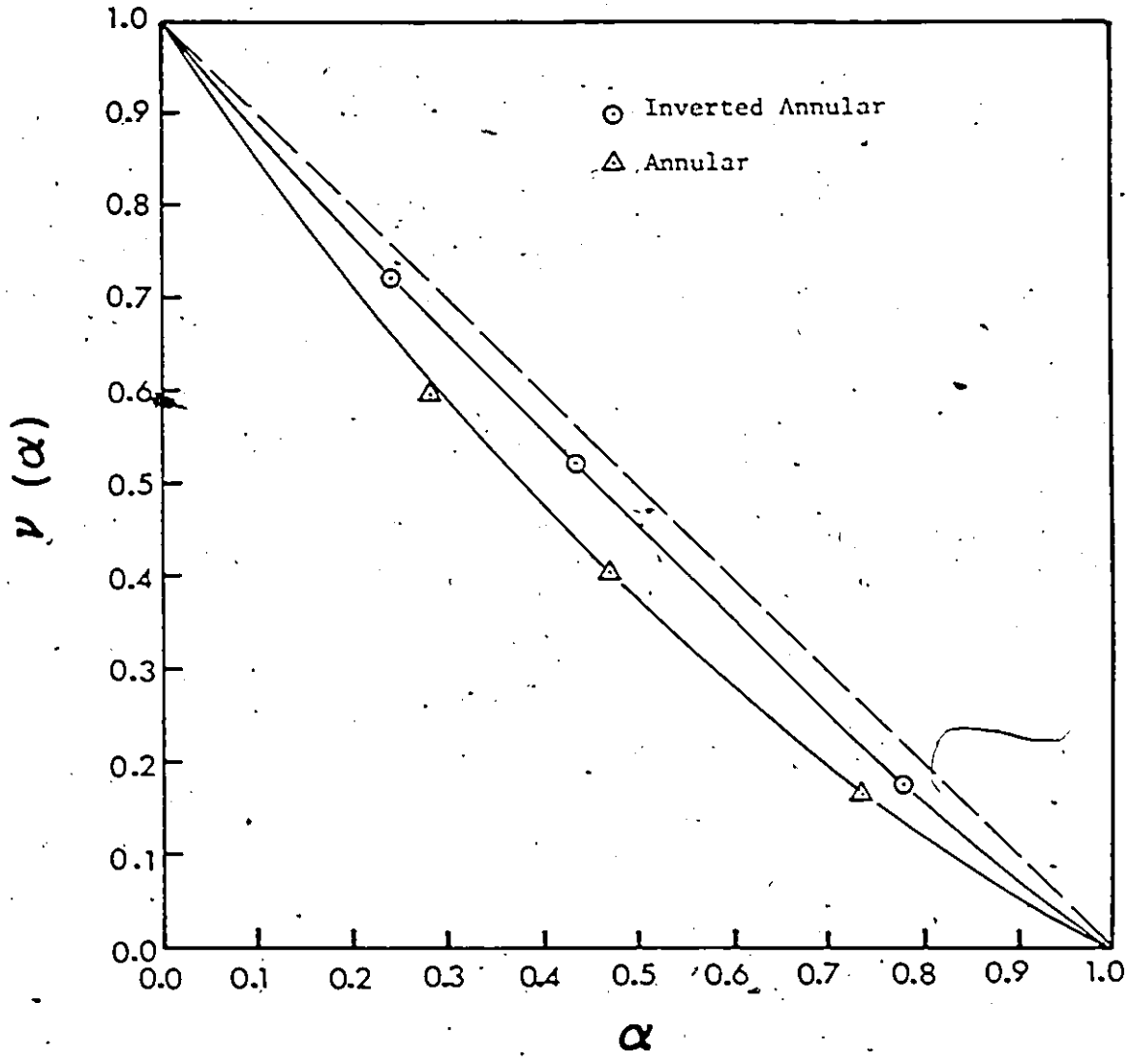

Figure 4.14 Result of Expt #14 showing the increase of the average energy of a required incident neutron spectrum with the addition of neutron reflector material

when neutron reflector is present as shown in Expt #13. It is thus an indirect proof that the required input neutron spectrum must shift to higher energy side when neutron reflector is added.

4.3.2.3 Test section II with neutron reflector (Expt #15)

In this experiment, the test section I in Expt #13 was replaced by the 51 mm thick carbon steel walled test section II. The ^{241}Am/Li source was moderated with a moderator of 105 mm diameter and wrapped with Cd sheet. The result is shown in Figure 4.15. From this figure, near linearity and flow pattern independence are observed. The smaller moderator diameter of 105 mm produced an input neutron spectrum with higher weighted averaged energy than the moderator diameter of 110 mm. This agrees with the hypothesis that the appropriate input neutron spectrum shifts to higher energy side when test section wall thickness increases.

4.3.2.4 Test section III with neutron reflector (Expt #16)

It remains to prove the relationship of the required spectrum with test section ID to complete the verification of the hypothesis. Experiment #16 was conducted with the 127 mm thin aluminum walled test section III. The Cd enclosure was lined with a layer of paraffin wax. The ^{241}Am/Li source was not used because there was already experimental evidence that ν stays above the $(1-\alpha)$ line for even the unmoderated source. Instead, a moderated ^{241}Am/Be neutron source was used. The moderator-can diameter was 83 mm and it was wrapped with Cd sheet. The result is shown in Figure 4.16. Near-linearity and flow pattern independence are observed, indicating an appropriate input

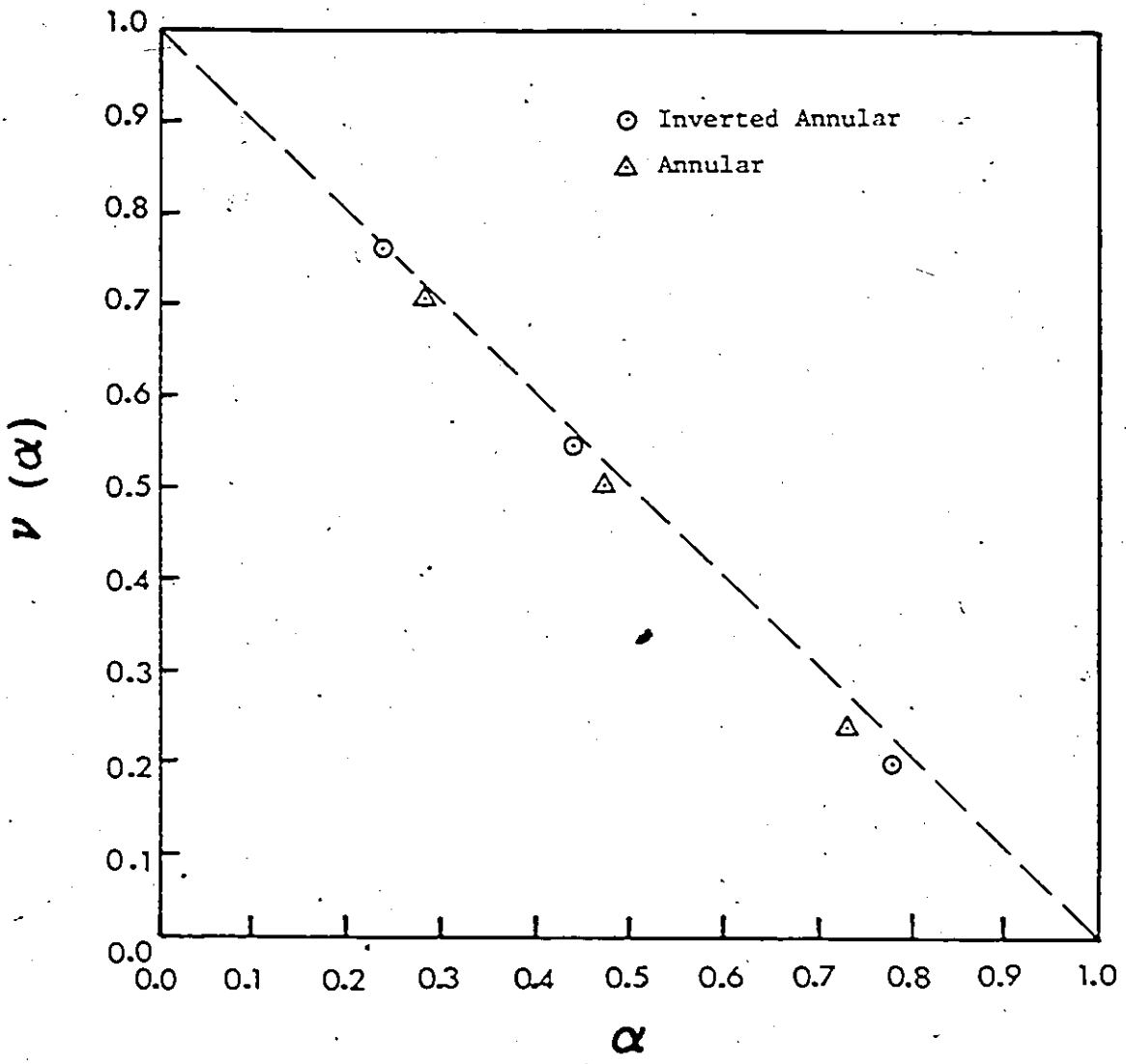

Figure 4.15 Result of Expt #15 showing the achievement of both linearity and flow pattern independence for test section II in the presence of neutron reflector; the incident neutron spectrum consisted of only epicadmium neutrons resulting from the moderation of the ^{241}Am/Li source with a moderator diameter of 105 mm and removing the subcadmium neutron component

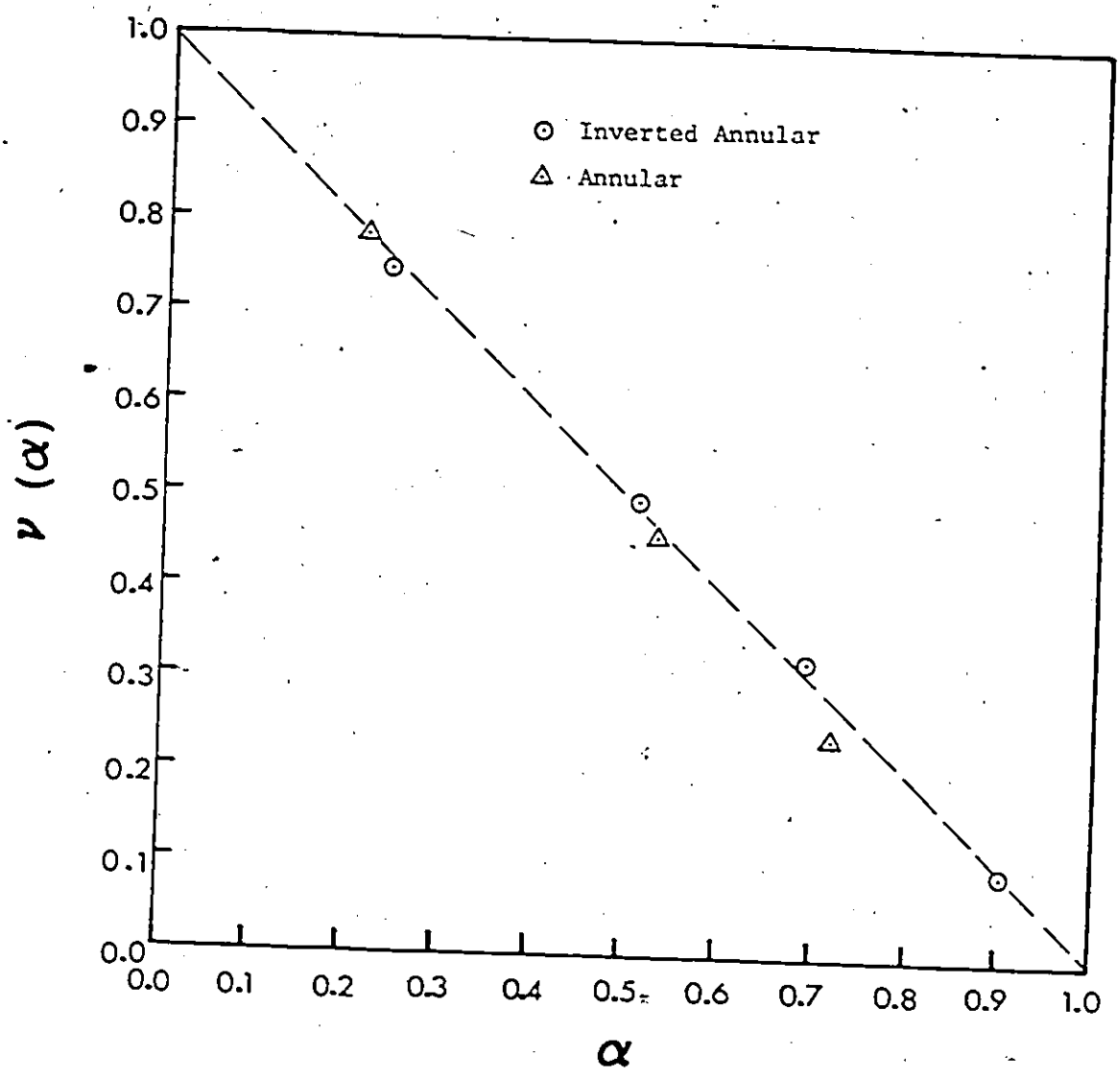

Figure 4.16 Result of Expt #16 showing the achievement of both linearity and flow pattern independence for test section III in the presence of neutron reflector; the incident neutron spectrum consisted of only epicadmium neutrons resulting from the moderation of the ^{241}Am/Be source with a moderator diameter of 83 mm and removing the subcadmium neutron component

neutron spectrum is reached.

The spectrum weighted average energies of unmoderated ^{241}Am/Li and ^{241}Am/Be are 0.4 MeV and 5.1 MeV respectively. However, the moderator-can diameter of 83 mm in this experiment is smaller than that of the moderator-can (110 mm) in Expt #13 where the test section was the 51 mm thin aluminum walled test section I. Thus, qualitatively, the weighted average of the incident neutron spectrum for the larger test section is higher than that for the smaller one. Monte Carlo calculations have been done to calculate the two spectra (see section 5.4.1). Indeed, the weighted average energies of the moderated ^{241}Am/Be and ^{241}Am/Li are 2.07 and 0.29 MeV respectively. This implies that, for the same neutron source, the required moderator diameter decreases or equivalently, the appropriate input energy spectrum shifts to the high energy end as the test section ID increases.

4.3.2.5 Test section IV with neutron reflector (Expt #17)

Although all the points in the hypothesis are essentially verified. Expt #17 was conducted to find the appropriate moderator for the 127 mm thick carbon steel walled test section IV. The set-up of Expt #17 was the same as in Expt #16 except for the test sections. However, the moderator was 70 mm in diameter and wrapped with Cd sheet. The result is shown in Figure 4.17. So, an appropriate spectrum was reached. The smaller moderator diameter (70 mm v.s. 83 mm) for the thick walled test section simply implies a harder input neutron spectrum, further confirming the hypothesis about wall thickness.

After these verification experiments, the hypothesis

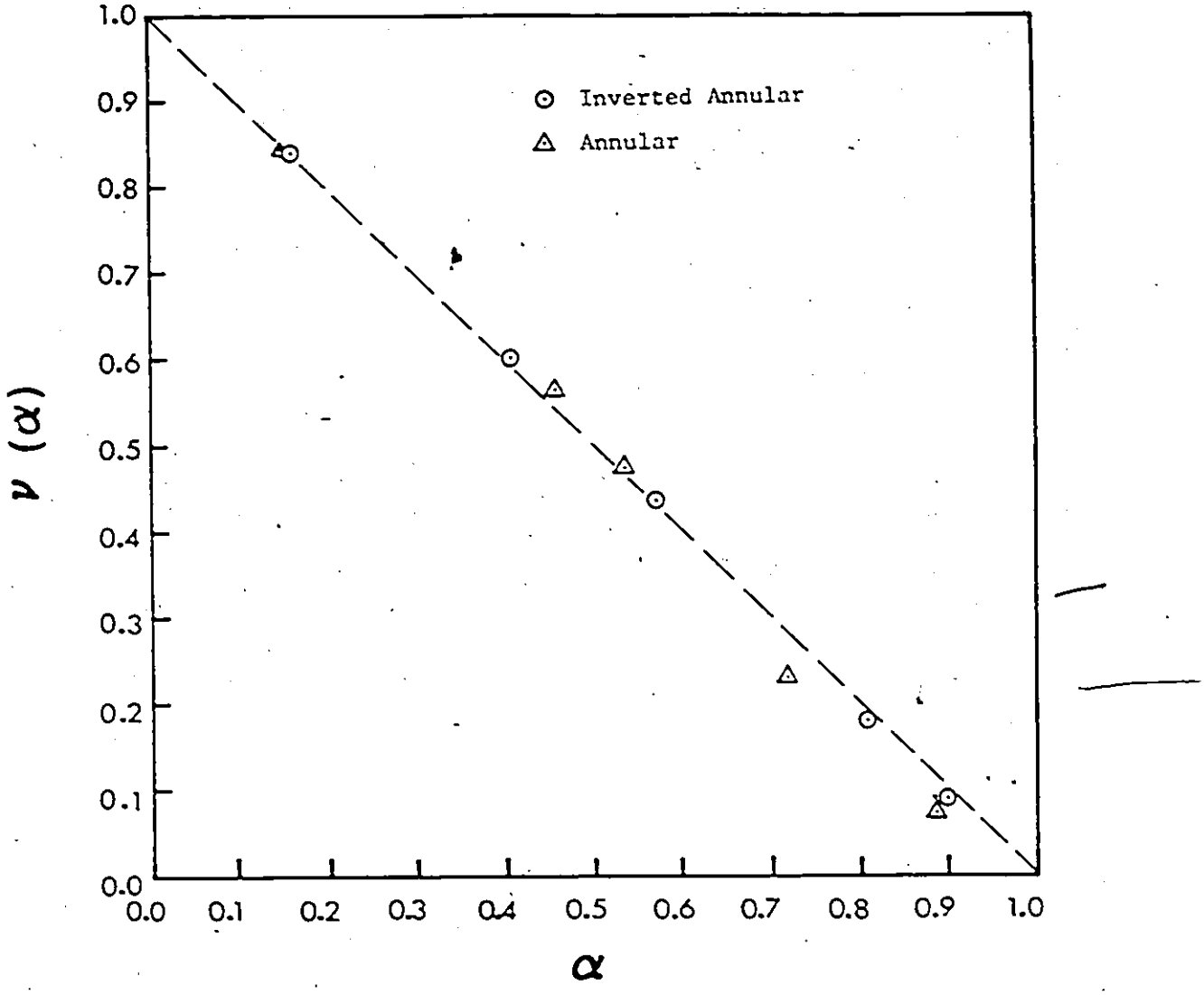

Figure 4.17 Result of Expt #17 showing the achievement of both linearity and flow pattern independence for test section IV in the presence of neutron reflector material; the incident neutron spectrum consisted of only epicadmium neutrons resulting from the moderation of the ^{241}Am/Be source with a moderator of 70 mm diameter.

is considered verified.

4.4 SUPPLEMENTARY EXPERIMENTS WITH TEST SECTION CONTAINING NON-RADIALLY DISTRIBUTED WATER PHASE

The previous experimental study has focussed on the radially symmetric annular and inverted annular flow pattern. Once linearity is established, radially non-symmetrical flow patterns can be considered as a perturbation. Supplementary experiments were conducted for radially non-symmetric annular, inverted annular, and stratified flow.

4.4.1 Radially Non-Symmetric Annular and Inverted Annular Flow (Expt #18)

Experiment #18 was conducted with the 127 mm thick walled test section IV. The geometry of the experimental set-up was the same as in Expt #17 where the ^{241}Am/Be source was moderated with the 70 mm moderator-can. In this experiment, a tube of water (diameter=40 mm) representing an inverted annular flow pattern of α=0.90, was placed in four different positions inside the test section, one at a time. These four positions are shown in Figure 4.18a. Each position represents a displaced inverted annular flow without radial symmetry with respect to the test section axis. Similarly, an empty tube of diameter 51 mm was placed in four positions, as shown in Figure 4.18b. The rest of the space was filled with water. Each position represented a displaced annular flow of α=0.16. The results are shown in Figure 4.19.

Let us first discuss the displaced inverted annular flow.

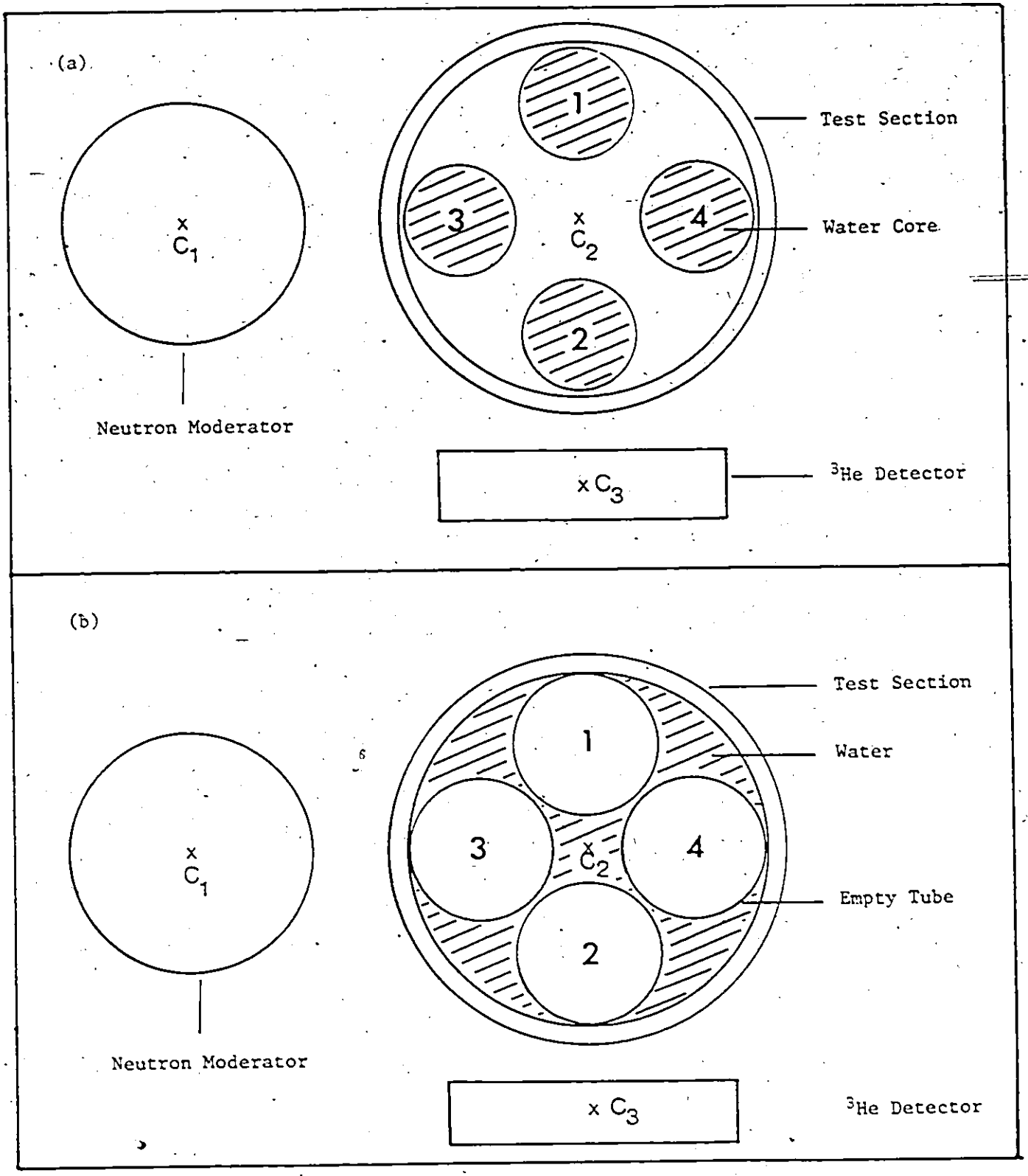

Figure 4.18 Configuration of water phase in displaced (a) annular and (b) inverted annular flow patterns

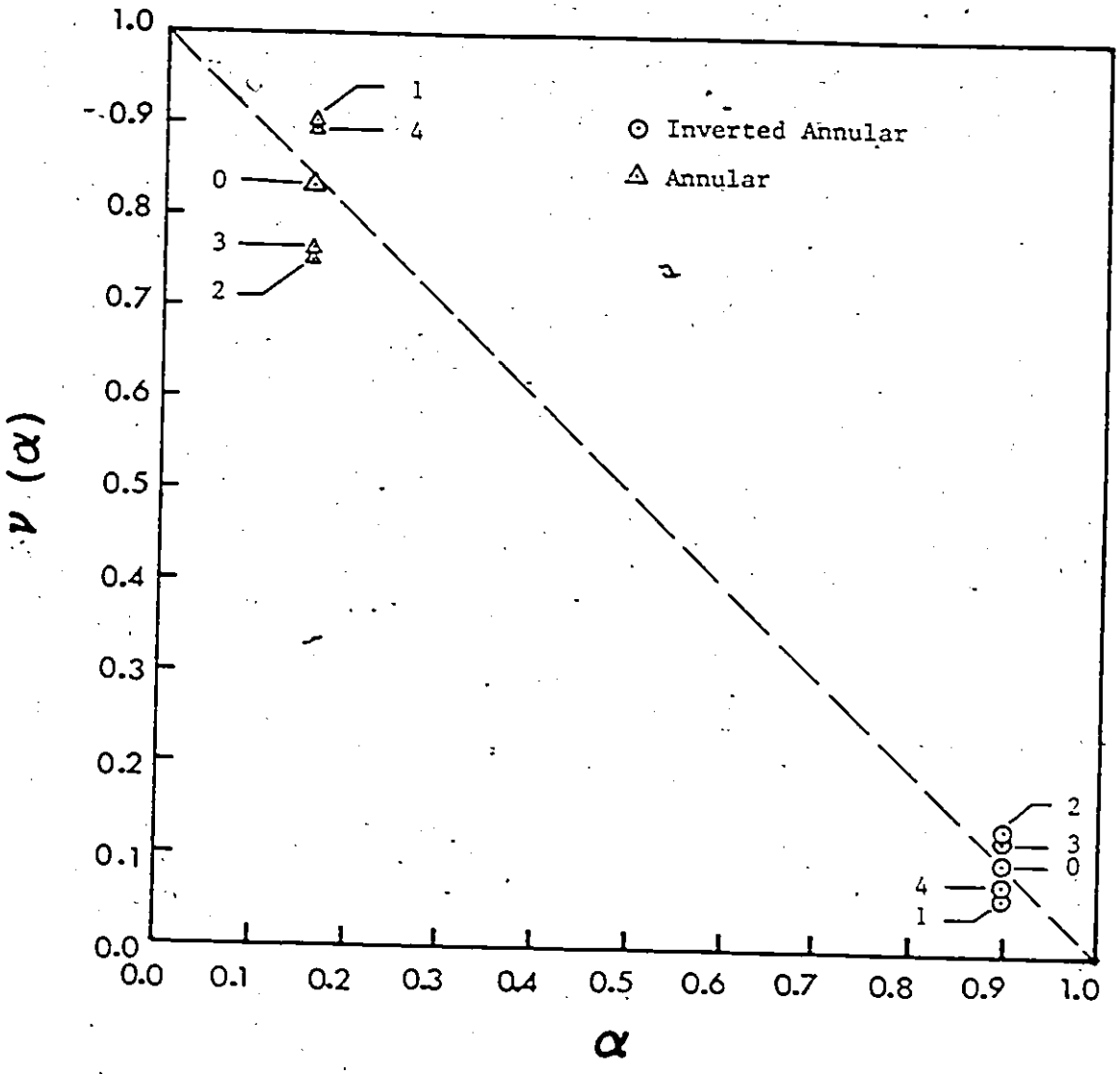

Figure 4.19 Result of Expt #18 showing the perturbation caused by the displaced annular and inverted annular water phase distribution

The point labelled 0 for inverted annular was obtained from Expt #17 with the radially symmetric inverted annular flow. The four points deviate from point 0 by a small amount ($\Delta\nu<0.03$). Thus the four positions yielded results which are minor perturbations from the radially symmetric water distribution. However, we still want to refine the detector responses.

Consider the data points 1 and 2. These two points are very close to being equi-distant to data point 0. From Figure 4.18a, the two corresponding tube positions 1 and 2 are bi-symmetric with respect to the C_2-C_3 axis, and are mirror reflections of each other about the C_1-C_2 axis. Thus, if a second detector had been placed diametrically opposite to the first detector at the same distance, its response would have been the reverse of the first detector. If the average of the two detector responses were used, the same ν as point 0 would be obtained regardless of whether the liquid phase were located as in position 1 or 2.

Consider data points 3 and 4 which are also quite equidistant from data point 0. The corresponding tube positions 3 and 4 are bi-symmetric with respect to the C_1-C_2 axis but mirror-reflections of each other about the C_2-C_3 axis. The extra detector would not change the ν. But, if another identical moderator were placed diametrically opposite to the first moderator, the detector response would be reversed for positions 3 and 4. Thus, a two detector and two moderator assembly would reduce the perturbation caused by displacement from radial symmetry.

Next, let us consider the displaced annular flow. The point 0 was obtained when the air core was placed in the centre of the test section. The perturbation caused by the displacement of the air core is somewhat larger than that for the displaced inverted annular flow but is still quite small ($\Delta v < 0.07$). The four data points 1, 2, 3, and 4 can be grouped into two pairs —— points 1 and 2, and points 3 and 4. Points 1 and 2 are quite equidistant from point 0 and so are points 3 and 4. By similar arguments as for the case of the inverted annular flow, the suggested two detector and two moderator assembly can reduce the perturbation caused by radial non-symmetry in the annular flow pattern.

4.4.2 Stratified Flow Pattern (Expt #19)

The next radially non-symmetric flow pattern to be considered is stratified flow. Expt #19 was conducted for stratified flow with the same set-up in the Expt #18. The water distribution in this experiment is shown in Figure 4.20. The water phase for each selected α was placed in position 1. After counting, the test section was rotated so that the water phase was in position 2 (the axis of the test section is vertical). The result of the experiment is shown in Figure 4.21.

From Figure 4.21, it is seen that $v(\alpha)$ for position 1 is always higher than that for position 2. The average lies very close to the $(1-\alpha)$ line. Since positions 1 and 2 are bi-symmetric about the C_1-C_2 axis but are mirror reflections of each other about the C_2-C_3 axis, an additional identical moderated neutron source would remove the discrepancy between positions 1

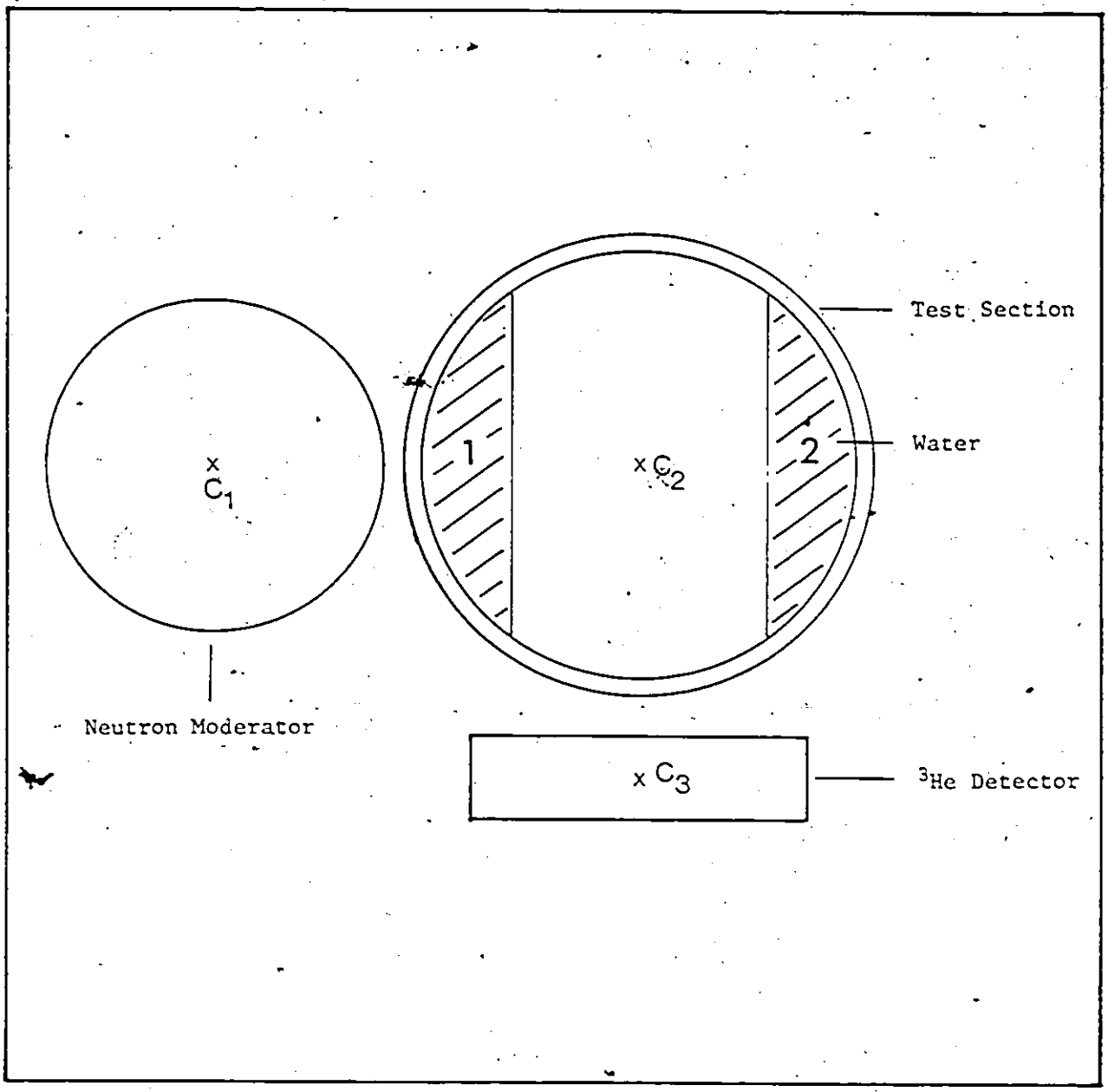

Figure 4.20 Configuration of water phase in stratified flow pattern

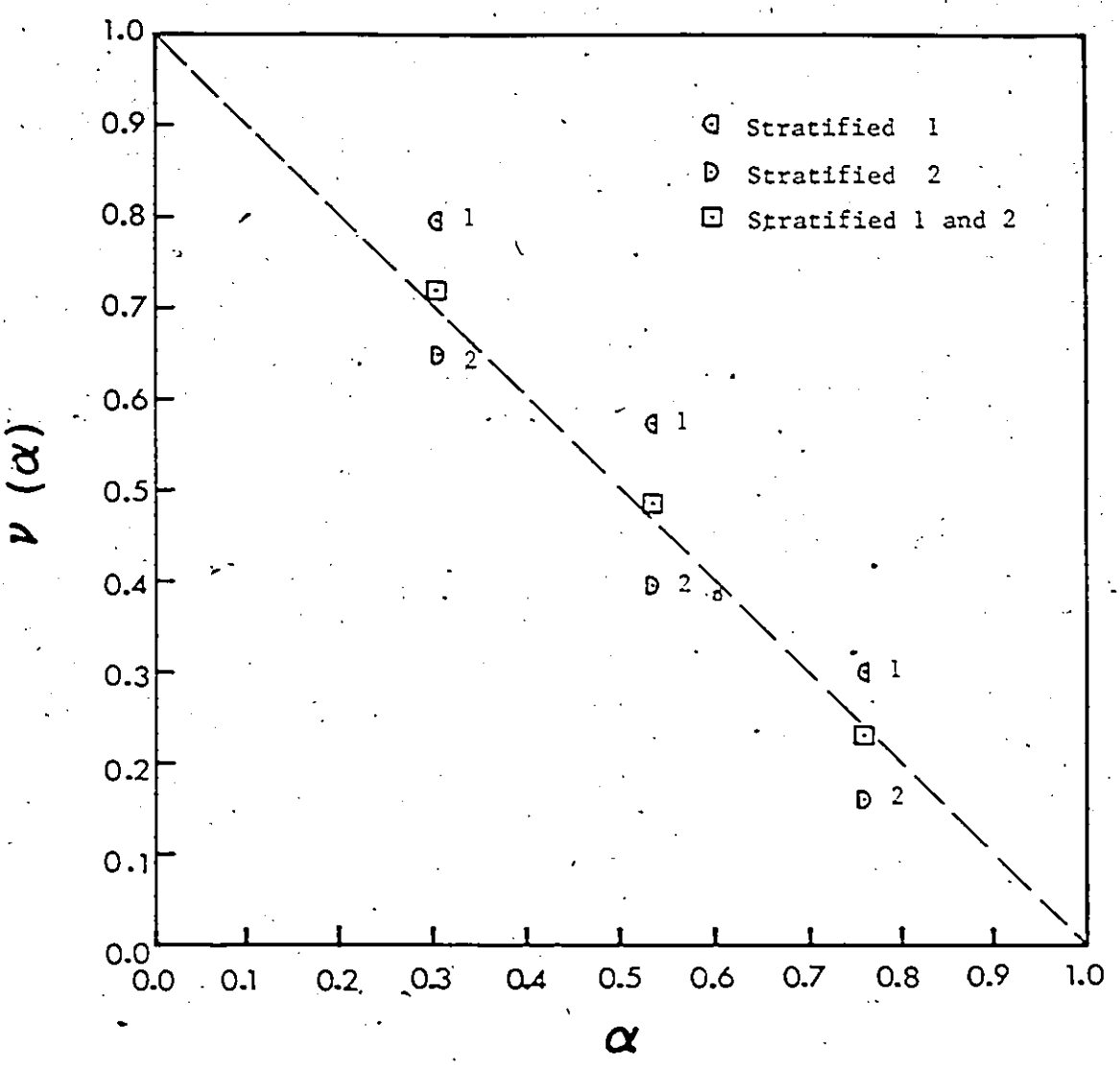

Figure 4.21 Result of Expt #19 showing the perturbation caused by the water phase distribution in stratified flow

and 2 yielding ν close to the $(1-\alpha)$ line.

4.5 CONCEPTUAL DESIGN OF A PORTABLE VOID FRACTION METER

We have gathered sufficient information to yield a conceptual design for a portable void fraction meter. This conceptual design is shown in Figure 4.22.

In Figure 4.22, the test section is horizontal. Two identical moderated sources are placed equidistant from the test section centre as shown. Two ^{3}He detectors are placed on opposite sides. The whole assembly is surrounded by shielding material (neutron reflector).

We have learned that source-moderator is needed to yield a required input neutron energy spectrum for a given combination of test section ID, wall thickness, and neutron reflector in order to achieve linearity and flow pattern independence for radially symmetric water distribution in the test section. The procedure to find the moderator diameter is postponed till the next chapter where a more quantitative understanding of our hypothesis is sought. Assuming that the correct moderator characteristics are known, then two detectors and two moderators are needed to remove perturbations in ν caused by possible water phase distributions which are not radially symmetric with the test section axis.

The important goal of forming from experimental observations a hypothesis which leads to a conceptual design of a portable void fraction meter is completed. However, it is important to better understand the trends included in the

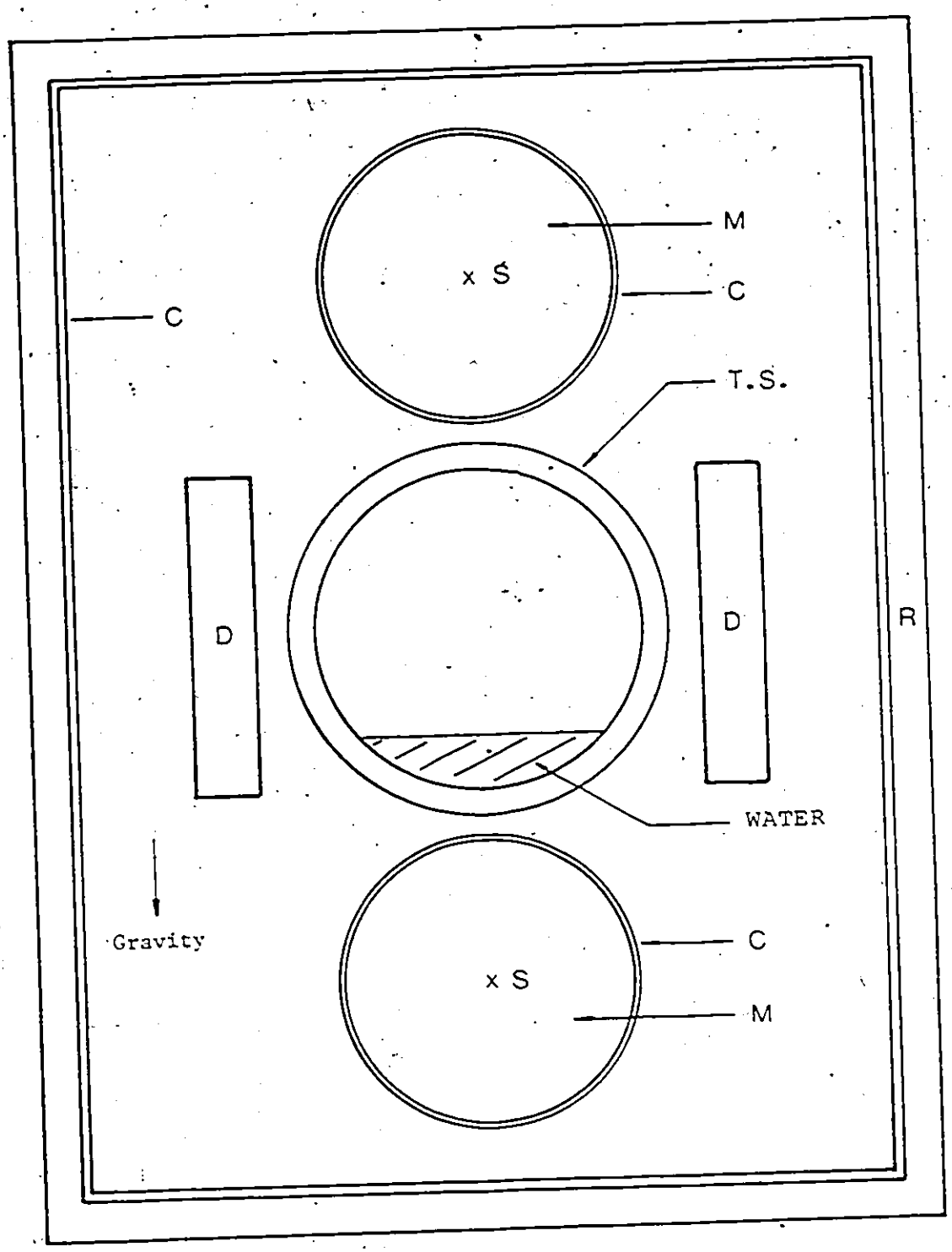

M - Neutron Moderator
S - Neutron Source
D - ^{3}He Detector
R - Shielding (Neutron Reflector)
C - Cd Sheet
T.S.- Test Section

Figure 4.22 Conceptual design of a portable void fraction meter using the technique of neutron scattering

hypothesis. This forms the subject of the next chapter.

CHAPTER FIVE

COMPUTATIONAL AND THEORETICAL STUDY

5.1 INTRODUCTION

Recall that the qualitative hypothesis formulated from experimental observations in the parametric study states that the key factor for successful application of the neutron scattering technique is the input neutron energy spectrum. Attempts were made to qualitatively examine this hypothesis, and this chapter is devoted to this purpose.

Since all the experiments were conducted with input neutrons with continuous energy spectra, the logical approach to understand the proposed hypothesis is to isolate monoenergetic input neutrons and study their effects. It is very difficult to do so experimentally. Thus, Monte Carlo computations were conducted to carry out "numerical experiments" with monoenergetic input (incident) neutrons in set-ups similar to the actual experiments conducted. Trends calculated in the Monte Carlo "numerical experiments" were useful in providing an explanation for the hypothesis. Based on a simple model of first collision probability and thermalization of neutrons, these trends are first interpreted theoretically. The hypothesis is then explained with the help of the observed trends.

After the understanding of the hypothesis is completed, a design procedure for a portable void fraction meter is given at the end of this chapter.

5.2 MONTE CARLO STUDY AND INTERPRETATION

Monte Carlo "numerical experiments" were performed on two test sections, namely the 51 mm and 127 mm thin aluminum walled test sections (I and III). For each test section, monoenergetic input neutrons in the form of a beam were used. A point detector was used to estimate the subcadmium neutron fluence (time-integrated neutron flux). The assembly of beam, test section, and detector was surrounded by an albedo region lined with Cd sheet to remove subcadmium neutrons reflected from the albedo region. The details of this set-up have been discussed in Chapter 3. Several groups of monoenergetic input neutrons were used. For each group, test sections containing water distributed in annular and inverted annular patterns were simulated. For each flow pattern, three void fractions, 0.25, 0.50, and 0.75, were examined.

5.2.1 Monte Carlo Results

The results for the two test sections are presented as follows.

5.2.1.1 51 mm thin aluminum walled test section

The effects of four groups of input neutron energies, IG=32, 24, 15, and 7, were studied. The energy ranges of these four groups were 4.1×10^{-7} to 1.1×10^{-6}, 9.6×10^{-4} to 2.0×10^{-3}, 1.1×10^{-1} to 3.0×10^{-1}, and 3.3 to 4.5 MeV respectively. The scattered, subcadmium neutron fluences ($E_n < 4.1\times10^{-7}$ MeV) at the point detector, i.e $\phi_{33}(\alpha)$ (neutrons/cm^2/eV/source neutron), were calculated. The results are tabulated in Table 5.1 and shown in

TABLE 5.1

$\phi_{33}(\alpha)$ FOR 51 mm Test Section I

IG	Flow Pattern	Void Fraction	$\phi_{33}(\alpha)$ ($\times 10^{-4}$ n/cm^2/eV)
7	Inverted Annular	0.00	3.80 ± 0.30
	"	0.25	2.58 0.30
	"	0.50	1.54 0.25
	Annular	0.75	0.55 0.15
	"	0.25	1.83 0.20
	"	0.50	0.95 0.15
		0.75	0.45 0.10
15	Inverted Annular	0.00	9.00 ± 0.45
	"	0.25	6.91 0.32
	"	0.50	4.40 0.25
	Annular	0.75	2.26 0.10
	"	0.25	5.90 0.30
	"	0.50	4.20 0.30
		0.75	1.74 0.20
24	Inverted Annular	0.00	12.75 ± 0.60
	"	0.25	11.25 0.40
	"	0.50	7.75 0.30
	Annular	0.75	4.75 0.20
	"	0.25	10.10 0.50
	"	0.50	7.13 0.20
		0.75	4.04 0.20
32	Inverted Annular	0.00	24.82 ± 1.00
	"	0.25	20.54 0.8
	"	0.50	15.47 0.5
	Annular	0.75	10.25 0.5
	"	0.25	22.66 0.5
	"	0.50	16.97 0.5
		0.75	11.24 0.3

Figures 5.1-5.4.

In Figures 5.1-5.4, the $\phi_{33}(1)$ was not calculated but was assumed to be zero since the empty test section would have been totally transparent to the neutron beam and no thermalization would have been possible. The errors quoted are at 68% confidence level and were obtained by running about 2 to 3 thousand particles for each datum point. The error could have been decreased by running more particles. However, since the error decreases with the number of histories m (particles) by $1/\sqrt{m}$ and the Monte Carlo simulation was expensive (approximately $20 per 1000 particles), the uncertainty observed was considered satisfactory.

The subcadmium neutron fluences $\phi_{33}(\alpha)$ shown in Figures 5.1-5.4 are normalized with $\phi_{33}(0)$. The normalized subcadmium neutron fluences are equivalent to the dimensionless neutron counting rate $\nu(\alpha)$. The results of normalization, $\nu(\alpha)$, are shown in Figures 5.5 and 5.6 for the annular and inverted annular flow patterns. The two figures will be used in later discussions.

5.2.1.2 <u>127 mm thin aluminum walled test section</u>

For this test section, five groups, IG=32, 24, 16, 11, and 1, were studied. The energy ranges corresponding to these 5 groups are 4.1×10^{-7} to 1.1×10^{-6}, 9.6×10^{-4} to 2.0×10^{-3}, 6.74×10^{-2} to 1.1×10^{-1}, 1.1 to 1.5, and 12.2 to 15 MeV respectively. The results are tabulated in Table 5.2 and shown in Figures 5.7-5.11. The errors quoted on the $\phi_{33}(\alpha)$ are at 68% confidence level and were obtained by running 2-3 thousand particles for each datum

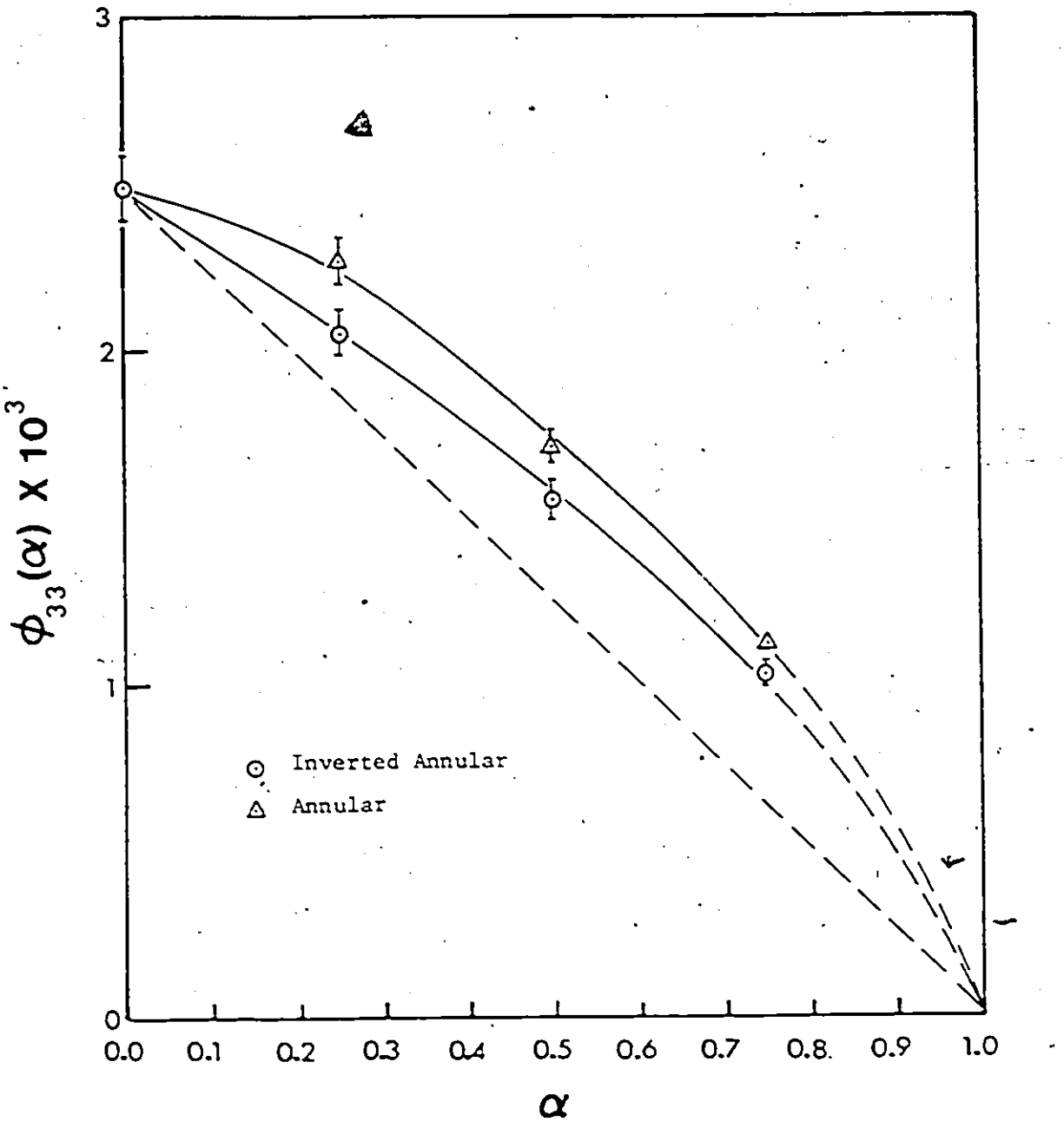

Figure 5.1 Scattered subcadmium neutron fluence, $\Phi_{33}(\alpha)$, by test section I estimated with Monte Carlo for Group 32 incident neutrons (4.1×10^{-7} MeV $\leq E_0 \leq 1.1 \times 10^{-6}$ MeV)

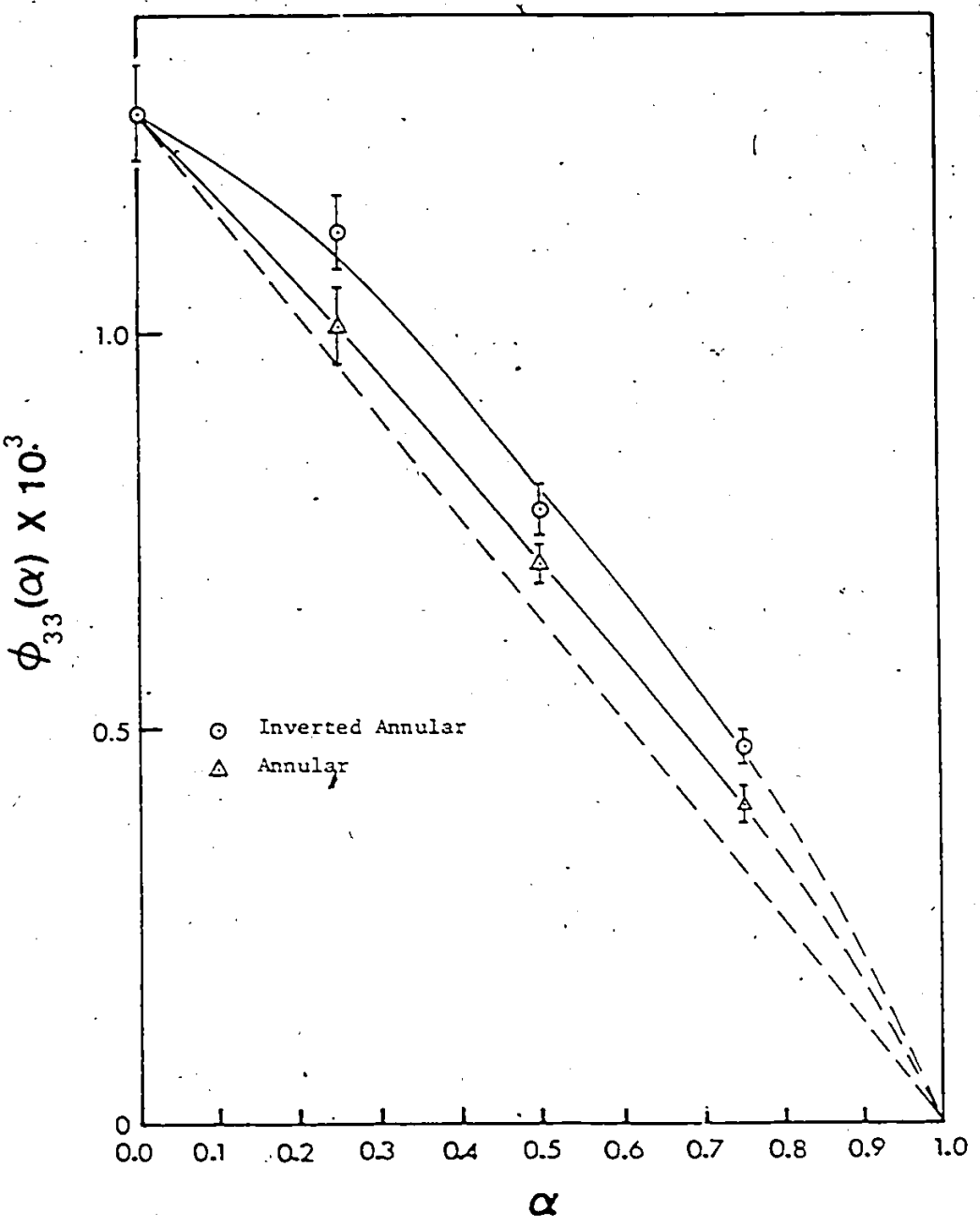

Figure 5.2 Scattered subcadmium neutron fluence, $\Phi_{33}(\alpha)$, by test section I estimated with Monte Carlo for Group 24 incident neutrons (9.6×10^{-4} MeV $\leq E_0 \leq 2.0 \times 10^{-3}$ MeV)

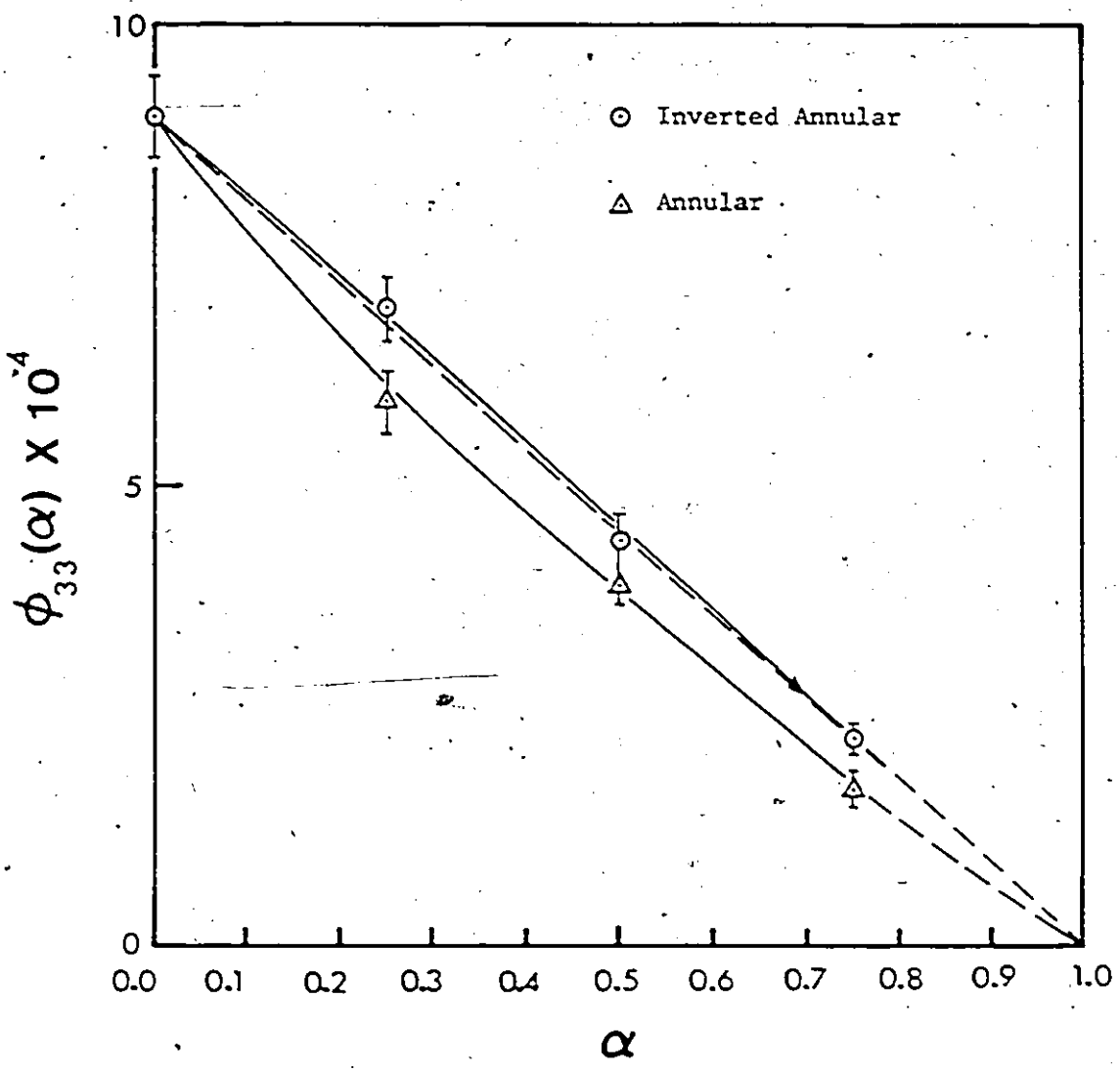

Figure 5.3 Scattered subcadmium neutron fluence, $\phi_{33}(\alpha)$, by test section I estimated with Monte Carlo for Group 15 incident neutrons (1.1×10^{-1} MeV $\leq E_0 \leq 3.0 \times 10^{-1}$ MeV).

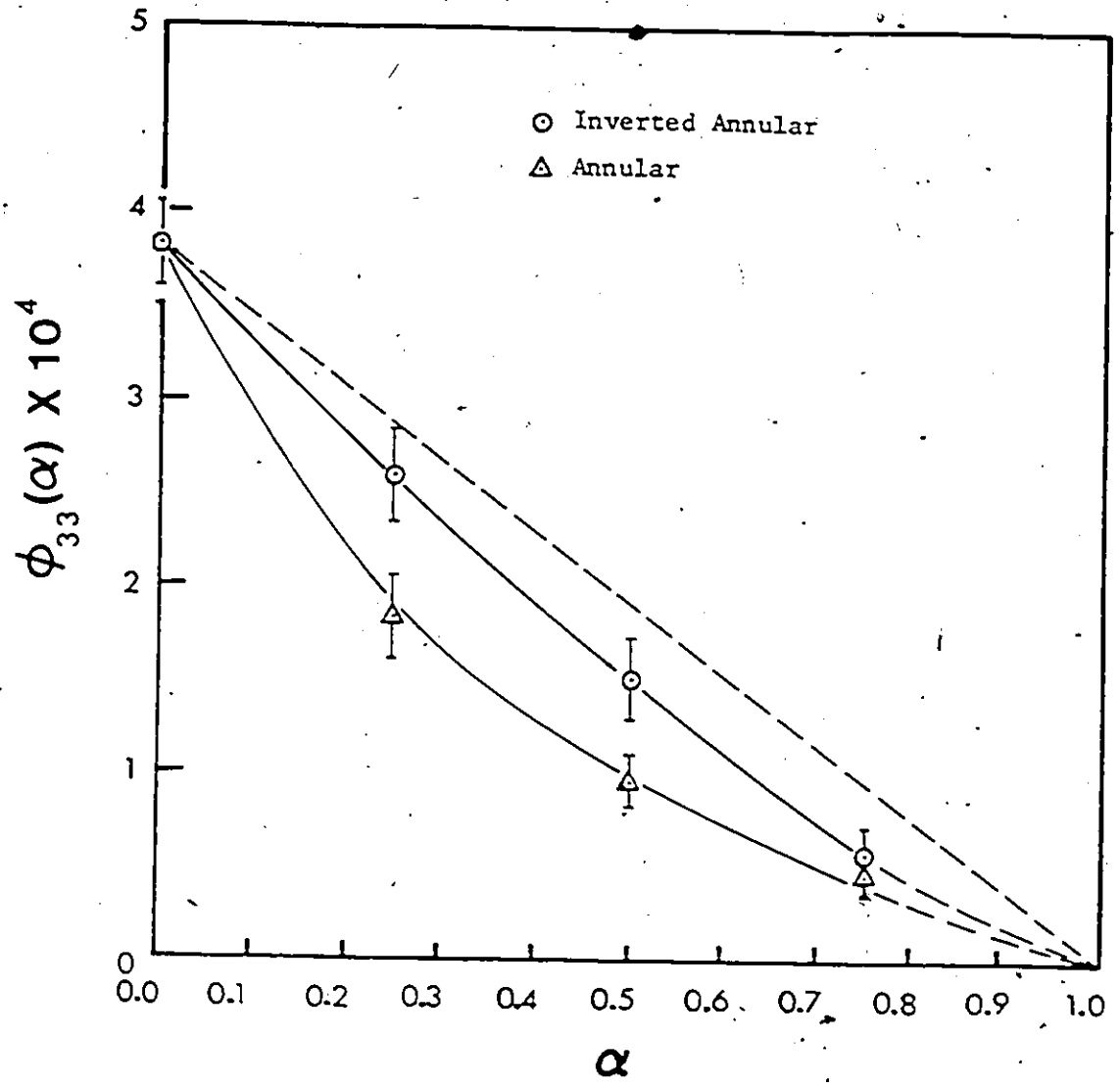

Figure 5.4 Scattered subcadmium neutron fluence, $\phi_{33}(\alpha)$, by test section I estimated with Monte Carlo for Group 7 incident neutrons (3.3 MeV $\leq E_0 \leq$ 4.5 MeV)

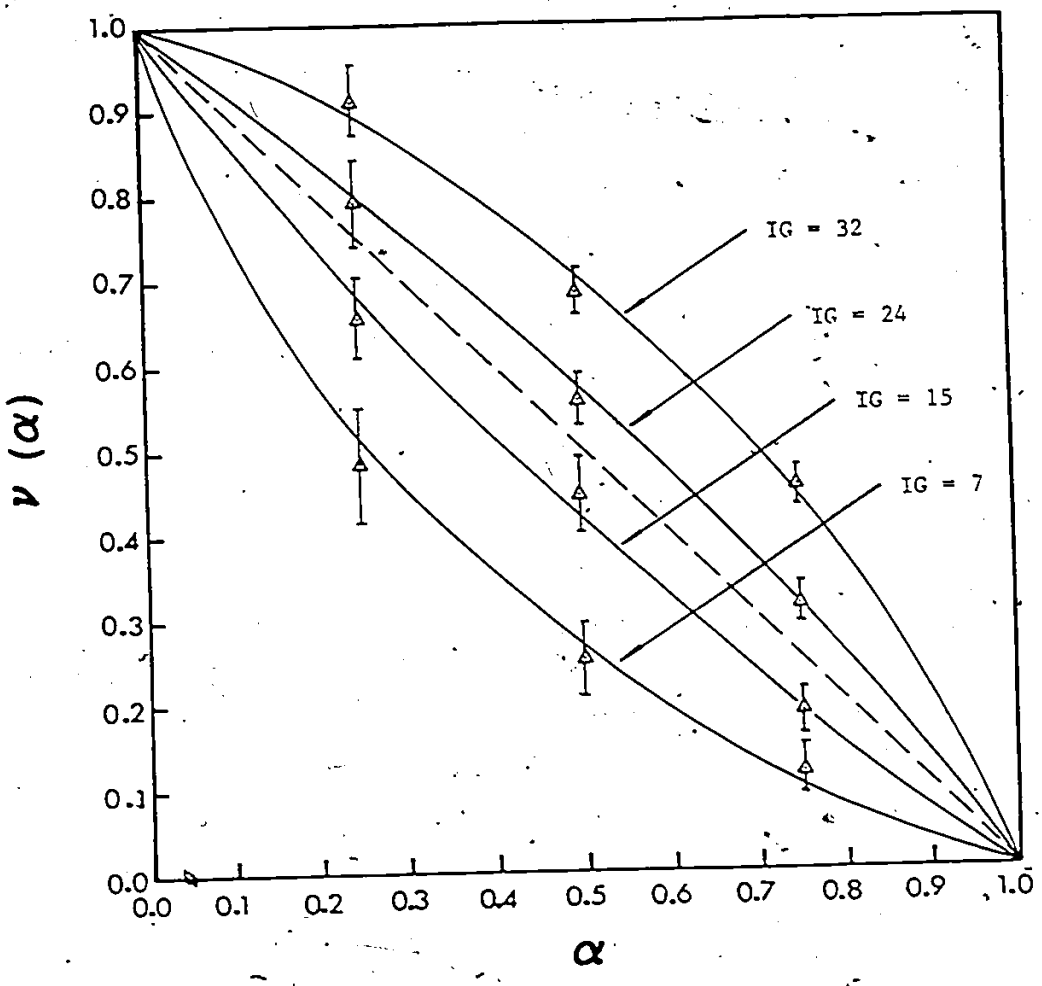

Figure 5.5 : Normalized $\Phi_{33}(\alpha)$, $\nu(\alpha)$, for annular flow pattern in test section I

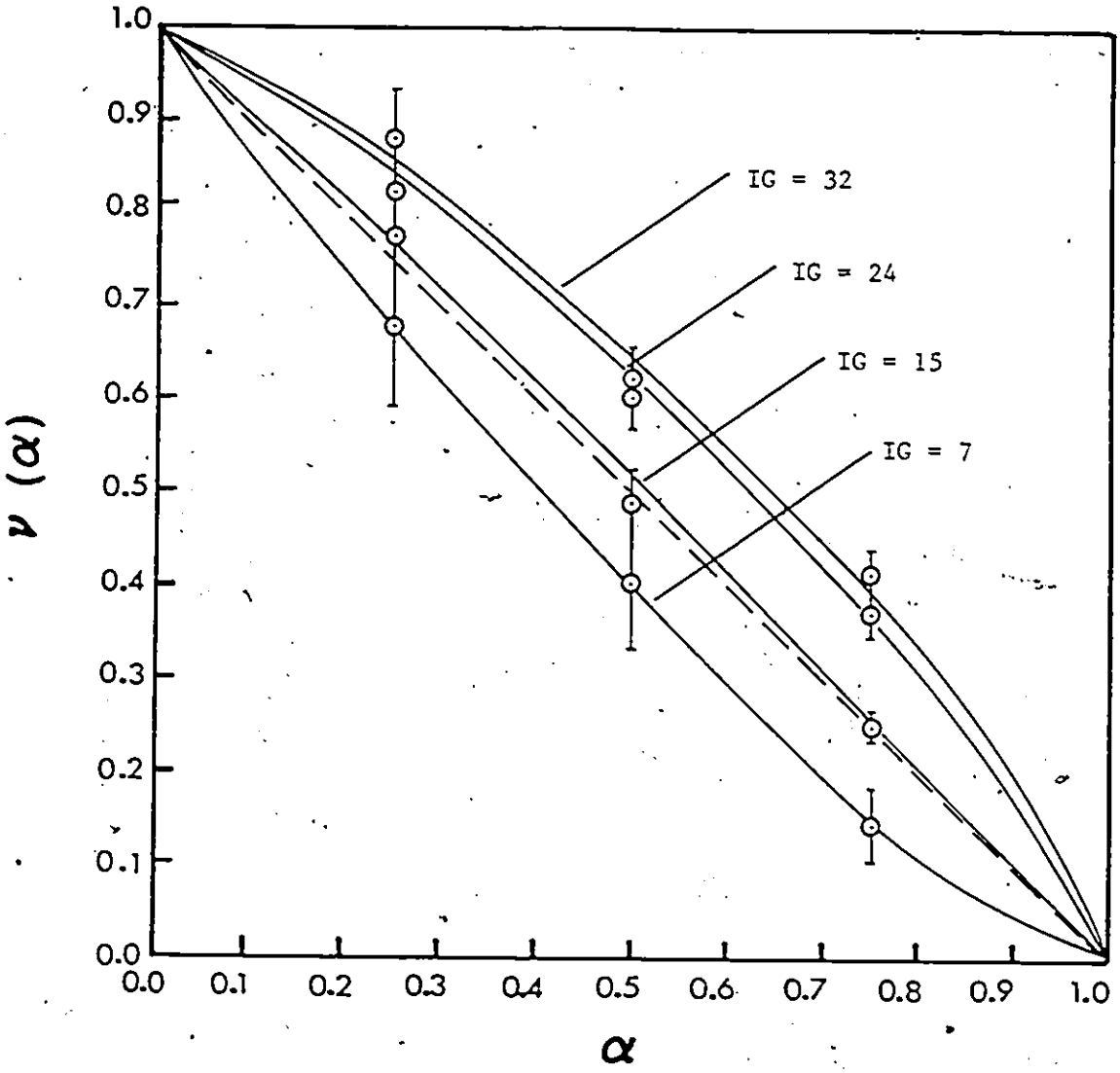

Figure 5.6 Normalized $\Phi_{33}(\alpha)$, $\nu(\alpha)$, for inverted annular flow pattern in test section I

TABLE 5.2

$\phi_{33}(\alpha)$ for 127 mm Test Section III

IG	Flow Pattern	Void Fraction	$\phi_{33}(\alpha)$ ($\times 10^{-4}$ n/cm^2/eV)
1	Inverted Annular	0.0	0.8857 ± 0.1701
	"	0.25	0.4858 0.1006
	"	0.50	0.3185 0.0564
	Annular	0.75	0.1187 0.0171
	"	0.25	0.3986 0.0837
	"	0.50	0.1541 0.0330
	"	0.75	0.0418 0.0100
11	Inverted Annular	0.0	3.345 ± 0.395
	"	0.25	2.225 0.251
	"	0.50	1.346 0.171
	Annular	0.75	0.7044 0.0542
	"	0.25	2.386 0.260
	"	0.50	1.208 0.155
	"	0.75	0.483 0.0753
16	Inverted Annular	0.0	5.122 ± 0.502
	"	0.25	4.097 0.402
	"	0.50	2.762 0.238
	Annular	0.75	1.620 0.130
	"	0.25	4.672 0.374
	"	0.50	3.711 0.386
	"	0.75	1.630 0.302
24	Inverted Annular	0.0	5.905 ± 0.467
	"	0.25	4.928 0.389
	"	0.50	3.840 0.284
	Annular	0.75	2.295 0.170
	"	0.25	5.769 0.473
	"	0.50	5.131 0.472
	"	0.75	3.201 0.349
32	Inverted Annular	0.0	16.17 ± 0.86
	"	0.25	14.13 0.65
	"	0.50	10.48 0.44
	Annular	0.75	6.615 0.26
	"	0.25	16.10 0.84
	"	0.50	15.63 0.81
	"	0.75	12.97 0.65

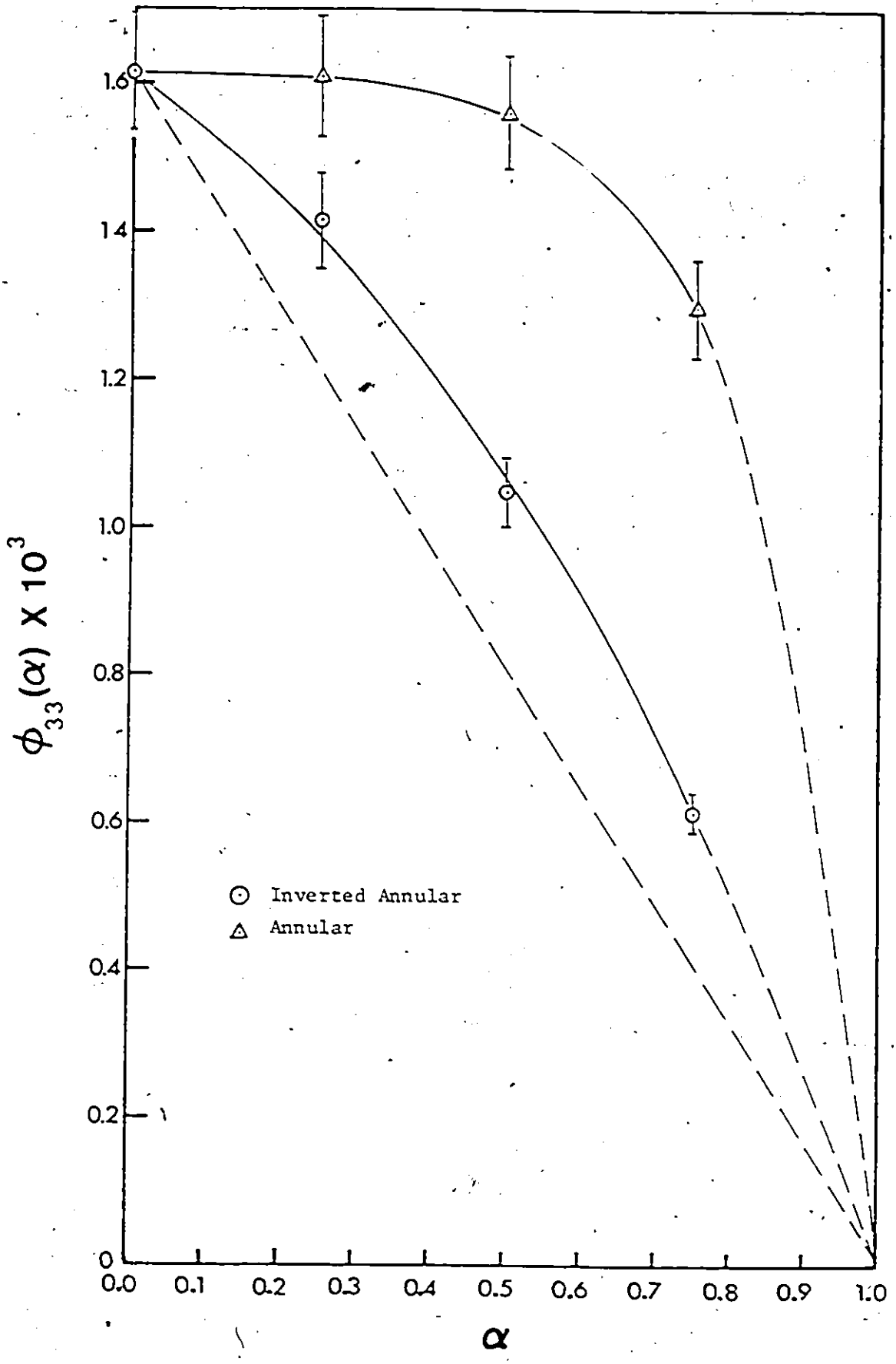

Figure 5.7 Scattered $\phi_{33}(\alpha)$ by test section III estimated with Monte Carlo for Group 32 incident neutrons (4.1×10^{-7} MeV $\leq E_0 \leq 1.1 \times 10^{-6}$ MeV)

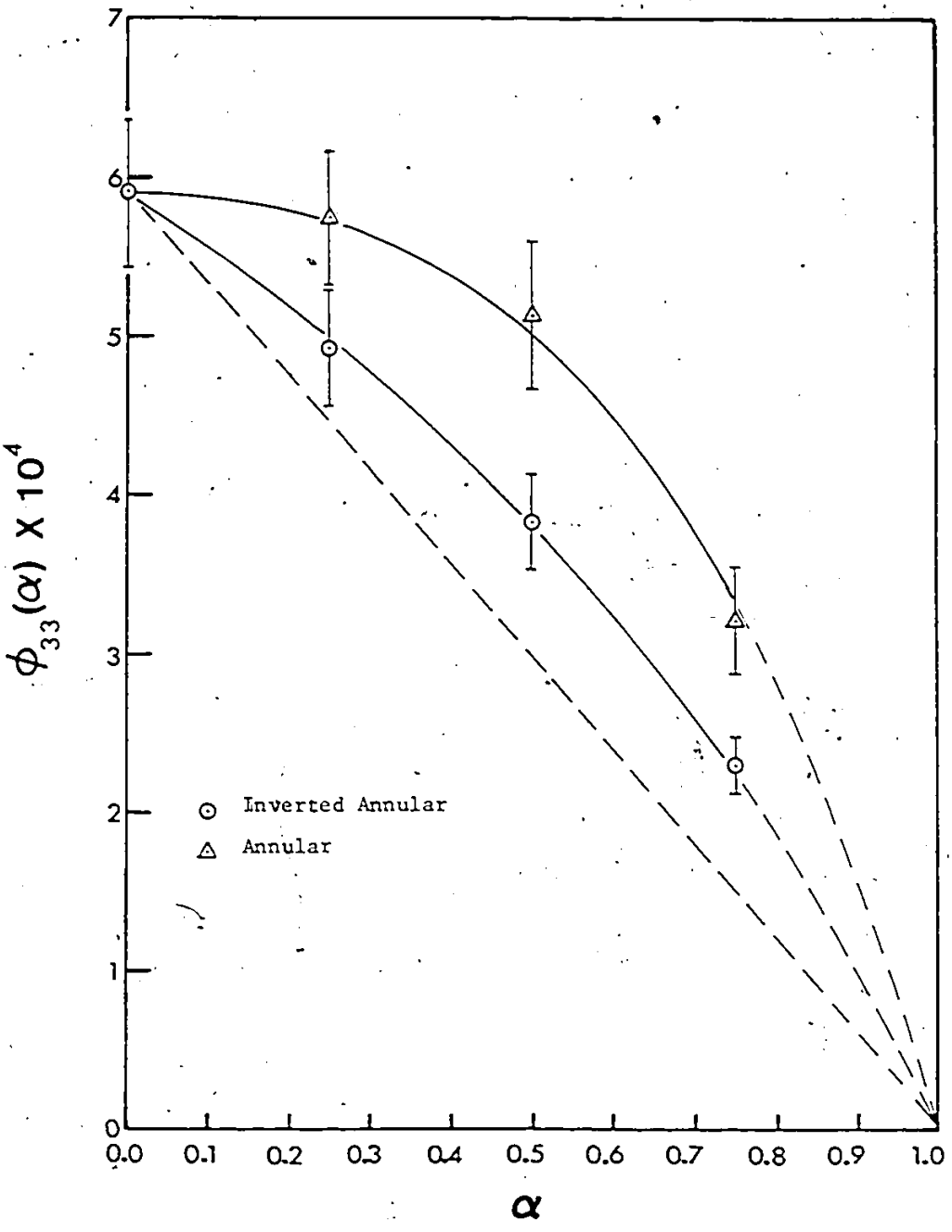

Figure 5.8 Scattered $\Phi_{33}(\alpha)$ by test section III estimated with Monte Carlo for Group 24 incident neutrons (9.6×10^{-4} MeV $\leq E_0 \leq 2.0 \times 10^{-3}$ MeV)

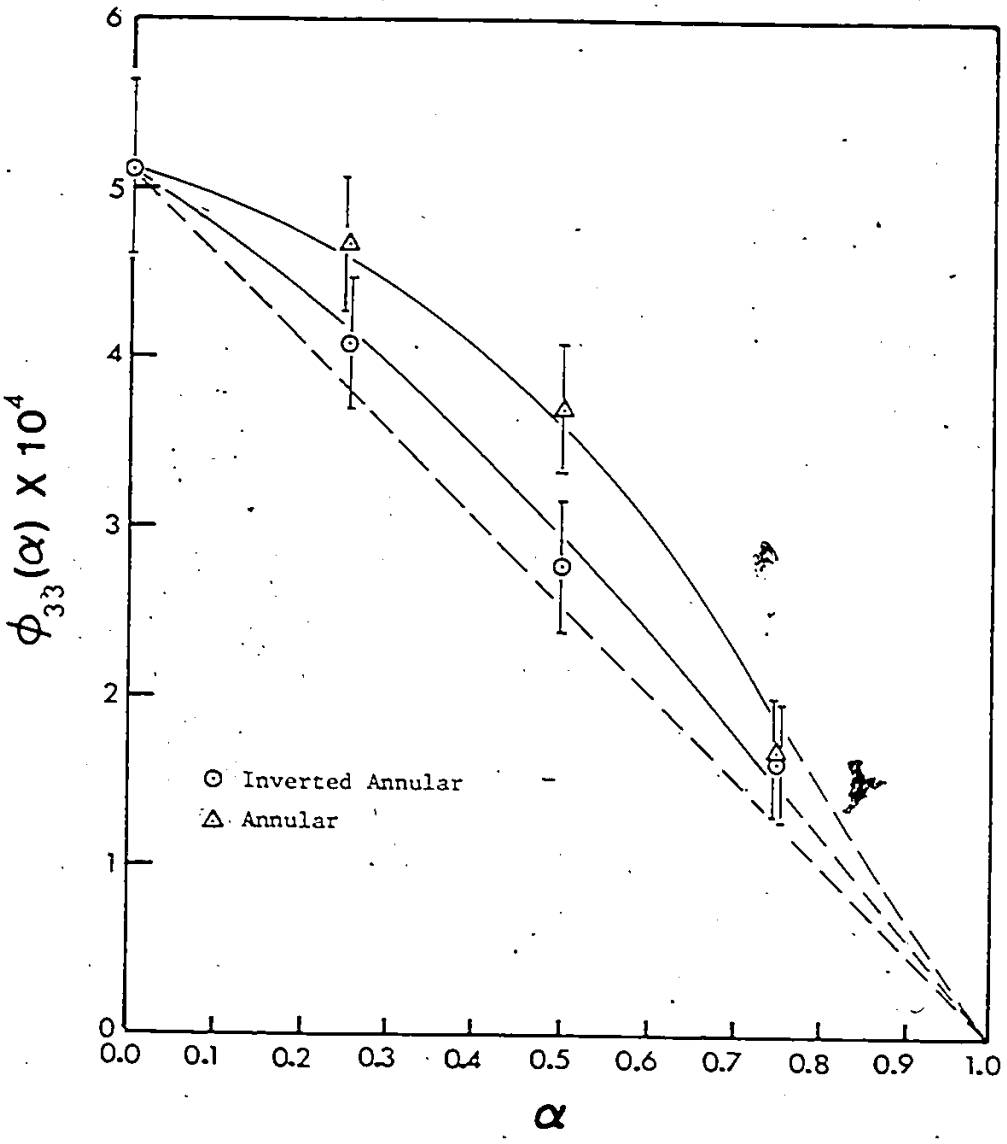

Figure 5.9 Scattered $\Phi_{33}(\alpha)$ by test section III estimated with Monte Carlo for Group 16 incident neutrons (6.7×10^{-2} MeV $\leq E_0 \leq 1.1 \times 10^{-1}$ MeV)

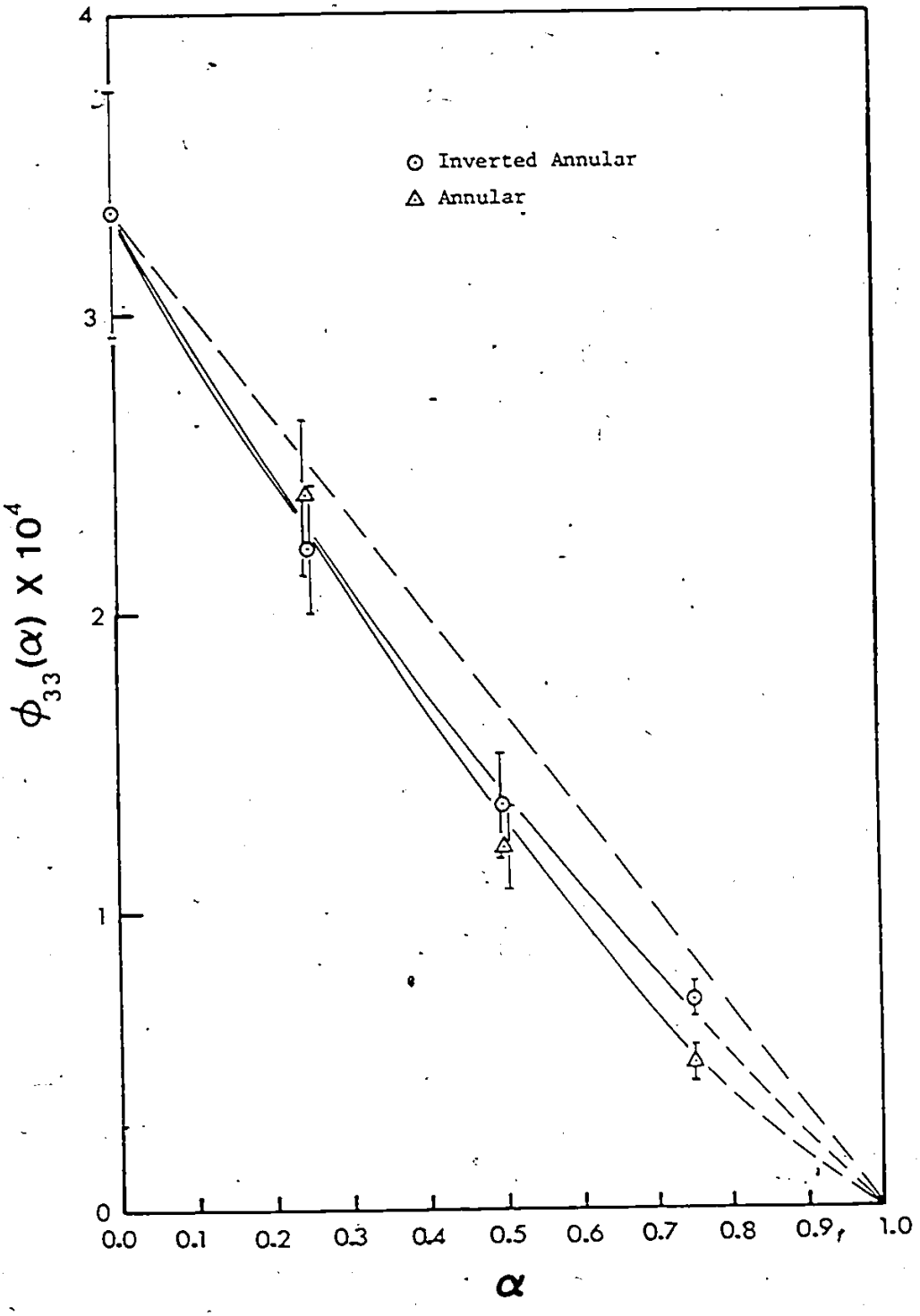

Figure 5.10 Scattered $\Phi_{33}(\alpha)$ by test section III estimated with Monte Carlo for Group 11 incident neutrons (1.1 MeV $\leq E_0 \leq$ 1.5 MeV)

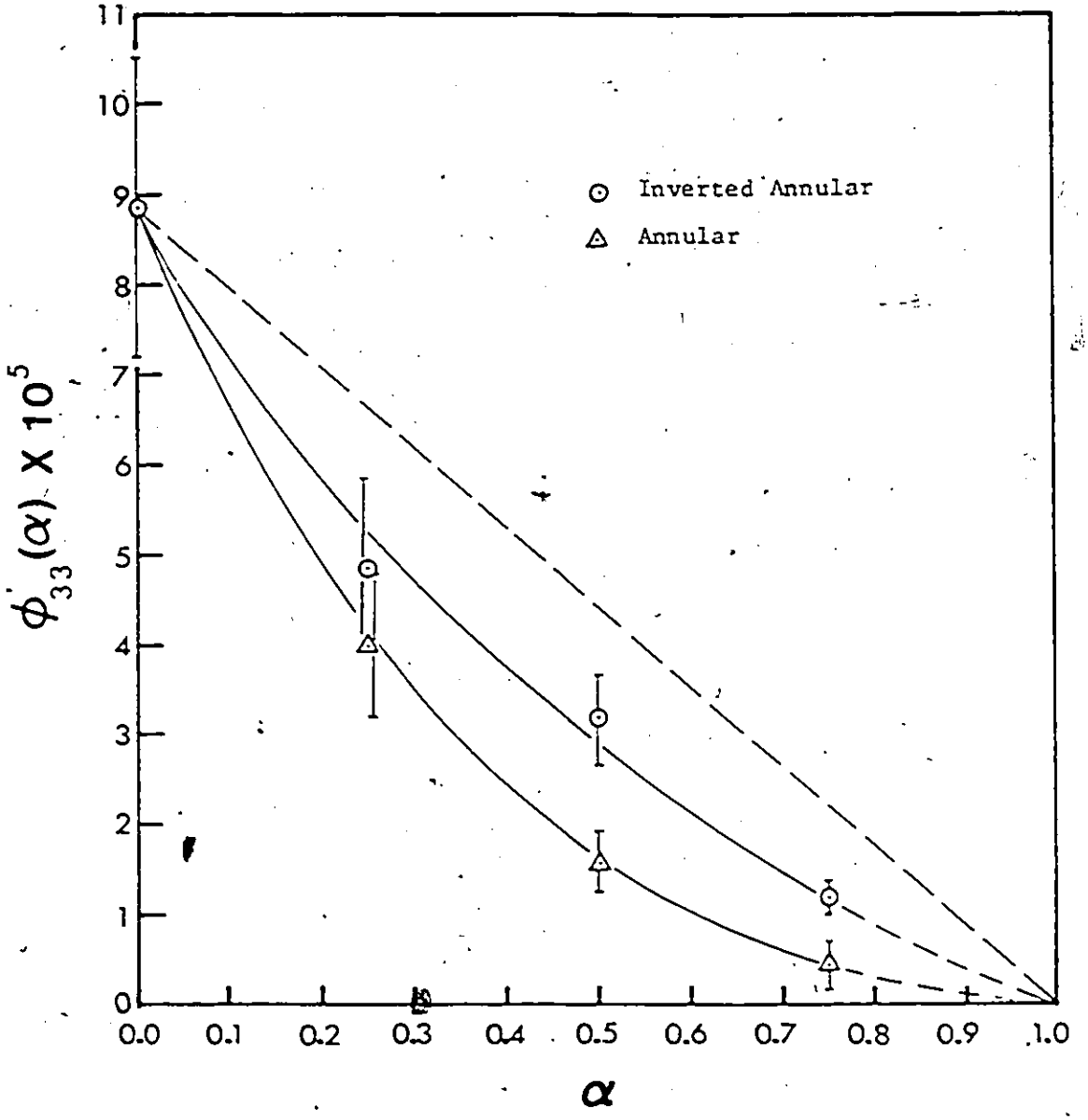

Figure 5.11 Scattered $\phi_{33}(\alpha)$ by test section III estimated with Monte Carlo for Group 1 incident neutrons (12.2 MeV $\leq E_0 \leq$ 15 MeV)

point.

The $\phi_{33}(\alpha)$ were normalized to yield $\nu(\alpha)$ as in the case of the 51 mm test section. The results are shown in Figures 5.12 and 5.13.

5.2.2. Trends Observed from the Monte Carlo Study

There are notable trends observed from the results of the Monte Carlo "numerical experiments".

5.2.2.1 Trends observed for 51 mm test section

Let us first consider the 51 mm test section. From Figures 5.1-5.4 and 5.5-5.6, the following trends are observed.

T1 In general, $\phi_{33}(\alpha)$ decreases with α and is neither linear nor flow pattern independent.

T2 For a given flow pattern and α, e.g. for $\alpha=0$, the magnitude of subcadmium neutron fluence decreases as the energy of input neutrons increases.

T3 For each flow pattern, starting with low energy input neutrons, the $\phi_{33}(\alpha)$ curve falls above the ideal linear line joining the two end points ($\alpha=0$ and 1). As the input neutron energy increases, the $\phi_{33}(\alpha)$ curve falls above the linear line by a smaller amount. Further increase of input neutron energy results in the $\phi_{33}(\alpha)$ curving below the ideal linear line. This trend can be seen more easily from Figures 5.5 and 5.6, where $\nu(\alpha)$'s are plotted.

T4 From Figure 5.5 and 5.6, at the lowest input neutron energy, e.g. IG=32, $\nu(\alpha)$ for annular flow is higher than that for inverted annular flow. As the input neutron energy

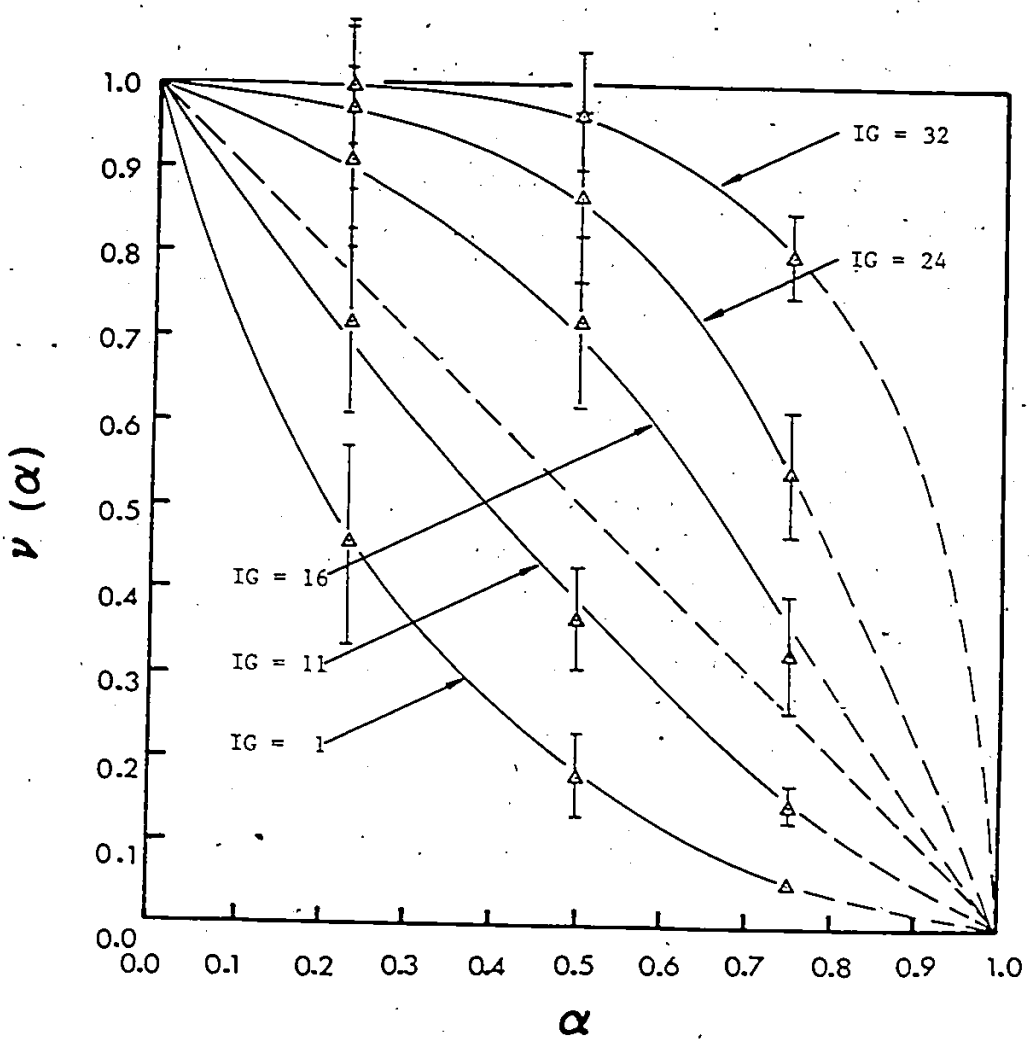

Figure 5.12 Normalized $\Phi_{33}(\alpha)$, $\nu(\alpha)$, for annualr flow pattern in test section III

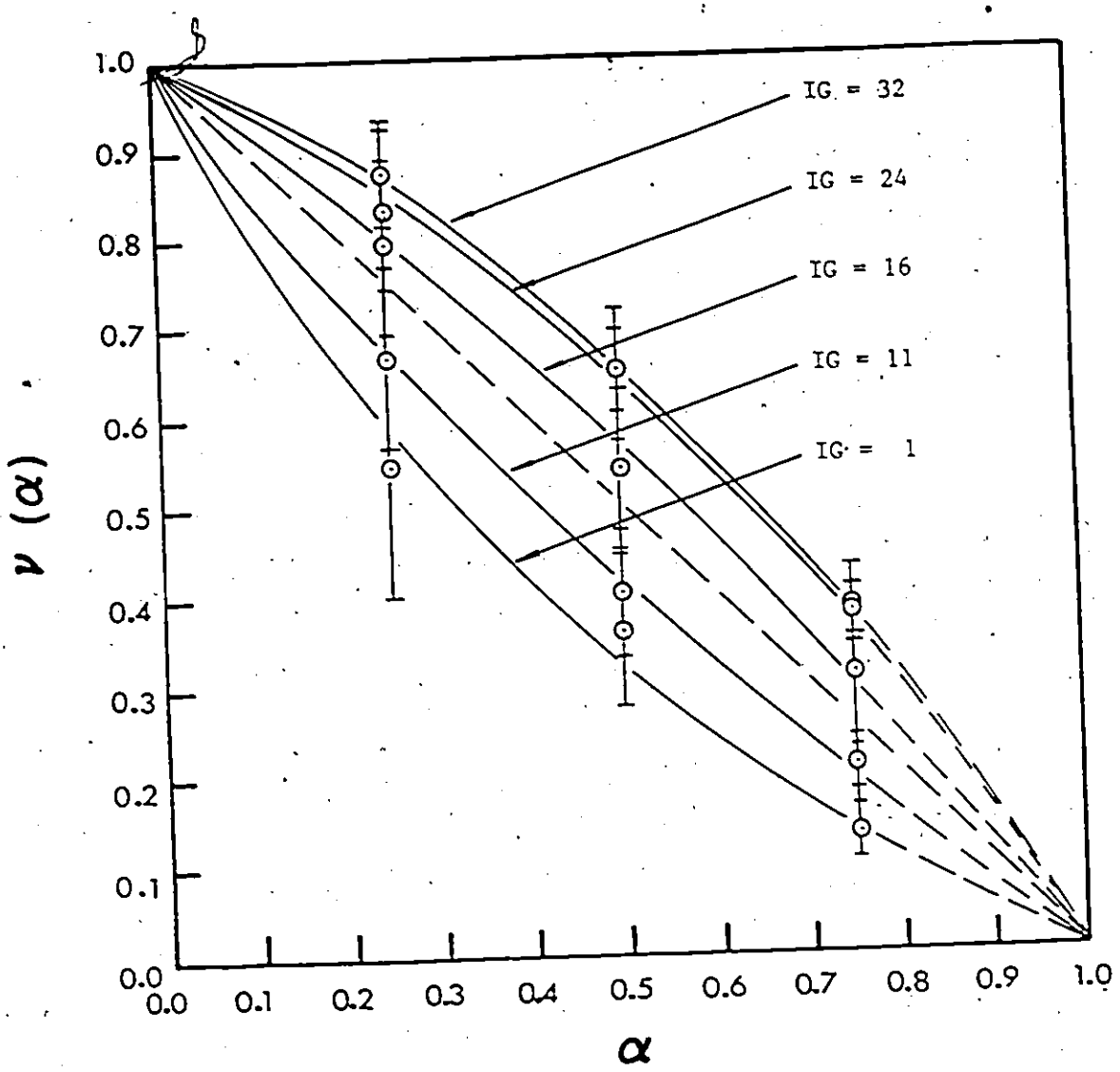

Figure 5.13 Normalized $\Phi_{33}(\alpha)$, $\nu(\alpha)$, for inverted annular flow pattern in in test section III

increases, $\nu(\alpha)$ starts to fall below that for inverted annular flow. In other words, it seems that $\nu(\alpha)$ for inverted annular flow, being non-linear in general, are closer to the $(1-\alpha)$ line than annular flow.

5.2.2.2 Trends observed for 127 mm test section

Let us now consider the 127 mm test section. All four trends observed in the 51 mm are also observed here (see Figure 5.7-5.11). However, an additional trend is observed as the following.

T5 For a test section of larger diameter, $\nu(\alpha)$ for a given input neutron energy seems to be higher than that for a smaller test section; there is an upward shift in $\nu(\alpha)$ when the test section diameter increases (compare Figures 5.12, 13 and Figures 5.5, 6).

The above five observed trends will be useful in the explanation of the hypothesis formed. This will be postponed till later, however. First, we shall try to interpret these observed trends.

5.2.3 Interpretation of trends observed in the Monte Carlo Study

To interpret the Monte Carlo results, the problem is viewed from a different angle. If we use an imaginary surface detector which completely surrounds the test section (including top and bottom of the test section) the subcadmium neutron counting rate will be proportional to the probability of a monoenergetic input neutron being thermalized (becoming a subcadmium neutron) by the test section. The response of this

surface detector will not be the same as a real detector (or the point detector in the Monte Carlo "numerical experiments") because it does not take into account the distance between the collision sites and the detector. However, the trend obtained should be similar to that of a real detector (ignoring escape of neutrons from the top and the bottom of the test section).

The thermalization probability $P_T(\alpha)$ of an input neutron in the beam is the product of two probabilities, $P_c(\alpha)$ and $P_s(\alpha)$. The probability $P_c(\alpha)$, the first collision probability, is that an input neutron of initial energy E_0 will make a first collision anywhere inside the test section of α. The probability $P_s(\alpha)$, the subsequent thermalization probability, is that the neutron, having made the first collision, will subsequently be thermalized when it leaves the test section (by suffering more collisions). We shall consider these two probabilities separately for the 51 mm test section.

5.2.3.1 First collision probability $P_c(\alpha)$ for 51 mm test section

Consider the Monte Carlo results for the 51 mm test section. The first collision probability $P_c(\alpha)$ for each input neutron energy group was evaluated. This probability could have been easily evaluated by integrating the flux of unattenuated neutrons across the beam width by assuming exponential attenuation, normalizing this integral by the beam flux, and subtracting the normalized integral from 1. However, in the Monte Carlo simulations, a beam sink of differential height has been assigned to count the number of uncollided input neutrons. The probability $P_c(\alpha)$ was thus evaluated using this information.

The results are shown in Figure 5.14-5.17. From these four figures, the following observations are made.

(1) $P_c(\alpha)$ for annular flow is always greater than that for inverted annular flow.

(2) $P_c(\alpha)$ for both flow patterns and for all energy groups, curves above the linear line joining $P_c(0)$ and $P_c(1)$.

(3) $P_c(\alpha)$ decreases as the input neutron energy increases, and at high input neutron energy, e.g. IG=7, $P_c(\alpha)$ for both flow patterns is close to being linear with α.

From these observations, if the subsequent thermalization probability $P_s(\alpha)$ is 1 or constant, the $P_T(\alpha)$ will be proportional to $P_c(\alpha)$, leading to a result contrary to observed trends in the Monte Carlo study (i.e. no curving below the linear line joining $P_T(0)$ and $P_T(1)$ for any input neutron group). Let us now consider $P_s(\alpha)$.

5.2.3.2 Subsequent thermalization probability $P_s(\alpha)$

In principle, a neutron, independent of its initial energy E_0, can be thermalized in a single collision. However, the probability of this happening is small in general. In our case, an input neutron probably needs a number of collisions inside the test section to become subcadmium (thermalized), dependent on its initial energy E_0. An equation has been derived <Appendix D> relating the probability $P_j(E_0)$ that a neutron will become subcadmium in exactly j collisions in the test section. This equation is

$$P_j(E_0) = \frac{E_c}{E_0} \frac{\ell n(E_0/E_c)^{j-1}}{(j-1)!} \qquad (5.1)$$

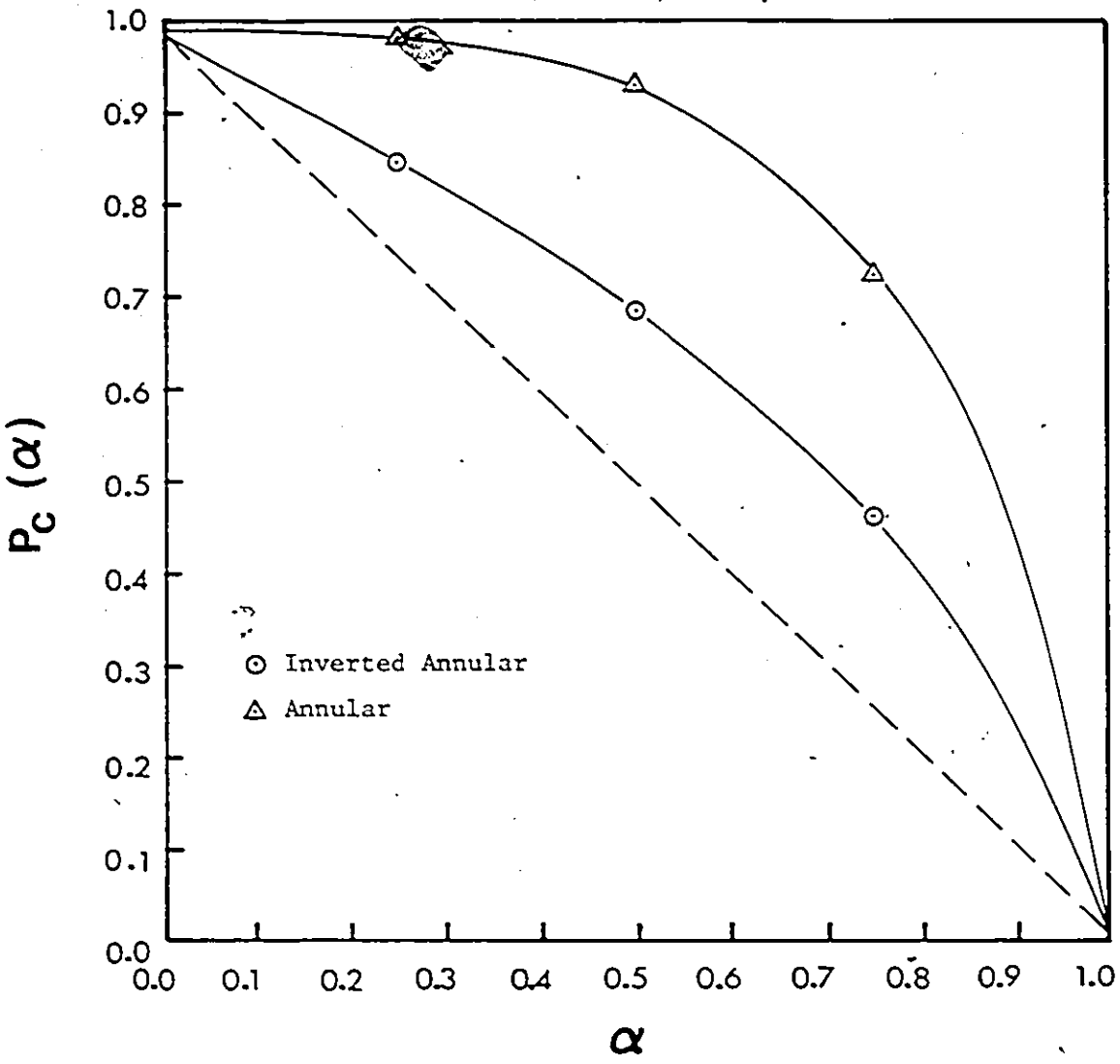

Figure 5.14 First collision probability, $P_c(\alpha)$, for Group 32 incident neutrons in test section I

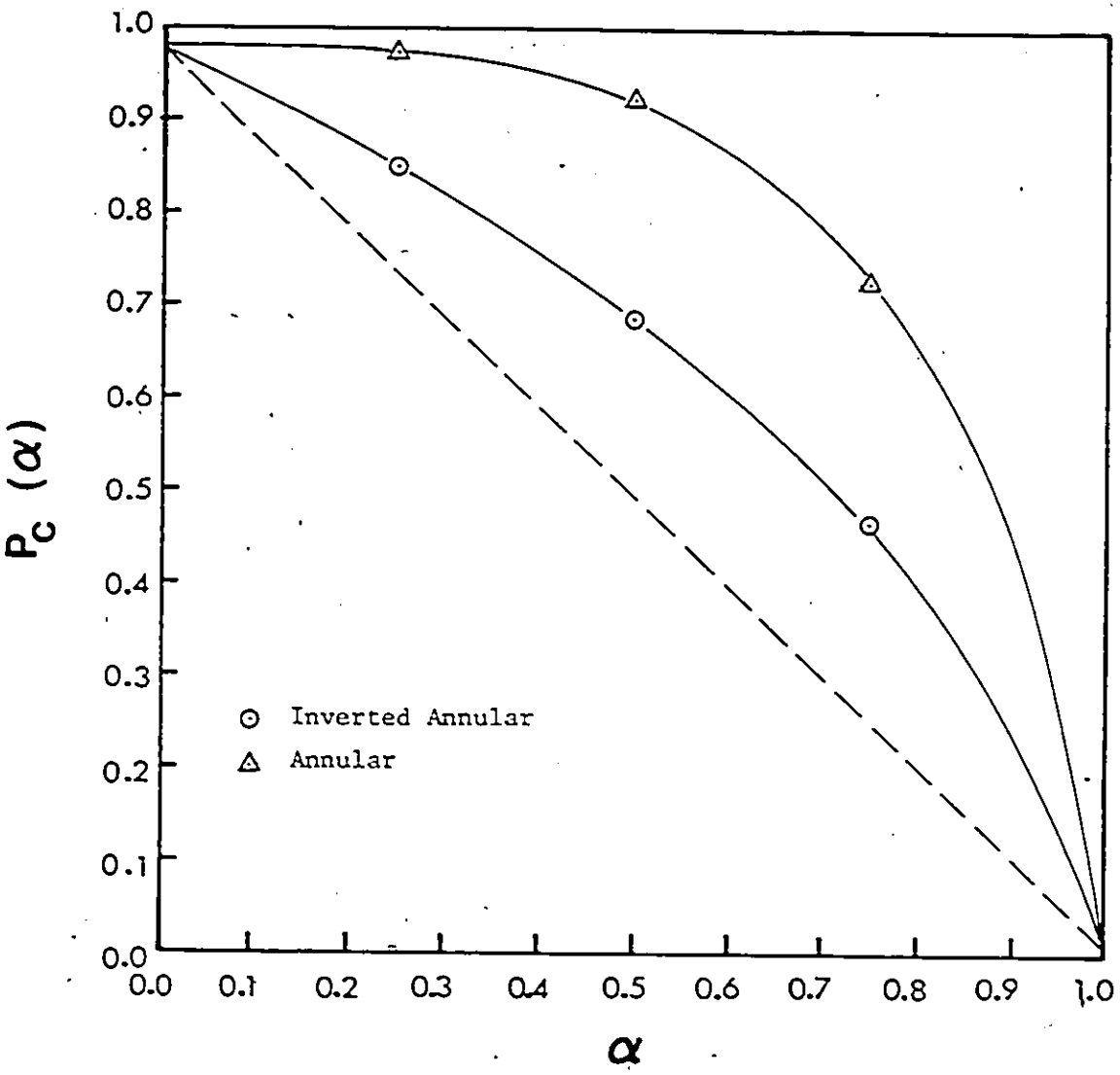

Figure 5.15 First collision probability, $P_c(\alpha)$, for Group 24 incident neutrons in test section I

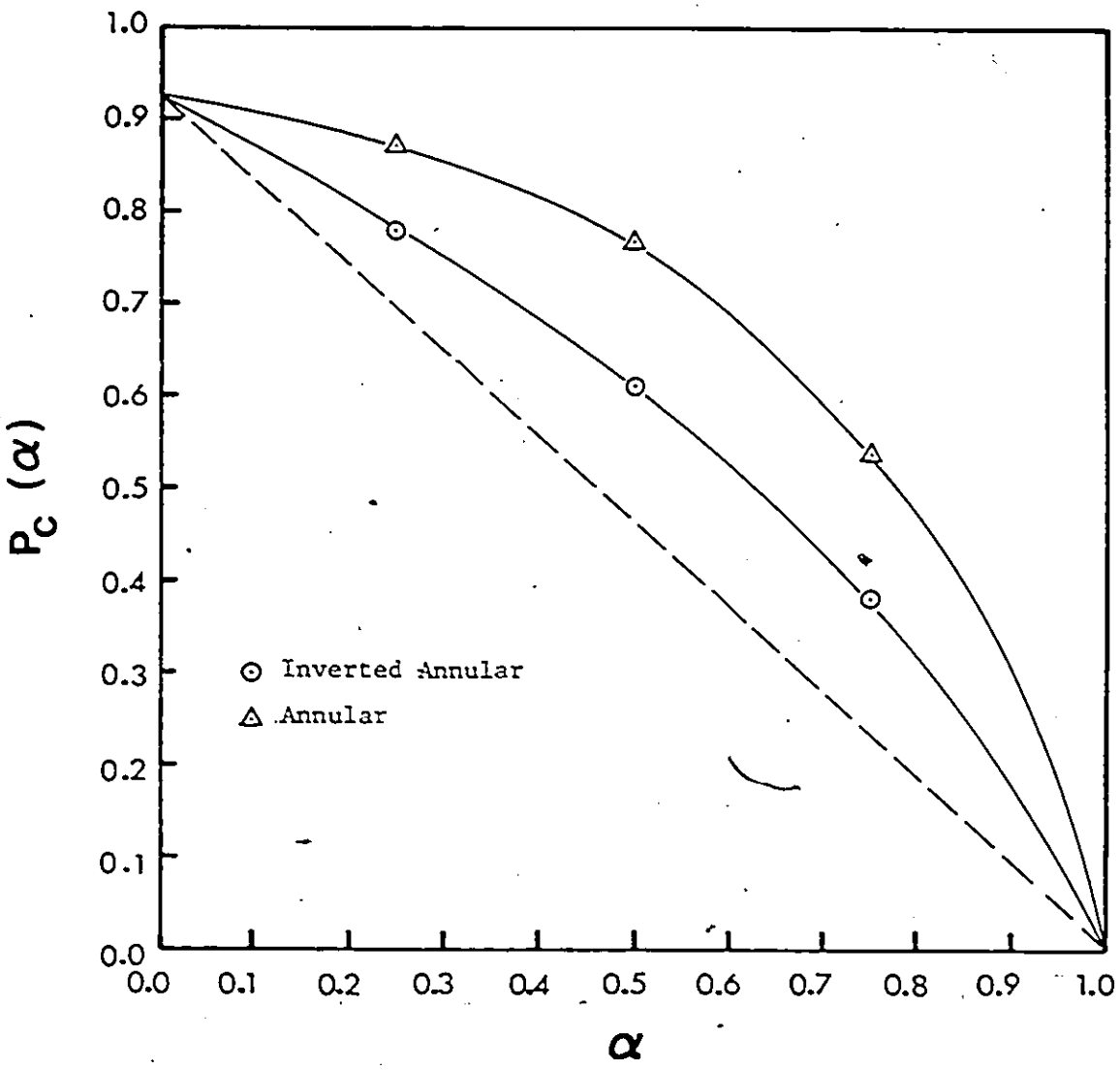

Figure 5.16 First collision probability, $P_c(\alpha)$, for Group 15 incident neutrons in test section I

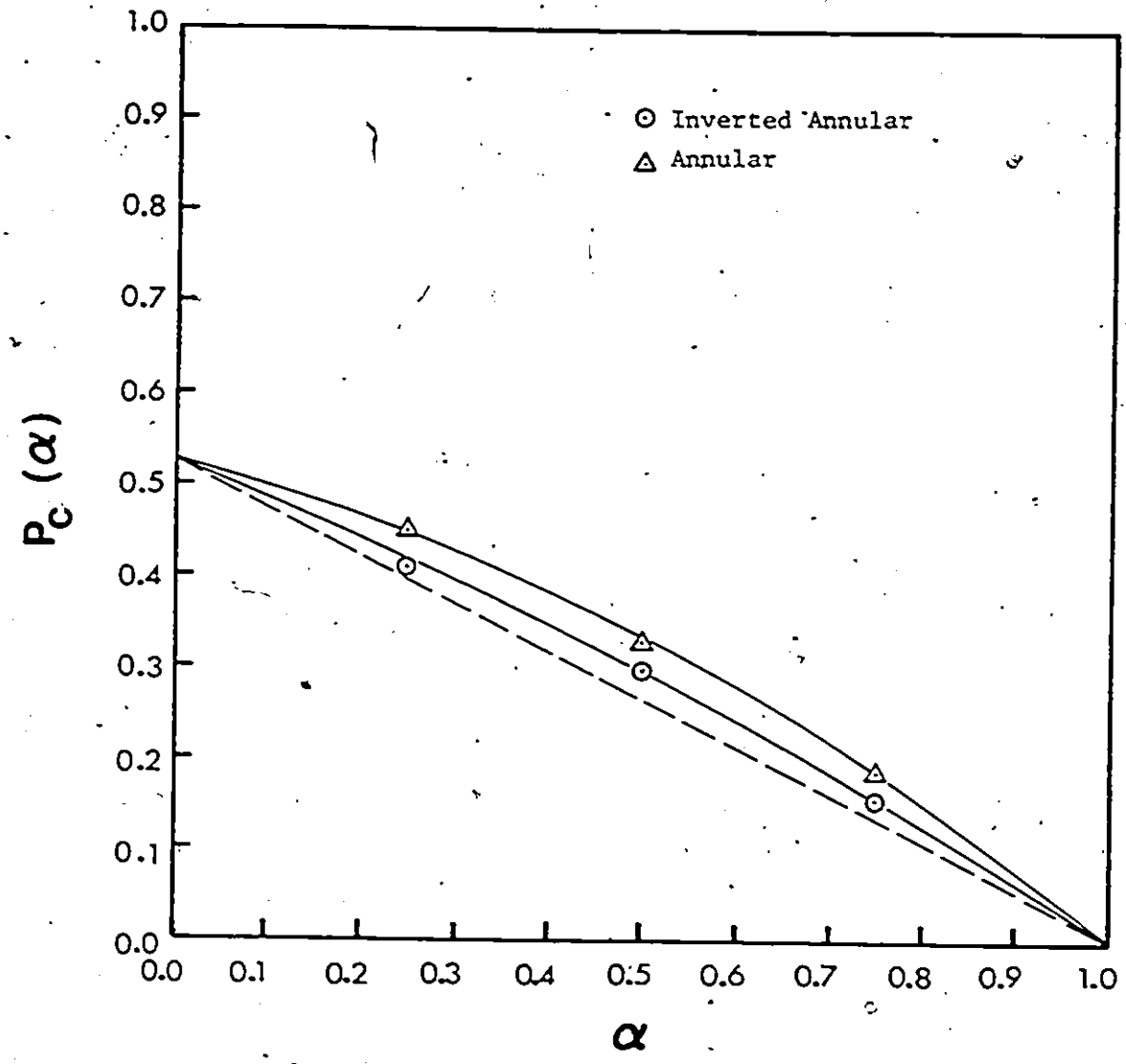

Figure 5.17 First collision probability, $P_c(\alpha)$, for Group 7 incident neutrons in test section I

where E_c = subcadmium neutron energy (0.41 eV)

The shapes of this probability distribution for two energies E_0 (1.125 and 2×10^6 eV) are shown in Figure 5.18 and 5.19. From these two figures, one can see that P_j peaks at a low number of collisions for low E_0 and at a high number of collisions for high E_0, which agrees with physical intuition.

From Eq.(5.1), one can determine the cumulative probability that a neutron with intial energy E_0 will reach subcadmium energy after suffering n or a lesser number of collisions. This cumulative probability P_n is

$$P_n(E_0) = \sum_{j=1}^{n} P_j(E_0) \qquad (5.2)$$

This cumulative probability $P_n(E_0)$ is just the $P_s(\alpha)$ that we are after (provided we know the number of collisions the neutron has suffered when it leaves the test section)

The cumulative probabilities $P_n(E_0)$ have been evaluated according to Eqs.(5.1) and (5.2) for a number of E_0 in energy groups used in the MORSE code. The results are shown in Figure 5.20.

Using Figure 5.20, one could evaluate $P_s(\alpha)$ if the number of collisions an input neutron suffers in a test section before escaping is known. However, the analytical development of this relationship is beyond the scope of the present work. Instead, the average number of collisions n (including the 1st collision and those made in the albedo region) obtained in the

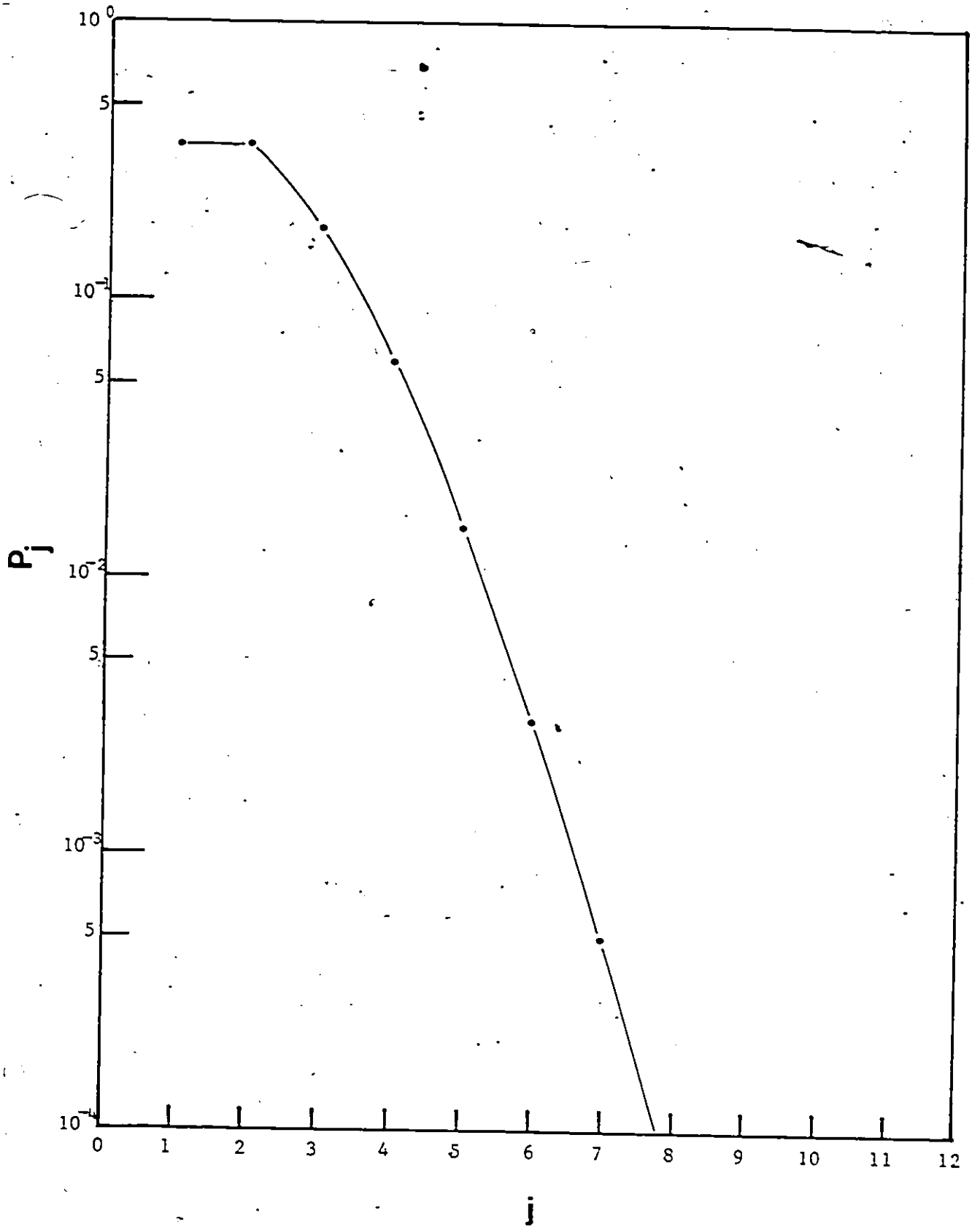

Figure 5.18 Distribution of probability of thermalization, $P_j(E_0)$, in exactly j collisions for incident neutron energy E_0 = 1.25 eV

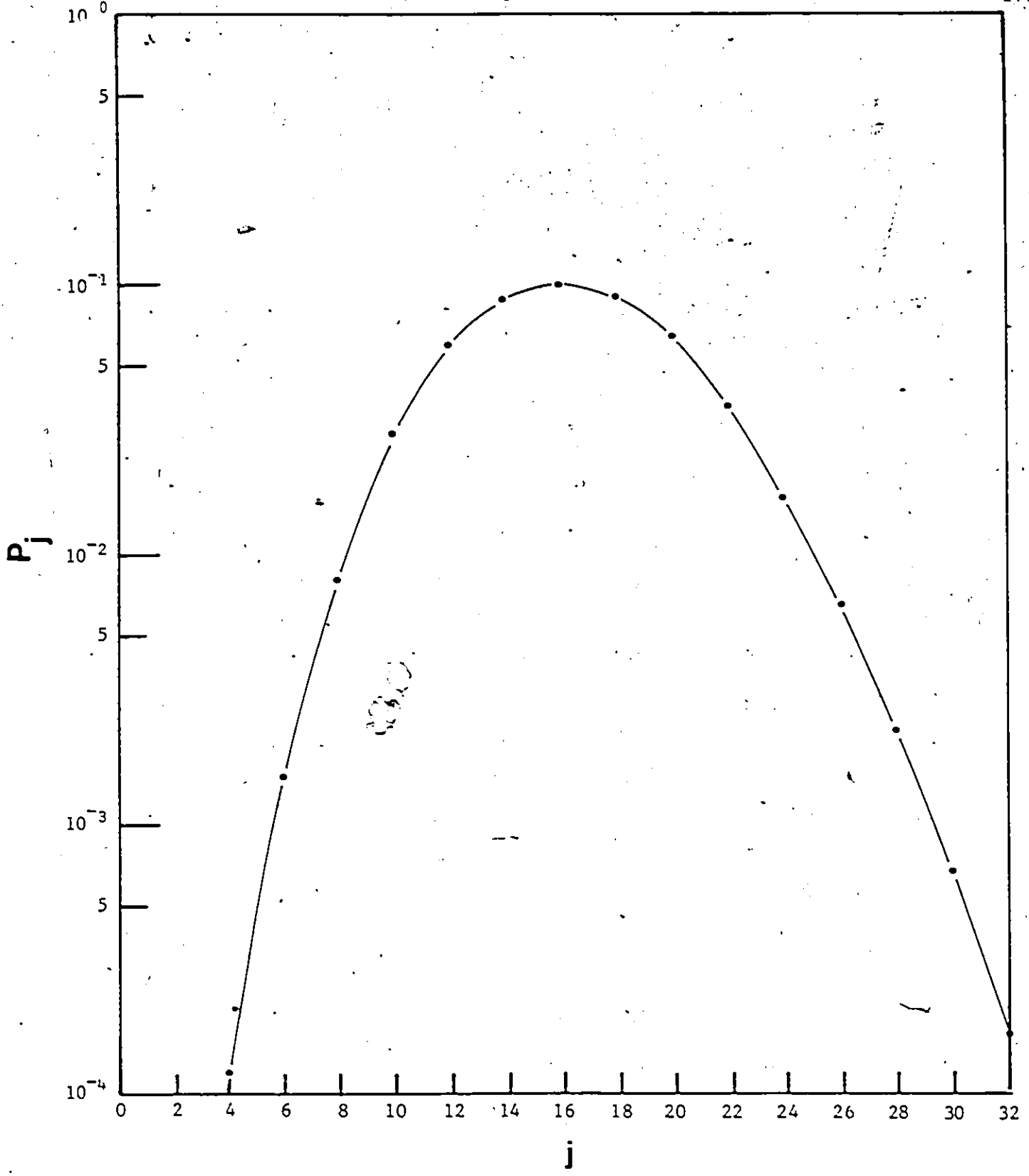

Figure 5.19 Distribution of thermalization probability, $P_j(E_0)$, in exactly j collisions for incident neutron energy $E_0 = 2 \times 10^6$ eV

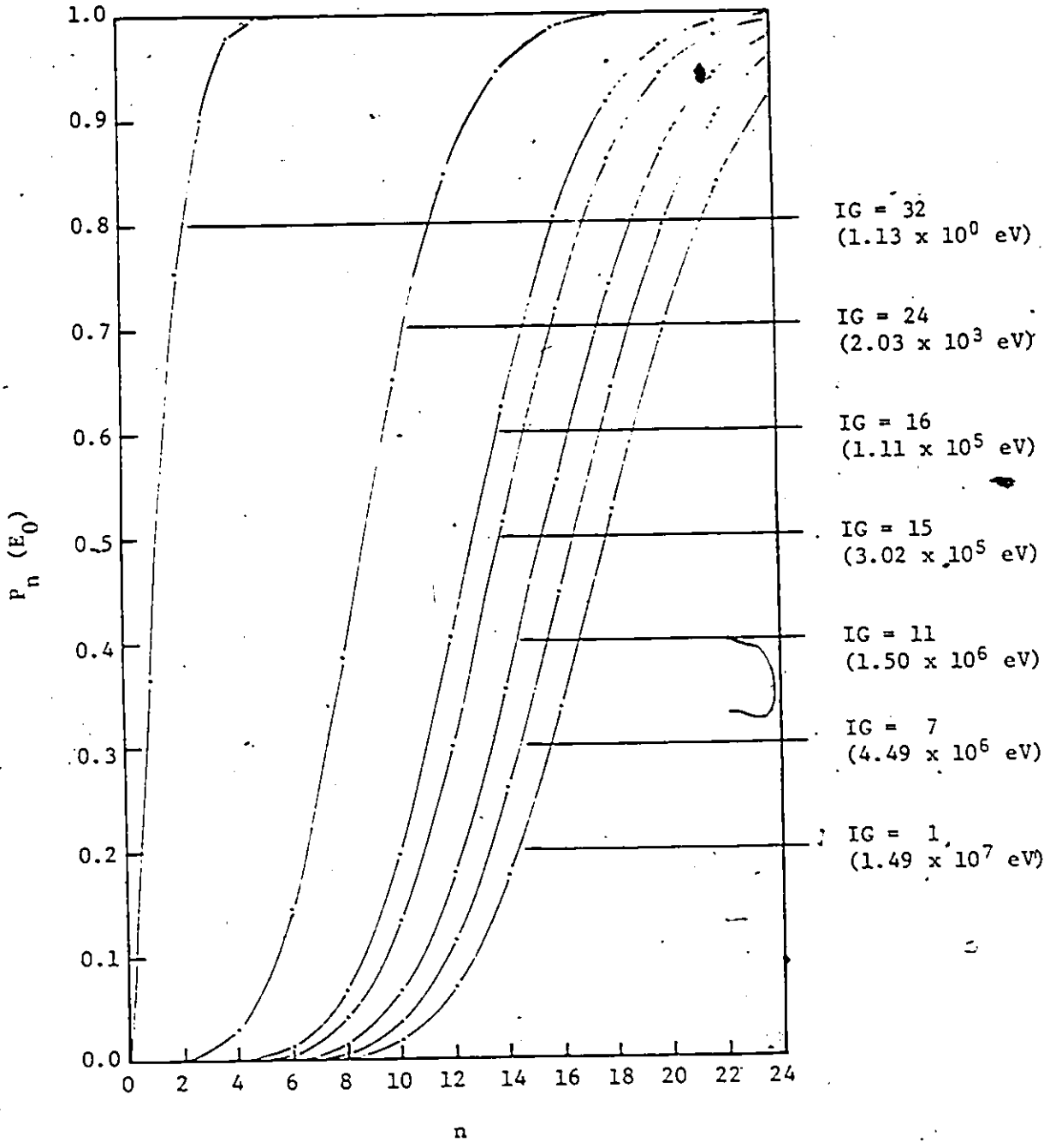

Figure 5.20 Cumulative probability $P_n(E_0)$

Monte Carlo simulation runs was used to evaluate $P_s(\alpha)$. The average number of collision and $P_s(\alpha)$ are tabulated in Table 5.3. The $P_s(\alpha)$ so evaluated are shown in Figure 5.21.

With $P_c(\alpha)$, $P_n(E_0)$, and $P_s(\alpha)$ evaluated, we are ready to interpret the trends observed in $\phi_{33}(\alpha)$.

5.2.3.3 Interpretation

We shall interpret the observed trends T1-T5 (see section 5.2.2) one by one.

Trend T1

The amount of water decreases with α. Hence the average number of collisions n decreases resulting in a decreasing $P_s(\alpha)$ for each input neutron energy group. The $P_c(\alpha)$ are all decreasing functions of α (see Figures 5.14-5.17). The $P_T(\alpha)$ is thus expected to decrease with α.

Trend T2

For a given flow pattern and constant α, it is intuitively clear that n decreases with E_0 because of the longer mean free path between collisions for a higher E_0. For a small test section, it is unlikely that n is sufficiently high to allow $P_n(E_0)$ to saturate at close to 1 (see $P_n(E_0)$ in Figure 5.20). This results in a decreasing $P_s(\alpha)$ when E_0 increases. The $P_c(\alpha)$, as observed from Figure 5.14-5.17, also decreases with E_0. This is readily understandable since the mean free path increases with E_0. Thus $P_T(\alpha)$ decreases with E_0.

Trend T3

The $P_c(\alpha)$ curve above the linear line joining $P_c(0)$ and

TABLE 5.3

$P_c(\alpha)$, n, and $P_s(\alpha)$ for 51 mm Test Section I

IG	Flow Pattern	α	Average # Collisions, n	$P_c(\alpha)$	$P_s(\alpha)$	$P_T(\alpha)$
7	Inverted Annular	0.0	12.9	0.53	0.17	0.090
	"	0.25	12.1	0.41	0.12	0.049
	"	0.50	11.0	0.30	0.07	0.021
	"	0.75	10.1	0.16	0.04	0.007
	Annular	0.25	11.2	0.45	0.08	0.037
	"	0.50	9.6	0.33	0.03	0.010
	"	0.75	9.2	0.19	0.02	0.004
15	Inverted Annular	0.0	14.2	0.93	0.54	0.501
	"	0.25	12.8	0.78	0.39	0.301
	"	0.50	11.9	0.61	0.29	0.177
	"	0.75	10.3	0.38	0.15	0.057
	Annular	0.25	11.5	0.87	0.25	0.218
	"	0.50	9.7	0.76	0.12	0.088
	"	0.75	8.4	0.54	0.06	0.030
24	Inverted Annular	0.0	13.1	0.98	0.91	0.891
	"	0.25	12.5	0.85	0.88	0.745
	"	0.50	11.4	0.68	0.80	0.546
	"	0.75	9.7	0.46	0.62	0.285
	Annular	0.25	10.5	0.98	0.71	0.692
	"	0.50	9.1	0.93	0.53	0.491
	"	0.75	7.7	0.73	0.35	0.251
32	Inverted Annular	0.0	8.5	0.99	1.0	0.986
	"	0.25	8.0	0.84	1.0	0.844
	"	0.50	7.0	0.68	1.0	0.681
	"	0.75	5.5	0.46	1.0	0.459
	Annular	0.25	6.4	0.92	1.0	0.982
	"	0.50	4.4	0.93	0.99	0.923
	"	0.75	3.1	0.73	0.92	0.664

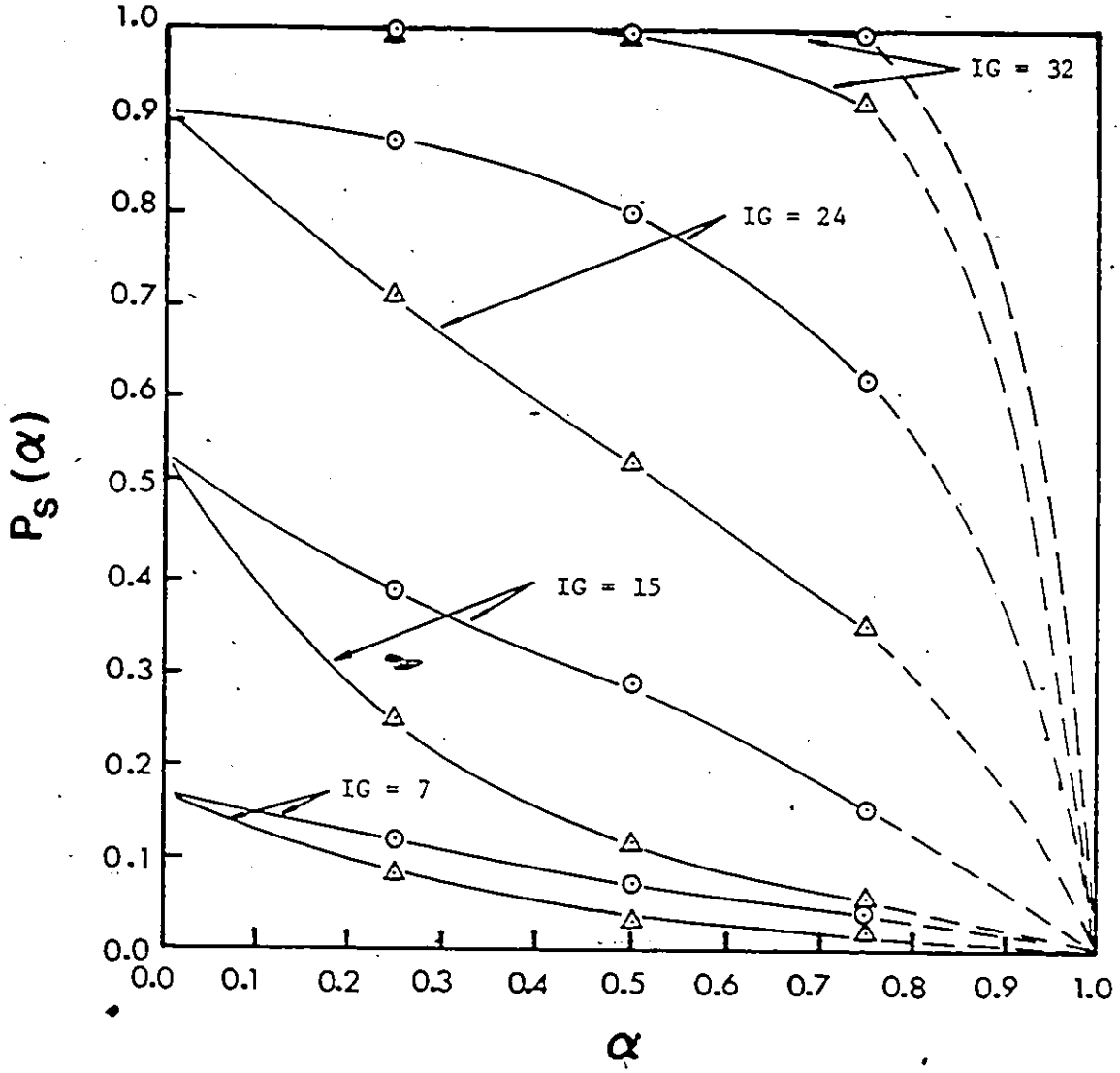

Figure 5.21 Subsequent thermalization probability, $P_S(\alpha)$, of incident neutrons of various E_0 in test section I

$P_c(1)$ for all E_0 (see Figures 5.11-5.15). However, at very high E_0, $P_c(\alpha)$ is close to linear. This near-linearity is caused by the long mean free path for high energy input neutrons.

For very low E_0, e.g. IG=32, due to the short mean free path, n will be sufficiently high for a wide range of α so that $P_s(\alpha)$ is easily saturated close to 1 (see Figure 5.20). Thus $P_T(\alpha)$ follows the same shape of $P_c(\alpha)$, and "bulges" (curving above the linear line joining the end points α=0 and 1)

As E_0 increases, $P_s(\alpha)$ is expected not to saturate at 1 but decreases more rapidly with α because n for different α's are not sufficiently high. Also, $P_s(\alpha)$ bulges less. Thus, $P_T(\alpha)$, a product of $P_c(\alpha)$ and $P_s(\alpha)$ will then "bulge" even less than $P_c(\alpha)$.

The "relaxation" of "bulging" continues. At very high E_0, e.g. IG=7, $P_c(\alpha)$ is near linear. Compounding this with $P_s(\alpha)$ which decreases with α, $P_T(\alpha)$ must "sag" (curving below the ideal linear line between end points α=0 and 1).

Thus the trend T3 that $\phi_{33}(\alpha)$ may curve both above and below linearity line, dependent on E_0 is understood.

Trend T4

Trend T4 can be understood by considering the trends of $P_c(\alpha)$ and $P_s(\alpha)$. From Figures 5.14-5.17, $P_c(\alpha)$ for annular flow lies above that for inverted flow for all energies E_0. However, the trend for $P_s(\alpha)$ is reversed, i.e. $P_s(\alpha)$ for annular flow always lies below that for inverted annular flow. The reversed trend can be explained by the geometry of the two flow patterns. The water phase for an annular flow pattern is concentrated near

the wall of a test section. As a result, the surface to volume ratio of the liquid phase is always higher in annular than inverted annular flow for any given α (see Appendix E). It is therefore easier for a neutron to escape or leak from the test section in annular than inverted annular flow, resulting in a smaller $P_s(\alpha)$.

For very low energy E_0, however, in spite of a smaller number of collisions suffered in annular flow, $P_s(\alpha)$ for both annular and inverted annular flow were close to 1 because the number of collisions required to thermalize is small. $P_T(\alpha)$ is then strictly dominated by $P_c(\alpha)$, resulting in $P_T(\alpha)$ for annular flow higher than in inverted annular flow. However, as the energy E_0 increases, $P_c(\alpha)$ for annular flow exceeds that for inverted annular flow by a smaller amount. At the same time, the effect of a lower $P_s(\alpha)$ for annular flow begins to show up, pulling $P_T(\alpha)$ below that for inverted annular flow.

Trend T5

For a test section of larger diameter, at a given α, the physical amount of water increases. Thus $P_c(\alpha)$ and $P_s(\alpha)$ are both expected to rise. However, $P_c(0)$ and $P_s(0)$ are limited to 1 for all E_0, i.e., $P_c(\alpha)$ and $P_s(\alpha)$ will rise more rapidly than $P_c(0)$ and $P_s(0)$ when the diameter of the test section increases. As a result $\nu(\alpha)$, gauging the deviation from linearity, shifts upwards.

The understanding of the five trends T1-T5 observed in $\phi_{33}(\alpha)$ for the two test sections is now considered complete. Moreover, some additional information on the effect of the

neutron reflector material can be extracted from the neutron thermalization model.

Effect of neutron reflector (albedo)

Consider input neutron energy groups 32 and 24. The total cross-section for these two groups are very close (Σ_t constant up to 3×10^3 eV). The random walk of a neutron in the test section should be very similar to yield the same average number of collisions n. However, from Table 5.3, n for Group 24 is almost twice as large as for Group 32. The discrepancy must be due to the neutron reflector. A Group 32 neutron needs a small number of collisions to become subcadmium. When this neutron leaves the test section, it is probably thermalized, and when it hits the albedo wall, it is absorbed by the cadmium sheet lining the albedo wall. However, for the same n, owing to its much higher E_0, a Group 24 neutron may leave the test section without being thermalized. When it hits the neutron reflector, it is returned with its energy reduced. If the energy of the returned neutron is still above the cadmium cut-off energy, it is sent back to the test section and forced to suffer further collisions, increasing its probability of thermalization. Similar to arguments given to the understanding of trend T5, $\nu(\alpha)$ will be shifted upwards. This trend has already been observed in the experiment conducted (Expt #8)

To complete the interpretation of the trends observed for $\phi_{33}(\alpha)$, it is interesting to compare $P_T(\alpha)$ and $\phi_{33}(\alpha)$ directly.

Comparison between $P_T(\alpha)$ and $\phi_{33}(\alpha)$

It is sufficient to compare $P_T(\alpha)$ and $\phi_{33}(\alpha)$ for the 51 mm test section. The thermalization probability $P_T(\alpha)$ was evaluated for all the four groups of input neutron energies by multiplying $P_c(\alpha)$ and $P_s(\alpha)$. The results are shown in Figure 5.22-5.25. Comparing these four figures with those for $\phi_{33}(\alpha)$ (Figures 5.1-5.4), it is evident that $P_T(\alpha)$ shows all similar trends observed for $\phi_{33}(\alpha)$.

Having understood the trends for $\phi_{33}(\alpha)$, we shall now attempt to explain the hypothesis.

5.3. INTERPRETATION OF HYPOTHESIS

With the five trends T1-T5 observed in the Monte Carlo study, attempts are made to interpret the hypothesis.

5.3.1 Requirement of Appropriate Input Neutron Energy Spectrum or Moderator Diameter for Linearity

For arguments, we shall consider the simplest system consisting of two groups of input neutron energies 1 and 2, with group 2 very much lower in energy than group 1. Suppose, for a small test section, e.g. 51 mm in diameter, the subcadmium neutron flux at a detector $\phi^1_{33}(\alpha)$ and $\phi^2_{33}(\alpha)$ for Groups 1 and 2 respectively are as shown in Figure 5.26. The $\phi_{33}(\alpha)$ for these two groups show all the 4 trends T1-T4. The $\phi_{33}(\alpha)$ are flow pattern dependent and non-linear, but decrease with α. The magnitude of $\phi_{33}(\alpha)$ decreases with input neutron energy E_0. For low E_0 (Group 2), $\phi^2_{33}(\alpha)$ "bulges" above the linear line for both flow patterns but $\phi^1_{33}(\alpha)$ "sags" for high E_0 (Group 1). For low E_0 (Group 2), $\phi^2_{33}(\alpha)$ for annular flow is higher than $\phi^1_{33}(\alpha)$ for

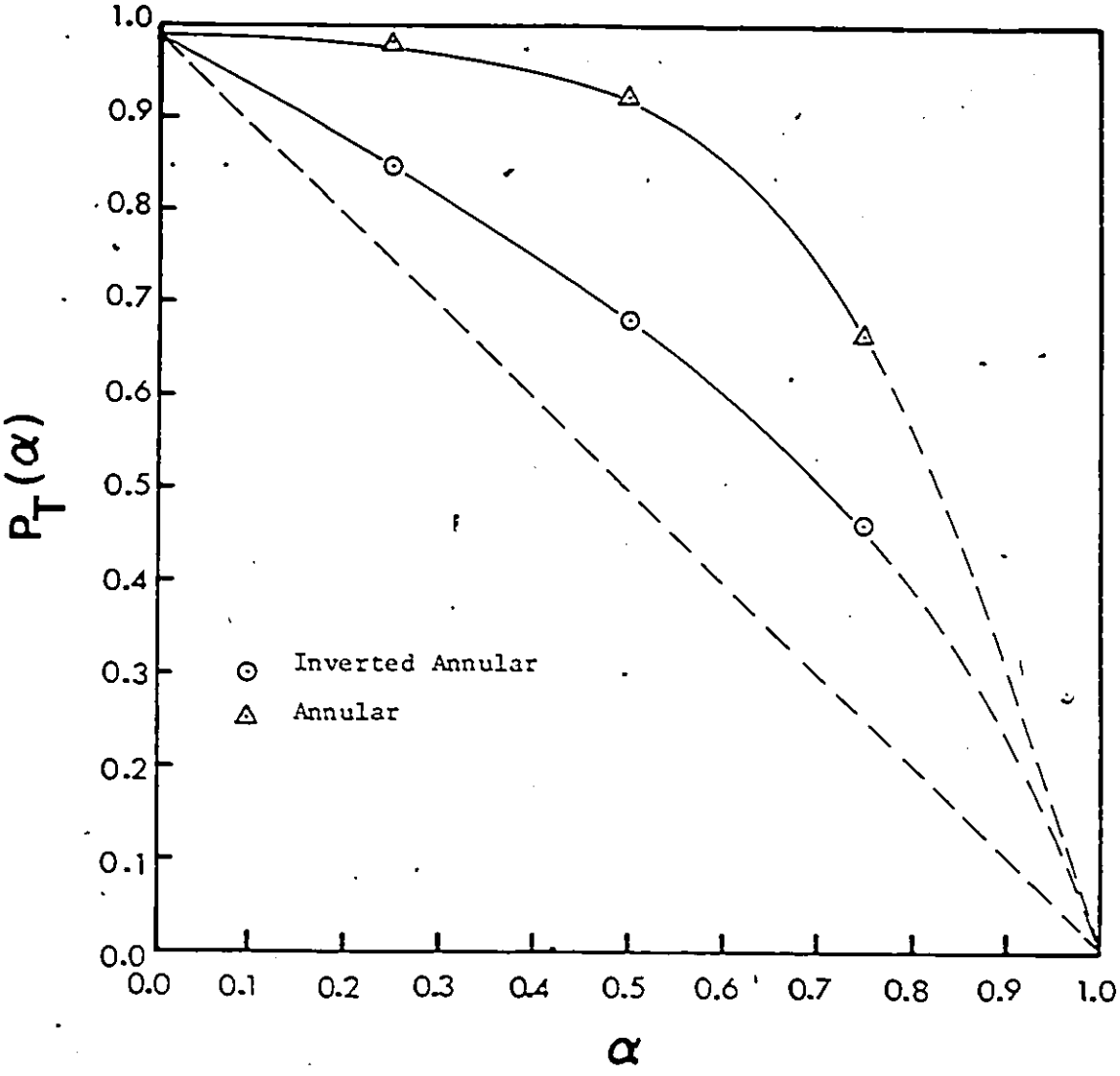

Figure 5.22 Thermalization probability, $P_T(\alpha)$, of Group 32 incident neutrons in test section I

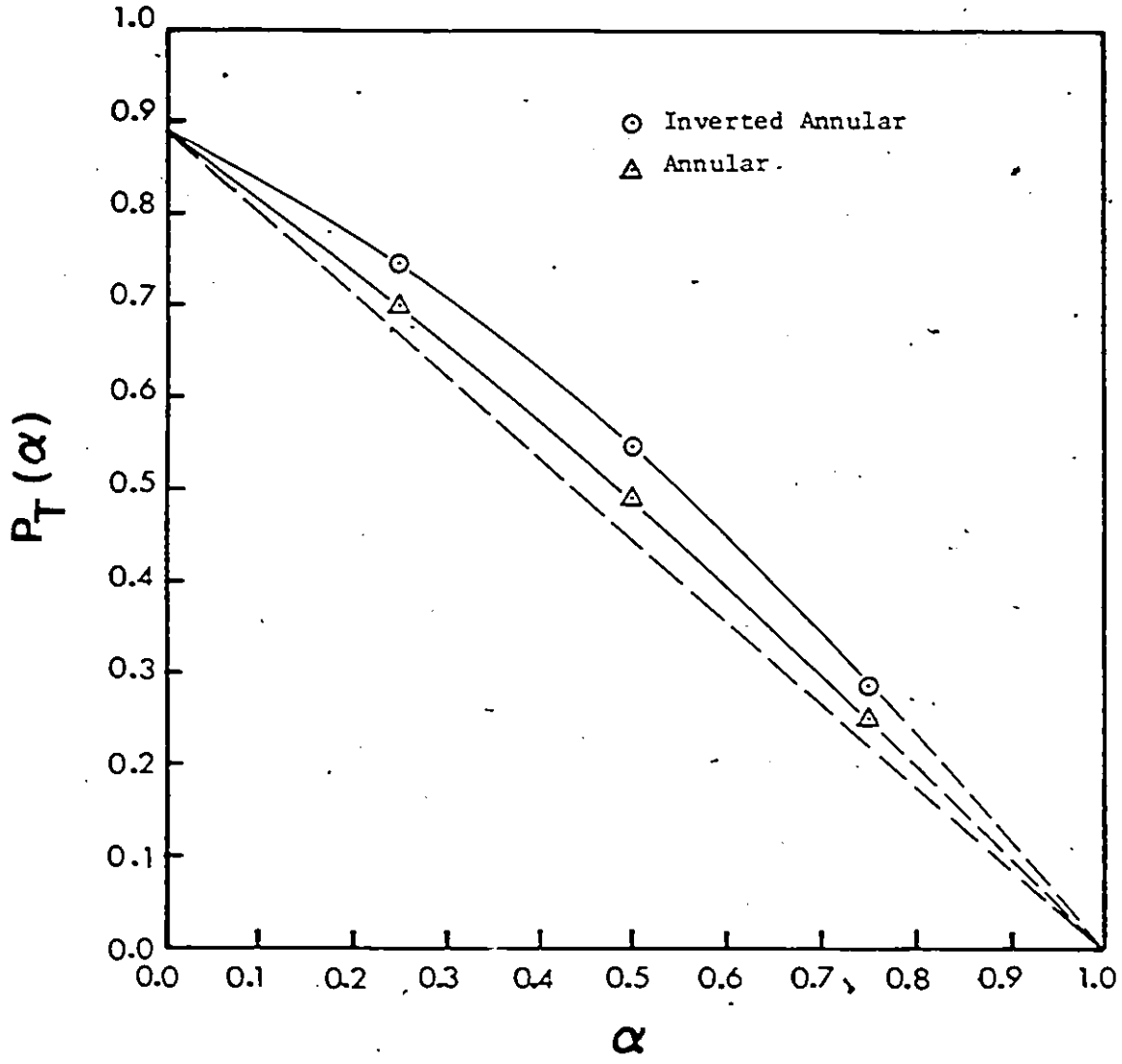

Figure 5.23 Thermalization probability, $P_T(\alpha)$, of Group 24 incident neutrons in test section I

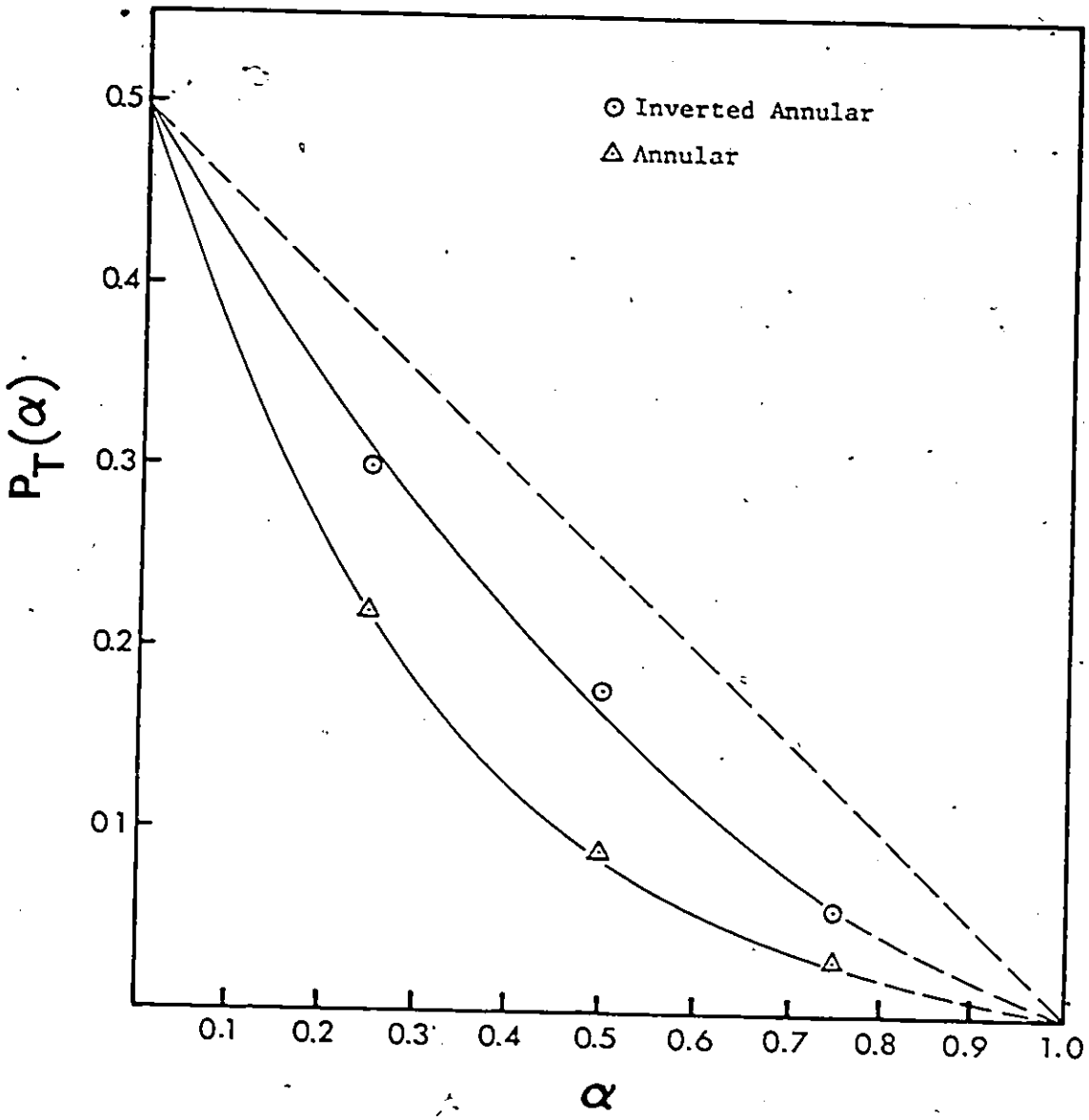

Figure 5.24 Thermalization probability, $P_T(\alpha)$, of Group 15 incident neutrons in test section I

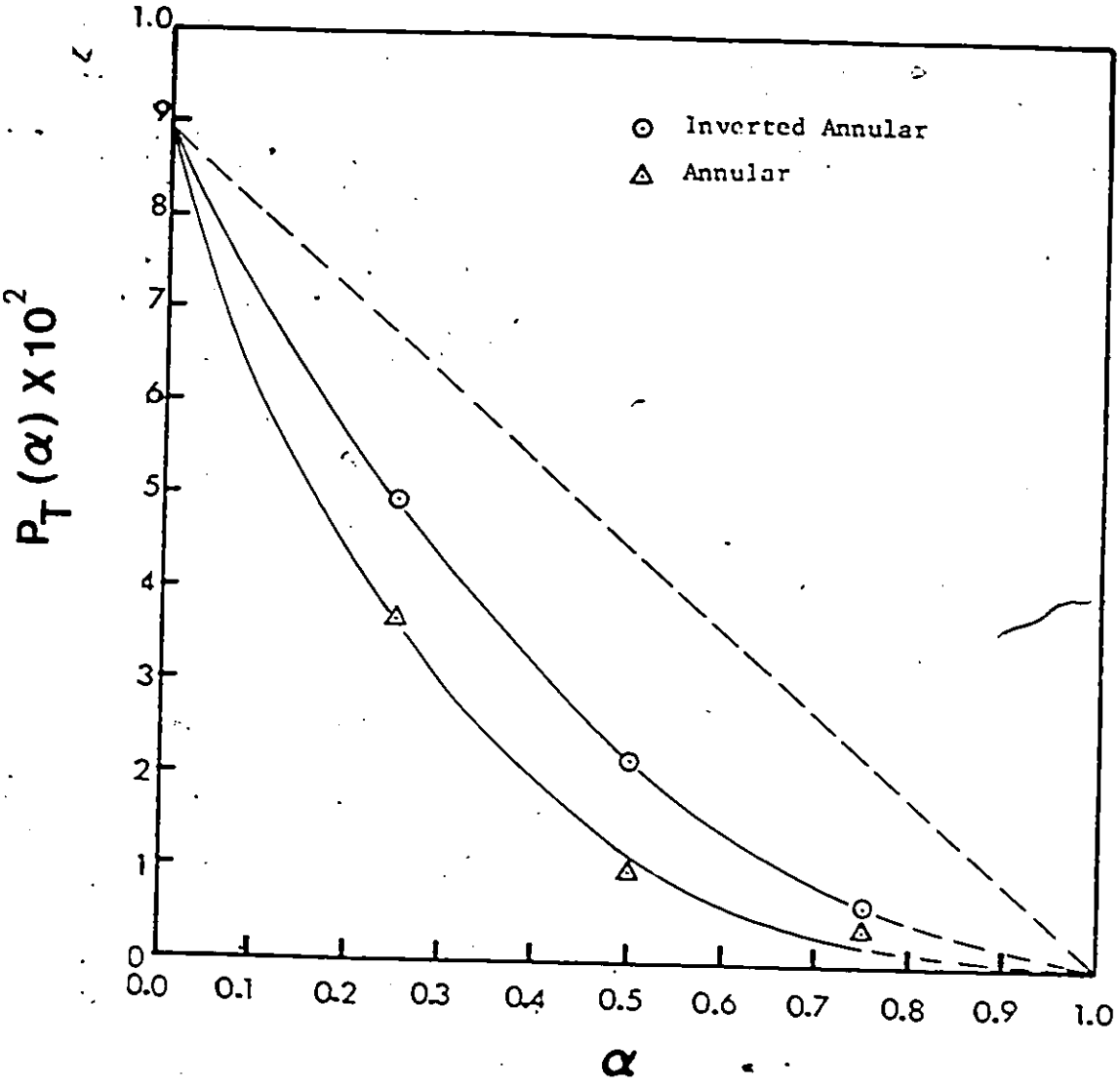

Figure 5.25 Thermalization probability, $P_T(\alpha)$, of Group 7 incident neutrons in test section 1

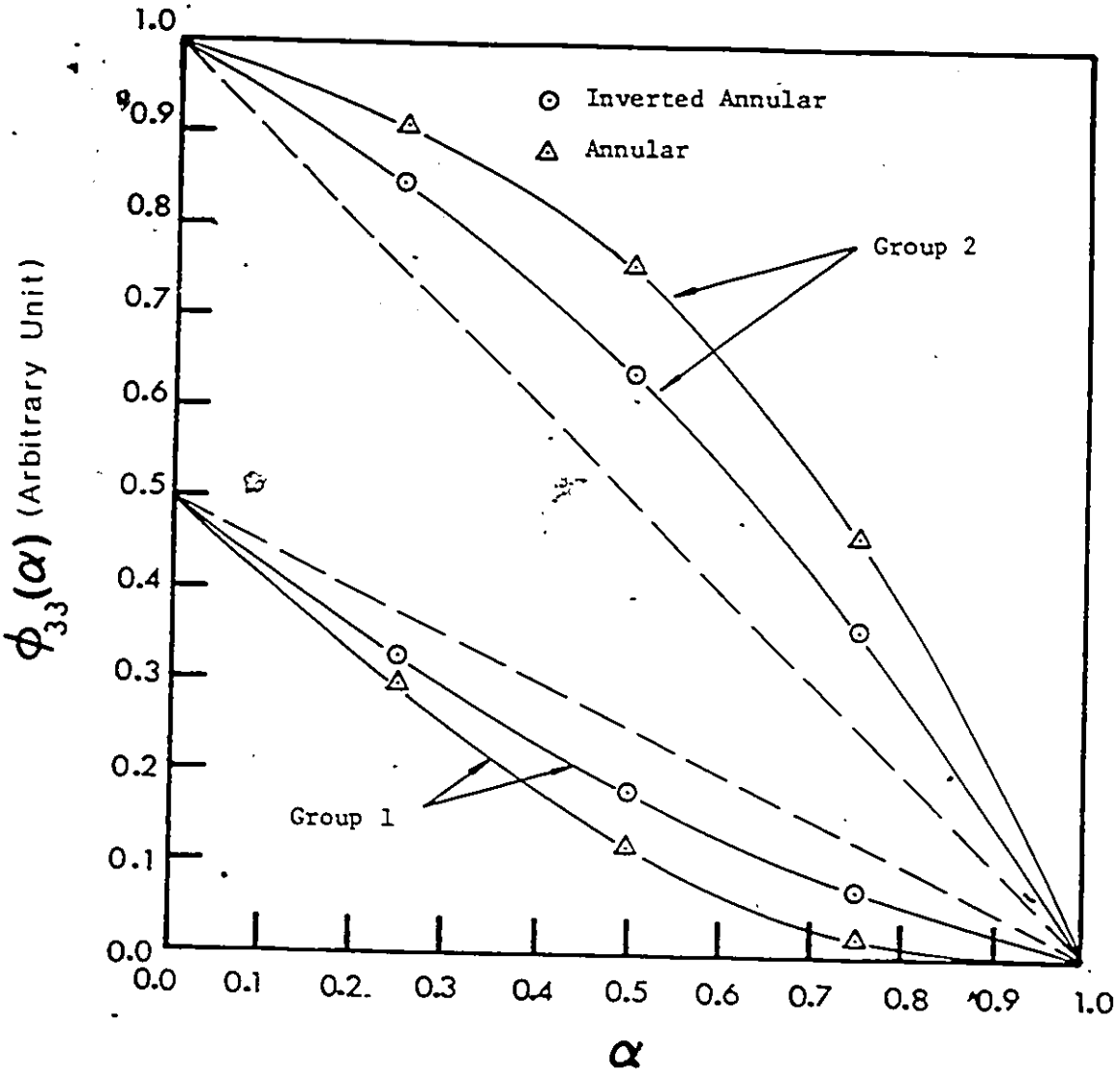

Figure 5.26 Arbitrary $\phi_{33}(\alpha)$ for two arbitrary groups of incident neutron energies, showing characteristic trends T1 - T4 observed in the group by group Monte Carlo study

inverted annular flow and the trend is reversed for high E_0 (Group 1). Before pursuing further discussions, we shall define some terms for later discussions. First, since it is the subcadmium neutron flux $\phi_{33}(\alpha)$ that we are discussing, we shall drop the subscript and replace it with the group number, e.g. $\phi_1(\alpha)$ now means $\phi_{33}(\alpha)$ for the group 1 input neutrons. As usual, we shall define a dimensionless neutron flux $\nu_i(\alpha)$ as $\phi_i(\alpha)/\phi_i(0)$ for the i^{th} input neutron group. We shall also define the deviation of $\nu_i(\alpha)$ from linearity, $\delta_i(\alpha)$, as

$$\delta_i(\alpha) = |(\nu_i(\alpha) - (1 - \alpha))| \tag{5.3}$$

With these definitions and those characteristic trends of these two groups, we can proceed to explain the requirement of appropriate input energy spectrum.

Consider an incident neutron beam consisting of the two groups of input neutrons with intensities a_1 and a_2. Consider one flow pattern at a time, e.g. annular flow. Intuitively, because of the "bulging" and "sagging" characteristics of $\phi_2(\alpha)$ and $\phi_1(\alpha)$, the total subcadmium neutron flux $\phi(\alpha)$ for the incident neutron beam can be linear with α upon superposition. However, the condition to achieve linearity in $\phi(\alpha)$ is derived as the following. The $\phi(\alpha)$ is given by

$$\phi(\alpha) = a_1\phi_1(0)\nu_1(\alpha) + a_2\phi_2(0)\nu_2(\alpha) \tag{5.4}$$

The total dimensionless subcadmium neutron flux $\nu(\alpha)$ is

non-linear in general and is given by

$$\nu(\alpha) = \phi(\alpha)/\phi(0)$$

$$= \frac{a_1\phi_1(0)\nu_1(\alpha) + a_2\phi_2(0)\nu_2(\alpha)}{a_1\phi_1(0) + a_2\phi_2(0)} \qquad (5.5)$$

or $$\nu(\alpha) = (1 - \alpha) + \delta(\alpha) \qquad (5.6)$$

In Eq.(5.6), $\delta(\alpha)$ is the deviation from linearity and can assume a positive or negative value.

We shall define a quantity R as

$$R = a_2\phi_2(0)/a_1\phi_1(0) \qquad (5.7)$$

Equating Eq.(5.6) to Eq.(5.5), we have

$$\delta(\alpha) = \frac{R\,\delta_2(\alpha) - \delta_1(\alpha)}{(1 + R)} = \frac{\delta_2(\alpha)[R - \delta_1(\alpha)/\delta_2(\alpha)]}{(1 + R)} \qquad (5.8)$$

Thus, from Eq. (5.8), one can see that if $\nu(\alpha)$ is to be linear, i.e. $\delta(\alpha)=0$,

$$R = \delta_1(\alpha)/\delta_2(\alpha) = a_2\phi_2(0)/a_1\phi_1(0) \qquad (5.9)$$

From Eq.(5.9), if $\delta_1(\alpha)/\delta_2(\alpha)$ is independent of α, there is one ratio a_2/a_1 such that an exact match is achieved to yield linearity throughout the entire range of α. This is the first

indication that a specific energy spectrum is required to achieve linearity, dependent on the deviations from linearity $\delta_i(\alpha)$ and $\phi_i(0)$ of each individual input energy group.

Physically, $\delta_1(\alpha)/\delta_2(\alpha)$ is not likely to be independent of α, requiring a different $R(\alpha)$ for exact match at each value of α. Since only one value of R can be used at a time in an attempt to match $\delta_1(\alpha)$ and $\delta_2(\alpha)$, perfect linearity cannot be achieved. However, if $\delta_1(\alpha)/\delta_2(\alpha)$ is close to 1 everywhere, and a value $R = 1$ is used, from Eq.(5.8),

$$\delta(\alpha) = \frac{R\delta_2(\alpha) - \delta_1(\alpha)}{(1 + R)}$$

$$= \frac{[\delta_2(\alpha) - \delta_1(\alpha)]R}{(1 + R)}$$

$$= [\delta_2(\alpha) - \delta_1(\alpha)]/2$$

$$= 0 \qquad (5.10)$$

Thus, near-linearity can be achieved, with $a_2/a_1 = \phi_1(0)/\phi_2(0)$. The condition that $\delta_1(\alpha)/\delta_2(\alpha) = 1$ simply means that $v_i(\alpha)$ of a very low input energy group ($v_i(\alpha)$ substantially greater than $(1 - \alpha)$) should be matched with that of a very high energy group ($v_i(\alpha)$ substantially less than $(1 - \alpha)$), and not with that of an intermediate energy group which tends to yield $v_i(\alpha)$ closer to being linear. To illustrate the above point, consider an example drawn from Figure 5.12.

Consider Groups IG=32 and 7. The $v_i(\alpha)$ for these two groups are far from linearity. The absolute values of $\delta_i(\alpha)$ with

i=1, 2 (1 for Group 7, and 2 for Group 32) are tabulated in Table 5.4. for α=0.25, 0.50, and 0.75. In the same table, the R required for each α to obtain an exact match is also listed. By examining the list of R's, we cannot say that the two $\delta_i(\alpha)$ curves are exact matches for each other. The R=1.15 required for α=0.50 is close to 1. If we combine the two curves using R=1.15 throughout, by Eq.(5.8), the $\delta(\alpha)$ after superposition, are calculated to be -0.037, 0, and 0.032 for α=0.25, 0.50, and 0.75. The resulting $\delta(\alpha)$ are small in spite of the substantial deviation of assumed R from that required.

Having matched $\nu_i(\alpha)$'s for the annular flow pattern with an R close to 1, we shall examine the case for the inverted annular flow pattern. The issue here is whether R = 1 (R used to match the annular flow) will also be good enough to combine the $\nu_i(\alpha)$ for inverted annular flow pattern to yield near-linearity given that $\delta_1(\alpha)/\delta_2(\alpha)$ may be quite different from 1.

Eq.(5.10) can be rewritten as

$$\delta(\alpha) = \frac{\delta_2(\alpha)}{2}\left[1 - \frac{\delta_1(\alpha)}{\delta_2(\alpha)}\right] \tag{5.11}$$

In Eq.(5.11), $\delta_1(\alpha)/\delta_2(\alpha)$ can vary from 0 to ∞. For the former case,

$$\delta(\alpha) = \delta_2(\alpha)/2 \tag{5.12}$$

For the latter case, since $\delta_1(\alpha)$ is finite, $\delta_2(\alpha)$ approach 0 for

TABLE 5.4

Matching of $\delta_i(\alpha)$ for Annular Flow

	$\alpha = 0.25$	$\alpha = 0.50$	$\alpha = 0.75$
$\delta_2(\alpha)$	0.14	0.20	0.20
$\delta_1(\alpha)$	0.24	0.23	0.14
Required $R(\alpha)$	1.71	1.15	0.70
$\delta(\alpha)$ $R=1.71$	0.0	0.041	0.075
$\delta(\alpha)$ $R=1.15$	-0.037	0.0	0.042
$\delta(\alpha)$ $R=0.70$	-0.084	-0.053	0.0

$\delta_1(\alpha)/\delta_2(\alpha)$ approaches ∞. Then,

$$\delta(\alpha) = -\delta_1(\alpha)/2 \qquad (5.13)$$

In general, we have observed that $\delta_1(\alpha)$ and $\delta_2(\alpha)$ are smaller than their counterparts for the annular flow pattern, and are small in magnitude. Thus, we expect the resulting $\delta(\alpha)$ to be also small for an R ≈ 1.

To illustrate the above point, again consider the $\nu_i(\alpha)$ for the same two energy groups for the inverted annular flow pattern (see Figure 5.13). The corresponding $\delta_i(\alpha)$ for these two groups are tabulated in Table 5.5 together with the required R's for exact match. The required R's are far from 1.15 used to match the $\nu_i(\alpha)$ for annular flow. However, using R=1.15 for superposition, the $\delta(\alpha)$ for α=0.25, 0.50, and 0.75 are calculated to be 0.026, 0.028, and 0.034 respectively. Thus, near-linearity is also achieved. This is due to the small $\delta_i(\alpha)$.

From the above arguments, we have seen the detected subcadmium neutron flux $\phi_i(\alpha)$ for two input neutron energy groups i, one curving above and one below the respective linear lines joining $\phi_i(0)$ and $\phi_i(1)$, can be combined to yield near-linear detector response. The condition is that the deviations from linearity $\delta_i(\alpha)$ are almost equal. The required ratio of intensities a_2/a_1 of the input neutrons is given by $\phi_1(0)/\phi_2(0)$, suggesting that a particular energy spectrum for input neutrons is required. Using the same ratio a_2/a_1, near-linearity in the combined subcadmium neutron flux $\phi(\alpha)$ can be achieved for both annular and inverted annular flow patterns, and thus near flow pattern independence.

TABLE 5.5

Matching of $\delta_i(\alpha)$ for Inverted Annular Flow

	$\alpha=0.25$	$\alpha=0.50$	$\alpha=0.75$
$\delta_2(\alpha)$	0.11	0.14	0.15
$\delta_1(\alpha)$	0.07	0.10	0.10
Required $R(\alpha)$	0.636	0.714	0.667
$\delta(\alpha)$ $R=1.15$	0.026	0.028	0.034

Extending the arguments for a two group system to a multigroup system, near-linearity can be achieved by combining pairs of input energy groups about a median energy group which separates those yielding "bulging" $\nu_i(\alpha)$ from those that yield "sagging" $\nu_i(\alpha)$. That is, with respect to this median energy group, a very low energy group combines with a very high one and an intermediately low one with an intermediately high one, etc. The required intensity ratio of each pair, however, is determined by the ratio of $\phi_i(0)$ of each pair. Since both $\phi_i(0)$ and the median enery group (being determined by the shape of $\nu_i(\alpha)$ for each group) depend on the test-section combination, an appropriate spectrum is required for a specific combination of test section diameter, wall thickness, and neutron reflectors. However, by the above arguments the appropriate spectrum needs not be unique. For example, the resulting spectrum by omitting a pair of high-low energy groups in an appropriate spectrum can still yield near linearity and therefore is another appropriate one.

Recall, in many experiments where unmoderated neutron sources were used, the subcadmium $\nu(\alpha)$ curves below the 45° (linear) line. This phenomenon can now be explained. For the specific combination of test section geometry, the subcadmium $\nu_i(\alpha)$ for each input energy group included in the unmoderated neutron source spectrum curves below its respective 45° line. This unmoderated neutron source spectrum contains too many high energy neutrons and is therefore not optimum. Upon moderation, lower energy group input neutrons are created at the expense of

high energy groups. The $\nu_i(\alpha)$ for these low energy groups curve above their respective 45^o lines. As a result, the resultant $\nu(\alpha)$ starts to shift up. At the appropriate amount of moderation, near linearity is achieved.

5.3.2 Increase of Average Input Neutron Energy or Decrease of Moderator Diameter with Test section Diameter

Suppose, in a small test section, the lowest input neutron energy group L requires a high input neutron energy group H for matching. From trend T5 previously discussed, we know that $\nu_i(\alpha)$ for both groups L and H shifts upwards when the test-section diameter increases. The $\nu_H(\alpha)$ can no longer match $\nu_L(\alpha)$. The $\nu_i(\alpha)$ for a group higher than H is now required for matching group L. As a result, the spectrum weighted average energy of the required spectrum generated by moderating the neutron source increases. This also means that the moderator diameter has to decrease.

5.3.3 Increase of Input Neutron Average Energy or Decrease of Moderator Diameter with Test-Section Wall Thickness and Addition of Neutron Reflector.

From experiments discussed in Chapter 4, we have established that the effect of a thicker test section wall and the addition of neutron reflector was to increase $\nu(\alpha)$. This effect can now be explained as the result of the increase of $\nu_i(\alpha)$ for individual groups. Thus, the increase of spectrum weighted average energy of the required spectrum can be explained in a similar manner to the case of increase intest-section diameter.

The understanding of the hypothesis formed is now considered complete.

5.4 COMPARISON BETWEEN MONTE CARLO RESULTS AND EXPERIMENTS.

A reasonably good understanding of the hypothesis has been sought through the trends observed in the group by group Monte Carlo study. It is interesting to compare the Monte Carlo result with experiments. Recall that, for both the 51 mm and 127 mm thin (Al) walled test sections (I and III), near-linearity in $\nu(\alpha)$ was achieved by moderating a neutron source (see Expt #13 in section 4.3.2.1 and Expt #16 in section 4.3.2.4). Recall also that, for both test sections, the scattered, subcadmium neutron fluences $\phi_i(\alpha)$ ($\phi_{33}(\alpha)$ yielded by the i^{th} input neutron group) were calculated with Monte Carlo simulations for several groups of input neutrons in a beam. In making the comparison, the spectrum of the neutrons emerging from the moderator is first calculated. The total scattered, subcadmium neutron flux is then determined by the superposition of $\phi_i(\alpha)$ with the calculated spectrum. The dimensionless counting rate $\nu(\alpha)$ is then determined by normalization, and compared with the $\nu(\alpha)$ obtained in the experiment. More detail of the comparison is given as following.

5.4.1 Calculation of Input Neutron Energy Spectra for 51 and 127 mm Test Sections

For the 51 mm thin (Al) walled test section I, the required diameter of the moderator for the $^{241}Am/Li$ neutron

source was experimentally determined to be 110 mm (see section 4.3.2.1). The spectrum of the neutrons emerging from the moderator was calculated by Monte Carlo simulation by a procedure discussed in Chater 3 (see section 3.3.3.3). The result is shown in Figure 5.27. The spectrum weighted average energy is 0.29 MeV.

For the 127 mm test section, the required diameter of the moderator for the ^{241}Am/Be source was experimentally determined to be 83 mm. The spectrum was similarly calculated, and the result is shown in Figure 5.28. The spectrum weighted average energy is 2.07 MeV.

5.4.2 Comparison with Experiments

For both test sections, the subcadmium neutron fluence $\phi_i(\alpha)$ for only a few input neutron energy groups were determined by Monte Carlo calculations due to limited computer time. The $\phi_i(\alpha)$ for other groups were obtained by linear interpolation. The interpolated $\phi_i(\alpha)$ for the 51 mm test section are tabulated in Table 5.6. Those for the 127 mm test section are tabulated in Table 5.7.

For each test section, the $\phi_i(\alpha)$'s were superimposed with the calculated input neutron energy spectrum for each α (α =0, 0.25, 0.5, and 0.75). The combined neutron flux was normalized by that for α=0 to yield $\nu(\alpha)$. The results for the 51 mm and 127 mm test sections are shown in Figure 5.29 and 5.30 respectively. From these two figures, near-linearity and thus flow pattern independence are observed. This confirms that each of the two moderator diameters results in a required input neutron energy

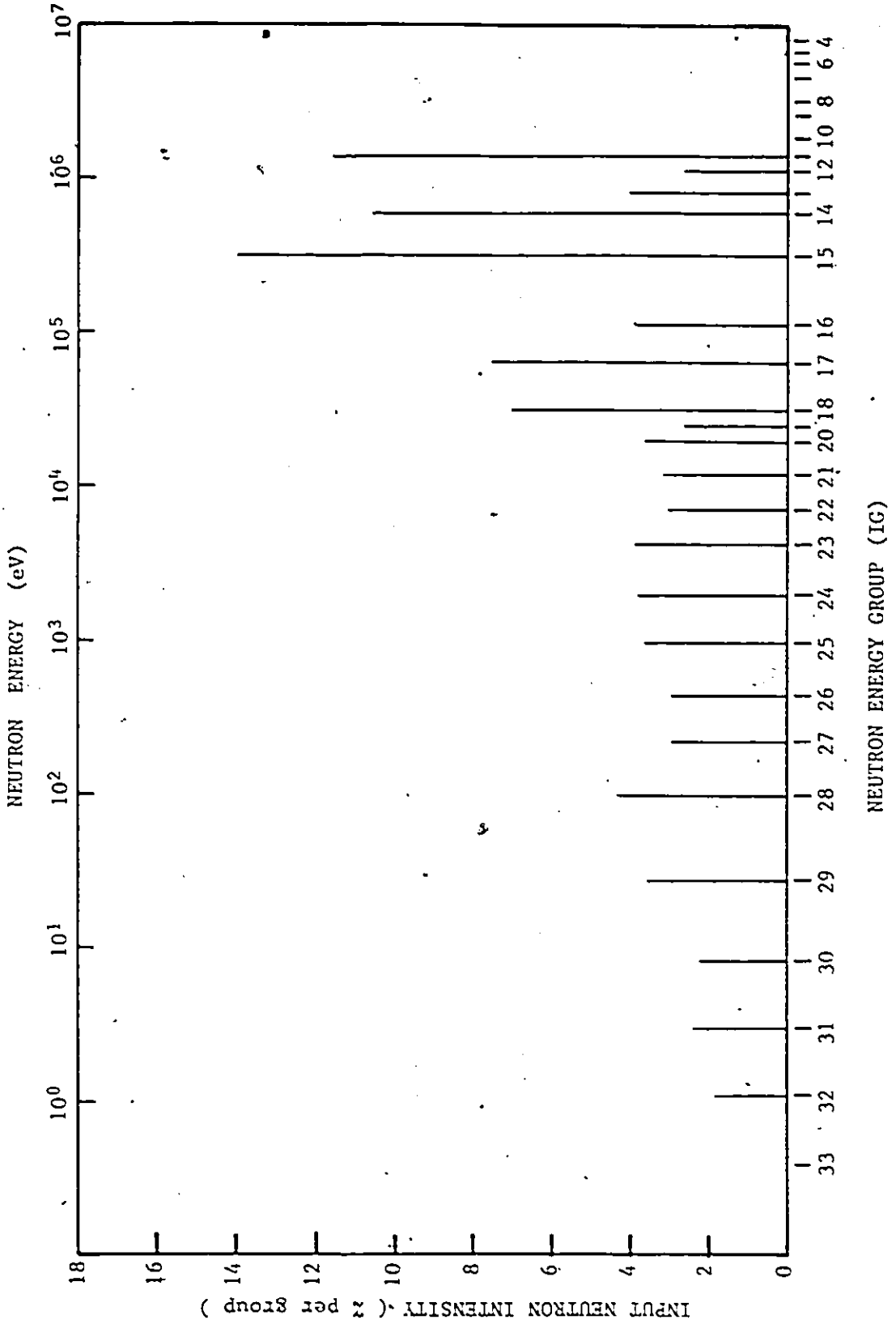

Figure 5.27 Energy spectrum A of moderated ^{241}Am/Li neutron source by a moderator of 110 mm diameter

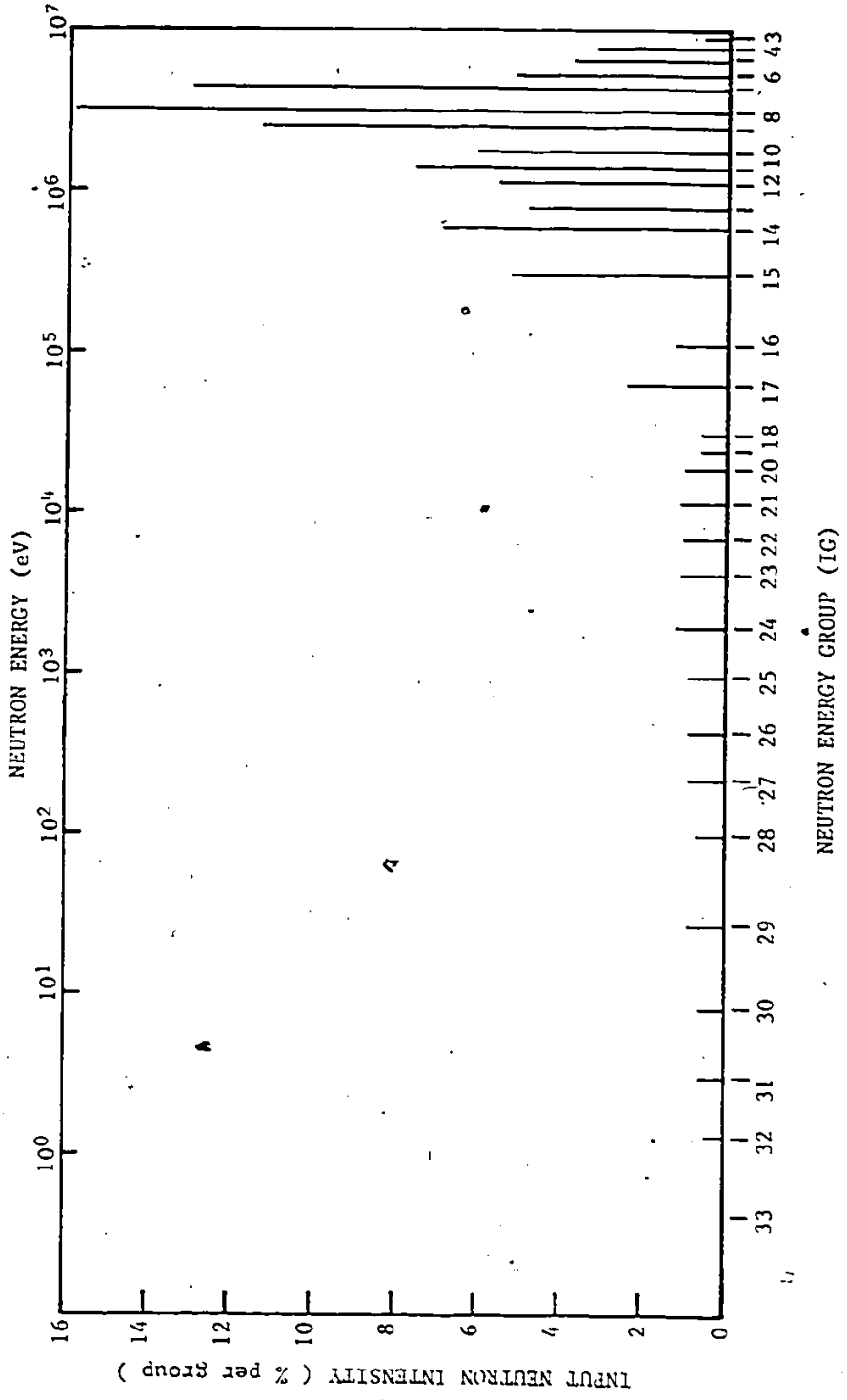

Figure 5.28 Energy spectrum B of moderated ^{241}Am/Be neutron source by a moderator of 83 mm diameter

TABLE 5.6

Interpolated $\phi_i(\alpha)$ for 51 mm Test Section I

		Inverted Annular			Annular		
IG	$\alpha=0$ ($\times10^{-4}$)	$\alpha=0.25$ ($\times10^{-4}$)	$\alpha=0.50$ ($\times10^{-4}$)	$\alpha=0.75$ ($\times10^{-4}$)	$\alpha=0.25$ ($\times10^{-4}$)	$\alpha=0.50$ ($\times10^{-4}$)	$\alpha=0.75$ ($\times10^{-4}$)
11	5.7	4.1	2.5	0.96	3.31	1.99	0.85
12	6.2	4.6	2.8	1.14	3.76	2.29	1.00
13	6.8	5.0	3.1	1.33	4.17	2.69	1.14
14	7.7	5.7	3.5	1.64	4.79	3.19	1.35
15	9.0	6.9	4.4	2.26	5.90	4.20	1.74
16	10.1	7.7	5.0	2.65	6.8	4.79	2.19
17	10.9	8.2	5.4	3.00	7.3	5.2	2.48
18	11.3	8.6	5.8	3.24	7.8	5.5	2.75
19	11.5	8.8	6.0	3.35	7.9	5.6	2.88
20	11.7	9.1	6.1	3.52	8.2	5.7	3.02
21	11.9	9.4	6.5	3.80	8.6	6.0	3.24
22	12.2	10.0	6.8	3.91	8.9	6.2	3.47
23	12.4	10.3	7.2	4.24	9.4	6.6	3.72
24	12.8	11.3	7.7	4.75	10.1	7.13	4.04
25	13.6	11.8	8.2	5.0	10.9	7.7	4.57
26	14.7	12.3	8.8	5.3	11.7	8.4	5.0
27	15.4	13.1	9.5	5.7	12.7	9.1	5.5
28	16.8	14.2	10.4	6.3	14.1	10.4	6.5
29	18.9	16.0	11.8	7.3	16.2	11.9	7.4
30	20.9	17.4	13.9	8.2	18.2	13.7	8.7
31	22.9	19.0	14.2	9.0	20.2	15.2	10.0
32	24.8	20.5	15.5	10.3	22.7	16.97	11.2

TABLE 5.7

Interpolated $\phi_i(\alpha)$ for 127 mm Test Section III

		Inverted Annular			Annular		
IG	$\alpha=0$ ($\times10^{-4}$)	$\alpha=0.25$ ($\times10^{-4}$)	$\alpha=0.50$ ($\times10^{-4}$)	$\alpha=0.75$ ($\times10^{-4}$)	$\alpha=0.25$ ($\times10^{-4}$)	$\alpha=0.50$ ($\times10^{-4}$)	$\alpha=0.75$ ($\times10^{-4}$)
3	1.79±0.25	1.12±0.15	0.69±0.10	0.33±0.03	1.13±0.15	0.54±0.08	0.23±0.03
4	2.12 0.29	1.36 0.17	0.83 0.11	0.41 0.04	1.40 0.17	0.68 0.10	0.26 0.04
5	2.39 0.31	1.55 0.19	0.95 0.13	0.48 0.04	1.61 0.19	0.80 0.11	0.31 0.06
6	2.61 0.33	1.71 0.20	1.04 0.14	0.53 0.04	1.79 0.21	0.89 0.12	0.35 0.06
7	2.80 0.35	1.84 0.21	1.12 0.14	0.57 0.05	1.94 0.22	0.97 0.13	0.38 0.06
8	3.01 0.37	1.99 0.22	1.21 0.15	0.62 0.05	2.11 0.24	1.06 0.14	0.42 0.07
9	3.17 0.38	2.10 0.23	1.27 0.16	0.66 0.05	2.24 0.25	1.13 0.15	0.45 0.07
10	3.28 0.39	2.18 0.24	1.32 0.17	0.69 0.05	2.34 0.26	1.18 0.16	0.47 0.07
11	3.35 0.40	2.23 0.25	1.35 0.17	0.70 0.05	2.39 0.26	1.21 0.16	0.48 0.08
12	3.84 0.43	2.75 0.29	1.74 0.19	0.96 0.08	3.02 0.29	1.91 0.21	0.80 0.14
13	4.21 0.45	3.14 0.32	2.04 0.20	1.15 0.09	3.50 0.31	2.43 0.27	1.04 0.18
14	4.48 0.46	3.43 0.35	2.25 0.25	1.29 0.10	3.85 0.33	2.81 0.31	1.22 0.22
15	4.88 0.48	3.84 0.38	2.57 0.23	1.49 0.12	4.36 0.35	3.37 0.36	1.47 0.27
16	5.12 0.50	4.10 0.40	2.76 0.24	1.62 0.13	4.67 0.37	3.71 0.39	1.63 0.30
17	5.44 0.49	4.43 0.40	3.19 0.26	1.89 0.15	5.11 0.41	4.28 0.42	2.26 0.32
18	5.69 0.48	4.70 0.39	3.54 0.27	2.11 0.16	5.47 0.44	4.74 0.45	2.77 0.34
19	5.75 0.48	4.76 0.39	3.61 0.27	2.15 0.16	5.54 0.45	4.83 0.45	2.87 0.34
20	5.78 0.47	4.80 0.39	3.67 0.27	2.19 0.16	5.60 0.45	4.91 0.46	2.95 0.34
21	5.84 0.47	4.86 0.39	3.74 0.28	2.24 0.17	5.67 0.46	5.00 0.47	3.06 0.35
22	5.87 0.47	4.89 0.39	3.79 0.28	2.26 0.17	5.72 0.47	5.06 0.47	3.13 0.35
23	5.89 0.47	4.91 0.39	3.82 0.28	2.28 0.17	5.75 0.47	5.10 0.47	3.17 0.35
24	5.91 0.47	4.93 0.39	3.84 0.28	2.30 0.17	5.77 0.47	5.13 0.47	3.20 0.35
25	11.3 0.68	9.77 0.53	7.36 0.36	4.58 0.22	11.2 0.67	10.7 0.65	8.36 0.51
26	13.9 0.77	12.1 0.59	9.02 0.40	5.65 0.24	13.8 0.76	13.3 0.73	10.84 0.58
27	15.1 0.82	13.1 0.62	9.81 0.42	6.61 0.25	15.0 0.80	14.5 0.77	11.95 0.62
28	15.7 0.84	13.6 0.64	10.2 0.43	6.40 0.26	15.6 0.82	15.1 0.79	12.97 0.64
29	16.1 0.85	14.0 0.65	10.4 0.44	6.56 0.26	16.0 0.83	15.5 0.81	12.84 0.65
30	16.2 0.86	14.1 0.65	10.5 0.44	6.60 0.26	16.1 0.84	15.6 0.81	12.94 0.65
31	16.2 0.87	14.1 0.65	10.5 0.44	6.61 0.26	16.1 0.84	15.6 0.81	12.96 0.65
32	16.2 0.86	14.1 0.65	10.5 0.44	6.62 0.26	16.1 0.84	16.5 0.82	13.00 0.65

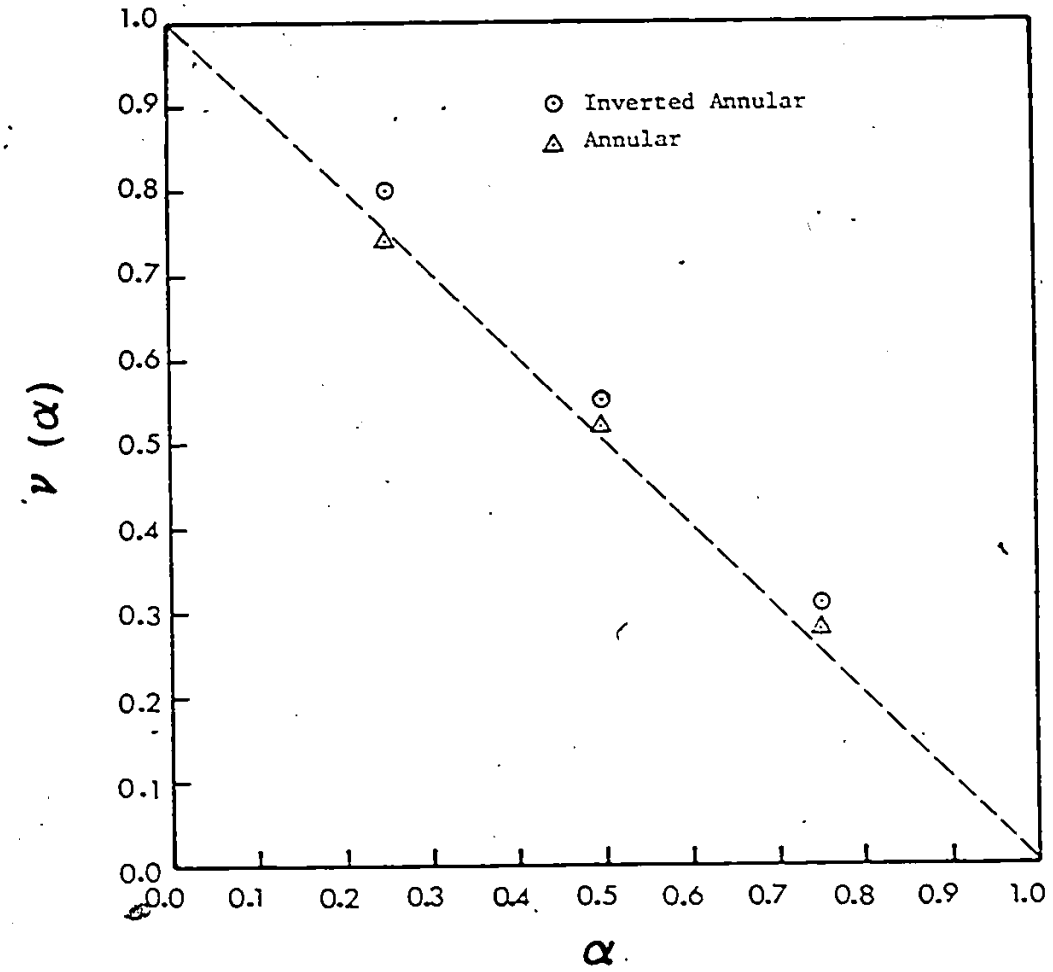

Figure 5.29 Dimensionless counting rate $\nu(\alpha)$ obtained by weighting $\nu_i(\alpha)$ for test section I with energy spectrum A (see Fig. 5.27)

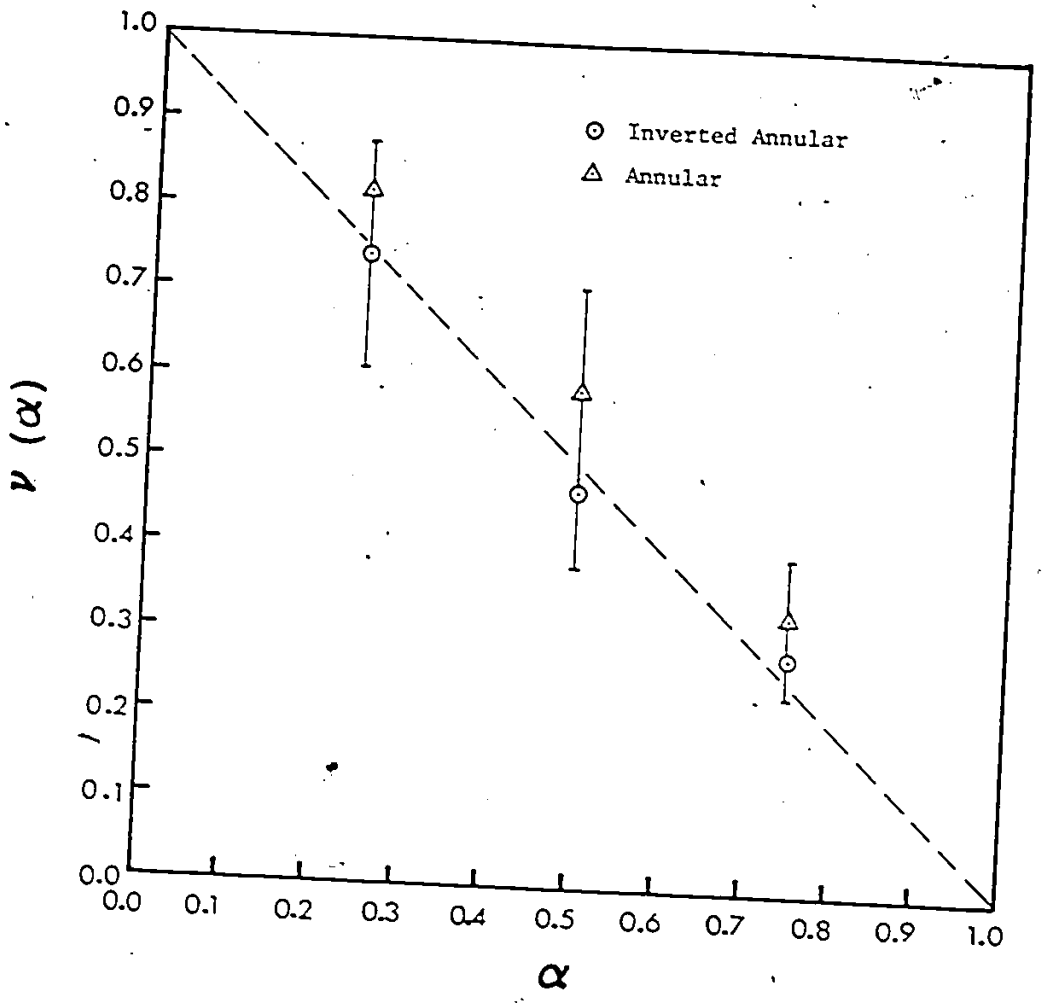

Figure 5.30 Dimensionless counting rate $\nu(\alpha)$ obtained by weighting $\varphi_i(\alpha)$ for test section III with energy spectrum B (see Fig. 5.28)

spectrum to achieve linearity and flow pattern independence.

5.5 COMMENTS ON EXPERIMENTS WITH REACTOR NEUTRON BEAM AND PROTABLE NEUTRON SOURCE

It is recalled that the neutron scattering technique has been tested using a neutron beam from the McMaster Nuclear Reactor (see section 2.3.1). Scattered neutron counting rate was observed to be nearly linear with α and flow pattern independent. It is also recalled that, when the technique was tested with an unmoderated $^{241}Am/Li$ neutron source, the scattered neutron counting rate was severely non-linear with α and flow pattern dependent (see Expt #0 in section 2.3.2). Expt #0 had been simulated with Monte Carlo calculations (see section 3.3.3.3). The reactor neutron beam experiment has also been simulated with Monte Carlo calculation by Banerjee et al <125>. The Monte Carlo simulations in both cases agreed with experiments. Both experiments were backed by Monte Carlo simulations and therefore the discrepancy is genuine. It is necessary and appropriate here to resolve this apparent discrepancy.

The inside diameters of test sections in both experiments were 51 mm and both test sections had thin aluminum walls. The clue is the incident neutron spectra in the two experiments. The incident neutron energy spectrum in Expt #0 was that of an unmoderated $^{241}Am/Li$ neutron source. It is shown in Figure 5.31. Shown also in this figure is the incident neutron spectrum (above cadmium cut-off energy) in the reactor experiment. This spectrum is obtained from McCormack <127> who measured the neutron spectrum of the McMaster Research reactor.

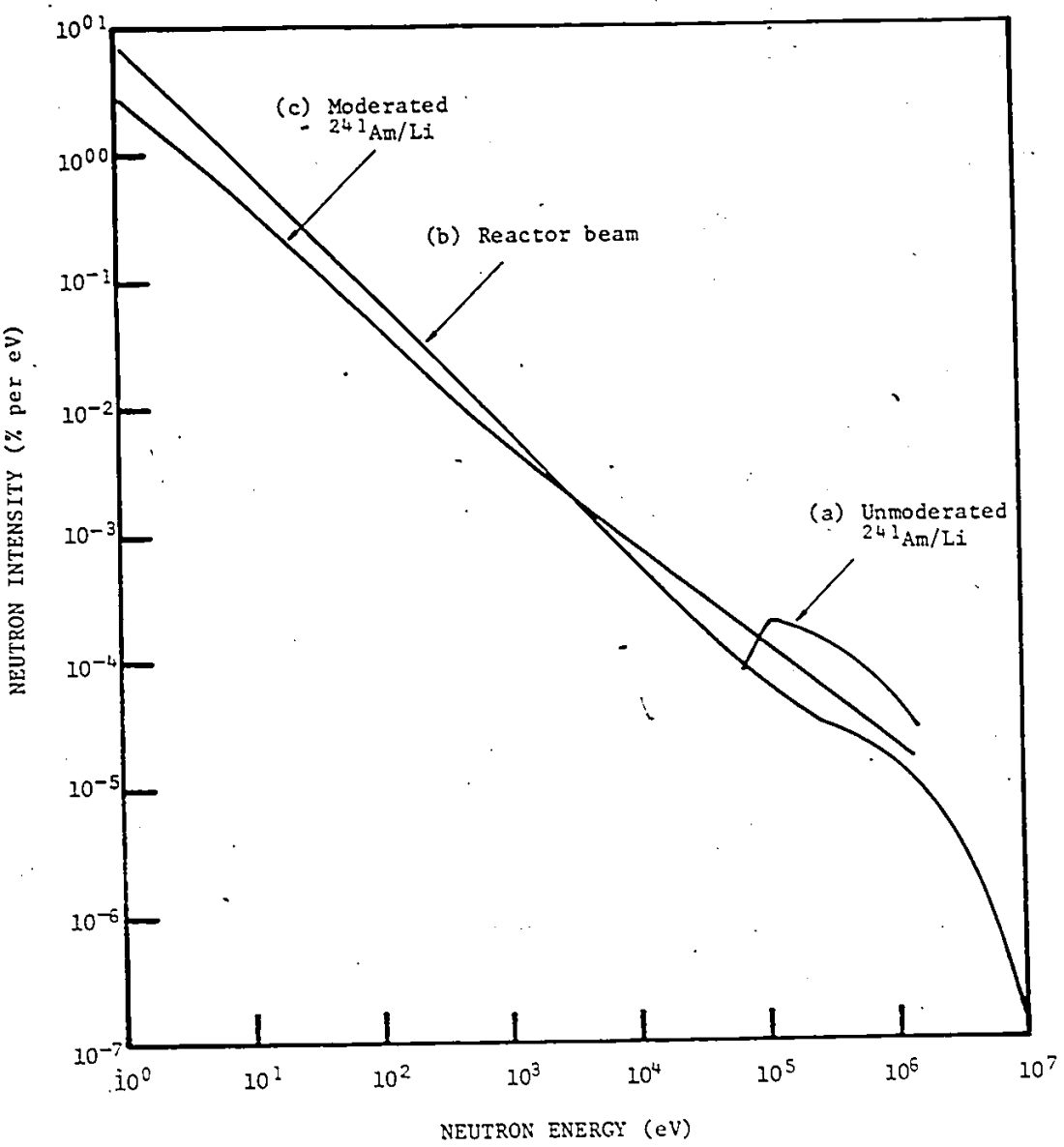

Figure 5.31 Incident neutron spectra of

(a) unmoderated ^{241}Am/Li neutron source

(b) McMaster Nuclear Reactor neutron beam

(c) moderated ^{241}Am/Li neutron source with a moderator of 110 mm

These two spectra are very different. There is no neutron with energy lower than 30 keV in the unmoderated ^{241}Am/Li source and most of the neutrons have energy between 0.1 to 1 MeV. These "hard" neutrons are difficult to thermalize in a small test section and resulted in the scattered neutron counting rate severely falling below the ideal straight line joining the two end-points (α=0 and 1). Moreover, because of the higher escape probability of a neutron in annular flow, the detector response for annular flow falls below that of inverted annular flow, resulting in significant flow pattern dependence. However, in the reactor beam spectrum, it happens that there is a significant amount of low energy neutrons present. About 53% neutrons in the reactor beam have energy lower than the lower limit of the ^{241}Am/Li source (30 keV). These low energy incident neutrons shift the detector response towards the ideal linear line. It could have been fortitious that the reactor beam spectrum was such that the effect of high and low incident neutrons balance out each other to yield near-linearity and near flow pattern independence.

It is interesting to compare the reactor beam spectrum with that obtained by moderating the ^{241}Am/Li source in Expt #13 (see section 4.3.2.1). Recall that the moderated ^{241}Am/Li spectrum yielded near linearity and flow pattern independence. The moderated ^{241}Am/Li spectrum is also shown in Figure 5.31. The reactor beam spectrum is not identical to the moderated ^{241}Am/Li spectrum but resembles it much better than the unmoderated neutron source spectrum. They need not be identical since the degree of near linearity achieved is slightly different

in the two cases. In the reactor beam experiment, the neutron counting rate for the inverted annular flow consistently underestimates void fraction while that for annular flow yields almost perfect prediction of void fraction (see Figure 2.2). In the case of the moderated ^{241}Am/Li source, the neutron counting rate slightly overestimates void fraction for both flow patterns (see Figure 4.13). This implies that there are more low energy neutrons in the reactor beam. In the energy range between 1 eV to 1.5 MeV, the ratio of low to high energy neutrons is certainly higher in the reactor beam spectrum (there is a cross-over of the two spectra at about 3 keV). At energy above 1.5 MeV there is a substantial number of neutrons which are not present in the moderated neutron source. However, the contribution of these hard neutrons to the counting rate of neutrons thermalized by the small test section is small and is probably off-set by the excess amount of low energy neutrons. Thus, it was definitely fortitious that the reactor beam spectrum yielded near linearity resulting in a premature conclusion in the previous work that the neutron counting rate is always linear to void fraction and flow pattern indepent.

The work to investigate how and why one can implement the neutron scattering technique with a portable neutron source is now considered complete. The next section is devoted to a proposed design procedure for a portable void fraction meter.

5.6 DESIGN PROCEDURE

The following is a proposed design procedure for a

portable void fraction meter. The emphasis is on the design of the neutron moderator.

Step 1 Determine the test section diameter and wall thickness for the intended industrial application.

Step 2 Determine the counting rate at a helium-3 detector (50 mm diameter x 100 mm length) that is needed for the application.

Step 3 Estimate the neutron source strength required to yield the intended counting rate. A rough figure is the intended counting rate x (2×10^3).

Step 4 With the estimated neutron source strength, determine the shielding thickness around the neutron source and the geometry of it by conducting some simple shielding calculations (e.g. using the concept of removal cross-section for the highest neutron energy, say 10 MeV).

Step 5 Conduct a Monte Carlo simulation. Simulate the geometry of the test section (diameter and wall) and the shielding (hydrogeneous neutron reflector material) exactly. Use a beam for the input neutron geometry. Use a point detector placed at the centre of the intended detector location to calculate the subcadmium neutron fluence. Pick a few groups of source neutron energy extending from epicadmium to 15 MeV.

For each source neutron energy group, run the Monte Carlo code to estimate the scattered subcadmium neutron fluence $\phi_1(\alpha)$ for a few values of α in each of two radially symmetric annular and inverted annular flow.

The number of neutron groups picked should be as many as possible. The $\phi_i(\alpha)$ for other source neutron energy groups can be obtained by interpolation.

Step 6 Obtain the energy spectra of a few commercially available neutron sources (unmoderated). Weight the group $\phi_i(\alpha)$ with the spectrum having the lowest average energy and check for linearity. If $\nu(\alpha)$ (even part of) for any flow pattern lie above the $(1-\alpha)$ line by a large amount (>0.05) move to the next spectrum with a higher average energy. Repeat the process until $\nu(\alpha)$ lies below $(1-\alpha)$. Work with this neutron source.

Step 7 Place the neutron source obtained in Step 6 in a moderator can with a large diameter. Run a Monte Carlo simulation to determine the spectrum of emergent neutrons above the cadmium cut-off energy. Weight the $\phi_i(\alpha)$ with this spectrum to obtain $\nu(\alpha)$. If $\nu(\alpha)$ lies above $(1-\alpha)$ go to a smaller moderator-can diameter. repeat this step. If $\nu(\alpha)$ is below $(1-\alpha)$ increase the moderator-can diameter and repeat this step until fair linearity of $\nu(\alpha)$ is observed for both flow patterns. Essentially, it is an exercise of high and low guesses. However, it does not need many runs to obtain the optimum moderator-can diameter.

Step 8 (Optional) Step 5 to 7 can be replaced by experimental procedures. Use a short length of the test section. Prepare a few inserts in annular and inverted annular flow patterns. Use a moderated neutron source and measure the subcadmium neutrons. Continue to change

moderator-can diameter until a fairly linear $\nu(\alpha)$ is obtained.

Step 9 Once the moderator-can diameter and neutron source are determined, the design can be finalized with two identical moderated neutron sources and two detector as shown in Figure 4.27 (see section 4.5)). The two detectors and two neutron sources are for reducing perturbations caused by radially non-symmetric flow patterns. The neutron reflector and the moderator are to be lined by cadmium sheet to remove subcadmium neutrons.

Conclusions from the present investigation are discussed in Chapter 6.

CHAPTER SIX

CONCLUSIONS, CONTRIBUTIONS, AND RECOMMENDATIONS

6.1 CONCLUSIONS

(1) In general, the counting rate of subcadmium neutrons as a result of thermalization of epithermal/fast neutrons in two-phase test section is not linear with void fraction and is flow pattern dependent.

(2) For radially symmetric water phase distribution about the axis of a test section, near-linearity and flow pattern independence can be achieved by carefully moderating an appropriately chosen neutron source generating an optimum incident neutron energy spectrum.

(3) The optimum incident neutron energy spectrum resulting from moderating the neutron source depends on test-section diameter, wall thickness, and the presence of neutron reflectors. The average energy of the required incident neutron spectrum increases with test-section diameter, test-section wall thickness, and the addition of neutron reflector material.

(4) If the optimum incident neutron energy spectrum is used on radially non-symmetric flow patterns such as displaced inverted annular, annular, and stratified flow, the detector response deviates mildly from linearity. However, this mild perturbation can be removed by using a two moderators and two detectors assembly.

6.2 CONTRIBUTIONS

(1) A technique to measure void fraction in a two-phase flow operating on the principle of multiple scattering of neutrons (thermalization) has been developed. This technique has the following advantages:

(i) Near linearity in response to α so that only two end points are needed for calibration (empty and full test section).

(ii) Near flow regime independence.

(iii) Time averaged response $\bar{N}(\bar{\alpha})$ in steady state measurement will also be near linear with the time averaged void fraction $\bar{\alpha}$ regardless of the geometry of a flow pattern.

(iv) Applicable in high pressure systems commonly found in industries where metal walled systems are used.

(2) The feasibility of implementing this technique with a portable system has been established, making this technique practical. The conditions for successful implementation have been determined, and understanding of these conditions has been obtained.

(3) Based on the understanding of the conditions governing a portable system, design procedures to be followed and a conceptual design for a portable void fraction meter have been given.

(4) The practical portable system for measuring void fraction has the potential of being used to measure other two-phase

flow quantities related to void fraction that industries are interested in, e.g. density and steam quality (provided the velocity slip ratio can be measured at the same time)

6.3 RECOMMENDATIONS

Good understanding of the factors leading to successful implementation of the technique with a portable system has been gained. However, there remain areas that could further increase the level of understanding or expedite the design process and yet have not been considered extensively. The following are some of these areas.

(1) Number of Collisions

The average number of collisions suffered by an input neutron of E_0 in a test section of a given α was not determined analytically but obtained from Monte Carlo runs. It is recommended here that some research work could be conducted to derive the analytical form so that, compounded with the probability $P_j(E_0)$ derived in this work, one can determine the subsequent thermalization probability $P_s(\alpha)$ and hence the thermalization probability $P_T(\alpha)$ for each individual input neutron energy group.

(2) Energy Spectra of Moderated Neutron Sources

A systematic study of the variation of the spectrum of a moderated neutron source with moderator diameter could be carried out with Monte Carlo simulations. It is recommended here that a library of moderated neutron source energy spectra could be obtained for various neutron sources. For a given test section,

by superposition of $P_T(\alpha)$ and the moderated neutron source spectra, the appropriate moderator diameter for a given neutron source could be determined.

(3) Correlation between Test Section and Moderator Diameter

For a given test section and neutron source, there is one moderator diameter which yields linearity and flow regime independence in the void fraction meter response. If the results of work recommended in (1) and (2) are available, then a correlation between test section and moderator diameter for a given neutron source could be developed. This correlation would be useful in speedy design of a portable void fraction meter. It is certainly worthwhile doing this, but the Monte Carlo runs necessary could not be done as a part of this dissertation because of funding limitations.

APPENDICES

APPENDIX A

ERROR ANALYSES

A1 Introduction

In the present work, the subcadmium neutron counts $N(\alpha)$ were converted to the dimensionless neutron counting rate $\nu(\alpha)$ according to Eq.(2.10) as

$$\nu(\alpha) = \frac{N(\alpha) - N(1)}{N(0) - N(1)} \qquad (A.1)$$

In Eq.(A.1), the subcadmium neutron counts N was obtained by "differential counting." (see section 3.2.3) according to

$$N(\alpha) = \langle n_1 \rangle - \langle n_2 \rangle \qquad (A.2)$$

where n_1 = sum of subcadmium and epicadmium neutron counts

n_2 = epicadmium neutron counts

and $\langle\ \rangle$ denotes the sample average obtained by repeating the counting k times.

The error in $\nu(\alpha)$ is thus related to the error in $\langle n_1 \rangle$ and $\langle n_2 \rangle$. The error analyses of $\nu(\alpha)$ are discussed in the following sections.

A2 Error in $\langle n_1 \rangle$ and $\langle n_2 \rangle$

The sample average $\langle n_i \rangle$ (i=1 or 2) is given by

$$\langle n_i \rangle = \left(\sum_{j=1}^{k} n_{ij} \right)/k \qquad (A.3)$$

In Eq.(A.3), n_{ij} is the neutron counts at the j^{th} sampling, and k is the total number of samples (repeated countings).

The standard deviation S of n_i is given by

$$S^2 = \left\{ \sum_{j=1}^{k} (n_{ij} - \langle n_i \rangle)^2 \right\}/(k - 1) \qquad (A.4)$$

The error in $\langle n_i \rangle$ or $\Delta\langle n_i \rangle$, at 68% confidence level, is is given by

$$\Delta\langle n_i \rangle = S/\sqrt{k} \qquad (A.5)$$

In other words, $\Delta\langle n_i \rangle$ is taken to be the uncertainty in the sample mean from the ensemble mean (true mean).

A3 Error in N(α)

Since N(α) is given by the difference between $\langle n_1 \rangle$ and $\langle n_2 \rangle$, the error in N(α), using the propagation of errors, is given by

$$\Delta N(\alpha) = \sqrt{(\Delta\langle n_1 \rangle)^2 + (\Delta\langle n_2 \rangle)^2} \qquad (A.6)$$

A4 Error in $\nu(\alpha)$

Since $\nu(\alpha)$ is given by Eq.(A.1), the error in $\nu(\alpha)$ or $\Delta\nu$, at 68% confidence level, is given by

$$\Delta\nu(\alpha) = \sqrt{\left(\frac{\partial\nu}{\partial N}\right)^2(\Delta N)^2 + \left(\frac{\partial\nu}{\partial N(0)}\right)^2(\Delta N(0))^2 + \left(\frac{\partial\nu}{\partial N(1)}\right)^2(\Delta N(1))^2}$$

$$= \frac{\sqrt{(N(0) - N(1))^2(\Delta N(\alpha))^2 + (N(\alpha) - N(1))^2(\Delta N(0))^2 + (N(\alpha) - N(0))^2(\Delta N(1))^2}}{(N(0) - N(1))^2} \qquad (A.7)$$

APPENDIX B

INPUT INSTRUCTIONS OF MORSE†

B.1 Random Walk Input Instruction

The input read by subroutine INPUT1 is as follows:

CARD A (20A4)

Title card.

(Any character other than a blank or alphanumeric in column one will terminate the job.)

CARD B (10I5,F5.0,2I5)

NSTRT - number of particles per batch.

NMØST - maximum number of particles allowed for in the bank(s); may equal NSTRT if no splitting, fission, and secondary generation.

NITS - number of batches.

NQUIT - number of sets of NITS batches to be run without calling subroutine INPUT.

NGPQTN* - number of neutron groups being analyzed.

NGPQTG* - number of gamma-ray groups being analyzed.

NMGP* - number of primary particle groups for which cross sections are stored; should be same as NGP (or the same as NGG when NGP = 0) on Card XB read by subroutine XSEC.

NMTG* - total number of groups for which cross sections are stored; should be same as NGP+NGG as read on Card XB read by subroutine XSEC.

NCØLTP - set greater than zero if a collision tape is desired; the collision tape is written by the user routine BANKR.

IADJM - set greater than zero for an adjoint problem.

AXTIM - maximum clock time in minutes allowed for the problem to be on the computer (360/91 c.p.u. time); e.g., 4.5 entered here allows 4 and 1/2 minutes.

MEDIA - number of cross-section media; should agree with NMED on Card XB read by subroutine XSEC.

---

*See Table B.1 for sample input.

†See Reference <123>.

Table B.1 Sample Group Input Numbers for Some Representative Problems*

Case A - Neutron Only Cross Sections (22 groups)

Case B - Gamma-Ray Only Cross Sections (18 groups)

Case C - Neutron-Gamma-Ray-Coupled Cross Sections (22-18 groups)

Input Variable	Problem Type: Case A Top 14 groups	Case B Top 17 groups	Case C Neutrons Only Top 14 groups	Case C Gamma Rays Only Top 17 groups	Case C Neutron-Gamma Top 14 Neutron, Top 17 Gamma Groups	
MORSE Input:						
NGPQTN	14	0	14	0	14	
NGPQTG	0	17	0	17	17	CARD B,
NMGP	22	18	22	18	22	Variables
NMTG	22	18	22	18	40	
NGP	22	18	22	0	22†	
NGG	0	0	0	18	18	CARD XB
INGP	22	18	40	40	40	Variables

*For cross sections with full downscatter, NDS = NGP, NDSG = NGG, INDS = INGP, and ITBL = number of downscatters + number of upscatters + 3. Usually, ISGG = number of upscatters + 4; i.e., NUS + 4.

†Must be = to total number of neutron groups in the data - otherwise it picks up gammas from wrong location.

MEDALB - albedo\scattering medium is absolute value of MEDALB; if MEDALB = 0, no albedo information to be read in, MEDALB < 0, albedo only problem - no cross sections are to be read, MEDALB > 0, coupled albedo and transport problem.

CARD C (4I5, 5E10.5)

ISØUR - source energy group if > 0, if ISØUR < 0 or if ISØUR = 0 and NGPFS ≠ 0, SØRIN is called for input of Cards E1 and E2.

NGPFS - number of groups for which the source spectrum is to be be defined. If ISØUR < 0, NGPFS ≥ 2.

ISBIAS - no source energy biasing if set equal to zero; otherwise the source energy is to be biased, and Cards E2 are required.

NØTUSD - an unused variable.

WTSTRT - weight assigned to each source particle.

EBØTN - lower energy limit of lowest neutron group (eV) (group NMGP).

EBØTG - lower energy limit of lowest gamma-ray group (eV) (group NMGP).

TCUT - age in sec at which particles are retired; if TCUT = 0, no time kill is performed.

VELTH - velocity of group NMGP when NGPQTN > 0; i.e., thermal-neutron velocity (cm/sec).

CARD D (7E10.4)

XSTRT, YSTRT, ZSTRT - coordinates for source particles.

AGSTRT - starting age for source particles.

UINP, VINP, WINP - source particle direction cosines if all are zero, isotropic directions are chosen.

Source data on Cards C and D will be overridden by any changes in subroutine SØURCE.

CARDS E1 (7E10.4) (Omit if ISØUR on Card C > 0 or if ISØUR = NGPFS = 0)

NGPFS values of FS, where FS equals the unnormalized fraction of source particles in each group.

CARDS E2 (7E10.4) (Omit if ISØUR > 0 or if ISØUR ≤ 0 and ISBIAS = 0)

if ISBIAS > 0, NGPFS values of BFS, the relative importance of a source in group I, are required.

CARDS F (7E10.4)

NMTG values of ENER, the energies (in eV) at the upper edge of the energy group boundaries.

NOTE: The lower energies of groups NMGP and NMTG were read on Card C.

CARD G (2I5,5X,36I1,5X,13I1) (Omit if NCØLTP on Card B ≤ 0)

NHISTR - logical tape number for the first collision tape.

NHISMX - the highest logical number that a collision tape may be assigned.

NBIND(J), J=1, 36 - an index to indicate the collision parameters to be written on tape.

NCØLIS(J), J=1, 13 - an index to indicate the types of collisions to be put on tape.

(see Tables B.2 for information concerning NBIND and NCØLIS.)

CARD E (Z12), on IBM-360; (Ø20) on CDC-6600; (4X,Ø12) on UNIVAC-1108

RANDØM - starting random number.

CARD I (7I5)

NSPLT - index indicating that splitting is allowed if > 0.

NKILL - index indicating that Russian roulette is allowed if > 0.

NPAST - index indicating that exponential transform is invoked if > 0 (subroutine DIREC required).

NØLEAK - index indicating that non-leakage is invoked if > 0.

IEBIAS - index indicating that energy biasing is allowed if > 0.

MXREG - number of regions described by geometry input (will be set to one if ≤ 0).

MAXGP - group number of last group for which Russian roulette or splitting or exponential transform is to be performed. For adjoint, set = NMTG or overstoring results.

Table B.2. Variables That May Be Written on Tape (NBIND)

J	Variable	J	Variable
1	NCØLL	19	WTBC
2	NAME	20	ETAUSD
3	IG	21	ETA
4	U	22	AGE
5	V	23	ØLDAGE
6	W	24	NREG
7	X	25	NMED
8	Y	26	NAMEX
9	Z	27	WATEF
10	WATE	28	BLZNT
11	IGØ	29	BLZØN
12	UØLD	30	VEL(IG)
13	VØLD	31	VEL(IGØ)
14	WØLD	32	TSIG
15	XØLD	33	PNAB
16	YØLD	34	NXTRA
17	ZØLD	35	EXTRA1
18	ØLDWT	36	EXTRA2

CARD J (6I5,4E10.5) (Omit if NSPLT + NKILL + NPAST = 0)

NGP1, NDG, NGP2 — from energy group NGP1 to energy group NGP2, inclusive, in steps of NDG and from region NRG1 to NRG2, inclusive, in steps of NDRG, the following weight standards and path-stretching parameters are assigned. If NGP1 = 0, groups 1 to MAXGP will be used; if NRG1 = 0, regions 1 to MXREG will be used (both in steps of one). Usually NDG = 1 and NDRG = 1.

NRG1, NDRG, NRG2 — (see above)

WTHTH1 - weight above which splitting will occur.

WTLØW1 - weight below which Russian roulette is played.

WTAVE1 - weight given those particles surviving Russian roulette.

PATH - path-length stretching parameters for use in exponential transform (usually $0 \leq PATH < 1$).

The above information is repeated until data for all groups and regions are input.

End Cards J with negative value of NGP1 (ex., -1 in columns 4 and 5).

CARDS K (7E10.4) (Omit if IEBIAS on Card I $\leq$ 0).

((EPRØB(IG,NREG), IG = 1, NMTG), NREG = 1, MXREG)

Values of the relative energy importance of particles leaving a collision in region NREG. Input for each region must start on a new card.

CARD L (4I5)

NSØUR - set $\leq$ 0 for a fixed source problem; otherwise the source is from fissions generated in a previous batch.

MFISTP - index for fission problem, if $\leq$ 0 no fissions are allowed.

NKCALC - the number of the first batch to be included in the estimate of k; if $\leq$ 0 no estimate of k is made.

NØRMF - the weight standards and fission weights are unchanged if $\leq$ 0; otherwise fission weights will be multiplied, at the end of each batch, by the latest estimate of k and the weight standards are multiplied by the ratio of fission weights produced in previous batch to the average starting weight for the previous batch. For time-dependent decaying systems, NØRMF should be > 0.

CARDS M (7E10.4) (Omit if MFISTP on Card L ≤ 0)

(FWLØ(I), I = 1, MXREG) values of the weight to be assigned fission neutrons.

CARDS N (7E10.4) (Omit if MFISTP on Card L ≤ 0)

(FSE(IG,IMED), IG = 1, NMTG), IMED = 1, MEDIA) the fraction of fission-induced source particles in group IG and medium IMED.

NOTE: Input for each medium must start on a new card.

CARDS O (7E10.5) (Omit if NGPQTN = 0 or NGPQTG = 0, i.e., include if coupled neutron-gamma-ray problem)

((GWLØ(IG,NREG) IG = 1, NMGP or NMTG - NMGP), NREG = 1, MXREG) - values of the probability of generating a gamma ray. NMGP groups are read for each region in a forward problem and NMTG-NMGP for an adjoint. Input for each region must start on a new card.

B.2 Combinatorial Geometry Input Instructions

The combinatorial geometry input data is read by the JØMIN subroutine, except for the region volumes VNØR(I), which are read by the GTVLIN subroutine whenever IVØPT = 3. For clarity of terminology, the terms "regions" and "media" have essentially the same meaning as in the Ø5R Geometry Package, but are constructed in a different manner. The term "zone" is the same as the "region" as defined in the original combinatorial geometry package. The term "body" has the same meaning as in the original combinatorial geometry package.

CARD CGA (2I5,10X,10A6)

IVØPT – option which defines the method by which region volumes are determined; if
IVØPT = 0, volumes set equal to 1,
IVØPT = 1, concentric sphere volumes are calculated,
IVØPT = 2, slab volumes (1-dim.) are calculated,*
IVØPT = 3, volumes are input by card.

IDBG – if IDBG > 0, subroutine PR is called to print results of combinatorial geometry calculations during execution. Use only for debugging.

JTY – alphanumeric title for geometry input (columns 21-80).

*Not operational.

CARDS CGB (2X,A3,1X,I4,6D10.3)

One set of CGB cards is required for each body and for the END card (see Table B.3). Leave columns 1-6 blank on all continuation cards.

ITYPE - specifies body type or END to terminate reading of body data (for example BØX, RPP, ARB, etc.). Leave blank for continuation cards.

IALP - body number assigned by user (all input body numbers must form a sequence set beginning at 1). If left blank, numbers are assigned sequentially. Either assign all or none of the numbers. Leave blank for continuation cards.

FPD(I) - real data required for the given body as shown in Table B.3. This data must be in cm.

CARDS CGC (2X,A3,I5,9(A2,I5))

Input zone specification cards. One set of cards required for each input zone, with input zone numbers being assigned sequentially.

IALP - IALP must be a nonblank for the first card of each set of cards defining an input zone. If IALP is blank, this card is treated as a continuation of the previous zone card.

IALP - END denotes the end of zone description.

NAZ - total number of zones that can be entered upon leaving any of the bodies defined for this input region (some zones may be counted more than once). Leave blank for continuation cards for a given zone. (If NAZ $\leq$ 0 on the first card of the zone card set, then it is set to 5). This is used to allocate blank common.

Alternate IIBIAS(I) and JTY(I) for all bodies defining this input zone.

IIBIAS(I) - specify the "ØR" operator if required for the JTY(I) body.

JTY(I) - body number with the (+) or (-) sign as required for the zone description.

Table B.3 Input Required on CGB Cards for Each Body Type

Card Columns Body Type	ITYPE 3-5	IALP 7-10	Real Data Defining Particular Body 11-20	21-30	31-40	41-50	51-60	61-70	Number of Cards Needed
Box	BØX	IALP is assigned by the user or by the code if left blank.	Vx	Vy	Vz	H1x	H1y	H1z	1 of 2
			H2x	H2y	H2z	H3x	H3y	H3z	2 of 2
Right Parallele-piped	RPP		Xmin	Xmax	Ymin	Ymax	Zmin	Zmax	1
Sphere	SPH		Vx	Vy	Vz	R	-	-	1
Right Circular Cylinder	RCC		Vx	Vy	Vz	Hx	Hy	Hz	1 of 2
			R	-	-	-	-	-	2 of 2
Right Elliptic Cylinder	REC		Vx	Vy	Vz	Hx	Hy	Hz	1 of 2
			R1x	R1y	R1z	R2x	R2y	R2z	2 of 2
Ellipsoid	ELL		V1x	V1y	V1z	V2x	V2y	V2z	1 of 2
			L	-	-	-	-	-	2 of 2
Truncated Right Cone	TRC		Vx	Vy	Vz	Hx	Hy	Hz	1 of 2
			L1	L2	-	-	-	-	2 of 2
Right Angle Wedge	WED or RAW		Vx	Vy	Vz	H1x	H1y	H1z	1 of 2
			H2x	H2y	H2z	H3x	H3y	H3z	2 of 2

Table 4.3 (Cont'd)

Card Columns Body Type	ITYPE 3-5	IALP 7-10	Real Data Defining Particular Body 11-20	21-30	31-40	41-50	51-60	61-70	Number of Cards Needed
Arbitrary Polyhedron	ARB		V1x	V1y	V1z	V2x	V2y	V2z	1 of 5
			V3x	V3y	V3z	V4x	V4y	V4z	2 of 5
			V5x	V5y	V5z	V6x	V6y	V6z	3 of 5
			V7x	V7y	V7z	V8x	V8y	V8z	4 of 5
			Face Descriptions (see note below)						5 of 5
Termination of Body Input Data	END								

NOTE: Card 5 of the arbitrary polyhedron input contains a four-digit number for each of the six faces of an ARB body. The format is 6D10.3, beginning in column 11. See the ARB write-up in Section 4.7 for an example.

CARDS CGD (14I5)

MRIZ(I) - MRIZ(I) is the region number in which the "Ith" input zone is contained (I = 1, to the number of input zones). Region numbers must be sequentially defined from 1.

CARDS CGE (14I5).

MMIZ(I) - MMIZ(I) is the medium number in which the "Ith" input zone is contained (I = 1, to the number of input zones). Medium numbers must be sequentially defined from 1.

CARDS CGF (7D10.5) (Omit if IVØPT ≠ 3)

VNØR(I) - volume of the "Ith" region (I = 1 to MXREG, the number of regions).

B.3 MØRSEC - Cross-Section Module Input Instructions

CARD XA (20A4)

Title card for cross sections. This title is also written on tape if a processed tape is written; therefore, it is suggested that the title be definitive.

CARD XB (13I5)

NGP* - the number of primary groups for which there are cross sections to be stored. Should be same as NMGP input in MØRSE.

NDS - number of primary downscatters for NGP (usually NGP).

NGG* - number of secondary groups for which there are cross sections to be stored.

NDSG - number of secondary downscatters for NGG (usually NGG).

INGP* - total number of groups for which cross sections are to be input.

ITBL - table length, i.e., the number of cross sections for each group (usually equal to number of downscatters + number of upscatters + 3).

ISGG - location of within-group scattering cross sections (usually equal to number of upscatters + 4).

NMED - number of media for which cross sections are to be stored - should be same as MEDIA input in MØRSE.

---

*See Table B.I for sample input.

NELEM - number of elements for which cross sections are to be read.

NMIX - number of mixing operations (elements times density operations) to be performed (must be ≥ 1).

NØEF - number of coefficients for each element, including P_0.

NSCT - number of discrete angles (usually $NØEF/2_{integral}$).

ISTAT - flag to store Legendre coefficients if greater than zero.

CARD XC (11I5)

IRDSG† - switch to print the cross sections as they are read if > 0.

ISTR† - switch to print cross sections as they are stored if > 0.

IFMU† - switch to print intermediate results of μ's calculation if > 0.

IMØM† - switch to print moments of angular distribution if > 0.

IPRIN† - switch to print angles and probabilities if > 0.

IPUN† - switch to print results of bad Legendre coefficients if > 0.

IDTF† - switch to signal that input format is DTF-IV format if [illegible]; otherwise, ANISN format is assumed.

IXTAPE - logical tape unit if binary cross section tape, set equal to 0 if cross sections are from cards. If negative, then the processed cross sections and other necessary data from a previous run will be read; in this case (IXTAPE < 0) no cross sections from cards and no mixing cards may be input. The absolute value of IXTAPE is the logical tape unit.

JXTAPE - logical tape unit of a processed cross-section tape to be written. This processed tape will contain the title card, the variables from common LOCSEC and the pertinent cross sections from blank common

†Switches are ignored if IXTAPE < 0.

I06RT - logical tape unit of a point cross-section tape in 06R format.

IGQPT - last group (MORSE multigroup structure) for which the 06R point cross sections are to be used ($\leq$ NMGP).

CARD XD (14I5) (Omit if IXTAPE $\leq$ 0)

Element identifiers for cross-section tape. If element identifiers are in same order as elements on tape, the efficiency of the code is increased due to fewer tape rewinds.

CARDS XE (Omit if IXTAPE $\neq$ 0)

If cross sections are in free-form, a card with ** in columns 2 and 3 must precede the actual data.

ANISN format if IDTF $\leq$ 0; otherwise, DTF-IV format. Cross sections for INGP groups with a table length ITBL for NELEM elements each with NCOEF coefficients.

CARDS XF (2I5,E10.5) (Omit if IXTAPE < 0)

NMIX (see Card XB) cards are required.

KM - medium number.

KE - element number occurring in medium KM (negative value indicates last mixing operation for that medium). Failure to have a negative value caused code not to generate angular probabilities for that media (LEGEND and ANGLE not called).

RHO - density of element KE in medium KM.

CARDS XG (I5) (Omit if I06RT $\leq$ 0)

NXPM - number of point cross-section sets per medium found on an 06R tape.

= 1, total cross section only,

= 2, total + scattering cross section,

= 3, total, scattering, and ν*fission cross section.

NOTE: Cross sections and cross-section input data may be checked independently of MORSE utilizing XCHEKR. The input to XCHEKR consists of the cross-section cards XA through XG preceded by a card as follows:
Format (4I5)

IADJM - set greater than zero for an adjoint problem.

MEDIA - number of cross-section media; should equal NMED on Card XB.

NMGP - number of primary particle energy groups for which cross sections are to be stored; should equal NGP on Card XB.

NMTG - total number of energy groups for which cross sections are to be stored. Should be equal to INGP on Card XB.

B.4 SAMBØ Analysis Input Instructions

The following data are read from cards by SCØRIN:

CARD AA (20A4)

Title information - will be immediately output.

CARD BB (8I5)

ND - number of detectors (set = 1 if ≤ 0).

NNE - number of primary particle (neutron) energy bins to be used (must be $\leq$ NE).

NE - total number of energy bins (set = 0 if ≤ 1)

NT - number of time bins for each detector (may be negative, in which case |NT| values are to read and used for every detector) (set = 0 if |NT| ≤ 1).

NA - number of angle bins (set = 0 if ≤ 1).

NRESP - number of energy-dependent response functions to be used (set = 1 if ≤ 0).

NEX - number of extra arrays of size NMTG to be set aside (useful, for example, as a place to store an array of group-to-group transfer probabilities for estimator routines).

NEXND - number of extra arrays of size ND to be set aside (useful, for example, as a place to store detector-dependent counters).

CARDS CC (3E10.4) (ND cards will be read)

X,Y,Z - detector location. (if other than point detectors are desired, the point locations must still be input and can be combined with additional data built in to user routines to fully define each detector).

Note that the distance between the above points and the XSTRT, YSTRT, ZSTRT values and the initial age, AGSTRT, will be used to define the lower limit of the first time bin.

CARD DD (20A4)

Title or units for total responses for all detectors. Will be used in columns 54 through 133 of the title for the print of these arrays.

CARD EE (20A4)

Title or units for each total response for all detectors.

CARDS FF (7E10.4)

Response function values. NMTG values will be read in each set of FF cards. Input order is from energy group 1 to NMTG (order of decreasing energy).

NOTE: Cards EE and FF are read in the following order: EE, FF1, . . . FFN, EE, FF1, . . . FFN, etc. NRESP sets of EE, FF cards will be read.

CARD GG (20A4) (Omit if NE $\leq$ 1)

Units for energy-dependent fluence for all detectors.

CARD HH[6](14I5) (Omit if NE $\leq$ 1)

Energy group numbers defining lower limit of energy bins (in order of increasing group number). The NNE (if > 0) energy must equal NGPQTN; the NE entry must be set to NMGP + NGPQTG for a combined problem, or else NGPQTG or NGPQTN.

CARD II (20A4) (Omit if |NT| $\leq$ 1)

Units for time-dependent total responses for all detectors.

CARD JJ (20A4) (Omit if |NT| $\leq$ 1 or NE $\leq$ 1)

Units for time and energy-dependent fluence for all detectors.

CARDS KK (7E10.4) (omit if NT $\leq$ 1)

NT values of upper limits of time bins for each detector (in order of increasing time and detector number). The values for each detector must start on a new card. |NT| values only are read if NT is negative. They are then used for every detector.

CARD LL (20A4) (Omit if NA $\leq$ 1)

Units for angle- and energy-dependent fluence for all detectors.

CARD MM (7E10.4) (Omit if NA $\leq$ 1)

NA values of upper limits of angle bins (actually cosine bins; the NA^{th} value must equal one).

Following the input for the SAMBØ analysis module, input cards for user-written routines INSCØR, SØURCE, and ENDRUN.

APPENDIX C

LISTING OF SUBROUTINE ALBDØ

```
SUBRØUTINE ALBDØ     74/74   ØPT=1          FTN 4.6+433D

      SUBRØUTINE ALBDØ (IG,U,V,W,WATE,IMED,NREG)
C     ALBEDØ REFLECTIØN ACCØRDING TØ THE BLACKNESS THEØRY (NAVAL REACTØR
C     HANDBØØK, 1964)    ESAM HUSSEIN, MC MASTER UNIV. MARCH, 1975.
      COMMØN /NØRMAL/ UNØRM,VNØRM,WNØRM
      COMMØN /LØCSIG/ISTART,ISCCØG,INABØG,IGABØG,IFPØRG,IFNGP,IFSPØG,
     1         IDSGØG,IPRBNG,IPRBGG,ISCANG,ISCAGG,ISPØRG,ISPØRT,INPBUF,
     2         ISIGØG,INFPØG,IABSØG,ITUTSG,NGP,NDS,NGG,NDSG,INGP,INDS,
     3         NMED,NELEM,NMIX,NCØEF,NSCT,NTS,NTG,NDSNGP,NDSNGG,IADJ,
     4         NME,LØC,INGS,INSG,I1,I0,KKK,IXTAPE,IDEL,ITEML,ITEMG,IRSG,
     5         IRDSG,ISTR,IPRIN,IFMU,IMOM,IDTF,ISTAT,IPUN
     6         ,NUS,NGN,IHT,INUS,INUSN,INGN,INGNP,INNN,IGGG
      COMMØN/ALBLØCK/ MEALB,ROO(11),R10(11)
      COMMØN SIGT(1)
      DIMENSION NSIG(1)
      EQUIVALENCE (SIGT(1), NSIG(1))
      DATA ICALL /1/
      DATA JCALL /1/
      IF(ABS(UNØRM).EQ.1.) GØ TØ 4
      IF(ABS(VNØRM).EQ.1.) GØ TØ 4
      IF(ABS(WNØRM).EQ.1.) GØ TØ 4
      GØ TØ 400
    4 CØNTINUE
      IFLAG=0
      IF(ICALL) 6,6,5
    5 ICALL=0
      WRITE(I0,1000)
 1000 FØRMAT(55H YØU ARE USING SLABS REFLECTIØN CØEFFICIENTS FØR ALBEDØ)
    6 CONTINUE
      MED=MEALB
      IGMED=(MED-1)*ISPØRG+IG
      PNAB=SIGT(IGMED + INABØG)
      NPNAB=PNAB*10.0
      XPNAB=NPNAB/10.0
      DPNAB=(PNAB-XPNAB)*10.0
      RROO=ROO(NPNAB+1)+DPNAB*(ROO(NPNAB+2)-ROO(NPNAB-1))
      RR10=R10(NPNAB+1)+DPNAB*(R10(NPNAB+2)-R10(NPNAB-1))
      WATE=WATE*RROO
      IF(WATE.EQ.0) RETURN
C     FØLLOW SUB. CØLISN TØ GET THE ØUT GØING ENERGY
      IF(IG-NGP) 10,10,15
   10 IH=IG
      NDSK=NSIG(INNN+IG)
      IS=(MED-1)*ISPØRG+IFSPØG+NSIG(INGS+IG)
      NADDPG=0
      ITE=NSIG(INGS+IH)
      GØ TØ 20
   15 NADDPG=IPRBGG-IPRBNG
```

```
      IH=IG-NGP
      NDSK=NSIG(IGGG+IH)
50    ITE=NSIG(INSG+IH)
      IS=(MED-1)*ISPØRG+ITE+IDSGØG
   20 IF(LØC) 25,25,35
   25 C9=0.0
      R=FLTRNF(0)
55    DØ 30 I=1,NDSK
      C9=C9+SIGT(IS+1)
      IF(C9-R) 30,40,40
   30 CØNTINUE
      I=NDSK
60    GØ TØ 40
   35 IND=LØC+NTG*(NREG-1)
      CALL GTIØUT(IS,I,NREG,NDSK,IG,WATE,IND)
   40 IG=IG+I-1-NUS
      IHD=IG
65    IF(IG.EQ.33)WATE=0.
      IF(IFLAG,EQ.1)RETURN
C     CALCULATE ØUT GØING DIRECTIONS FRØM THE REFLECTION CØEFF.
C     TH IS THE ANGLE WITH THE Z AXIS
C     FY IS THE ANGLE WITH THE X AXIS
70    C     U= SIN TH * CØS FY
C     V= SIN TH * SIN FY
C     W= CØS TH
C     XUINC = CØS THE ANGLE BETWEEN THE INCØMING PARTICLE AND THE
C     ØUTWARD NØRMAL TØ THE ALBDØ SURFACE. (ALWAYS NEGATIVE)
75    C     XUREF = CØS THE ANGLE BETWEEN THE ØUTGØING PARTICLE AND THE
C     ØUTWARD NØRMAL TØ THE ALBDØ SURFACE (ALWAYS PØSITIVE)
      XUINC=UNØRM+VNØRM*V+WNØRM*W
      XUREF=-RR10*XUINC/RROO
      IF(ABS(UNØRM).EQ.1.0) GØ TØ 100
80    IF(ABS(VNØRM).EQ.1.0) GØ TØ 200
      IF(ABS(WNØRM).EQ.1.0) GØ TØ 300
C 100 UNØRM=1. , THE REFLECTING SLAB IS THE (Y - Z) PLANE
C     W WILL NØT BE CHANGED, CØSTH=W, XUREF=U
  100 U=XUREF/UNØRM
85    SINTH=SQRT(1.0-W*W)
      CØSFY=XUREF/SINTH
      SINFY=SQRT(1.0-CØSFY**2)
      V=SINTH*SINFY
      RETURN
90    C 200 VNØRM=1. ,THE REFLECTING SLAB IS THE (X-Z) PLANE
C     W WILL NØT BE CHANGED, CØSTH=W , XUREF=V
  200 V=XUREF/VNØRM
      SINTH=SQRT(1.0-W*W)
      SINFY=XUREF/SINTH
95    CØSFY=SQRT(1.0-SINFY**2)
      U=SINTH*CØSFY
      RETURN
C 300 WNØRM=1. , THE REFLECTING SLAB IS THE (X-Y) PLANE
C     FY WILL NØT BE CHANGED, XUREF=CØSTH
100   300 W=XUREF/WNØRM
      SINTH=SQRT(1.0-XUREF**2)
      UPV=SQRT(U*U+V*V)
      CØSFY=U/UPV
```

```
      SINFY=V/UPV
105   U=SINTH*COSFY
      V=SINTH*SINFY
      RETURN
C 400 SPECULAR REFLECTION IS USED FOR NON PLANER GEOMETRIES
  400 IF(JCALL) 410,410,405
110   405 JCALL=0
      WRITE(IO,3000)
 3000 FORMAT(58H,YOU ARE USING SPECULAR REFLECTION FOR NON PLANER SURFAC
     *ES)
  410 DOT=2.*(UNORM*U+VNORM*V+WNORM*W)
115   U=U-DOT*UNORM
      V=V-DOT*VNORM
      W=W-DOT*WNORM
      IFLAG=1
      GOTO 6
120   END
```

APPENDIX D

DERIVATION OF $P_j(E_0)$

In principle, a neutron, independent of its initial energy E_0, can be thermalized in a single collision with a hydrogen nucleus. However, the probability of this happening depends on the initial energy E_0. After one collision with a hydrogen nucleus, the energy of the neutron can be anywhere between 0 and E_0. The probability density distribution of this neutron having an energy E_1 below E_0 after the collision is $1/E_0$. Thus, the probability P_1 of the neutron energy falling below the subcadmium neutron energy E_c after exactly one collision is E_c/E_0, and is very small when E_0 is high (e.g. 2.5×10^{-7} for E_0 = 2 MeV).

If the neutron suffers two collisions, it can become a subcadmium neutron by first being down scattered into E_c from E_1. The probability $dP(E_1)$ of it being scattered into any energy dE_1 about E_1 from E_0 in the first collision is

$$dP_1(E_1) = dE_1/E_0 \tag{D.1}$$

Thus, the probability dP_2 of the neutron being subsequently scattered into the subcadmium energy E_c from E_1 is then $dP_2=(E_c/E_1)(dE_1/E_0)$. The probability that the neutron becomes subcadmium neutron in exactly 2 collisions P_2 is then

$$P_2 = \int_{E_c}^{E_0} \frac{E_c}{E_1}\frac{dE_1}{E_0}$$

$$= \frac{E_c}{E_0} \ln(E_0/E_c) \tag{D.2}$$

The probability that the neutron becomes subcadmium neutron after exactly 3 collisions is the integral of the differential probability $dP_3(E_2)$ of it being scattered to dE_2 about energy E_2 after 2 collisions. Similar to Eq.(D.2), $dP_3(E_2)$ is

$$dP_3(E_2) = \int_{E_2}^{E_0} \frac{dE_2}{E_1} \frac{dE_1}{E_0} \tag{D.3}$$

The probability P_3 is then

$$\begin{aligned} P_3 &= \int_{E_c}^{E_0} \frac{E_c}{E_2 E_0} \ln(E_0/E_2)\, dE_2 \\ &= \frac{E_c}{E_0} \int_{E_c}^{E_0} \ln(E_0/E_2) \frac{dE_2}{E_2} \\ &= \frac{E_c}{E_0} \frac{\ln(E_0/E_c)^2}{2} \end{aligned} \tag{D.4}$$

In a similar manner, the probability P_4 that the neutron becomes subcadmium in exactly 4 collisions is

$$P_4 = \frac{E_c}{E_0} \frac{\left[\ln(E_0/E_c)\right]^3}{2 * 3} \tag{D.5}$$

By induction, the probability $P_j(E_0)$ that the neutron becomes subcadmium neutron in exactly j collisions is

$$P_j(E_0) = \frac{E_c}{E_0} \frac{\left[\ln(E_0/E_c)\right]^{j-1}}{(j-1)!} \tag{D.6}$$

APPENDIX E

ESCAPE OF NEUTRON FROM ANNULAR FLOW TEST SECTION

From the Monte Carlo study, it was observed that, for a fixed α, a neutron seems to suffer a smaller number of collisions in a test section of annular flow pattern than in inverted annular flow pattern. This phenomenon can be explained by a higher surface area to volume ratio in annular flow.

The number of collisions suffered by a neutron in a volume of water decreases with the leakage probability. The escape or leakage of neutrons occurs at the exterior, but collision, leading to the slowing down of neutrons, occurs throughout the whole of the interior of water portion. Thus, the leakage probability increases with the surface area to volume ratio. It can be shown that the surface area to volume ratio r is always higher for annular flow as the following.

For a given test section of inside diameter D_0, the void fraction α for inverted annular flow is given by

$$\alpha = 1 - (D_c/D_0)^2 \qquad (E.1)$$

where D_c = diameter of water core

and for annular flow,

$$\alpha = (D_a/D_0)^2 \qquad (E.2)$$

where D_a = diameter of core of air

For inverted annular flow, ignoring surface areas at both top and

bottom, the surface area A_c and volume of the water core V_c are given by

$$A_c = \pi D_c H \tag{E.3}$$

and $$V_c = \pi D_c^2 H/4 \tag{E.4}$$

where H = height of water core

For inverted annular flow, the surface area A_a and volume V_a of the water portion are given by

$$A_a = \pi D_0 H \tag{E.5}$$

$$V_a = \pi (D_0^2 - D_a^2) H/ 4 \tag{E.6}$$

Hence, from Eqs.(E.3),(E.4),(E.5), and (E.6), the surface area to volume ratios, r_c and r_a, for inverted annular and annular flows are

$$r_c = 4/D_c \tag{E.7}$$

and $$r_a = 4/[D_0 (1 - D_a^2/D_0^2)] \tag{E.8}$$

The ratio r_a/r_c is then

$$r_a/r_c = (D_c/D_0) / (1 - D_a^2/D_0^2) \tag{E.9}$$

Substituting Eqs.(E.1) and (E.2) into Eq.(E.9), we have

$$r_a/r_c = (1 - \alpha)^{\frac{1}{2}}/ (1 - \alpha)$$

$$= 1 / (1 - \alpha)^{\frac{1}{2}} \tag{E.10}$$

From Eq.(E.10), since $\alpha < 1$, $r_a > r_c$. The leakage is therefore always higher in annular flow than inverted annular flow for any α, and it can also be seen that the relative leakage increases rapidly as α approaches 1. It is concluded that a neutron suffers lesser number of collisions in annular flow than inverted annular flow for a fixed α.

APPENDIX F

ERROR IN MEASURED $\bar{\alpha}$ DUE TO DYNAMIC FLUCTUATION OF VOID FRACTION

This appendix is intended to clarify the statement in section 2.3.1 that, in steady state measurement of the time averaged void fraction $\bar{\alpha}$, the time averaged detector response $\bar{N}(\bar{\alpha})$ does not necessarily follow the same calibration curve obtained with stagnant test sections.

Suppose the detector response (neutron counting rate), $N(\alpha)$, is calibrated against stagnant test sections (mock-ups) of known α, and a calibration curve $f(\alpha)$ is obtained in the form

$$N(\alpha) = f(\alpha) \tag{F.1}$$

In steady state measurements, the void fraction α fluctuates and thus the detector response $N(\alpha)$. At each instant t, we can assume that Eq.(F.1) holds. That is,

$$N(\alpha(t)) = f(\alpha(t)) \tag{F.2}$$

However, over a time span T, the time averaged detector response $\bar{N}(\bar{\alpha})$ is given by

$$\bar{N}(\bar{\alpha}) = \frac{1}{T}\int_0^T f(\alpha(t))dt \tag{F.3}$$

The time averaged void fraction $\bar{\alpha}$ is then given by

$$\bar{\alpha} = \frac{1}{T}\int_0^T \alpha(t)dt \tag{F.4}$$

From Eqs. (F.3) and (F.4), it is evident that $\bar{N}(\bar{\alpha})$ does not

necessarily follow the same relationship as $f(\bar{\alpha})$. That is,

$$\bar{N}(\bar{\alpha}) \neq f(\bar{\alpha}) \tag{F.5}$$

unless $f(\alpha)$ belongs to a special class of functions. A linear calibration curve belongs to this class.

Suppose $f(\alpha)$ is linear and is given by

$$f(\alpha) = a + m\alpha \tag{F.6}$$

Then, $\bar{N}(\bar{\alpha})$, by Eq.(F.3), is given by

$$\begin{aligned} \bar{N}(\bar{\alpha}) &= \frac{1}{T}\int_0^T [a + m\alpha(t)]dt \\ &= a + \frac{m}{T}\int_0^T \alpha(t)dt \\ &= a + m\,\bar{\alpha} \end{aligned} \tag{F.7}$$

Thus, $\bar{N}(\bar{\alpha})$ follows the same relationship with $\bar{\alpha}$ as $N(\alpha)$ with α, i.e. is also linear with $\bar{\alpha}$.

From the above discussions, it is evident that, when a non-linear calibration curve obtained with stagnant test section is used to measure steady state time averaged void fraction $\bar{\alpha}$, substantial systematic error may result. In fact, Harms and Forrest <128> have shown that, in the measurement of void fraction with thermal neutron attenuation, the systematic error $\Delta\bar{\alpha}$ caused by this kind of dynamic effect, can be as high as 0.2.

REFERENCES

1. Bird, R.B., Stewart, W.E., and Lightfoot, E.N., Transport Phenomena, John Wiley & Sons.

2. Collier, J.G., Convective Boiling and Condensation, McGraw-Hill, 1972.

3. Wallis, G.B., One Dimensional Two Phase Flow, McGraw-Hill, 1969.

4. Ginoux, J.J. (editor), Two Phase Flow and Heat Transfer with Application to Nuclear Reactor Design Problems, McGraw-Hill, 1978.

5. Agee, L.J., Banerjee, S., Duffey, R.B., and Hughes, E.D., "Some Aspects of Two-Fluid Models and Their Numerical Solutions", paper presented at 2nd OECD/NEA Specialists' Meeting on Transient Two-Phase Flow, Paris, 1978.

6. Boure, J.A., "On a Unified Presentation of the Non-Equilibrium Two-Phase Flow Model", Non-Equilibrium Two Phase Flows, pp 1-10, ASME, New York, 1975.

7. Hughes, E.D., Lyczkowski, R.W., and McFadden, J.H., "An Evaluation of State-of-the-Art Two-Velocity Two-Phase Flow Models and their Applicability to Nuclear Reactor Transient Analysis", EPRI Report NP-143, 1976.

8. Yadigaroglu, G., and Lahey, R.T., "On the Various Forms of the Conservation Equations in Two-Phase Flow", Int. J. of Multiphase Flow, Vol 2, pp 447-494, 1978.

9. Delhaye, J.M and Achard, J.L., "On the Averaging Operators Introduced in Two-Phase Flow Modelling", paper presented at 1st OECD/NEA Specialists' Meeting on Transient Two-Phase Flow, Toronto, 1976.

10. Ishii, M., "Thermo-Fluid Dynamic Theory of Two-Phase Flow", Eyrolle, Paris, 1975.

11. Nigmatulin, R.E., "Averaging in Mathematical Modelling of Heterogeneous and Dispersed Mixtures", Paper presented at Int. Centre for Ht. and Mass Transfer Symposium, Yugoslavia, 1978.

12. Banerjee, S. and Chan, A.M.C., "Analysis of the Averaged and Local Instantaneous Formulations", Int. J. Multiphase Flow, Vol. 6, pp. 1-24, 1980.

13. Banerjee S. and Hancox, W.T., "Transient Thermalhydraulics Analysis for Nuclear Reactors", In Proc. 6th Int. Heat Transfer Conf. Key note Lectures, pp 311-337, 1978.

14. Banerjee, S. and Lahey, R.T., "Advances in Two-Phase Flow Instrumentation", Advances in Nuclear Science and Technology, Vol 13, Plenum Publishing Corporation, 1981.

15. Hewitt, G.F. and Lovegrove, P.C., "Experimental Methods in Two-Phase Flow Studies", Electric Power Research Institute Report, EPRI NP-118, 1976.

16. Lahey, R.T., "A Review of Selected Void Fraction and Phase Velocity Measurement Techniques", Lecture presented at Fluid Dynamics Institute Short Course on Two Phase Flow Measurement Techniques, Dartmouth College, New Hampshire, Auguest, 1978.

17. Johnson, H.A and Abou-Sabe, A.H., "Heat Transfer and Pressure Drop for Turbulent Flow of Air-Water Mixture in a Horizontal Pipe", Transactions ASME, pp 977-987, 1952.

18. Hewitt, G.F., King, I., and Lovegrove, P.C., "Holdup and Pressure Drop Measurements in the Two-Phase Annular Flow of Air-Water Mixtures", U.K. Atomic Energy Report, AERE-R3764, 1961.

19. Banerjee, S., Heidrick, T.R. and Rhodes, E., "Development and Calibration of Instrumentations for Measurements in Transient Two-Phase Flow", Proceedings of 2nd CSNI Specialists' Meeting on Transient Two-Phase Flow (OECD/NEA), Paris, June, 1978.

20. Agostine, G., Era, A., and Premoli, A., "Density Measurements of Steam-Water Mixtures Flowing in a Turbulent Channel under Adiabatic and Heated Conditions, CISE Milan Report CISE-R-291, 1969.

21. Banerjee, S. and Jolly, D.O.P., "Analysis of Steady-State Steam-Water Mass Velocity Measurements", Final Report EG & G (subcontract No. S-8561), 1977.

22. Smith, J.E., "Gyroscopic/Coriolis Mass Flow Meter", Canadian Controls and Instrumentation, Vol. 29, Jan, 1978.

23. Hsu, Y.Y., Simon, F.F., Graham, R.W., "Application of Hot-Wire Anemometry for Two-Phase Flow Measurements such as Void Fraction and Slip Velocity", in ASME Symposium Volume on Multiphase Flow, pp 26-34, 1963.

24. Goldsmidt, V.W., "Measurement of Aerosol-Concentration with a Hot-Wire Anemometer", J. Colloid Sci., Vol 20, pp 617-634, 1965.

25. Delhaye, J.M., "Hot Film Anemometry in Two-Phase Flow, "Eleventh National ASME/AIChE Heat Transfer Conference, Mineapolis, pp 58-69, August, 1969.

26. Shiralkar, B.S. and Lahey, R.T., "Diabatic Local Void Fraction Measurements in Freon-114 with a Hot Wire Anemometer", ANS Trans., Vol 15, Part 2, pp 880, 1972.

27. Kobori, T., "Application of the Needle Contact Probe to Blowdown Test", Proceedings of the Second CSNI Specialists' Meeting on Transient Two-Phase Flow, Paris, June, 1978.

28. Delhaye, J.M., Semeria, R., and Flamand, J.C., "Measurement with a Micro-Thermocouple of the Local Void Fraction and the Temperature of the Liquid and Vapour in Two-Phase Flow with Phase Change", CEA Report R-4302, 1972.

29. Wenger, H.C. and Smetana, J., "Hydrogen Density Measurements using an Open-ended Microwave Cavity", IEEE Transactions on Instrumentation and Measurements, IMA 21, pp 102-105, 1972.

30. Stuchly, S.S., Rzepecka, M.A. and Hamid, M.A.K., "Microwave Open-ended Cavity as Void Fraction Monitor for Organic Coolants" IEEE Transactions on Independent Electronics and Control Instrumentations, Vol. IECI-21, pp 78-80, 1974.

31. Daves Manufacturing Co., "Microwave Liquid Level Gauge for Use in a High Radiation Environment", US Patent Application No. 174133, 1980.

32. Barschdorff, D., Class, G., Loffel, R., and Reimann, J., "Mass Flow Measuring Techniques", in Transient Two-Phase Flow, pp 835-867, Hemisphere Press, Washington 1978.

33. Snyder,S.C. and Baker, A.G., "Infrared Technique for measuring Steam Density", EG & G Report M-02282, 1982.

34, Ramaswamy, A., Agamy, S.A., and Banerjee, "Measurement of Noncondensible Distribution of Two-Phase Flow Experiments Using Ultraviolet Attenuation Techniques", IUTAM Symposium Nancy/France , Springer-Verlag, 1983.

35. Miller, N. and Mitchii, R.F., "The Development of a Universal Probe for Measurement of Local Voidage in Liquid/Gas Two Phase Flow System", ASME Symposium Volume, Two-Phase Flow Instrumentation, 1969.

36. Danel, F. and Delhaye, J.M., "An Optical Probe for Measuring Local Voidage in Two-Phase Flow", Mesres, Aug-Sept, 1971, pp 99-101.

37. Delhaye, J.M. and Galaup, J.P., "Measurement of Local Void Fraction in Freon 12 with a 0.1 mm optical Fibre Probe", European Two-Phase Flow Meeting, June 1974, Harwell, paper A6.

38. Jones, O.C. Jr. and Zimmer, G.A., "Optical Probe for Local Void Fraction and Interface Velocity Measurements", Rev. Sci. Instrum., Vol 49, pp 1090-1094, 1978.

39. Vince, M., Breed, H.E., Lahey, R.T. Jr., "The Development of a High Temperature Optical Void Probe", Trans. Am. Nucl. Soc., Vol 30, pp 502-3, 1978.

40. Vince, M.A., Breed, H., Krycuk, G., Lahey, R.T. Jr., "Optical Probe for High Temperature Local Void Fraction Determination", Appl. Opt., Vol. 21, No. 5, pp 886-892, 1982.

41. Lockett, M.J. and Safekorori, A.A., "Light Transmission Through Bubble Swarms", AIChE Journal, Vol 23, No. 3, pp 395-398, 1977.

42. Lahey, R.T. Jr., "Review of some selected Nonintrusive Nuclear and Optical Techniques for the Determination of Void Fraction, Flow Regime, and Two-Phase Flow Rate", Trans. Am. Nucl. Soc., Vol. 39, pp 1006-9, 1981.

43. Chang, J.S., Ischikawa, Y., and Irons, G., "Flow Regime Characterization and Liquid Film Thickness in Horizontal Gas-Liquid Flow by Ultrasonic Method", Measurements Polyphase Flow, ASME PRESS, pp 7-12, 1982.

44. Chang, J.S., Ischikawa, Y., Irons, G.A., Morala, E.C., and Wan, P.T., "Void Fraction Measurement by an Ultrasonic Transmission Technique in Bubbly Gas-Liquid Two-Phase Flows", IUTAM Symposium Nancy/France, Springer-Verlag, pp 319-336, 1983.

45. Hoogendorn, C.J., "Gas-Liquid Flow in Horizontal Pipes", Chem Engng. Sci, Vol 8, pp 205-217, 1959.

46. Cimorelli, L. and Evangelisti, R., "The Application of the Capacitance Method for Void Fraction Measurement in Bulk-Boiling Conditions", Int. J. Heat Transfer, Vol 10, pp 277-288, 1967.

47. van Vonderen, A.C.M. and van Vlaardingen, H.F., "Impedance Void Gauge for Cylindrical Channels", Europ. Two-Phase Flow Group Meeting, Milan, June, 1970, Paper B10.

48. Carrard, G. and Ledwidge, T.J., "Measurement of Slip Distribution and Average Void Fraction in an Air-Water Mixture", Int. Symp. on Two-Phase Systems, Haifa, Israel, Aug-Sept, 1971, pp 3-13.

49. Subbotin, V.I., Sorokin, D.N., Tzyganok, A.A., and Gribov, A.A., "Investigation of Vapour Bubbles Effect on Temperature of Heat Transferring Surface at Nucleate Boiling", 5th Int. Ht. Transfer Conf. Sci. Council Japan, Sept. 1974, Vol 4, 1974.

50. Rosehart, R.G.D., Rhodes, R.G., and Scott, D.S., "Studies of Gas-Liquid Slug Flow Void Fraction Meter, Void Fraction and Slug Characteristics", Chem. Engng, Vol 10, pp 57-64, 1975.

51. Merilo, M., Dechene, R.L., and Cichowles, W.M., "Void Fraction Measurement with a Rotating Field Conductance Gauge", Journal Heat Transfer, Vol. 99, pp 330, 1977.

52. Khalil, A. and McIntosh, G., "Experimental Measurement of Void Fraction in Cryogenic Two-Phase Upward Flow", Cryogenics (GB), Vol. 21, No. 7, pp 411-14, 1981.

53. Kobori, T., "Development of Void Fraction for Transient Two-Phase Flow", in Transient Two-Phase Flow, Vol. 2, pp 692-701, Hemisphere Press, Washington, 1978.

54. Kobori, T., "Application of the Needle Contact Probe to Blowdown Test", Proceedings of the Second CSNI Specialists' Meeting on Transient Two-Phase Flow (OECD/NEA), Paris, June, 1978.

55. Arave, A.E., Goodrich, L.D., and Schulz, G.L., "A Liquid Level Detector for LOFT Two-Phase Environments", in Transient Two-Phase Flow, Vol. 2, pp 747-788, Hemisphere press, 1978.

56. Vince, M.S., Krychuk, G., and Lahey, R.T. Jr., "Development of a Radio Frequency Excited Local Impedance Probe", Nucl. Eng. & Design (Netherlands), Vol. 67, No.1, pp 125-36, 1981.

57. Abuaf, N., Feierabend, T.P., Zimmer, G.A., and Jones, O.C. Jr., "Radio Frequency Probe for Bubble Size and Velocity Measurement", Rev. Sci. Instrum. (USA), Vol. 50, No. 10, pp 1260-3, 1979.

58. Lynch, G.F. and Segel, S.L., "Direct Measurement of the Void Fraction of Two-Phase Fluid by Nuclear Magnetic Resonance", Int. J. Heat Mass Transfer, Vol 20, pp 7-14, 1977.

59. Saxe, R.F., "Use of Nuclear Magnetic Resonance Techniques for the Measurement of Two-Phase Phenomena", Final Report, DOE/ER/10627-T1, 1983.

60. English, D., Blacker, P.T., and Simons, W.E., "Boiling and Density Studies at Atmospheric Pressure, U.K. Atomic Energy Authority Report, AERE BO/M20, 1955.

61. Styriknovich, M.A. and Nevstruuva, E.I., "Investigation of Vapour-Content Distribution in Boiling Boundary Layer by the Beta-Radioscop Method", Dobel. Akad. Nauk. SSSR., Vol 130, pp 1019-1022, 1960.

62. Perkins, H.C., Yusuf, M. and Leppert, G., "A Void Measurement Technique for Local Boiling", Nuclear Science and Engineering, Vol. 1, pp 304-311, 1961.

63. Zirnig, W., "Beta Absorption Measuring System for Steam-Water-Air Mixture Density in Containment LOCA Experiments" Proceedings of the Second CSNI Specialists' Meeting on Transient Two-Phase Flow, OECD/NEA, Paris, June 1978.

64. Schrock, V.E., "Radiation Attenuation Techniques in Two-Phase Flow Measurement, Eleventh National ASME/AIChE Heat Transfer Conference, Minneapolis, pp 24-35, 1969.

65. Smith, A.V., "Transient Density Measurements in Two-Phase Flow Using X-rays", Journal British Nuclear Energy Society, Vol. 10, pp 99-106, 1971.

66. Vince, M.A. and Lahey, R.T. Jr., "On the Development of an Objective Flow Regime Indicator", Int. J. Multiphase Flow (GB), Vol. 8, No. 2, pp 93-124, 1982.

67. Jeandey, Ch., "Multibeam X-ray Densitometer for Flow Pattern and Void Fraction Determination in Steam Water Mixtures", Measurements in Polyphase Flow, Heidrick, T.R. & Patel, B.R., Eds, ASME G 00209, pp 19-28, 1982.

68. Fournier Th. and Jeandey. Ch., "Optimization of an Experimental Setup for Void Fraction Determination by the X-ray Attenuation Technique", Measuring Techniques in Gas-Liquid Two-Phase Flows, IUTAM Symposium Nancy/France, Springer-Verlag, 1983.

69. Schlosser, P.A., DeVuono, A.C., Kulacki, F.A., and Munshi, "Analysis of High-Speed CT Scanners for Non-Medical Applications", IEEE Trans. Nucl. Sc., Vol NS-27, No.1, pp 788, 1980.

70. DeVuono, A.C., Schlosser, P.A., Kulacki, F.A., and Munshi, "Design of an Isotopic CT Scanner for Two-Phase Measurements", IEEE Trans. Nucl Sci., Vol NS-27, No.1, pp 814, 1980.

71. Iizuka, M., Mordoka, S., Ishizuka, T., Konagai, C., and Kimua, H., "Two-Phase Flow Measurement by CT Scanner", Trans. Am. Nucl. Soc., Vol. 43, p. 790-1, 1982.

72. Ikeda, T., Kotani, K., Mzaeda, Y., Kohno, H., "Preliminary Study on Application of X-ray CT Scanner to Measurement of Void Fractions in Steady State Two-Phase Flows", J. Nucl.

Sci. Technology, Vol. 20, pp 1-12, 1983.

73. Narabayashi, T., Tobimatsu, T., Nagasaka, H., "Measurement of Transient Flow Pattern by High Speed Scanning X-ray Void Fraction Meter", IUTAM Syposium Nancy/France, Springer-Verlag, pp 259-280, 1983.

74. Bailey, R.V., Zmola , P.C., and Taylor, F.M., "Transport of Gas Through Liquid Gas Mixtures", ORNL-CF-55-12-118, 1955.

75. LeVert, F.E. and Helminsky, E., "A Dual Energy Method for Measuring Void Fractions in Flowing Mediums", Nuclear Technology, Vol. 19, pp 58-60, 1973.

76. Evangelisti, R. and Lupoli, P., "The Void Fraction in an Annular Channel at Atmospheric Pressure", Int. J. Heat Mass Transfer, Vol. 12, pp 699-711, 1969.

77. Zakharova, E.A., Kolchugin, B.A., and Kosniukhin, I.P., "Vapour Void-Fraction in Annular Channels at Separated and Joint Heat Supplied", 4th Int. Heat Transfer Conference, Paris, Vol. 5, paper B5.5, 1970.

78. Gustaffsson, B. and Kjellen, B., "Two-Phase Flow in a 9-Rod Bundle with Inclined Power Distribution", European Two-Phase Flow Group Meeting, RISO paper A5, Denmark, 1971.

79. Chan, A.M.C. and Banerjee, S., "Design Aspects of Gamma Densitometers for Void Fraction Measurements in Small Scale Two-Phase Flow", Nucl. Instrum. Methods, Vol 190, pp 135-148, 1981.

80. Fortescue, T., Ohlmer, E., and West, G., "LOBI Spectrum-Stablized Gamma Densitometers", Measuring Techniques in Gas-Liquid Two-Phase Flows, IUTAM Symposium Nancy/France, Springer-Verlag, pp 229-254, 1983.

81. Lassahn, G.D., "LOFT Three-Beam Densitometer Data Interpretation", TREE-NUREG-1111, 1977.

82. Heidrick, T.R., Saltvold, J.R., and Banerjee, S., "Application of a 3-Beam Gamma Densitometer to Two-Phase Flow Design and Density Measurements, AIChE Symposium Series-Nuclear, Solar and Process Heat Transfer, Vol 73, pp 248-255, 1977.

83. John, H., Reimann, J., Alsmeyer, H., Hahn, H., Megerk, A., "Serial 5-beam Gamma Densitometer for Measuring of Two-Phase Flow Density", Report KFK-2783, 1979.

84. Reimann, J., John, H., Loeffel, R., Solbrig, C.W., Chen, L.L., Good, R.R., "Mass Flow Rate Measurements in Horizontal Steam-Water Flow with a Drag Disc Turbine Transducer, a Gamma Densitometer and the Radiotracer Technique", ANS/ASME Topical Meeting on Reactor Thermal-

Hydraulics, Saratoga, NY, USA, 1980.

85. Hau, K.F. and Banerjee, S., "Measurement of Mass Flux in Two-Phase Flow using Combinations of Pitot Tubes and Gamma Densitometers", AIChE J., Vol 27, pp 177-184, 1981.

86. Kulacki, F.A, Schloser, P.A., DeVuono, A.C., Munshi, P., "Preliminary Study of the Application of Reconstruction Tomography to Void Fraction Measurements in Two-Phase Flows", ANS/ASME Topical Meeting on Reactor Thermal-hydraulics, Saratoga, NY, USA, 1980.

87. Chan, A.M.C., "Void Fraction and Phase Distribution Measurements in Transient Two-Phase Flows", Measuring Techniques in Gas-Liquid Two-Phase Flows, IUTAM Symposium Nancy/France, Springer-Verlag, 1983.

88. Zielke, L.A., Grant, K.W., MacKinnon, J.G., "Void Fraction by Gamma Scattering, Final Report", EPRI-NP-1493, 1980.

89. Gay, R.R., Ohkawa, K., Lahey, R.T. Jr.,"The Measurement of Void Fraction with the Side-Scatter Gamma Technique", Proc. of the 26th International Instrumentation Symposium, Seattle, WA, USA, 1980, pp 253-60.

90. Ohkawa, K. and Lahey, R.T. Jr. "Development of a Gamma-ray Scattering Densitometer and its Application to the Measurement of Two-Phase Density Distribution in an Annular Test Section", NUREG/CR-3374, 1983.

91. Kondic, N. and Lassahn G., "Nonintrusive Density Distribution Measurement in Dynamic High Temperature Systems", 24th Int. Instrumentation Symp., Albuquerque, USA, 1978.

92. Kehler, P., "Measurement of Slow Flow Velocities by the Pulsed Neutron Activation Technique", Proc. of the USNRC Review Group Conference on Advanced Instrumentation for Reactor Safety Research, NUREG/CP-0015, 1980.

93. Kehler, P., "Pulsed Neutron Activation Techniques for the Measurement of Two-Phase Flow", Proc. of the USNRC Review Group Conference on Advanced Instrumentation for Reactor Safety Research, NUREG/CP-0007, 1979.

94. Perez-Griffo, M.L., Block, R.C., and Lahey, R.T. Jr., "Basic Two-Phase Flow Measurements using ^{16}N Tagging Techniques", Proc. of the ANS/ASME/NRC International Topical Meeting on Nuclear Reactor Thermalhydraulics, NUREG-CP-0014, 1980.

95. Perez-Griffo, M.L., Block, R.C., and Lahey, R.T. Jr., "Measurement of Flow in Large Pipes by the Pulsed Neutron Activation Method", Nucl Sc. and Eng., Vol 82, pp 19-33, 1982.

96. Lin, T.F., Block, R.C., Jones, O.C., Lahey, R.T. Jr., and Murase, M., "Two-Phase Flow Measurement using a Pulsed Photon Activation (PPA) Techniques", Measuring Techniques in Gas-Liquid Two-Phase Flows, IUTAM Symposium Nancy/France, Springer-Verlag, 1983.

97. Moss, R.A. and Kelly, A.J., "Neutron Radiographic Study of Limiting Planar Heat Pipe Performance", Int. J. Heat and Mass Transfer, Vol. 13, pp. 491-502, 1970.

98. Harms, A.A., Lo, S., and Hancox, W.T., "Measurement of Time-Average Voids by Neutron Diagnosis", J. Applied Physics, Vol. 42, No. 10, pp 4080-4082, 1971.

99. Younis, M.H., "Void Disturbances in Two-Phase Flow Systems", Ph. D. Thesis, McMaster University, 1978.

100. Hancox, W.T., Forrest, C.F., and Harms, A.A., "Void Determination in Two-Phase Systems Employing Neutron Transmission", ASME Publication, Proceedings of AIChE-ASME Heat Transfer Conf., Denver, Col, 1972.

101. Younis, M.H., Hoffmann, T.W., and Harms A.A., "Neutron Diagnosis of Two-Phase Flow", Nucl. Instrum. & Methods, Vol 187, pp 489-497, 1981.

102. Frazzoli, F.V. and Magrini, A., "Neutron Gauge for Measurement of High Void Fraction in Water-Steam Mixtures", Nucl. Technology, Vol. 45, pp 177-182, 1978.

103. Tominaga, H., Wada, N., Tachikawa, N., Kuramochi, Y., Horinchi, S., Sase, Y., Amano, H., Okubo, N., and Nishikawa, H., "Simultaneous Utilization of Neutrons and Gamma rays from ^{252}Cf for Measurement of Moisture and Density", Int. J. Appl. Radiat. Isot., Vol 34, pp 429-436, 1983.

104. Hussein, E., Banerjee, S., and Meneley D.A., "A New Fast Neutron Scattering Technique for Local Void Fraction Measurement in Two-Phase Flow", in Thermal-hydraulics of Nuclear Reactors, Vol II, Papers presented at 2nd Int. Topical Meeting on Nuclear Reactor Thermalhydraulics, Santa Barbara, Jan 11-14, 1983.

105. Semel, S. and Helf, S., "Measurement of Low Concentrations of Moisture by Fast Neutron Moderation", Int. J. Applied Rad and Isotopes, Vol 20, pp 229-239, 1969.

106. Jackson, C.N. Jr., Allemann, R.T., and Speer, W.G., "Neutron Densitonmeter for Measuring Void Fraction in Steam-Water Flow", Trans. Am. Nucl. Sc., Vol. 11, No. 1, pp 366-367, 1968.

107. Sha, W.T. and Bonilla, C.F., "Out of Pile Steam Fraction Determination by Neutron-Beam Attenuation", Nucl. Appl., Vol 1, pp 69-75, 1965.

108. Rousseau, J.C., Czerny J., and Reigel, B., "Void Fraction Measurements During Blowdown by Neutron Absorption or Scattering Methods", Invited paper presented at OECD/NEA Specialists' Meeting on Transient Two-Phase Flow, Toronto, 1976.

109. Banerjee, S., "Radiation Methods for Two-Phase Flow Measurements", Invited Lecture at USNRC Two-Phase Instrumentation Review Meeting, Washington, Jan., 1977.

110. Banerjee, S., Chan, A.M.C., Ramanathan, N., and Yuen, P.S.L., "Fast Neutron Scattering and Attenuation Technique for Measurement of Void Fractions and Phase Distribution in Transient Flow Boiling", Proceedings 6th Int. Heat Transfer Conf., Vol. 1, pp 351, 1978.

111. Yuen, P.S.L., "Fast Neutron Technique for Void Fraction Measurement", M. Eng. Thesis, McMaster University, 1978.

112. Banerjee, S., Yuen, P.S.L., and Vandenbroek, M.A., "Calibration of a Fast Neutron Scattering Technique for Measurement of Void Fraction in Rod Bundles", Transactions ASME Journal of Heat Transfer, Vol. 101, pp 295, 1979.

113. Ducrose, G., "Determination du taux de wide et de la configuration d'un ecoulement diphasique a l'aide d'un faiseau du neutrons", Doctor of Engineering Thesis, Universite de Paris, 1980.

114. Knoll, G.F., Radiation Detection and Measurement, John Wiley & Sons, 1979.

115. Radiation Sources for Laboratory and Industrial Use, 1974/75, Amersham/Searle Corporation.

116. Neutron Sources: Americium-241/Beryllium and Californium-252, Technical bulletin 76/7, Amersham/Searle Corporation.

117. Price, W.T., Nuclear Radiation, 2nd Ed. McGraw-Hill, 1964.

118. Mughabghab, S.F. and Garber, D.I., Neutron Cross-Sections, Vol II, BNL-325, 3rd Ed., Brookhaven National Laboratory, 1973.

119. Herbst, L.T., Electronic for Nuclear Particle Analyses, Oxford University Press, 1970.

120. Glasstone, S., and Edlund, M., The Elements of Nuclear Reactor Theory, D. Van Nostrand Company, Inc., 1954.

121. Henry, A.F., Nuclear-Reactor Analysis, The MIT Press, 1975.

122. Schaeffer, N.M., Reactor Shielding for Nuclear Engineers, U.S. Atomic Energy Commission, TID-25951, 1972.

123. Emmett, M.B. (Editor), "MORSE-CG, General Purpose Monte Carlo Multigroup Neutron and Gamma-Ray Transport Code Combinatorial Geometry", RSIC Computer Code Collection, CCC-203, Oak Ridge National Laboratory.

124. Greenspan, H., Kelber, C.N., and Okrent, D., (editors), Computing Methods in Reactor Physics, Gordon & Breach Science Publishers, 1968.

125. Hussein, E., Banerjee, S., and Meneley, D., "Simulation of a Neutron Scattering Method for Measuring Void Fraction in Two-Phase Flow", Nucl. Eng. & Des., Vol. 53, pp 393-405, 1979.

126. Radkowsky, A., NAVAL Reactor Handbook, Vol. I, United States Atomic Energy Commission, 1964.

127. McCormack, G.R., "Investigation of Neutron Spectra", M.Sc. Thesis, McMaster University, 1975.

128. Harms, A.A. and Forrest C.F., "Dynamic Effects in Radiation Diagnosis of Fluctuating Voids", Nucl. Sci & Engn., Vol 46, pp 408-413, 1971.